



Defence Research and  
Development Canada

Recherche et développement  
pour la défense Canada



# **RADARSAT-2 mode selection for maritime surveillance**

Roger De Abreu, Matt Arkett, Angela Cheng, Tom Zagon,  
Paris W. Vachon and John Wolfe

This publication is protected by copyright.

Defence R&D Canada warrants that the work was performed in a professional manner conforming to generally accepted practices for scientific research and development.

This report is not a statement of endorsement by the Department of National Defence or the Government of Canada.

Defence R&D Canada – Ottawa

External Client Report  
DRDC Ottawa ECR 2011-168  
November 2011

Canada



# **RADARSAT-2 mode selection for maritime surveillance**

Roger De Abreu, Matt Arkett, Angela Cheng, Tom Zagon, Derek Mueller  
Canadian Ice Service, Environment Canada

Paris W. Vachon, John Wolfe  
DRDC Ottawa

Prepared For:  
Canadian Space Agency  
John H. Chapman Space Centre  
6767 Route de l'Aéroport  
Saint-Hubert, Quebec J3Y 8Y9

This publication is protected by copyright.

Defence R&D Canada warrants that the work was performed in a professional manner conforming to generally accepted practices for scientific research and development.

This report is not a statement of endorsement by the Department of National Defence or the Government of Canada.

## **Defence R&D Canada – Ottawa**

External Client Report  
DRDC Ottawa ECR 2011-168  
November 2011

Principal Author

*Original signed by Paris W. Vachon*

---

Paris W. Vachon

Defence Scientist

Approved by

*Original signed by Caroline Wilcox*

---

Caroline Wilcox

Head, Radar Applications and Space Technologies Section

Approved for release by

*Original signed by Chris McMillan*

---

Chris McMillan

Chair, Defence R&D Canada – Ottawa Document Review Panel

This report is the final project deliverable to the Canadian Space Agency under the Government Related Initiatives Program project "RADARSAT-2 Mode Selection for Maritime Surveillance".

- © Her Majesty the Queen in Right of Canada, as represented by the Minister of National Defence, 2011
- © Sa Majesté la Reine (en droit du Canada), telle que représentée par le ministre de la Défense nationale, 2011

## **Abstract**

---

The main objective of the RADARSAT-2 Mode Selection for Maritime Surveillance (R2MS2) project was to identify and recommend ScanSAR-based maritime surveillance modes for RADARSAT-2 (R-2), while also preparing for exploitation of the RADARSAT Constellation Mission (RCM). The primary focus of R2MS2 was on the performance of wide swath, ScanSAR modes of operation including ScanSAR Wide (SCW) and ScanSAR Narrow (SCN). The following maritime surveillance applications were considered: sea ice surveillance; ice island monitoring; iceberg detection; ship detection; wind speed estimation; oil spill detection; and ocean feature detection. Furthermore, several image quality issues were considered: application look-up table (LUT) performance in converting floating point numbers in the processor into integers in the image product; the block adaptive quantization (BAQ) setting for reduction of raw data volume; and noise subtraction for mitigation of the visual impact of the noise floor for low signal to noise ratio acquisitions. Finally, several tools were developed for DRDC Ottawa's Image Analyst Pro (IA Pro) software test bed to support R2MS2 data processing needs. For the maritime surveillance applications considered, the approach included a combination of theoretical analysis and field trials to gather new data sets of known targets, with validation whenever possible. The trials often focused on the collection of R-2 Fine Quad (FQ) mode imagery such that all linear polarization choices (i.e., HH, HV, VV, and VH) were simultaneously available. Then, observations could be extended to the ScanSAR cases through appropriate modification of the noise floor, spatial resolution, and radiometric resolution. Along with recommended surveillance modes by application, multiple use (i.e., one acquisition serving multiple maritime applications) opportunities were identified that would streamline order planning and maximize R-2 utilization.

## Résumé

---

Le principal objectif du projet de sélection de modes RADARSAT-2 adaptés à la surveillance maritime (R2MS2) était d'identifier et de recommander des modes de surveillance maritime ScanSAR pour RADARSAT-2 (R-2), tout en préparant l'exploitation de la mission de la constellation RADARSAT (MCR). Le projet R2MS2 a mis l'accent principalement sur la performance des modes de fonctionnement ScanSAR à large bande, y compris le mode ScanSAR large (SCW) et le mode ScanSAR étroit (SCN). Voici les applications de surveillance maritime qui ont été examinées : surveillance des glaces de mer; surveillance des îles de glace; détection des icebergs; détection des navires; estimation de la vitesse du vent; détection de déversements d'hydrocarbures et détection des caractéristiques des océans. On a aussi tenu compte de plusieurs questions liées à la qualité des images : performance de la table de consultation (LUT) des applications dans la conversion des nombres à point flottant du processeur en nombres entiers dans les produits d'image; le réglage de la quantification adaptative des blocs (BAQ) en vue d'une réduction du volume de données brutes et de la soustraction du bruit en vue de l'atténuation de l'incidence visuelle du plancher de bruit pour les acquisitions du rapport signal/bruit. Enfin, plusieurs outils ont été mis au point pour le banc d'essai du logiciel Image Analyst Pro (IA Pro) de RDDC Ottawa à l'appui des besoins en traitement de données du projet R2MS2. Pour les applications de surveillance maritime examinées, l'approche a compris une combinaison d'analyses théoriques et d'essais sur le terrain en vue de la collecte de nouveaux jeux de données de cibles connues, moyennant validation dans la mesure du possible. Les essais ont souvent porté sur la collecte d'images en mode fin à quadruple polarisation (FQ) R-2, de sorte que tous les choix de polarisation rectiligne (c'est-à-dire HH, HV, VV et VH) étaient disponibles simultanément. Il était alors possible d'élargir les observations aux cas ScanSAR par la modification appropriée du plancher de bruit, la résolution spatiale et la résolution radiométrique. Outre les modes de surveillance recommandés par application, on a repéré des possibilités d'utilisation multiple (c'est-à-dire une acquisition pouvant servir dans le cas de plusieurs applications maritimes) qui permettraient de rationaliser la planification de l'ordonnancement et d'optimiser l'utilisation de R-2.

## **Executive summary**

---

### **RADARSAT-2 mode selection for maritime surveillance**

**Roger De Abreu; Matt Arkett; Angela Cheng; Tom Zagon; Derek Mueller; Paris W. Vachon; John Wolfe; DRDC Ottawa ECR 2011-168; Defence R&D Canada – Ottawa; November 2011.**

**Introduction:** The RADARSAT-2 Mode Selection for Maritime Surveillance (R2MS2) project was established in 2008 as a collaborative R&D activity between the Canadian Ice Service (CIS) and Defence R&D Canada – Ottawa (DRDC Ottawa). With funding in part from the Canadian Space Agency (CSA) via their Government Related Initiatives Program (GRIP), the main objective of the R2MS2 project was to identify and recommend ScanSAR-based maritime surveillance modes for RADARSAT-2 (R-2), while also preparing for exploitation of the RADARSAT Constellation Mission (RCM). The key idea was to examine dual use (*i.e.*, one acquisition serving multiple maritime applications) opportunities that would streamline order planning and maximize R-2 utilization. Maritime surveillance requirements often compete from a SAR perspective, with certain applications focussing on the ocean clutter, while other applications require suppression of the ocean clutter.

The focus of R2MS2 was on the performance of wide swath, *i.e.*, ScanSAR modes of operation including ScanSAR Wide (SCW) and ScanSAR Narrow (SCN). ScanSAR maximizes the area coverage rate, a key requirement for maritime surveillance. The following maritime surveillance applications were considered: sea ice monitoring; ice island monitoring; iceberg detection; ship detection; wind speed estimation; oil spill detection; and ocean feature detection. Furthermore, the following image quality issues were considered: application look-up table (LUT) performance in converting floating point numbers in the processor into integers in the image product; and the block adaptive quantization (BAQ) setting for reduction of raw data volume. Finally, several tools were developed for DRDC Ottawa's Image Analyst Pro (IA Pro) software test bed to support R2MS2 data processing needs and other SAR users.

For the maritime surveillance applications considered, the approach included a combination of theoretical analysis and field trials to gather new data sets of known targets, with validation whenever possible. The trials often focused on the collection of R-2 Fine Quad (FQ) mode imagery such that all linear polarization choices (*i.e.*, HH, HV, VV, and VH) were simultaneously available. Then, observations could be extended to the ScanSAR cases through appropriate modification of the noise floor, spatial resolution, and radiometric resolution.

#### **Results:**

- Sea ice monitoring – There exists a mature operational capability to chart sea ice type (*e.g.*, first year ice, multiyear ice, open water) based primarily upon radar backscatter and image texture. An extensive database of R-2 SCW dual-polarization images of sea ice was acquired and backscatter signatures as a function of ice type were collected. It was shown that use of cross polarization can dramatically improve the estimation of ice concentration and ice type separability in some cases. Dual polarization imagery should be routinely used for sea ice monitoring along with maximum possible swath width.

- Ice island monitoring – Ice islands are large (*i.e.*, kilometre scale) masses of ice that calve from ice shelves. Several ice islands were systematically tracked and imaged with R-2 FQ and other modes over a period of 1.5 years. It was shown that cross-polarization is superior to co-polarization for detecting ice islands by signature difference alone, large ice islands in mid-winter conditions are easily detectable using SCW. SCW in dual polarization is recommended for routine ice island monitoring.
- Iceberg detection – Similar to ice islands, icebergs are floating masses of ice, but on a much smaller scale. Icebergs may be mistaken for ships in SAR images, so ship/iceberg discrimination is an important operational requirement. A field trial off the coast of Greenland resulted in R-2 FQ mode imagery of validated icebergs, which were used to simulate iceberg signatures in other R-2 beam modes. It was shown that the probability of iceberg detection increases with increasing iceberg size, increasing incidence angle, decreasing wind speed, and increasing resolution, with less variability for cross-polarization than for co-polarization. In general, dual-polarization data with best possible resolution is recommended. As such SCN would be superior to SCW.
- Ship detection – Ship detectability was evaluated by extending existing ship detectability models to incorporate the R2MS2 findings, especially for the co-polarization ratio and the cross-polarization ocean backscatter. According to the models co-polarization performs better than cross-polarization for larger incidence angles, and vice versa. In general, dual polarization with best possible resolution is recommended. SCN is a suitable choice for ship detection.
- Wind speed estimation – An emerging operational application for coastal meteorology, wind speed estimation from SAR imagery was assessed by acquiring R-2 FQ mode imagery over operational Canadian meteorological buoys over several years. The most important outputs of this work were a new co-polarization ratio and a new backscatter model for cross polarization. The latter appears to represent a quantum leap in maritime surveillance since wind speeds may be estimated from the cross polarization channel in the absence of wind direction or SAR geometry, especially for high wind speed situations. The cross polarization backscatter result touched most of the applications considered in this project.
- Oil spill detection – This was perhaps the most difficult maritime surveillance application to address since it is very difficult to get imagery over a known oil spill. The adopted strategy was to acquire R-2 imagery over a known region of oil seeps, in this case the Coal Oil Point Seep Field off Santa Barbara. Although the make-up of the oil seep field could be different from that of oil spills, it provides a representative target that can be routinely imaged under a variety of wind conditions. It was shown that VV performed better than HH for oil detection, especially at higher incidence angles. Certainly SCW will be suitable for oil spill detection provided the oil spill is sufficiently large.
- Ocean feature detection – This application is being operationalized in DND, but is difficult to assess since the features of interest are large in scale. As such, FQ proved to be difficult to work with. Instead, we focused on a few test cases that arose from the Spaceborne Ocean Intelligence Network project, which is using SCN and SCW with VV polarization. Little more could be done other than affirming that these are good choices.
- LUT performance – This was evaluated by re-processing scenes with different available LUTs and with different numbers of bits. For low backscatter regions, the quantization can become coarse, resulting in estimated statistics becoming LUT dependent.

- BAQ setting – This is difficult to evaluate since a given scene can only be acquired with a single BAQ setting. Instead, it was necessary to collect scenes with different BAQ settings on successive ascending and descending passes, an imperfect solution due to the time difference between acquisitions. Nevertheless, it is apparent that lower numbers of raw data bits (*e.g.*, 2-bits BAQ vs. 4-bits BAQ) can result in a loss in image texture.
- IA Pro tools – Scale-lock forces a common appearance when multiple images from a swath are loaded; new map projections such as Lambert conic conformal, useful at high latitudes, were made available; the distributed target analysis tool was modified to support data transects in an arbitrary direction and polygonal analysis regions; a noise subtraction tool was implemented to mitigate the visual appearance of the instrument noise floor for low signal-to-noise ratio images.

**Significance:** Dual use of R-2 maritime imagery will serve to reduce acquisition conflicts and improve efficiency in the use of available R-2 resources. R2MS2 has affirmed conventional knowledge in some cases, but has provided new insights to acquisition and polarization choices in other cases, thereby improving the utility of both R-2 and RCM for maritime surveillance.

**Future plans:** Although the R2MS2 project is now complete, several recommendations arose for additional work. These include quantitative evaluation of the Maritime Satellite Surveillance Radar (MSSR) modes that are being implemented on R-2 through the Polar Epsilon project, and evaluation of the maritime surveillance performance of the Compact Polarimetry capability that will be available on RCM.

## Sommaire

---

### RADARSAT-2 mode selection for maritime surveillance

**Roger De Abreu; Matt Arkett; Angela Cheng; Tom Zagon; Derek Mueller; Paris W. Vachon; John Wolfe ; DRDC Ottawa ECR 2011-168 ; R & D pour la défense Canada – Ottawa; novembre 2011.**

**Introduction :** Le projet de sélection de modes RADARSAT-2 adaptés à la surveillance maritime (R2MS2) a été lancé en 2008 comme activité de collaboration en recherche et développement (R et D) entre le Service canadien des glaces (SCG) et R & D pour la défense Canada – Ottawa (RDDC Ottawa). Financé en partie par l'Agence spatiale canadienne (ASC) dans le cadre de son programme d'initiatives gouvernementales en observation de la Terre (IGOT), le projet R2MS2 avait pour principal objectif d'identifier et de recommander des modes de surveillance maritime ScanSAR pour RADARSAT-2 (R-2), tout en préparant l'exploitation de la mission de la constellation RADARSAT (MCR). Le but était principalement d'examiner les possibilités d'utilisation double (*c'est-à-dire* les cas où une acquisition sert à plusieurs applications maritimes) qui permettraient de rationaliser la planification de l'ordonnancement et d'optimiser l'utilisation de R-2. Les besoins de surveillance maritime entrent souvent en concurrence du point de vue du radar à synthèse d'ouverture (SAR), certaines applications portant sur le fouillis d'échos d'océan, tandis que d'autres requièrent la suppression du fouillis d'échos d'océan.

Le projet R2MS2 a mis l'accent sur la performance de la bande au sol large, *c'est-à-dire* les modes de fonctionnement ScanSAR, y compris le mode ScanSAR large (SCW) et le mode ScanSAR étroit (SCN). Le mode ScanSAR permet d'optimiser le taux de couverture du territoire, ce qui constitue une exigence clé pour la surveillance maritime. Voici les applications de surveillance maritime qui ont été examinées : surveillance des glaces de mer; surveillance des îles de glace; détection des icebergs; détection des navires; estimation de la vitesse du vent; détection de déversements d'hydrocarbures et détection des caractéristiques des océans. On a aussi tenu compte de plusieurs questions liées à la qualité des images : performance de la table de consultation (LUT) des applications dans la conversion des nombres à point flottant du processeur en nombres entiers dans les produits d'image, et le réglage de la quantification adaptive des blocs (BAQ) en vue d'une réduction du volume de données brutes. Enfin, plusieurs outils ont été mis au point pour le banc d'essai du logiciel Image Analyst Pro (IA Pro) de RDDC Ottawa à l'appui des besoins en traitement de données du projet R2MS2 et d'autres utilisateurs SAR.

Pour les applications de surveillance maritime examinées, l'approche a compris une combinaison d'analyses théoriques et d'essais sur le terrain en vue de la collecte de nouveaux jeux de données de cibles connues, moyennant validation dans la mesure du possible. Les essais ont souvent porté sur la collecte d'images en mode fin à quadruple polarisation R-2, de sorte que tous les choix de polarisation rectiligne (*c'est-à-dire* HH, HV, VV et VH) étaient disponibles simultanément. Il était alors possible d'élargir les observations aux cas ScanSAR par la modification appropriée du plancher de bruit, la résolution spatiale et la résolution radiométrique.

## Résultats :

- Surveillance des glaces de mer – Il existe une capacité opérationnelle évoluée à cartographier le type de glace de mer (p. ex. glace de l'année, glace de plusieurs années, eaux libres) en fonction surtout de la rétrodiffusion du radar et de la texture des images. On a acquis une base de données exhaustive d'images R-2 à double polarisation SCW de glace de mer, et on a recueilli des signatures de rétrodiffusion en fonction du type de glace. On a montré que l'utilisation de la polarisation croisée permet d'améliorer énormément l'estimation de la concentration de glace et la visibilité par type de glace dans certains cas. Les images à double polarisation devraient automatiquement servir à la surveillance des glaces de mer, de même que la largeur maximale possible de la bande au sol.
- Surveillance des îles de glace – Les îles de glace sont de grosses (c'est-à-dire de l'échelle du kilomètre) masses de glace vélées de plates-formes de glace. Plusieurs îles de glace ont été systématiquement suivies et prises sur image en mode FQ R-2 et d'autres modes sur une période de 1,5 an. On a montré que la polarisation croisée est supérieure à la copolarisation pour la détection des îles de glace uniquement d'après la différence de signature, et que les îles de glace dans condition d'hiver sont facilement détecté avec le mode SCW. On recommande le mode SCW en double polarisation pour la surveillance courante des îles de glace.
- Détection des icebergs – Tout comme les îles de glace, les icebergs sont des masses flottantes de glace, mais à une échelle beaucoup plus petite. On peut les méprendre pour des navires dans des images SAR, d'où l'importance de la discrimination navire/iceberg comme exigence opérationnelle. Un essai sur le terrain au large de la côte du Groenland a permis d'obtenir des images R-2 d'icebergs validés en mode FQ, qui ont servi à la simulation de signatures d'iceberg dans d'autres modes de faisceau R-2. On a montré que la probabilité de détection des icebergs augmente avec l'accroissement de leur taille, l'augmentation de l'angle d'incidence, la diminution de la vitesse du vent et l'accroissement de la résolution, la variabilité étant moindre pour la polarisation croisée que dans le cas de la co-polarisation. En règle générale, on recommande les données en mode de double polarisation avec la meilleure résolution possible. Le mode SCN serait supérieur au mode SCW.
- Détection des navires – La détectabilité des navires a été évaluée par l'élargissement de la détectabilité actuelle des modèles de navire de manière à y intégrer les constatations du projet R2MS2, notamment en ce qui concerne le rapport de copolarisation et la rétrodiffusion d'océan à polarisation croisée. D'après les modèles, la copolarisation donne de meilleurs résultats que la polarisation croisée dans le cas des grands angles d'incidence, et vice versa. En général, on recommande la double polarisation avec la meilleure résolution possible. Le mode SCN convient bien à la détection des navires.
- Estimation de la vitesse du vent – On a évalué l'estimation de la vitesse du vent à partir d'images SAR, une application opérationnelle émergente de la météorologie côtière, en acquérant des images R-2 en mode FQ à l'aide de bouées météorologiques canadiennes opérationnelles pendant plusieurs années. Les résultats les plus importants de ce travail ont été un nouveau rapport de copolarisation et un nouveau modèle de rétrodiffusion pour la polarisation croisée. Ce dernier semble représenter un bond en avant en surveillance

maritime, du fait qu'en l'absence de direction du vent ou de géométrie SAR, il permet d'estimer la vitesse du vent à partir du canal en polarisation croisée, notamment en cas de vitesse élevée du vent. Le résultat concernant la rétrodiffusion en polarisation croisée a touché la plupart des applications examinées dans le cadre du présent projet.

- Détection de déversements d'hydrocarbures – C'est peut-être l'application de surveillance maritime la plus difficile à examiner, du fait qu'il est très difficile d'obtenir des images d'un déversement d'hydrocarbures connu. La stratégie adoptée a été d'acquérir des images R-2 d'une région connue pour le suintement de pétrole, en l'occurrence le champ de suintement de Coal Oil Point (Coal Oil Point Seep Field) au large de Santa Barbara. Même si la composition du champ de suintement de pétrole peut différer de celle de déversement d'hydrocarbures, elle fournit une cible représentative dont il est possible de prendre souvent des images dans toute une gamme de conditions éoliennes. On a montré que la polarisation VV offre un meilleur rendement que la polarisation HH en vue de la détection des déversements d'hydrocarbures, surtout à l'angle d'incidence supérieur. Le mode SCW ne manquera pas de convenir à la détection de déversements d'hydrocarbures, à condition que les déversements soient assez importants.
- Détection des caractéristiques des océans – Cette application, en voie de mise en œuvre au MDN, est difficile à évaluer, du fait que les caractéristiques d'intérêt sont à grande échelle. Il s'est avéré difficile de travailler en mode FQ. L'accent a plutôt été mis sur quelques cas d'essai qui ont découlé du projet de réseau spatial de renseignement sur l'océan (RSRO), qui se sert des modes SCN et SCW avec la polarisation VV. Il n'y a guère plus à dire que d'indiquer qu'il s'agit de bons choix.
- Rendement de la LUT – On a évalué le rendement en traitant de nouveau des scènes à l'aide de différentes LUT et de différents nombres de bits. Dans les régions à faible rétrodiffusion, la quantification peut devenir grossière, ce qui a pour effet que les statistiques estimées viennent à dépendre de la LUT.
- Réglage de la BAQ – C'est une application difficile à évaluer, du fait qu'une scène donnée peut uniquement être acquise à un réglage unique de la BAQ. Il a plutôt fallu recueillir des scènes à différents réglages de la BAQ à des passages ascendants et descendants successifs, une solution imparfaite en raison de la différence de temps entre les acquisitions. Il est néanmoins ressorti que de faibles quantités de données binaires brutes (p. ex. BAQ à 2 bits par rapport à une BAQ à 4 bits) peuvent entraîner une perte de texture d'image.
- Outils de IA Pro – Le verrouillage d'échelle force une apparence commune lorsque plusieurs images d'une bande au sol sont chargées; de nouvelles projections cartographiques, comme la projection conique conforme de Lambert, utile à hautes latitudes, sont devenues disponibles; l'outil d'analyse de cible répartie a été modifié pour prendre en charge les transects de données dans une direction arbitraire et des régions d'analyse polygonale; un outil de soustraction du bruit a été mis en place pour atténuer l'apparence visuelle du plancher de bruit de l'instrument pour les images à faible rapport signal/bruit.

**Importance :** La double utilisation de l'imagerie maritime R-2 servira à réduire les conflits d'acquisition et à améliorer l'efficience dans l'utilisation des ressources R-2 disponibles. Le projet R2MS2 a réaffirmé les connaissances classiques dans certains cas, mais a donné de

nouveaux points de vue aux choix d'acquisition et de polarisation dans d'autres cas, ce qui augmente l'utilité de R-2 et de MCR pour la surveillance maritime.

**Perspectives :** Même si le projet R2MS2 est maintenant terminé, plusieurs recommandations en ont découlé en vue de recherches additionnelles, dont une évaluation quantitative des modes du radar de surveillance maritime par satellite (RSMS) en voie d'intégration à R-2 dans le cadre du projet Polar Epsilon, ou encore une évaluation du rendement, pour la surveillance maritime, de la capacité de polarimétrie compacte qui deviendra disponible dans la MCR.

This page intentionally left blank.

# Table of contents

---

Abstract .....	i
Résumé .....	ii
Executive summary .....	iii
Sommaire .....	vi
Table of contents .....	xi
List of figures .....	xiv
List of tables .....	xx
Acknowledgements .....	xxii
1 Introduction.....	1
1.1 RADARSAT-2 .....	1
1.2 RCM .....	3
1.3 Sentinel-1.....	4
1.4 R2MS2 literature review .....	4
1.5 Objectives .....	5
1.6 Outline .....	5
2 Sea ice monitoring .....	6
2.1 Background .....	6
2.2 Data and methods .....	6
2.3 Analysis and results.....	8
2.3.1 Sea Ice backscatter HH vs. HV.....	8
2.3.2 Sea Ice – Open water separation.....	8
2.3.3 Ice typing .....	11
2.3.3.1 Winter .....	14
2.3.3.2 Summer.....	14
2.4 Mode recommendations .....	18
2.4.1 RADARSAT-2 .....	18
2.4.2 RCM .....	18
2.5 Future analysis.....	19
3 Ice Island monitoring .....	20
3.1 Background .....	20
3.2 Data and methods .....	23
3.3 Analysis and results.....	25
3.3.1 Generic background.....	26
3.3.2 Specific backgrounds.....	29
3.3.2.1 Modelled wind .....	29
3.3.2.2 Open water / FYI .....	31
3.3.2.3 Undeformed MYI.....	31

3.3.2.4	Ridged MYI .....	31
3.3.3	Analysis of covariance.....	34
3.4	Mode recommendations .....	35
3.4.1	RADARSAT-2 .....	35
3.4.2	RCM .....	36
3.5	Future analysis.....	36
4	Iceberg detection.....	38
4.1	Background .....	38
4.2	Data and methods .....	38
4.2.1	Fine mode iceberg data.....	39
4.2.1.1	Iceberg signature – Fine mode .....	40
4.2.1.2	Iceberg signature – Simulated SCN mode .....	49
4.2.2	Fine mode wind data.....	55
4.2.2.1	Advances in cross-polarization wind speed estimation .....	56
4.2.2.2	Ocean signature – Fine mode.....	57
4.2.2.3	Ocean signature – Simulated SCN mode .....	58
4.2.3	SCN mode sea ice data .....	59
4.2.3.1	Sea Ice signature – SCW mode.....	60
4.2.3.2	Sea Ice signature – Simulated SCN and Fine mode.....	60
4.3	Results and analysis.....	61
4.3.1	Fine mode iceberg detection .....	61
4.3.2	SCN mode iceberg detection .....	63
4.3.3	POD trends .....	66
4.4	Mode recommendations .....	69
4.4.1	RADARSAT-2 .....	69
4.4.2	RCM .....	70
4.5	Future analysis.....	70
5	Ship Detection .....	71
5.1	Background .....	71
5.2	Data and method.....	71
5.3	Results and analysis.....	72
5.4	Mode recommendations .....	78
5.4.1	RADARSAT-2 .....	78
5.4.2	RCM .....	78
5.5	Future analysis.....	79
6	Wind speed estimation.....	80
6.1	Background .....	80
6.2	Data and processing methodology.....	80
6.3	Results and analysis.....	82
6.3.1	Co-polarization ratio .....	82
6.3.2	Cross polarization ocean backscatter .....	85

6.3.3	Summary .....	93
6.4	Mode recommendations .....	93
6.4.1	RADARSAT-2 .....	93
6.4.2	RCM .....	94
6.5	Future analysis.....	94
7	Oil spill detection.....	95
7.1	Background .....	95
7.2	Data and methods .....	96
7.3	Results and analysis.....	99
7.3.1	Oil vs. ocean backscatter .....	99
7.3.2	Contrast ratios between ocean and oil .....	106
7.3.3	Difference in contrast ratios between HH and VV .....	110
7.4	Mode recommendations .....	111
7.4.1	RADARSAT-2 .....	111
7.4.2	RCM .....	112
7.5	Future Analysis.....	112
8	Ocean feature detection .....	113
8.1	Background .....	113
8.2	Data and method.....	113
8.3	Results and analysis.....	115
8.4	Mode recommendations .....	115
8.4.1	RADARSAT-2 .....	115
8.4.2	RCM .....	116
8.5	Future analysis.....	116
9	Image quality issues.....	117
9.1	Background .....	117
9.2	16-bits vs. 8-bits and application LUTs.....	117
9.3	BAQ selection .....	129
9.4	Recommendations .....	140
9.5	Future analysis.....	141
10	IA Pro upgrades .....	142
10.1	Scale-Lock tool and Re-projection tool.....	142
10.2	Distributed Target Analysis tool .....	144
10.3	Noise Subtraction tool .....	145
11	RADARSAT mode selection .....	147
12	Conclusions.....	148
	References .....	149
	List of symbols/abbreviations/acronyms/initialisms .....	155

## List of figures

---

Figure 1: HH and HV backscatter for all sea ice types over all seasons and NESZ for SCWA. ....	7
Figure 2: HH backscatter for all sea ice types over all seasons, including OW backscatter for various wind speeds and NESZ for SCWA. ....	9
Figure 3: HV backscatter for all sea ice types over all seasons, including OW backscatter for various wind speeds and NESZ for SCWA. ....	9
Figure 4: S. Beaufort Sea, 2008-09-15, showing a subset of a R-2 SCWA image: (a) HH; and (b) HV (near-range on the left). ....	10
Figure 5: HV backscatter for individual sea ice types over all seasons, including OW backscatter for various wind speeds and NESZ for SCWA. ....	11
Figure 6: Appearance of New Ice in SCW HH and HV (near-range). There is adequate contrast (4 dB) between smooth New Ice and OW in HH (left), allowing charting (centre). Both New Ice and OW backscatter are below NESZ and are indistinguishable in HV (right). ....	12
Figure 7: 2010 S. Beaufort Sea false colour R-2 SCWA images before (left) and after (right) noise subtraction. In each case, the HV image was assigned to both the Red and Green channels, while HH was assigned to Blue (near-range on the left). ....	13
Figure 8: HH backscatter for individual sea ice types over winter season with NESZ for SCWA. ....	15
Figure 9: HV backscatter for individual sea ice types over winter season with NESZ for SCWA. ....	15
Figure 10: R-2 SCW, 2010-07-24. MYI and Grey Ice have similar tones in HH, while in HV, there is strong contrast between ice types simplifying the identification of hazardous MYI. ....	16
Figure 11: HH and HV backscatter for individual sea ice types over summer season, with NESZ for SCWA. ....	17
Figure 12: Winter (2008-12-19) and summer (2009-07-06) R-2 SCW HH and HV images over Barrow Strait. The loss of wintertime contrast between the bright MYI floes and the surrounding darker smooth FYI makes summertime ice typing very difficult using HH or HV R-2 modes. ....	17
Figure 13: An ice island (Target 2) adrift in the Arctic Ocean north of Meighen Island on 18 May 2009. Note the surface undulations and higher freeboard than the surrounding ice. Photo courtesy Sierra Pope (University of Ottawa). ....	21
Figure 14: R-2 FQ imagery of ice island targets used in this study displayed as a Pauli decomposition (R: HH-VV, single-bounce; G: (HV+VH)/2, volume scattering; B: HH+VV, double-bounce). ....	22
Figure 15: The drift of the three ice islands tracked in this study. ....	23

Figure 16: Mean backscatter for ice islands of meteoric and marine ice type versus date. The HH NESZ is given for SCW (NESZ sc) and single beam (NESZ st) modes.....	27
Figure 17: Mean backscatter for ice islands of meteoric and marine ice type versus incidence angle. The HH NESZ is given for SCW (NESZ sc) and single beam (NESZ st) modes.....	27
Figure 18: Contrast ratio between meteoric ice islands against a generic background versus date.....	28
Figure 19: Contrast ratio between marine ice islands against a generic background versus date.....	28
Figure 20: Contrast ratio between meteoric ice islands against an open ocean with a wind speed of 8 m/s at relative azimuth angles of 0° (lower error bar) and 90° (upper error bar).....	30
Figure 21: Contrast ratio between marine ice islands against an open ocean with a wind speed of 8 m/s at relative azimuth angles of 0° (lower error bar) and 90° (upper error bar).....	30
Figure 22: Contrast ratio between meteoric ice island and undeformed MYI vs. ambient temperature.....	32
Figure 23: Contrast ratio between marine ice island and MYI vs. ambient temperature. ....	32
Figure 24: Contrast ratio between meteoric ice island and ridged MYI vs. ambient temperature.....	33
Figure 25: Contrast ratio between marine ice island and ridged MYI vs. ambient temperature..	33
Figure 26: Large pinnacle iceberg validated during the 2009 West Greenland campaign. Photo provided by Provincial Aerospace Limited (PAL) 2009. ....	39
Figure 27: Iceberg waterline length histogram for 2009 West Greenland campaign.....	40
Figure 28: HH maximum pixel intensity as a function of iceberg size and incidence angle.....	41
Figure 29: HH mean pixel intensity as a function of iceberg size and incidence angle. ....	41
Figure 30: HV maximum pixel intensity as a function of iceberg size and incidence angle.....	42
Figure 31: HV mean pixel intensity as a function of iceberg size and incidence angle. ....	42
Figure 32: 20 m small dome iceberg Fine mode SAR signature in decibels (wind speed: 0.9 m/s).....	43
Figure 33: 44 m small wedge iceberg Fine mode SAR signature in decibels (wind speed: 13.2 m/s).....	44
Figure 34: 70 m medium pinnacle iceberg Fine mode SAR signature in decibels (wind speed: 18.2 m/s).....	45
Figure 35: 109 m medium pinnacle iceberg Fine mode SAR signature in decibels (wind speed: 12.0 m/s). ....	46
Figure 36: 180 m large drydock iceberg Fine mode SAR signature in decibels (wind speed 19.0 m/s).....	47

Figure 37: 256 m large tabular iceberg Fine mode SAR signature in decibels (wind speed 16.7 m/s).....	48
Figure 38: 20 m small dome iceberg simulated SCN mode SAR signature in decibels (see Figure 32).....	50
Figure 39: 44 m small wedge iceberg simulated SCN mode SAR signature in decibels (see Figure 33).....	51
Figure 40: 70 m medium pinnacle iceberg simulated SCN mode SAR signature in decibels (see Figure 34).....	52
Figure 41: 109 m medium pinnacle iceberg simulated SCN mode SAR signature in decibels (see Figure 35).....	53
Figure 42: 180 m large drydock iceberg simulated SCN mode SAR signature in decibels (see Figure 36).....	54
Figure 43: 256 m large tabular iceberg simulated SCN mode SAR signature in decibels (see Figure 37).....	55
Figure 44: Fine mode Iceberg POD as a function of incidence angle and polarization.....	67
Figure 45: Fine mode Iceberg POD as a function of wind speed and polarization.....	67
Figure 46: Iceberg POD as a function of image mode, target size, incidence angle and polarization.....	67
Figure 47: Iceberg POD in FYI for SCN as a function of target size, incidence angle and polarization.....	69
Figure 48: Iceberg POD in MYI for SCN as a function of target size, incidence angle and polarization.....	69
Figure 49: Main GUI window for the SDPT.....	73
Figure 50: GUI illustrating the Full Swath Analysis component of the SDPT.....	73
Figure 51: GUI illustrating the Sensor-Specific Calculator of the SDPT.....	74
Figure 52: Full-Swath Analysis of Minimum Detectable Ship Length in meters vs. incidence angle for R-2 heritage beam modes, HH-polarization.....	75
Figure 53: Full-Swath Analysis of Minimum Detectable Ship Length in meters vs. incidence angle for R-2 heritage beam modes, HV-polarization.....	76
Figure 54: Full-Swath Analysis of Minimum Detectable Ship Length in meters vs. incidence angle for R-2 SCN and MSSR modes, HH-polarization.....	76
Figure 55: Full-Swath Analysis of Minimum Detectable Ship Length in meters vs. incidence angle for R-2 SCN and MSSR modes, HV-polarization.....	77
Figure 56: Full-Swath Analysis of Minimum Detectable Ship Length in meters vs. incidence angle for R-2 MSSR, FQ, and UF modes, HH-polarization.....	77
Figure 57: Full-Swath Analysis of Minimum Detectable Ship Length in meters vs. incidence angle for R-2 MSSR, FQ, and UF modes, HV-polarization.....	78
Figure 58: East coast buoy locations considered.....	81

Figure 59: West coast buoy locations considered. ....	81
Figure 60: Case study showing buoy location, sub-scene over which a mean $\sigma^o$ is calculated, the associated incidence angle and buoy reported wind direction. ....	82
Figure 61: Plot of observed co-polarization ratio vs. incidence angle with various polarization ratio models overlaid. ....	83
Figure 62: Observed co-polarization ratio vs. incidence angle along with the model fit. ....	83
Figure 63: Scatter plot of HH-derived wind speed vs. buoy wind speed using Kirchhoff co-polarization ratio. ....	84
Figure 64: Co-polarization $\sigma^o$ vs. incidence angle along with the associated NESZ. ....	86
Figure 65: Cross-polarization $\sigma^o$ vs. incidence angle along with the associated NESZ. ....	86
Figure 66: Co-polarization $\sigma^o$ vs. wind speed along with the associated NESZ. ....	87
Figure 67: Cross-polarization $\sigma^o$ vs. wind speed along with the associated NESZ. ....	87
Figure 68: Observed cross-polarization backscatter vs. observed wind speed with model fits....	88
Figure 69: Scatter plot of HH-derived wind speed vs. buoy wind speed using Equation (9).....	90
Figure 70: Scatter plot of VV-derived wind speed vs. buoy wind speed. ....	90
Figure 71: Scatter plot of HV-derived wind speed vs. buoy wind speed using Equation (10)....	91
Figure 72: Scatter plot of VH-derived wind speed vs. buoy wind speed using Equation (10)....	91
Figure 73: R-2 SCWA VV-polarization derived wind speed for Hurricane Bertha. ....	92
Figure 74: R-2 SCWA VH-polarization derived wind speed for Hurricane Bertha. ....	92
Figure 75: Sonar return amplitude map of the Coal Oil Point Seep Field used in this study to determine the location of the oil seeps [27]. ....	97
Figure 76: An example of the sampling method used on the oil seep and the surrounding ocean clutter background. ....	98
Figure 77: HH oil backscatter as a function of wind speed and incidence angle. ....	100
Figure 78: VV oil backscatter as a function of wind speed and incidence angle. ....	101
Figure 79: Difference in oil backscatter values (VV – HH). ....	102
Figure 80: HH ocean backscatter for all oil seeps grouped by estimated wind speed. ....	103
Figure 81: VV ocean backscatter for all oil seeps grouped by estimated wind speed. ....	103
Figure 82: The difference in ocean backscatter values (VV – HH). ....	104
Figure 83: Easy detectability: La Goleta Seeps, 2009-11-20 (contrast ratio of 11.8 dB in HH). The outline of the seep is shown in red. ....	106
Figure 84: Moderate detectability: La Goleta Seeps, 2009-09-02 (contrast ratio of 6.3 dB HH)....	107
Figure 85: Difficult detectability: La Goleta Seeps, 2009-10-27 (contrast ratio of 2.4 dB in HH)....	107

Figure 86: Contrast ratios between the oil slick and ocean clutter in HH adjusted relative to the SCW noise floor.....	108
Figure 87: Contrast ratios between the oil slick and ocean clutter in VV adjusted relative to the SCW noise floor.....	109
Figure 88: Difference in contrast ratios between VV and HH adjusted relative to the SCW noise floor.....	110
Figure 89: AVHRR image from 2009-05-22 of ocean features associated with the Gulf Stream.....	114
Figure 90: Nearly concurrent R-2 SCNA images overlaid on the AVHRR image of Figure 89. The yellow boxes outline the image chips over which distributed target analysis was performed.....	114
Figure 91: Ocean backscatter transects across ocean features enumerated in Figure 90.....	115
Figure 92: Gain in dB vs $\theta_{inc}$ for various output LUTS for: a) 16-bit LUTs; and b) 8-bit LUTs.	118
Figure 93: Ratio of 16-bit LUT to 8-bit LUT: a) for the 4 output LUTs considered; and b) zoom-in on the Mixed and Ice LUT ratios.....	119
Figure 94: $\sigma^o$ quantization as per Equations (15) and (16): a) 16-bits; and b) 8-bits. The logarithmic quantization cases are notional. ....	121
Figure 95: Linear $\sigma^o$ quantization for $\theta_{inc} = 20^\circ$ for various output LUTs for: a) 16-bit LUTs; and b) 8-bit LUTs.....	122
Figure 96: Linear $\sigma^o$ quantization for $\theta_{inc} = 30^\circ$ for various output LUTs for: a) 16-bit LUTs; and b) 8-bit LUTs.....	123
Figure 97: Linear $\sigma^o$ quantization for $\theta_{inc} = 40^\circ$ for various output LUTs for: a) 16-bit LUTs; and b) 8-bit LUTs.....	124
Figure 98: Linear $\sigma^o$ quantization for $\theta_{inc} = 50^\circ$ for various output LUTs for: a) 16-bit LUTs; and b) 8-bit LUTs.....	125
Figure 99: $\sigma^o$ quantization for 6 ocean regions as a function of the estimated mean value of $\sigma^o$ when using 3 different output LUTs for an R-2 S3 image of the Strait of Gibraltar acquired 2009-07-01: a) HV polarization; and b) HH polarization. ....	127
Figure 100: $\sigma^o$ quantization for 6 ocean regions as a function of the critical intensity for ship detection when using 3 different output LUTs for an R-2 S3 image of the Strait of Gibraltar acquired 2009-07-01: a) HV polarization; and b) HH polarization. ....	128
Figure 101: Scenario for BAQ analysis between two passes near Baffin Island indicating where a sub-scene (yellow box) can be analysed at the same incidence angle: a) ascending pass with 2-bits BAQ overlaid on the descending pass; and b) descending pass with 4-bits BAQ overlaid on the ascending pass.....	130
Figure 102: Analysis sub-scenes for the 12/13 December 2008 case near Baffin Island corresponding to incidence angles of: a) $38^\circ$ ; b) $39^\circ$ ; and c) $40^\circ$ .....	131
Figure 103: Approximate analysis sub-scene at $38^\circ$ incidence for Baffin Island scene for: a) 2-bits BAQ; and b) 4-bits BAQ.....	132

Figure 104: Approximate analysis sub-scene at 39° incidence for Baffin Island scene for: a) 2-bits BAQ; and b) 4-bits BAQ.....	133
Figure 105: Approximate analysis sub-scene at 40° incidence for Baffin Island scene for: a) 2-bits BAQ; and b) 4-bits BAQ.....	134
Figure 106: Analysis sub-scenes for the 3/4 March 2009 case in the northwest Canadian Arctic corresponding to incidence angles of: a) 39.5°; b) 40°; and c) 41.5° .....	135
Figure 107: Approximate analysis sub-scene at 39.5° incidence for the northwest Arctic scene for: a) 2-bits BAQ; and b) 4-bits BAQ.....	136
Figure 108: Approximate analysis sub-scene at 40.5° incidence for the northwest Arctic scene for: a) 2-bits BAQ; and b) 4-bits BAQ.....	137
Figure 109: Approximate analysis sub-scene at 41.5° incidence for the northwest Arctic scene for: a) 2-bits BAQ; and b) 4-bits BAQ.....	138
Figure 110: Image sequence loaded in IA Pro: a) as loaded; and b) after application of the Scale-Lock tool and the Re-projection tool to LCC.....	143
Figure 111: Arbitrary Transect option available in the IA Pro Distributed Target Analysis Tool .....	144
Figure 112: Polygonal Region option available in the IA Pro Distributed Target Analysis Tool .....	145
Figure 113: R-2 SCWA HV-polarization image near Mackenzie Delta, 2008-03-06: a) as processed; and b) following noise subtraction.....	146

## List of tables

---

Table 1: R-2 modes of interest to R2MS2 and their nominal parameters. ....	2
Table 2: RCM modes of interest for R2MS2 and their nominal parameters. ....	3
Table 3: ScanSAR polarization modes by application, ca. 2008 (adapted from [64]). ....	4
Table 4: Sea Ice Stage of Development classes for operational ice monitoring (after MANICE [5]). Note, “Seasonal” is not an official class, but is used here for additional context. ....	13
Table 5: Characteristics of tracked ice islands at the beginning of the study. ....	24
Table 6: Polarization of the R-2 images used in this study. ....	24
Table 7: Multiple comparisons between polarizations in analysis of covariance models. Polarizations are listed from left to right according to decreasing effect on the absolute contrast ratio (best to worst polarization). Significantly different pairs are marked with superscript letters. Covariate and interaction effects were held constant for these comparisons. ....	35
Table 8: Factors and covariates in ANCOVA models aside from polarization with main effect (not including factor/covariate interactions) sizes significantly greater than zero. ....	35
Table 9: Sample wind signature data. ....	57
Table 10: Sample sea ice signature data as provided by CIS. ....	60
Table 11: R-2 Fine mode iceberg POD for wind directions 0° to 30° from the SAR look direction (Red small; Blue medium; Green large). ....	61
Table 12: R-2 Fine mode iceberg POD for wind directions 30° to 60° from the SAR look direction (Red small; Blue medium; Green large). ....	62
Table 13: R-2 Fine mode iceberg POD for wind directions 60° to 90° from the SAR look direction (Red small; Blue medium; Green large). ....	62
Table 14: R-2 Fine mode iceberg POD in sea ice (Red small; Blue medium; Green large). ....	63
Table 15: Simulated R-2 SCN mode iceberg POD for wind directions 0° to 30° from the SAR look direction (Red small; Blue medium; Green large). ....	64
Table 16: Simulated R-2 SCN mode iceberg POD for wind directions 30° to 60° from the SAR look direction (Red small; Blue medium; Green large). ....	64
Table 17: Simulated R-2 SCN mode iceberg POD for wind directions 60° to 90° from the SAR look direction (Red small; Blue medium; Green large). ....	65
Table 18: Simulated R-2 SCN iceberg POD in sea ice (Red small; Blue medium; Green large). ....	65
Table 19: Number of images collected for each oil seep. ....	97
Table 20: HH oil backscatter arranged by wind speed and incidence angle. ....	100
Table 21: VV oil backscatter arranged by wind speed and incidence angle. ....	101

Table 22: Multiple regression of backscatter (dependent variable) against wind speed and incidence angle (independent variables) .....	104
Table 23: Multiple regression of contrast ratio (dependent variable) against wind speed and incidence angle (independent variables).....	105
Table 24: Mean contrast ratios between oil and ocean in the HH channel, arranged by wind speed and incidence angle.....	108
Table 25: Mean contrast ratios between oil and ocean in the VV channel, arranged by wind speed and incidence angle.....	109
Table 26: Predicted increase in contrast ratio (y) for oil slick detection when using VV over HH.....	111
Table 27: Mean difference of contrast ratios between VV and HH, arranged by wind speed and incidence angle .....	111
Table 28: Point target analysis measurements of a ship comparing original data processed with various application LUTs with the same data sets logarithmically quantized to 160 dB DR. ....	128
Table 29: Distributed target analysis for the Baffin Island sub-scenes, HH polarization. ....	138
Table 30: Distributed target analysis for the Baffin Island sub-scenes, HV polarization. ....	139
Table 31: Distributed target analysis for the northwest Arctic sub-scenes, HH polarization.....	140
Table 32: Primary, Secondary, and MSSR mode recommendations.....	147

## **Acknowledgements**

---

We thank the Canadian Space Agency (CSA) for their support provided through the Government Related Initiatives Program (GRIP) from 1 April 2008 through to 31 March 2010.

We thank Mr. Dean Flett and acknowledge his critical contributions to the RADARSAT-2 Mode Selection for Maritime Surveillance (R2MS2) project. He was the proposer and first Project Manager, and went on to serve as the CSA Project Officer for R2MS2.

Chapter 4 was developed by C-CORE under contract to the Canadian Ice Service.

All RADARSAT-2 data and products presented in this document are copyright MacDonald, Dettwiler and Associates Ltd. - All Rights Reserved.

# **1 Introduction**

---

The RADARSAT-2 Mode Selection for Maritime Surveillance (R2MS2) project was established in 2008 as a collaborative R&D activity between the Canadian Ice Service (CIS) and Defence R&D Canada – Ottawa (DRDC Ottawa). With funding in part from the Canadian Space Agency (CSA) via their Government Related Initiatives Program (GRIP), the main objective of the R2MS2 project was to identify and recommend ScanSAR-based maritime surveillance modes for RADARSAT-2 (R-2), while also preparing for exploitation of the RADARSAT Constellation Mission (RCM). The key idea was to examine dual use (*i.e.*, one acquisition serving multiple maritime applications) opportunities that would streamline order planning and maximize R-2 utilization. This document is the final project deliverable for the R2MS2 project.

The maritime domain presents many data acquisition challenges for wide swath SAR sensors such as R-2. Certain applications, such as ship and iceberg detection, prefer suppression of the ocean clutter to enhance target detectability. Other applications, such as oil spill detection and ocean feature detection, prefer maximization of the ocean clutter as the very essence of their detection methodology. These are competing requirements that can be addressed through appropriate selection of incidence angle ranges and polarizations, with competing pressures arising from the image quality (*e.g.*, spatial and radiometric resolution and noise floor) and the users' data acquisition choices.

## **1.1 RADARSAT-2**

Owned and operated by MacDonald, Dettwiler and Associates Ltd. (MDA), R-2 was launched in December 2007 and has been in operational service since early 2008 (comprehensive information on the satellite, mission, and R-2's modes of operation will not be replicated here; for further information please see <http://www.asc-csa.gc.ca/eng/satellites/radarsat2/default.asp> and <http://gs.mdacorporation.com/SatelliteData/Radarsat2/Radarsat2.aspx>).

R-2 has been pressed into operational service by the Government of Canada for many maritime surveillance activities. The ScanSAR modes are the key modes of operation for maritime surveillance since they offer the widest available imaging swaths. These include ScanSAR narrow (SCN) with SCNA and SCNB variants, and ScanSAR wide (SCW) with SCWA and SCWB variants (see Table 1, adapted from [29], for a summary of the R-2 modes relevant to R2MS2).

Many of R-2's modes are equivalent to those of the predecessor mission RADARSAT-1 (R-1) (see <http://www.asc-csa.gc.ca/eng/satellites/radarsat1/default.asp>). These are referred to as the R-1 heritage modes. But whereas R-1 imagery were only available with HH polarization (*i.e.*, horizontal transmit, horizontal receive), R-2 ScanSAR offers more polarization choices including single polarization (HH or VV or VH or HV) and dual polarization (HH+HV or VV+VH).

R-2 also offers new modes with respect to R-1. Many of these have higher resolution, but of greatest interest to R2MS2 is the Fine Quad (FQ) mode which provides quad polarization (HH+HV+VV+VH). The FQ mode was used for many of the evaluation trials conducted within R2MS2 to better understand the impact of polarization choice.

R-2 exploitation within the Department of National Defence (DND) is being implemented through the Polar Epsilon (PE) project. One R-2 capability that is currently being implemented by PE is the Maritime Satellite Surveillance Radar (MSSR) modes [3]. These modes amount to “beefed-up” SCN modes and are available in two configurations: the Ocean Surveillance, Very wide swath, Near incidence (OSVN) mode and the Detection of Vessels, Wide swath, Far incidence (DVWF) mode. OSVN is intended to simultaneously serve several maritime surveillance applications by providing a wide swath with dual polarization, while DVWF is intended for ship detection only. The MSSR modes are expected to become operationally available in 2011.

*Table 1: R-2 modes of interest to R2MS2 and their nominal parameters.*

Mode	Pro-duct	Pixel Spacing (Rx A) [m]	Reso-lution (Rx A) [m]	Swath [km]	Inc. [°]	Looks (Rx A)	ENL	Polarization
<b>SCNA</b>	SCN	25x25	91-49 x60	300	20-39	2x2	>3	HH or VV or HV or VH or HH+HV or VV+VH
<b>SCNB</b>	SCN	25x25	61-43 x60	300	31-47	2x2	>3	HH or VV or HV or VH or HH+HV or VV+VH
<b>SCWA</b>	SCW	50x50	183-82 x100	500	20-49	4x2	>6	HH or VV or HV or VH or HH+HV or VV+VH
<b>SCWB</b>	SCW	50x50	183-86 x100	450	20-46	4x2	>6	HH or VV or HV or VH or HH+HV or VV+VH
<b>FQ</b>	SLC	4.7x5.1	5.2x7.6	25	18-49	1x1	1	HH+HV+VV+VH
<b>OSVN</b>	SCF	50x50	70x130 (avg)	530	18-51	6x2	8.6	HH+HV or VV+VH
<b>DVWF</b>	SCS	20x20	28x43 (avg)	450	33-57	5x1	3.6	HH

RxA – range by azimuth;

ENL – equivalent number of looks;

SCN – ScanSAR narrow

SCW – ScanSAR wide

SLC – single-look complex;

SCF – ScanSAR fine;

SCS – ScanSAR sampled.

## 1.2 RCM

Currently scheduled for launch starting in 2016, RCM will be a fleet of three SAR satellites that will continue to provide C-band SAR imagery after the R-2 era (see <http://www.asc-csa.gc.ca/eng/satellites/radarsat/default.asp> and [14]). The RCM satellites will be smaller and less capable than R-2 and consequently will feature different capabilities compared to those of R-2.

RCM will not include any R-1 heritage modes *per se* (see Table 2). Instead, a suite of new modes will be available. The Medium Resolution 50 m mode and the Ship Detection mode can be thought of as duals to the R-2 OSVN and DVWF modes, and are expected to be the maritime surveillance work horses.

RCM will include some new polarization capabilities compared to R-2, including dual co-polarization (*i.e.*, VV+HH) and Compact Polarimetry (CP) [43]. CP is a special dual-polarization mode that combines circular transmit polarization with dual linear receive polarization. CP offers some polarimetric target information, but across much broader swaths than is possible for quad-polarization. The applications potential for CP on RCM is still being evaluated [8].

RCM will also include the Doppler anomaly (the difference between the predicted and actual Doppler centroid) in each product. The Doppler anomaly is expected to be beneficial for ocean current applications.

While the focus of R2MS2 was not RCM, many of the lessons learned will be applicable to RCM exploitation for maritime surveillance.

*Table 2: RCM modes of interest for R2MS2 and their nominal parameters.*

Mode	Res. [m]	Swath (acc.) [km]	Looks (RxA)	NESZ [dB]	Polarization
<b>Low Resolution (LR) 100 m</b>	100	500 (500)	8x1	-22	HH or VV or HV or VH or HH+HV or VV+VH or VV+HH or CP
<b>Medium Resolution (MR) 50 m</b>	50	350 (500)	4x1	-22	HH or VV or HV or VH or HH+HV or VV+VH or VV+HH or CP
<b>Low Noise (LN)</b>	100	350 (500)	4x2	-25	HH or VV or HV or VH or HH+HV or VV+VH or VV+HH or CP
<b>Ship Detection (SD)</b>	var.	350 (600)	4x2	var.	HH or VV or HV or VH or HH+HV or VV+VH or CP

## 1.3 Sentinel-1

Although not addressed explicitly here, R2MS2 has been carried out with full awareness of the European Space Agency (ESA) Sentinel-1 mission. The ESA Sentinels are operational satellites that will support the Global Monitoring for Environment and Security (GMES) program. Scheduled for launch in 2013 and 2014, the Sentinel-1 mission will consist of a constellation of two satellites that will carry C-band SAR, and represents the follow-on mission to ESA's ENVISAT Advanced SAR (ASAR). The Sentinel-1 radars will support a variety of applications including maritime surveillance. Whereas Sentinel-1 will have several modes of operation, the work horse mode is expected to be the Interferometric Wide (IW) mode with its 250 km swath, 5x20 metre spatial resolution (ground-range by azimuth, worst case), a single look, and selectable dual polarization (*i.e.*, HH+HV or VV+VH). Performance of the IW mode for maritime surveillance applications, including ship detection, iceberg detection, wind retrieval, oil spill detection, sea ice detection, and ship wake detection has been compared elsewhere to operational practice with RADARSAT-1 and ASAR [59]. It is expected that there will be some degree of inter-operability between Sentinel-1 and RCM.

## 1.4 R2MS2 literature review

The R2MS2 project kicked-off with a literature review and application survey to establish the state-of-the-art as it was understood in late 2008 [63]. The mode recommendations Table 3 were based upon the conventional wisdom of the time. The main activity of the balance of the R2MS2 project was to carry out a series of targeted maritime trials using actual R-2 data to validate and update the initial mode recommendations. The literature survey also identified the knowledge and data gaps, and provided an R&D strategy for each maritime application considered.

*Table 3: ScanSAR polarization modes by application, ca. 2008 (adapted from [63]).*

	Sea Ice	Icebergs	Ships	Oil Spill & Ships	Wind / Hurricanes	Ocean Features
<b>Operations Prior to R-2</b>	SCW HH	not operational	SCNB HH	SCNA HH	SCNA HH	not operational
<b>R-2 Prelaunch Understanding</b>	SCW HH+HV	SCNB HH+HV	SCNB HH+HV	SCNA VV	SCNA VV+VH	SCNA VV
<b>MSSR as of June 08</b>	OSVN HH+HV	OSVN HH+HV	DVWF	OSVN VV	OSVN VV+VH	OSVN VV
<b>Operations as of Dec 08</b>	SCW HH	not operational	SCNB HH	SCNA HH	SCNA HH	not operational
<b>Other Potential Modes for R&amp;D</b>	SCW VV+VH HH+VV quad-pol	SCNB VV+VH HH+VV quad-pol	SCNA HH+HV HH+VV quad-pol	SCNB VV	SCNA HH+HV HH+VV	SCW VV

## **1.5 Objectives**

The purpose of R2MS2 was to characterize the performance of the various R-2 ScanSAR modes for operational marine applications. The main objective was, on an application basis, to identify preferred and secondary R-2 modes for operational detection and monitoring activities. The secondary objective was to advise on the suitability of RCM modes for maritime surveillance.

The R2MS2 objectives were met by conducting a series of field trials in which R-2 imagery were acquired over validated or known *in situ* conditions and features. Each maritime surveillance application required a different acquisition strategy. These will be discussed in the context of each application considered. The specific applications considered are slightly different from what was considered in the literature survey [63] and area summarized below.

The project scope also included evaluation of certain image quality parameters, in particular, some of those that may be chosen by the user. In particular, the application Look Up Table (LUT) and the number of bits (8-bits or 16-bits) that may be used in forming the image were considered. Also, the data may be acquired with various Block Adaptive Quantization (BAQ) settings (1 to 4 bits), which controls the number of raw data bits used to store the raw data numbers on the spacecraft.

Finally, much of the quantitative analysis that was carried out used the custom image analysis software referred to as IA Pro that was developed at DRDC Ottawa. Certain capabilities of IA Pro were implemented or improved as part of the R2MS2 project.

## **1.6 Outline**

This document is organized as follows:

- Section 2 addresses sea ice monitoring;
- Section 3 addresses ice island monitoring;
- Section 4 addresses iceberg detection;
- Section 5 addresses ship detection;
- Section 6 addresses wind speed estimation;
- Section 7 addresses oil spill detection;
- Section 8 addresses ocean feature detection;
- Section 9 addresses certain image quality issues;
- Section 10 addresses enhancements made to the IA Pro image exploitation tool;
- Section 11 summarizes the findings and observations.

## **2 Sea ice monitoring**

---

### **2.1 Background**

As described in [40], the use of C-band SAR for operational sea ice monitoring is well-established. In support of off-shore marine activities (*e.g.*, ship navigation, offshore resource development), national operational ice services focus on extracting a range of ice parameters from satellite data, particularly SAR. Common is the need for these services to extract sea ice information over large marine areas, thus necessitating the use of wide swath SAR modes (*i.e.*, ScanSAR). The primary parameters of interest are the estimation of ice concentration (vs. open water (OW)) and the typing of sea ice into WMO ice thickness classes. The benefits and challenges of using single channel SAR data (HH or VV) for ice monitoring have been understood since the integration and use of both ERS-1 (VV) and R-1 (HH) into operational ice services. These services all utilize expert ice analysts to visually interpret SAR imagery – the human visual system is adept at dealing with the inherent ambiguity between the appearance of sea ice and water and between various ice classes. Ice image analysts utilize image tone, texture, context, feature shape and size to identify ice and classify it into its various thickness classes, *e.g.*, first year ice (FYI), multi-year ice (MYI).

R-2 provides data at multiple polarizations (HH+HV or VV+VH) at ScanSAR swaths. In [63], it was suggested that the use of dual channel ScanSAR data could improve the detection and classification of sea ice, beyond what is possible with single channel ScanSAR data. Essentially this means employing the cross-polarized channel (HV or VH) in the interpretative process, in place of, or in concert with the co-polarized channel (HH or VV). Of primary interest here is whether the cross-polarized channels improve the separability of sea ice and water and separability of ice types. Since image tone is the primary discriminating feature used in sea ice interpretation, the focus in this study is the relative backscatter of sea ice types versus water within R-2 ScanSAR co-polarized and cross-polarized modes. The study examines the performance of these modes within both warm (melt) and cold (winter) seasons.

### **2.2 Data and methods**

The study utilizes 48 R-2 SCW scenes collected over a variety of Canadian sea ice regimes throughout the period May 2008 to May 2010. From these scenes, 531 samples of absolute sea ice backscatter ( $\sigma^0$ ) were extracted over sea ice – 440 HH+HV signatures and 91 HH-only signatures. Study scenes were chosen to represent a variety of sea ice regimes (*i.e.*, pack, marginal and fast) (see Figure 1), ice types and a variety of seasonal conditions (winter, summer). To reduce sampling bias, study scenes were broken up into a fixed sampling grid and the most homogenous ice target in the center of each grid was sampled. Each sampled pixel was converted to  $\sigma^0$  (power) and averaged over a user-defined polygon using IA Pro. The resultant mean  $\sigma^0$  was converted to decibels for analysis. Operational image analysis charts, and where available, *in situ* observations were used to link the measured SAR backscatter to the ice type.

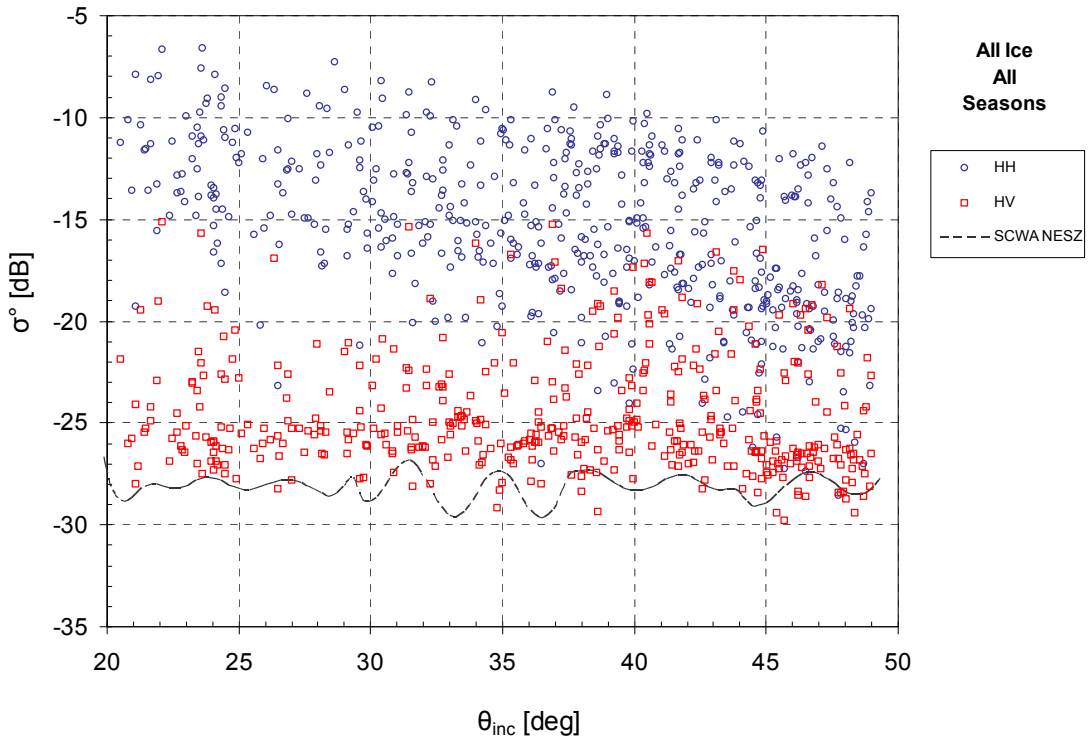


Figure 1: HH and HV backscatter for all sea ice types over all seasons and NESZ for SCWA.

The dataset is presented here based on two seasons – Winter and Summer. Recognizing that C-band SAR sea ice signatures demonstrate strong sensitivity to the presence of water within the upper layers of the sea ice volume (including snow cover), the sampled data were categorized as either Winter or Summer samples. For Winter samples, it was assumed that temperatures were cold enough to restrict the amount of liquid water in the overlying snow cover to a small amount, *i.e.*, less than 2% by volume. For Summer samples, it was assumed that the sea ice volume and overlying snow cover is in a state of melt and liquid water could be present on top and throughout the ice volume.

Since the ocean is the background in which sea ice must be detected and assessed for amount and type, estimates of its backscatter are required at HH and HV polarization. For comparison, modelled ocean HH backscatter (CMOD5 modified for HH) under a variety of wind conditions – wind speeds (4, 8 and 12 m/s) and wind directions relative to SAR azimuth direction ( $0^\circ$  and  $90^\circ$ ) – are plotted against the collected sea ice signatures. HV ocean backscatter was estimated using the empirical model described elsewhere in this report (Section 6).

## 2.3 Analysis and results

### 2.3.1 Sea Ice backscatter HH vs. HV

As expected, sea ice backscatter was found to be significantly larger at HH compared to HV. The mean HH intensity ( $\sigma_{\text{HH}}$ ) measured over all ice types, over all seasons was  $-14$  dB, while only  $-23$  dB at HV polarization ( $\sigma_{\text{HV}}$ ). Sampled sea ice backscatter at HH showed an expected decrease with incidence angle. At C-band HH, surface scattering dominates over seasonal ice types and a reduction in sea ice tone with incidence angle is common. Sea ice analysts dislike this range-ward darkening and prefer to work with an image in which similar ice types appear consistently across the 500 km SCW swath. The R-2 processing system attempts to correct for this through application of incidence-angle-dependant output look-up tables (LUTs) that are designed to radiometrically balance the range-ward appearance of an image during product quantization.

As with most natural features, the signal-to-noise ratio (SNR) of sea ice is much lower at cross-polarization than co-polarization. In SCW mode, sea ice scatters just above the NESZ and in many cases is noise limited. At HV (or VH), sea ice backscatter shows no dependence on incidence angle due to the dominance of volume scattering at this polarization. These results suggest that a balancing LUT is not required for HV imagery. Unfortunately, the current R-2 processor must apply the same LUT to both ScanSAR channels. Ideally, users should be able to specify a separate LUT for each channel.

### 2.3.2 Sea Ice – Open water separation

The separation of sea ice and ocean in a SAR scene is the initial step in the estimation of ice concentration and/or mapping of an ice edge. As shown in Figure 2, at C-band HH, there is unfortunately considerable overlap between ice and ocean backscatter for most sea states. Simplified, in the near range of SCW images (*i.e.*,  $20^\circ$  to  $30^\circ$ ), sea ice appears darker against the brighter ocean. In the mid-range of the swath (*i.e.*,  $30^\circ$  to  $40^\circ$ ), the signatures of sea ice and open water tend to overlap. In the far range (*i.e.*,  $40^\circ$  to  $50^\circ$ ), their signatures reverse with ice appearing brighter than the background ocean. This considerable within-scene variability in the appearance of the OW background at HH and its impacts on ice detection is illustrated in Figure 4(a). In this typical summer scene, the mapping of the ice edge and the estimation of the ice concentration is a challenge for even an experienced ice analyst. Automated methods of segmenting ice and open water have been stymied by the high level of tonal ambiguity in C-band HH (and VV) imagery.

Although the SNR for sea ice is significantly lower at HV compared to HH, the separation of ice and OW is considerably improved by using the HV channel (Figure 4 (b)). At HV polarization, OW backscatter has been found to be near or below the NESZ, independent of incidence angle (Figure 3). As a result, the ocean appears consistently dark in tone across the entire ScanSAR swath. This eases both the visual and automated separation of ice and open water, resulting in more rapid and accurate estimates of ice concentration.

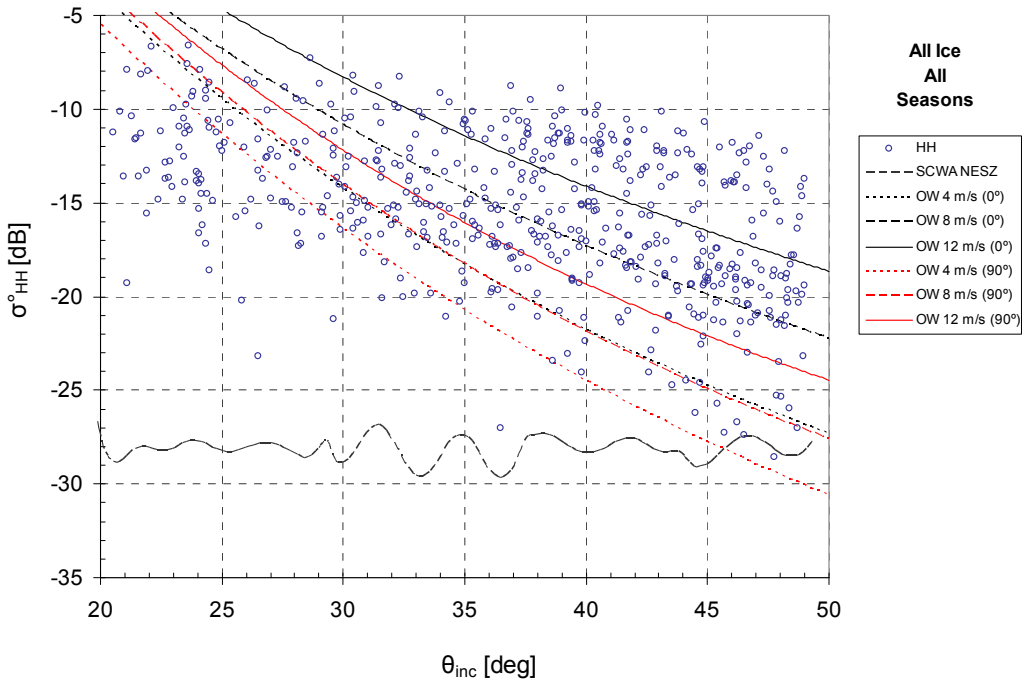


Figure 2: HH backscatter for all sea ice types over all seasons, including OW backscatter for various wind speeds and NESZ for SCWA.

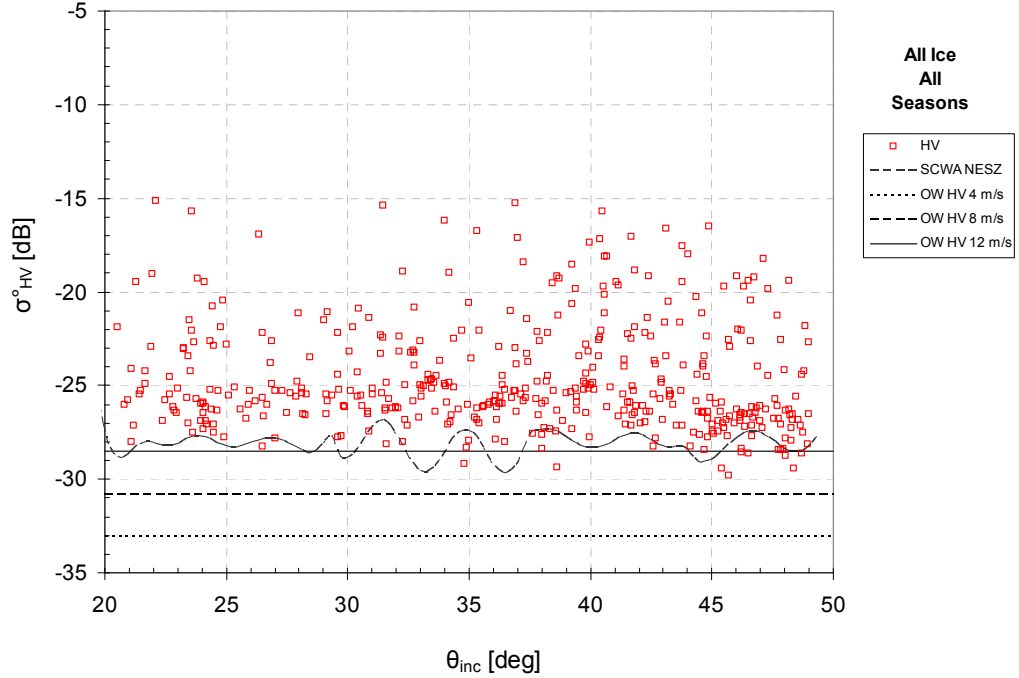
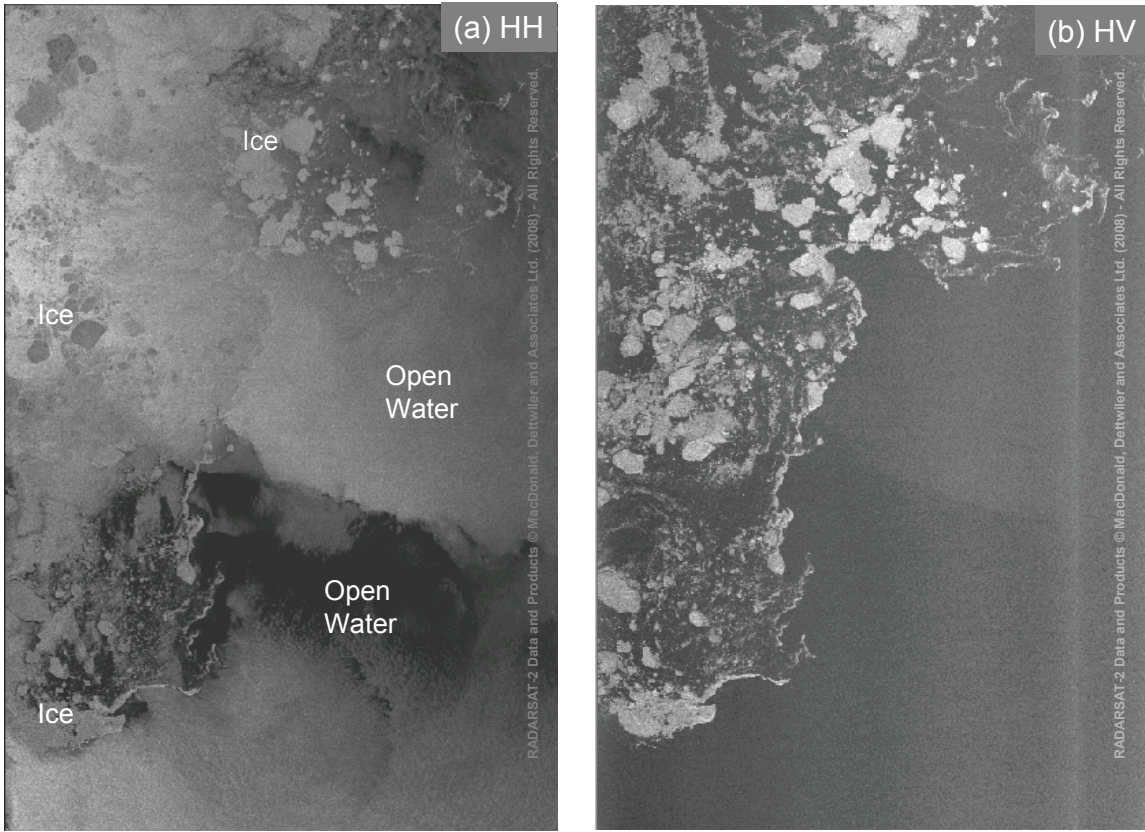


Figure 3: HV backscatter for all sea ice types over all seasons, including OW backscatter for various wind speeds and NESZ for SCWA.



*Figure 4: S. Beaufort Sea, 2008-09-15, showing a subset of a R-2 SCWA image: (a) HH; and (b) HV (near-range on the left).*

CIS analysts now routinely use the HV channel to estimate ice concentration given this improved contrast. Figure 5 and Figure 6 indicate that the backscatter of New Ice (0 to 10 cm) is often noise-limited in ScanSAR HV making its detection sometimes difficult. This is consistent with the experience of operational ice analysts who recognize that given the likelihood of new ice scattering at or below the noise floor at HV polarization, the combined use of both HH and HV channels is required for the detection of all sea ice types.

Given the small SNR in HV, the range-ward variation of the R-2 noise floor manifests itself as tonal banding that hinders the visual and automated interpretation of this channel. CIS analysts have complained that this banding, readily apparent in false colour combinations of HH and HV imagery (Figure 7), is distracting to scene interpretation. The effects of this tonal variation can be minimized through the use of post-processing techniques that rely on a model of the mode's NESZ included in each R-2 product. Figure 7 also shows the effects and benefits of "noise subtraction". The banding has been largely eliminated and the image has a much improved consistency of colour (tone) across its full range.

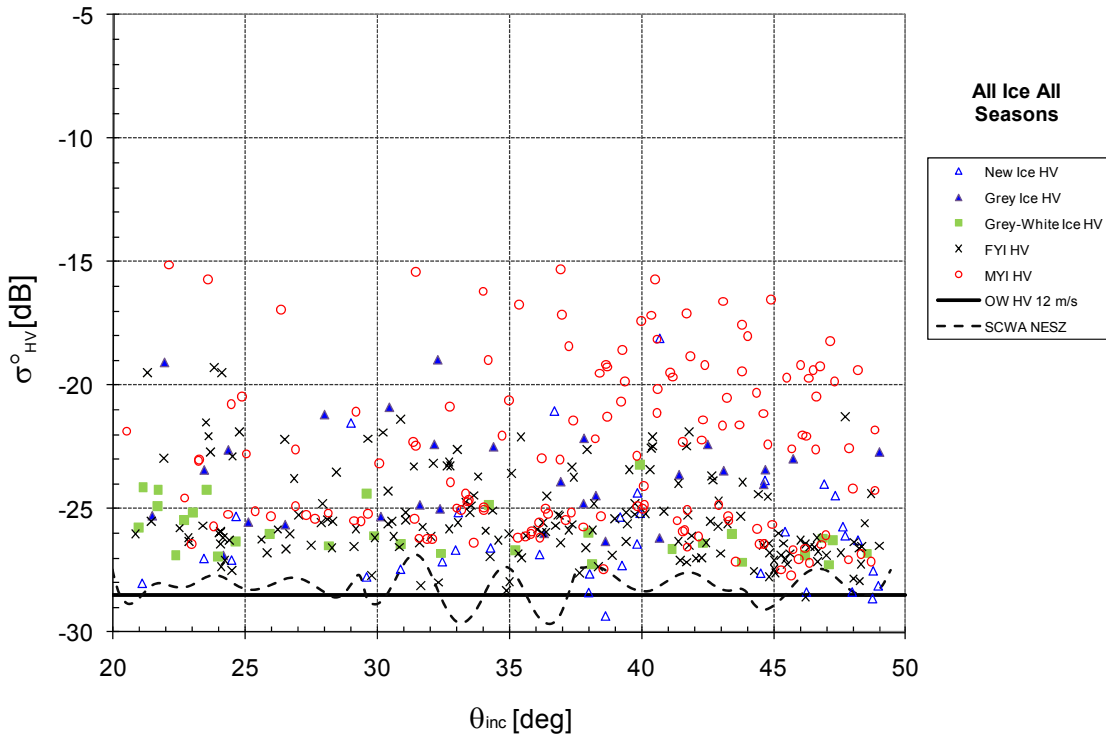


*Figure 5: HV backscatter for individual sea ice types over all seasons, including OW backscatter for various wind speeds and NESZ for SCWA.*

### 2.3.3 Ice typing

In order to estimate the risk represented by an ice regime, mariners require some estimate of its inherent strength. This cannot be observed directly via remote sensing, but information regarding the thickness of sea ice can be inferred by an estimate of its stage of development or growth. Generally, the sea ice classes described in Table 4 are used to operationally report on sea ice type and associated thicknesses. Old ice is considerably thicker, denser and thus stronger than seasonal ice. As such, in an ice regime where old ice may occur, its separation from thinner, weaker seasonal ice classes is a high priority. A seasonal ice regime represents a very wide range of ice thickness and related strengths. Operational ice services must also be able to reliably characterize the stage of development within these seasonal regimes. There exists considerable operational experience using single channel (HH or VV) C-band satellite SAR imagery for ice typing. As with other microwave-based sensors, the performance of ERS-1/2, R-1, ASAR and R-2 in ice typing can be described as good to excellent in cold, winter conditions, and poor in warm summer seasons.

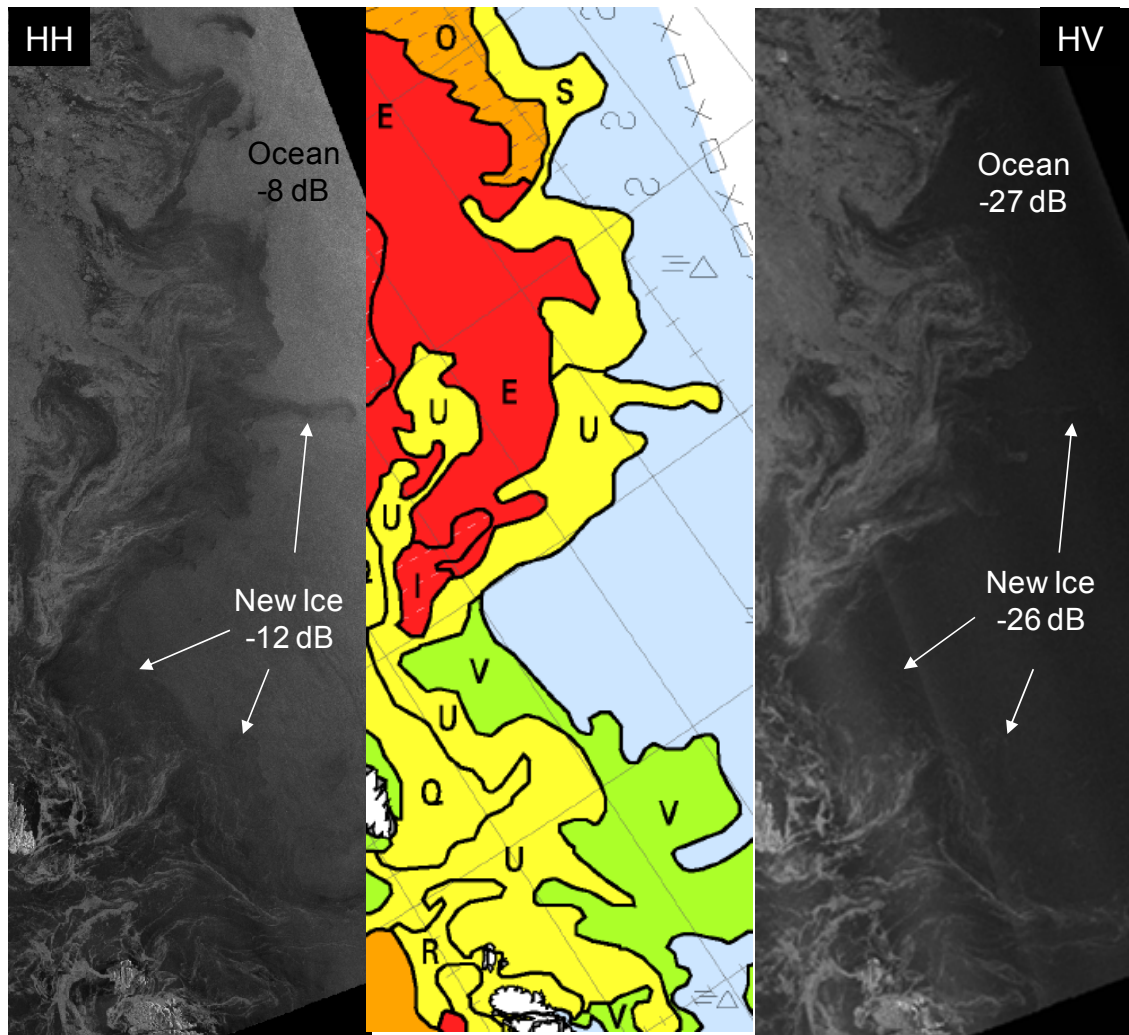


*Figure 6: Appearance of New Ice in SCW HH and HV (near-range). There is adequate contrast (4 dB) between smooth New Ice and OW in HH (left), allowing charting (centre). Both New Ice and OW backscatter are below NESZ and are indistinguishable in HV (right).*

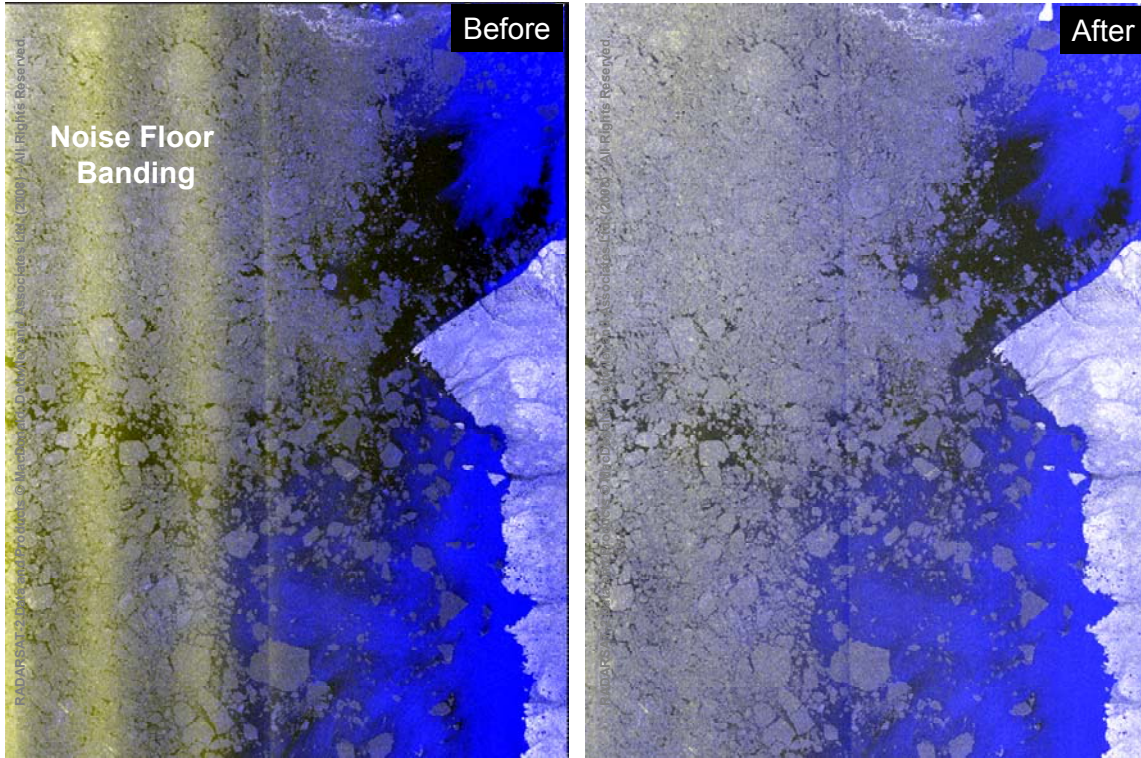


*Figure 7: 2010 S. Beaufort Sea false colour R-2 SCWA images before (left) and after (right) noise subtraction. In each case, the HV image was assigned to both the Red and Green channels, while HH was assigned to Blue (near-range on the left).*

*Table 4: Sea Ice Stage of Development classes for operational ice monitoring (after MANICE [5]). Note, “Seasonal” is not an official class, but is used here for additional context.*

<b>Seasonal Ice</b>	<b>Ice that grows and melts in one year</b>	<b>0 to 200 cm</b>
New Ice	Includes Nilas	0 to 10 cm
Young Ice	Grey Ice	0 to 15 cm
	Grey-White	15 to 30 cm
FYI	Thin FYI	30 to 70 cm
	Medium FYI	70 to 120 cm
	Thick FYI	> 120 cm
<b>Old Ice</b>	<b>Ice that has survived at least one summer's melt</b>	<b>&gt; 200 cm</b>
	Second year ice	Old ice that has survived one summer's melt
	MYI	Old ice that has survived at least two summers' melt

### **2.3.3.1 Winter**

The strong reliance on data from R-1 by operational ice services is testament to their ability to reliably type ice over much of the year using single channel HH polarized data. The identification of ice types is at its best during the cold periods when the ice and its overlying snow cover are dry, thus allowing maximum penetration and interaction with the ice surface and volume at C-band. Figure 8 shows that across the ScanSAR range, MYI backscatter is well separated from less thick seasonal FYI and Grey-White and New Ice types. Again, the ability of C-band HH data to reliably identify MYI within an ice regime is critical given the hazard this ice type represents to most classes of ships. The results also show that based on magnitude alone, it is difficult to separate MYI from much thinner Grey Ice at this polarization. In this case analysts rely on other interpretative clues – texture, shape and context – to separate the two very different ice types. Smooth New Ice in the far range often scatters near or below the noise floor and can be very difficult to detect even in HH, especially with the background ocean appearing dark as well (Figure 2).

Figure 9 provides the HV winter backscatter for various ice types. As noted, there is a significant drop in the magnitude of the signatures. Unfortunately, the signatures of seasonal ice types overlap in HV, thus providing poorer typing than HH. This is somewhat expected given that surface scattering typically dominates over these more saline ice volumes and there is little signal depolarization. Since volume scattering dominates for MYI, as shown here, the respective HV backscatter is higher than for seasonal ice types. Figure 10 illustrates how this manifests itself in R-2 imagery in a positive way. In winter, the identification of MYI in a high concentration, mixed ice regime using HH is not straightforward in the presence of Grey Ice and other deformed seasonal ice types. Surface scattering of seasonal ice types and volume scattering from MYI are at similar magnitudes making ice typing difficult in this case. In the HV channel, volume scattering dominated, making the MYI stand out against the darker seasonal ice regime. The ability of R-2 HV to more easily identify hazardous MYI within a mixed winter ice regime is important to operational ice monitoring.

### **2.3.3.2 Summer**

Ice typing in the summer period is confined to separating the remaining seasonal FYI from MYI. The seasonal increase in liquid water within overlying snow volumes and on the ice surface results in reduced penetration at both C-band HH and HV. The resultant loss of tonal and textural contrast makes summer ice typing extremely difficult with C-band SAR. Figure 11 shows the sampled backscatter over FYI and MYI ice volumes at both HH and HV polarization. At HH, the strong winter contrast between FYI and MYI (Figure 8) has disappeared. This has been a well-known seasonal limitation for RADARSAT and other C-band SAR's since their operational implementation by ice services in the nineties. There was some interest in whether HV data could somehow alleviate this problem. As shown in Figure 11 and Figure 12, contrast between these ice types is even poorer in HV as the signatures overlap and are driven down towards the noise floor. Ice services are actively exploring the ability of L-band SAR to improve summer ice typing.

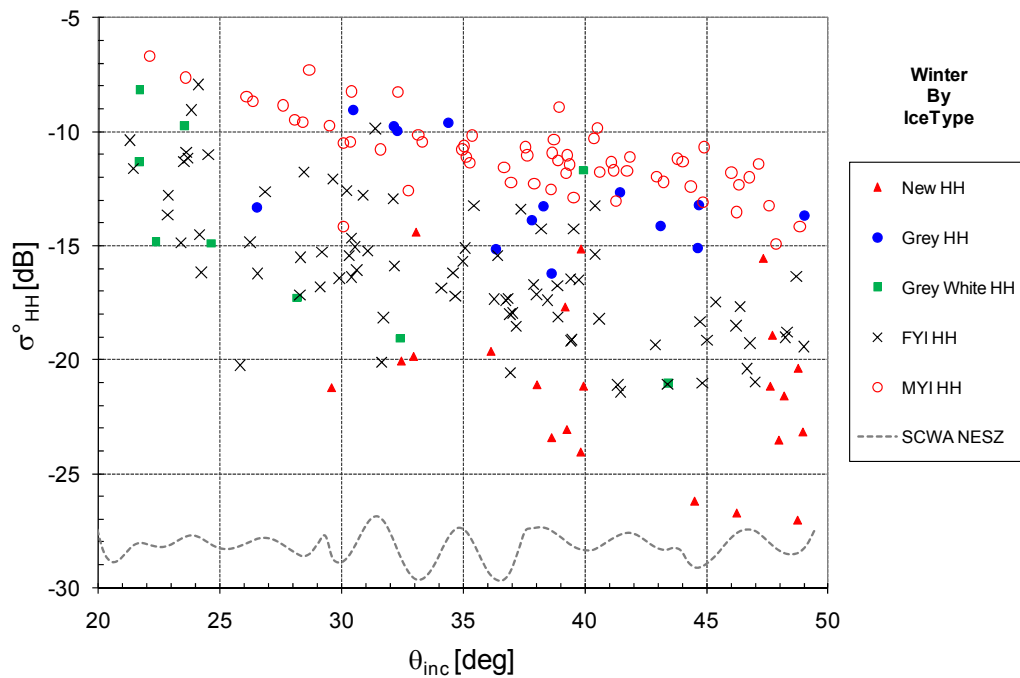


Figure 8: HH backscatter for individual sea ice types over winter season with NESZ for SCWA.

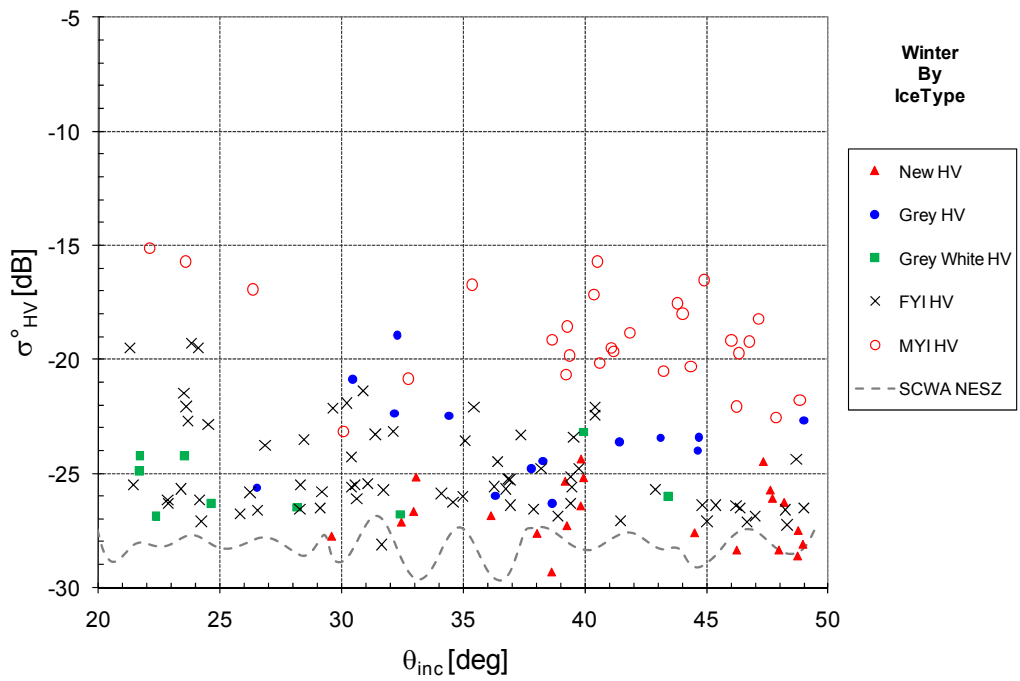


Figure 9: HV backscatter for individual sea ice types over winter season with NESZ for SCWA.

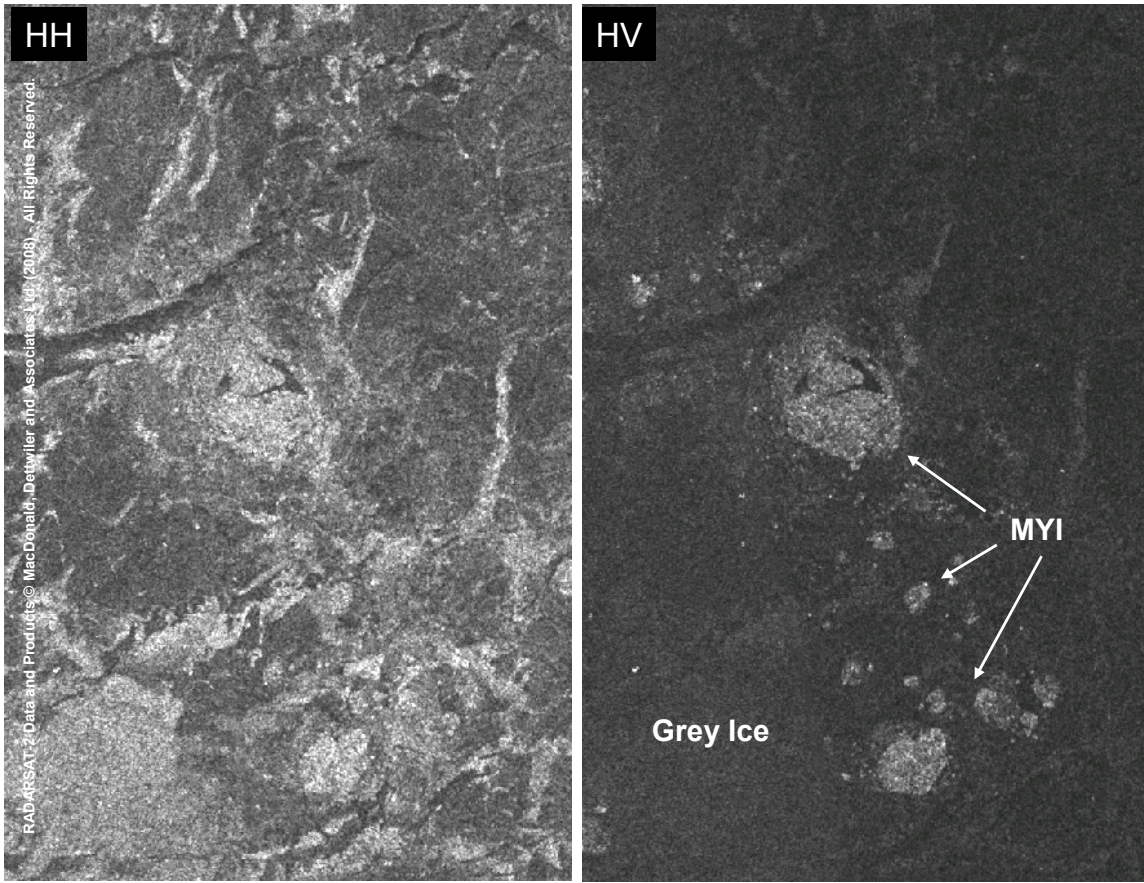


Figure 10: R-2 SCW, 2010-07-24. MYI and Grey Ice have similar tones in HH, while in HV, there is strong contrast between ice types simplifying the identification of hazardous MYI.

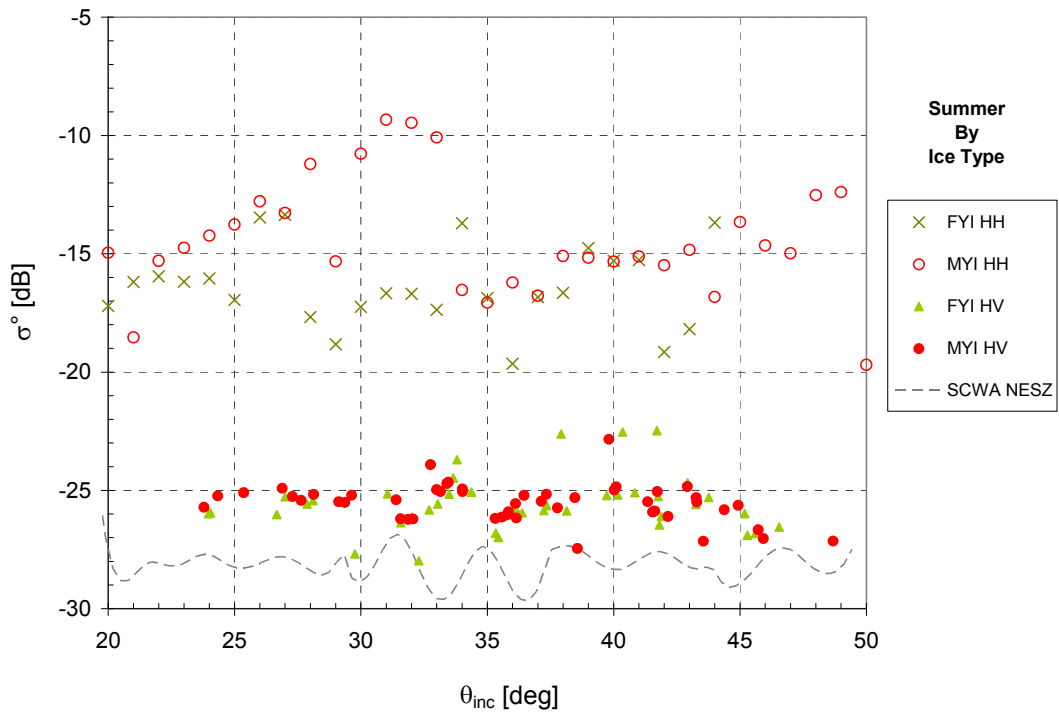


Figure 11: HH and HV backscatter for individual sea ice types over summer season, with NESZ for SCWA.

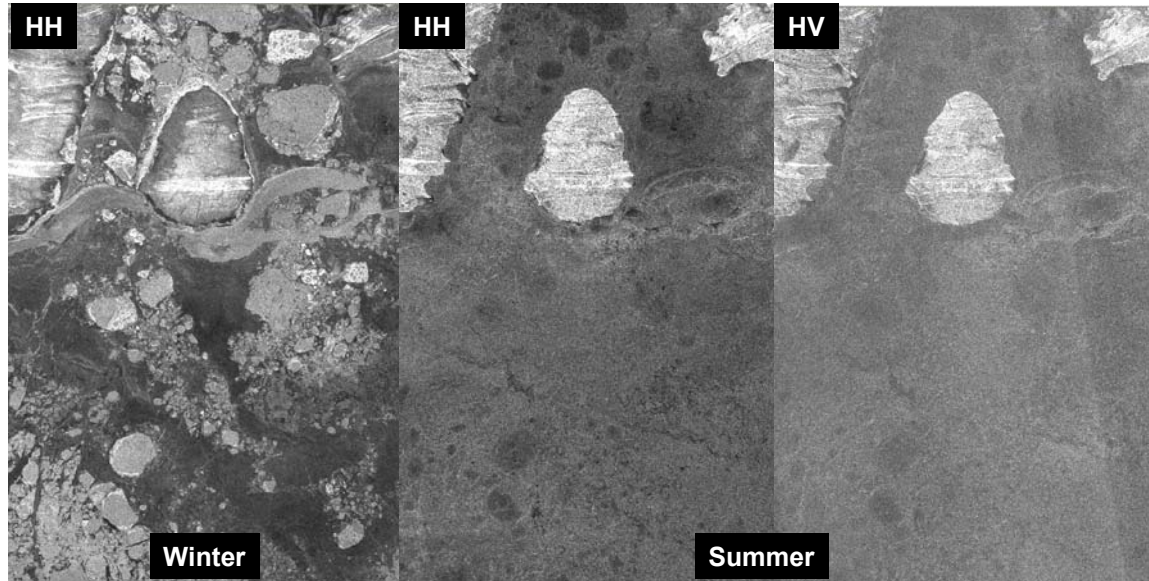


Figure 12: Winter (2008-12-19) and summer (2009-07-06) R-2 SCW HH and HV images over Barrow Strait. The loss of wintertime contrast between the bright MYI floes and the surrounding darker smooth FYI makes summertime ice typing very difficult using HH or HV R-2 modes.

## **2.4 Mode recommendations**

### **2.4.1 RADARSAT-2**

Results indicate that significant improvements in both the estimation of ice concentration and wintertime sea ice typing are possible with the routine use of HH+HV data. In pre-launch studies, this potential of dual channel R-2 was identified. This study and the subsequent incorporation of R-2 HH+HV data into the workflow of operational ice services validates the advantages of moving to routine use of dual channel R-2 for ice monitoring. The benefits of HH+HV are more significant in the colder winter periods, but the mode also can help to improve the estimation of ice concentration in summer as well. As such, HH+HV should be considered the Primary Mode for operational ice monitoring. The heritage mode HH should still be considered a valuable Secondary Mode.

The most significant challenge with the adoption of HV into the workflow is the poorer SNR and the resultant effects on image interpretation (NESZ banding) and ice detection (*i.e.*, loss of new ice). However, post processing and user education can alleviate these issues. Another challenge is the requirement to occasionally increase the quantization of the acquired data so that dual channel data can be down linked in near-real time. As described in Section 9.3, the lowering of BAQ (block adaptive quantization) from 4 bits to 2 bits can result in a loss of image texture, especially in darker scenes. Indeed, in preliminary examinations of the effects of increased quantization on ice interpretation, ice analysts could detect this change in image quality.

### **2.4.2 RCM**

Given the results of this study, it is unclear what should be the Primary Mode for operational ice monitoring with RCM. The HH+HV Medium Resolution mode offering 350 km swath at 50 m resolution seems like the best candidate. However, this study makes the case that the utility of the HV mode within the RCM will be closely tied to the system's NESZ. Currently, for most RCM modes, like the Medium Resolution mode, the worst-case NESZ is specified to be -22 dB. This is considered acceptable for HH, where the SNR has been shown here to be more than adequate for ice monitoring in most cases. However, to realize the benefits of HV in terms of estimating total ice concentration, the NESZ in Medium Resolution mode will have to be significantly and routinely better than -22 dB. If not, the detection of seasonal ice will be noise limited. Recognizing this possibility, a Low-Noise mode was added to the RCM whereby resolution was traded for sensitivity. In this mode the worst case NESZ is estimated to be -25 dB, while the resolution is reduced to 100 m.

Also important is the fact that the Medium Resolution mode in RCM will be 1-look in azimuth and regularly employ onboard 2-bit BAQ to accommodate the downlink capacity. Evidence to date suggests that a reduction in BAQ (*i.e.*, increased quantization) may have some effect on image quality that could impact its use in sea ice monitoring. Fortunately, the new, similarly-designed R-2 OSVN mode offers the ability to evaluate these issues pre-launch to better assess the use of the Medium Resolution mode for ice monitoring.

Operational ice services may routinely opt for the Low Resolution (LR) mode in HH+HV. Its broad 500 km swath will ensure important lower-latitude ice regimes, like the Gulf of the St.

Lawrence, are covered every 12 hours, instead of the 24 hours required by the Medium Resolution mode. As such, daily workflow and requirements for reporting will likely play a role in mode selection for RCM.

Finally, RCM will provide Compact Polarimetry (CP) in most modes. This new polarization option will offer polarimetric-like sea ice information over surveillance swaths. Preliminary analysis indicates that this mode could be rich in ice information [8] and its use for sea ice monitoring could be routine in the era of the RCM.

## 2.5 Future analysis

R-2 OSVN mode offers improved swath and resolution compared to R-2's existing modes and should be evaluated by operational ice services as an alternative to SCN and SCW. Also, as mentioned, the mode can also be used to assess RCM's Medium Resolution mode pre-launch. As will be shown later in the report, further study on the effects of BAQ on image quality and sea ice interpretation is required given the potential offered by the OSVN and the RCM Medium Resolution Modes. The Canadian Ice Service is actively investigating the utility of CP for operational sea ice monitoring. This work should continue. The study is remiss in not examining the utility of R-2's VV+VH mode compared to HH+HV. While some VV data was collected, it was insufficient to support full consideration here. An extension of this study to include this mode is warranted given that VV+VH will be the default polarization for Sentinel-1.

## **3 Ice Island monitoring**

---

### **3.1 Background**

Ice islands are large masses of ice that calve from Arctic ice shelves [24]. Climate warming and the increased presence of leads have led to an increase in the calving rate of ice shelves in the recent decade relative to the latter half of the 20<sup>th</sup> century [10], [31], [32]. This ice type is considered to be a hazard to navigation and structures such as petroleum exploration platforms [15] and as such, its detection and surveillance falls within the operational mandate of the CIS. Ice islands, while similar to icebergs in some respects, can be composed of a variety of ice types, which interact differently with microwaves. This is further complicated by the fact that ice islands are surrounded by Arctic pack ice, and can break into numerous fragments making their detection difficult.

An operational goal of the CIS is to detect ice islands using wide-swath SAR data (*i.e.*, ScanSAR) regardless of the surrounding ocean cover/state so they may be charted and their drift monitored. *A priori*, the ability to detect an ice island is a function of a variety of factors including:

1. The ice island type, size and shape;
2. The surrounding ocean cover/state (the background);
3. The ambient temperature, which varies diurnally and seasonally thus affecting the properties of the ice surface and volume; and
4. The SAR mode (*i.e.*, polarization, resolution, swath width, frequency) and acquisition geometry.

In light of the above, the objective is to evaluate the detectability of ice islands over the broadest range of all factors listed above in order to recommend the preferred and secondary R-2 ScanSAR beam modes for this application. A quantitative approach was employed where ice island detectability was taken as the contrast between the target backscatter and the background backscatter. While understood as important, textural differences and any historical context that an analyst might utilize in detecting an ice island are not considered here.

The ice shelves that fringe the northern coast of Ellesmere Island formed some 3,500 to 5,500 years ago as landfast sea ice that thickened over time as ice froze to the underside and snow accumulated on its surface [24]. In the case of some ice shelves, this was augmented by mass input from glaciers. These processes give rise to two main surface ice types – *meteoric ice*, derived from in situ precipitation or glacial inflow and *marine ice*, derived from basal freeze-on of salt or brackish water [33]. Areas where marine ice is exposed at the surface are often laden with marine sediments that have been transported through the ice via basal freeze-on and long term surface ablation. These geophysical differences in ice type are important for the detection of ice islands using remote sensing because they govern, to a large extent, the backscatter signature of these targets.

The surface of Arctic ice shelves and ice islands is marked by a ridge and trough morphology that is readily recognizable both from the air (Figure 13) and in SAR imagery (Figure 14). This pattern contrasts with the more chaotic ridging of sea ice and the even texture of large undeformed floes. Ice islands vary greatly in size from 775 km<sup>2</sup>, the largest known ice island (T-2, 1948) to ice island ‘fragments’ of several hundred metres in length [4], [Mueller, unpublished data]. After calving from the ice shelves at the northern tip of Ellesmere Island, they generally drift to the southwest in the Beaufort Gyre towards Alaska, although they can also drift south into the Canadian Arctic Archipelago, see Figure 2 in [61]. These ice masses thin over time and can fragment into smaller pieces, but they can also agglomerate with multiyear pack ice [23]. Ice island drift is fairly chaotic over short timescales, since current and wind reversals will alter their immediate trajectories. Drift is typically the fastest at the end of summer (around the time when the pack is at its minimum extent). Drift speeds of 30 km per day are possible but rare.



*Figure 13: An ice island (Target 2) adrift in the Arctic Ocean north of Meighen Island on 18 May 2009. Note the surface undulations and higher freeboard than the surrounding ice. Photo courtesy Sierra Pope (University of Ottawa).*

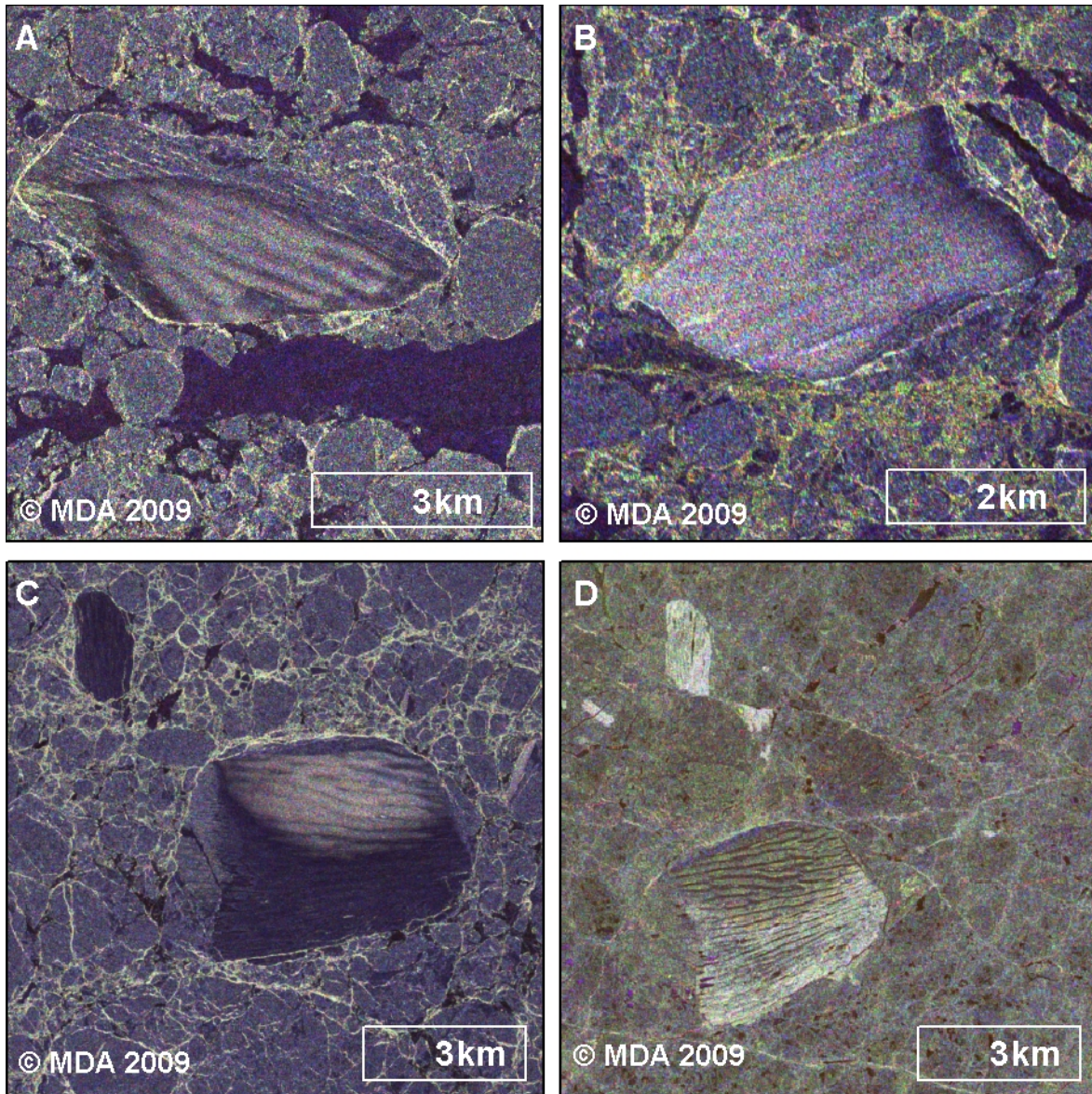


*Figure 14: R-2 FQ imagery of ice island targets used in this study displayed as a Pauli decomposition (R: HH–VV, single-bounce; G: (HV+VH)/2, volume scattering; B: HH+VV, double-bounce).*

(A) Target 1, with broad surface undulations of meteoric ice (central triangle), surrounded by multiyear landfast sea ice on two sides (FQ10, 2009-11-04 23:21:39 UTC). (B) Target 2, with meteoric ice, except for a small fringe on the far right. Surface undulations are less apparent compared to Figure 13, likely due to imaging geometry (FQ2, 2009-12-25 15:15:34 UTC); (C) Target 7 (middle) with a combination of brighter-toned meteoric ice and darker-toned marine ice and Son of 7 (upper left), which broke off of Target 7, with marine ice (FQ19, 2009-11-09 14:17:11 UTC); (D) Target 7 and Son of 7 in mid-summer when water in the snow and ice surface reverses the SAR signature of the various ice types (FQ3, 2009-07-13 15:27:33 UTC).

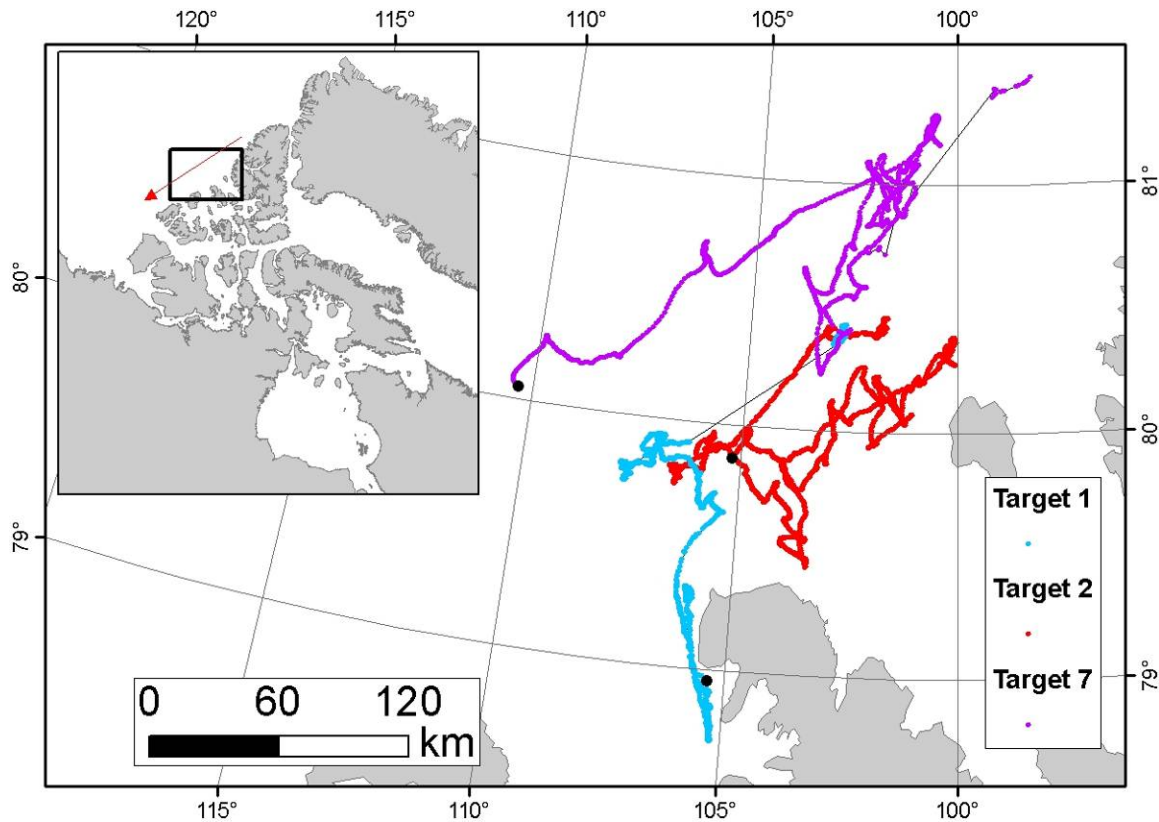


*Figure 15: The drift of the three ice islands tracked in this study.*

*Each ‘target’ was selected from wide beam R-2 imagery in May and beacons were deployed in May (Targets 1 and 2) and in July (Target 7). The map depicts observations up to 2010-03-31 (indicated by a black dot). The inset map shows the location of the drift tracks north of the Canadian Arctic Archipelago and the red arrow indicates the typical (or expected) drift direction for ice islands calving from Canadian Arctic ice shelves at the northern coast of Ellesmere Island.*

### 3.2 Data and methods

Two different types of data were used to carry out this analysis – R-2 imagery and ice island tracking beacon data. The former data were sampled to provide statistics on ice island detectability whereas the latter data type were used to validate imagery by providing an independent means of locating ice islands within the imagery (Figure 15).

Three ice islands (named Target 1, 2 and 7, see Table 5) were tracked over time using satellite beacons. Two Metocean CALIB ARGOS beacons were deployed on 2009-05-18 (Target 1 and 2) and one Metocean Iridium GPS beacon was deployed on 2009-07-16 (Target 7). These beacons provided positional data (dozens of times per day) except during the occasional outage (22 and 47 days during summer 2009 for Target 1 and 7, respectively). The beacons also transmitted the temperature of the beacon housing (Target 1 and 2) or the air temperature (Target 7). These data were filtered to remove obviously spurious data and the average of all beacon temperatures reporting from within 20 km of each image footprint within 6 hours prior to the

acquisition of the image were incorporated in the analysis. One ice island (Son of 7) that appeared to have broken off, and was always adjacent to, Target 7, was readily identifiable in the imagery and was therefore incorporated into the study.

*Table 5: Characteristics of tracked ice islands at the beginning of the study.*

<b>Ice island</b>	<b>Source ice shelf</b>	<b>Surface ice type</b>	<b>Length [km]</b>	<b>Width [km]</b>	<b>Area [km<sup>2</sup>]</b>
<b>Target 1</b>	Ward Hunt	Meteoric with some attached MYI	6.2	2.7	11
<b>Target 2</b>	Ward Hunt	Meteoric, with a small band of Marine along one edge	4.4	2.3	7
<b>Target 7</b>	Markham	Meteoric and Marine	5.8	4.0	18
<b>Son of 7</b>	Markham	Marine	2.6	1.0	2

*Table 6: Polarization of the R-2 images used in this study.*

<b>Ice island</b>	<b>Quad Pol</b>	<b>Dual Pol</b>		<b>Single Pol</b>				<b>Total</b>
		<b>HH+HV</b>	<b>VV+VH</b>	<b>HH</b>	<b>VV</b>	<b>HV</b>	<b>VH</b>	
<b>Target 1</b>	19	81	12	13	-	-	-	125
<b>Target 2</b>	16	84	12	14	-	-	-	126
<b>Target 7</b>	16	81	11	11	-	1	-	120
<b>Son of 7</b>	13	74	11	8	-	1	-	107
<b>Total</b>	<b>64</b>	<b>320</b>	<b>46</b>	<b>46</b>	-	<b>2</b>	-	<b>478</b>

Ice island positional data were employed to plan R-2 acquisitions from September 2009 until March 2010 (Table 6). FQ imagery were acquired for each of the three main targets once every three weeks at three different incidence angles (below 27°, between 27° and 34°, and from 34° to 41°; in 2010 incidence angles above 41° were made available so these were added to the acquisition plan). These acquisitions were supplemented by SCN imagery once every three weeks in HH+HV and VV+VH and by weekly CIS operational SCW HH+HV (8-bit) imagery. Occasional Spotlight, UltraFine, Fine, Standard, and Wide beam mode images were also used in the study, when available.

Ice island targets were identified in the imagery with help of the beacon position, if required, and the shape of each target was delineated with a polygon in ArcINFO (ESRI). Images were subsequently calibrated to sigma nought backscatter power (in linear scale), projected to Albers Equal Area projection (with nearest-neighbour resampling) and pixels falling within each target polygon were extracted. Basic statistics (mean and variance) were computed and the procedure was repeated to generate mean incidence angle and NESZ for each polygon.

In order to determine the detectability of each feature, a sampling of the pixels surrounding each target was performed. All pixels falling within a 900 m swath surrounding each target were sampled as above. The result is a representation of the surrounding ocean cover which was typically a mix of MYI (ridged and/or undeformed) and infrequent open water leads. This sample type is henceforth referred to as the *generic background*. In addition to the naturally

heterogeneous generic background, each FQ scene was sampled, as above, using an 800 x 800 m polygon to delineate representative *specific background* areas that were near each target. Specific backgrounds that were sampled include smooth/undeformed floes of MYI and heavily ridged areas of MYI as well as OW/FYI areas. A final specific background category, open water under wind stress at 4, 8 and 12 m/s was modelled for all polarizations to estimate sigma nought at the incidence angle of each target. Minimum and maximum sigma nought were obtained for wind azimuth relative to SAR look directions of 0° and 90° using CMOD-4 for VV as well as an empirically-derived cross-polarization model (Section 6).

The detectability of targets was evaluated with the contrast ratio defined as:

$$\text{Contrast Ratio} = \sigma^{\circ}_{\text{Target}} - \sigma^{\circ}_{\text{Background}} \quad (1)$$

where  $\sigma^{\circ}$  is the normalized radar cross-section expressed in decibels for the target and background. Higher absolute contrast ratios indicate better target detectability with respect to the background in question. A contrast ratio of 0 dB indicates that a target backscatter is indistinguishable from the background, whereas a contrast ratio of 3 indicates that the target backscatters twice the microwave energy than the background (or 200% more).

Aside from bivariate analysis of the contrast ratio with respect to date, temperature, incidence angle *etc.*, the absolute contrast ratio was modelled using ANCOVA. Due to temporal pseudoreplication in the dataset (each target was sampled on many occasions, which violated the assumption of sample independence), a random effect related to each target was accounted for along with fixed effects related to two factors (polarization and ice island ice type) and two covariates (incidence angle and ambient temperature). This linear mixed effect model (equivalent to an ANCOVA with repeated measures) was fit to explain the square-root of the absolute contrast ratio (this variable was transformed to normalize model residuals) with the explanatory variables listed above along with all two-way interaction terms [36]. The model was simplified by removing the least significant terms, starting with interaction terms, until just before the overall model became significantly less predictive [11]. This minimally adequate model was used to evaluate the hypothesis that the square-root of the absolute contrast ratio was different between the four SAR polarizations using a multiple comparison between these four factors. A different model was fit and analyzed for all observed background types as well as each background type with respect to the two different ice island ice types.

### 3.3 Analysis and results

Ice island backscatter was found to be highly variable, with a strong dependence on polarization and ice type, as illustrated by the higher backscatter values in meteoric ice islands versus marine ice islands (see Figure 16 and Figure 17). A two-way analysis of variance and post-hoc comparison from the entire dataset indicated that the mean backscatter was significantly ( $p < 0.001$ ) different across ice types and polarizations. The highest backscatter was observed in meteoric ice with VV polarization and the lowest backscatter was obtained with VH polarization over marine ice types.

The exception to this general rule occurred during the summer when HH and HV backscatter from meteoric ice was reduced (approximately from the 2<sup>nd</sup> week in June to the 4<sup>th</sup> week in

August) while marine ice backscatter remained unchanged (Figure 16). Based on only one SCW scene, this signature shift (or lack of a shift, in the case of marine ice islands) is likely also pronounced in VV and VH over this same period.

The backscatter of both meteoric and marine ice islands was negatively correlated with incidence angle ( $\theta$ ) (Figure 17). With slopes of  $-0.19$  to  $-0.24$ , this relationship was strongest in HH and VV, particularly for marine ice islands. The cross-polarized slopes were only one-fifth of this and the only non-significant association was between VH backscatter for meteoric ice islands.

The mean backscatter from all targets and at all polarizations exceeded the noise threshold for the scenes from which they were measured (Figure 16 and Figure 17). SCW NESZ was  $-26$  dB at worst, while other modes had variable but generally lower noise levels. The first quartile of the target backscatter was below the NESZ in 1.4% of the HV scenes and 1.5% of the VH scenes. This suggests that, in certain cases, the mean backscatter of targets is biased due to a poor SNR. However, in general, the noise threshold was sufficiently low to unambiguously detect ice islands.

### 3.3.1 Generic background

For most of the study, ice island backscatter was sufficiently different from the generic background (in this case, a regime of multiyear pack ice with infrequent leads) to be detectable. Meteoric ice islands tended to have a higher backscatter than the generic background and therefore had a positive contrast ratio, whereas marine ice tone was typically darker than the background, resulting in a negative contrast ratio (Figure 18 and Figure 19). The notable exception to this trend was during the summer period when signature reversals occurred. In the case of marine ice islands, this meant a change in the backscatter of the background against a relatively constant target backscatter. This resulted in poor contrast ratios only during a brief transition into and out of a period of background signature shift (Figure 19). Meteoric ice island contrast ratios overlapped with zero throughout this period and remained low for some observations during the fall and even went negative later in the winter for cross-polarized contrast ratios (particularly for Target 1; see Figure 18).

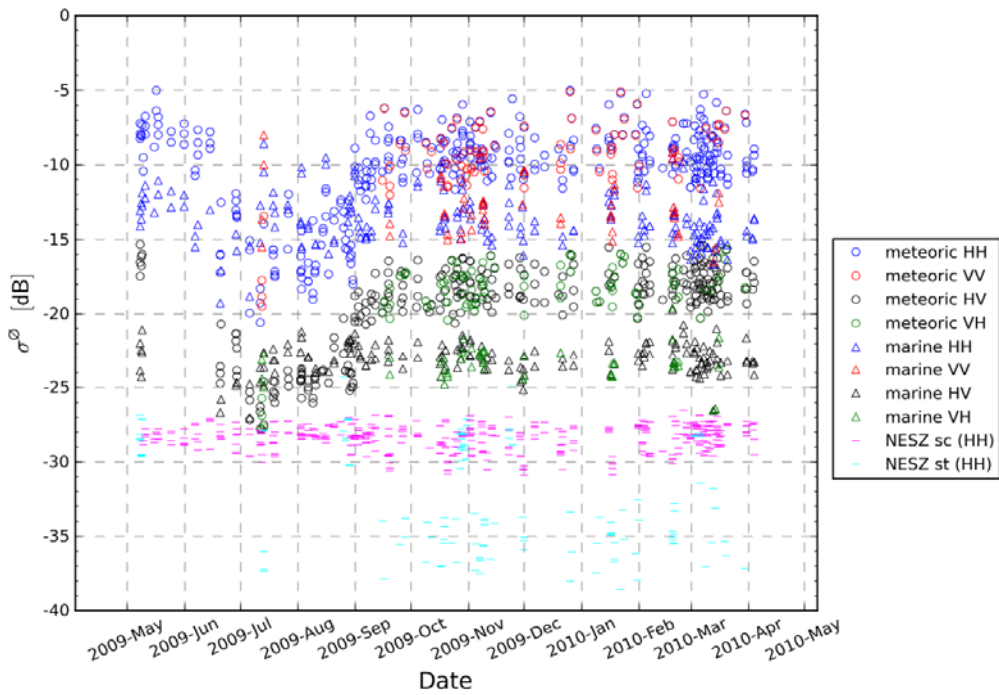


Figure 16: Mean backscatter for ice islands of meteoric and marine ice type versus date. The HH NESZ is given for SCW (NESZ sc) and single beam (NESZ st) modes.

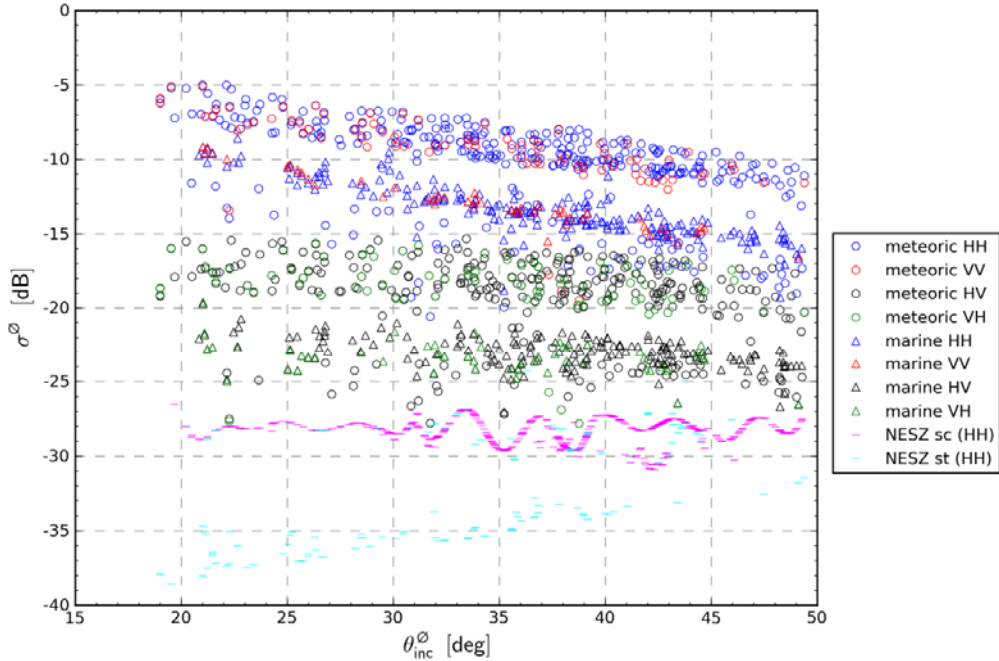


Figure 17: Mean backscatter for ice islands of meteoric and marine ice type versus incidence angle. The HH NESZ is given for SCW (NESZ sc) and single beam (NESZ st) modes.

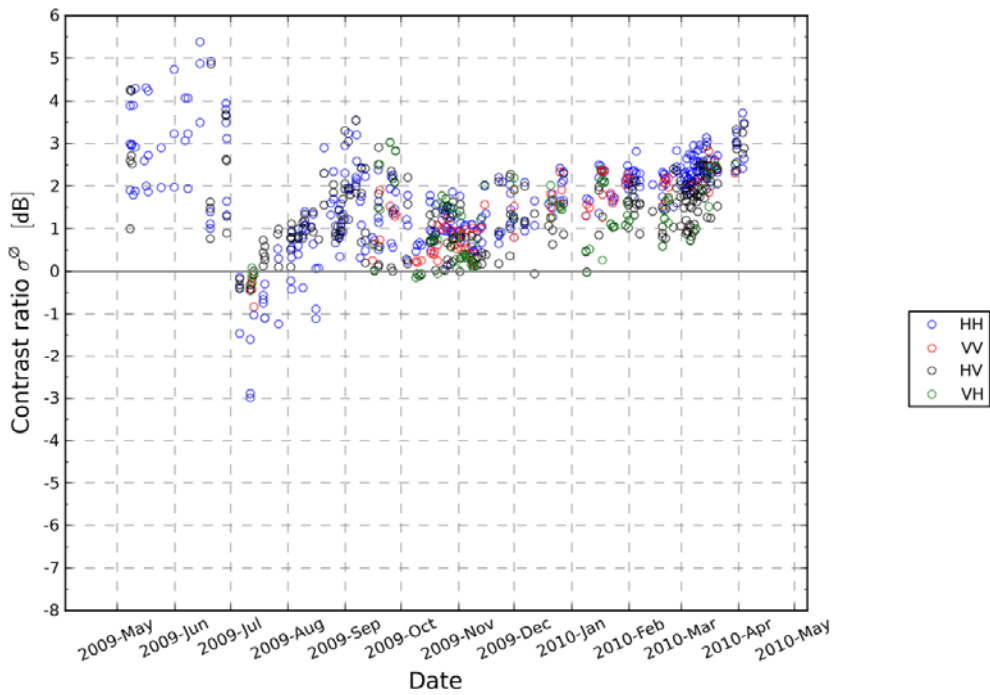


Figure 18: Contrast ratio between meteoric ice islands against a generic background versus date.

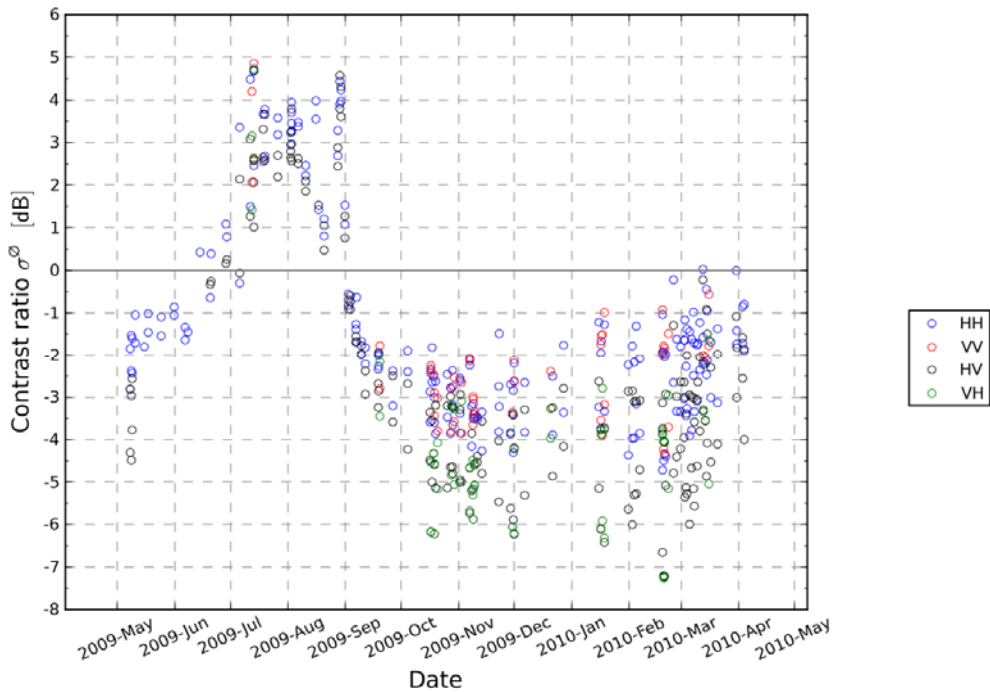


Figure 19: Contrast ratio between marine ice islands against a generic background versus date.

### **3.3.2 Specific backgrounds**

#### **3.3.2.1 Modelled wind**

There is a strong dependence between co-polarized SAR backscatter, incidence angle ( $\theta$ ), the relative wind direction ( $\varphi$ ), and wind speed over open water, *e.g.*, [30]. Given this relationship, the modeled co-polarized ice island to wind contrast ratios were also observed to depend on incidence angle (*e.g.*, Figure 20 and Figure 21). Co-polarized contrast ratios crossed the x-axis over a critical range of incidence angles where wind-roughened ocean clutter was comparable to ice island signatures;  $\varphi = 0^\circ$  (wind blowing towards the radar) produced a negative contrast ratio while  $\varphi = 90^\circ$  (wind blowing across the radar look direction) produced a positive contrast ratio, which raised the possibility of an undetectable ice island at some intermediate value of  $\varphi$  at that wind speed. For meteoric ice this potentially ambiguous zone was from incidence angles of  $20^\circ$  to  $35^\circ$  for HH and  $21^\circ$  to  $39^\circ$  for VV at a wind speed of 4 m/s. At 12 m/s, this zone shifts further downrange to  $24^\circ$  to  $49^\circ$  for HH and  $25^\circ$  to  $39^\circ$  for VV. The situation is similar for marine ice, where at 4 m/s, the potentially ambiguous zone ranges from  $22^\circ$  to  $35^\circ$  for HH and  $22^\circ$  to  $29^\circ$  for VV at wind speeds of 4 m/s. At 12 m/s, this zone was found to be from  $29^\circ$  to  $48^\circ$  for HH and  $34^\circ$  to  $49^\circ$  for VV. It should be noted that these ambiguous incidence angles represent a worst case in the observed data. Many observations within these ranges had contrast ratios that were far from zero.

Cross-polarized SAR backscatter over wind-roughened water does not vary appreciably with incidence angle or relative azimuth (Section 6). Therefore, contrast ratios in the cross-polarized channels were less influenced by incidence angle and were represented by a single point, rather than a range of values across all relative azimuths. Since cross-polarized SAR returns are also very low, high contrast ratios were typically noted for both meteoric and marine ice island types. However, cross-polarized meteoric ice island contrast ratios near 1 were noted at the highest wind speed (12 m/s). The overall distribution of contrast ratios at 8 m/s with respect to incidence angle can be seen in Figure 20 and Figure 21. Contrast ratios at wind speeds of 4 and 12 m/s had the same overall pattern as in Figure 20 and Figure 21, but with scale changes on the ordinal axis as described above.

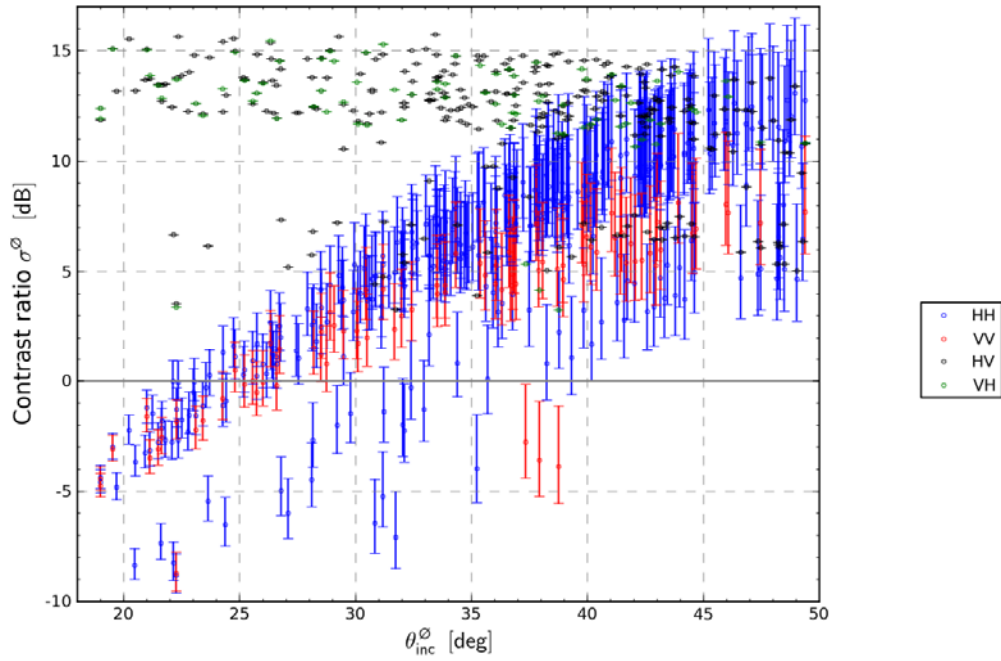


Figure 20: Contrast ratio between meteoric ice islands against an open ocean with a wind speed of 8 m/s at relative azimuth angles of  $0^\circ$  (lower error bar) and  $90^\circ$  (upper error bar).

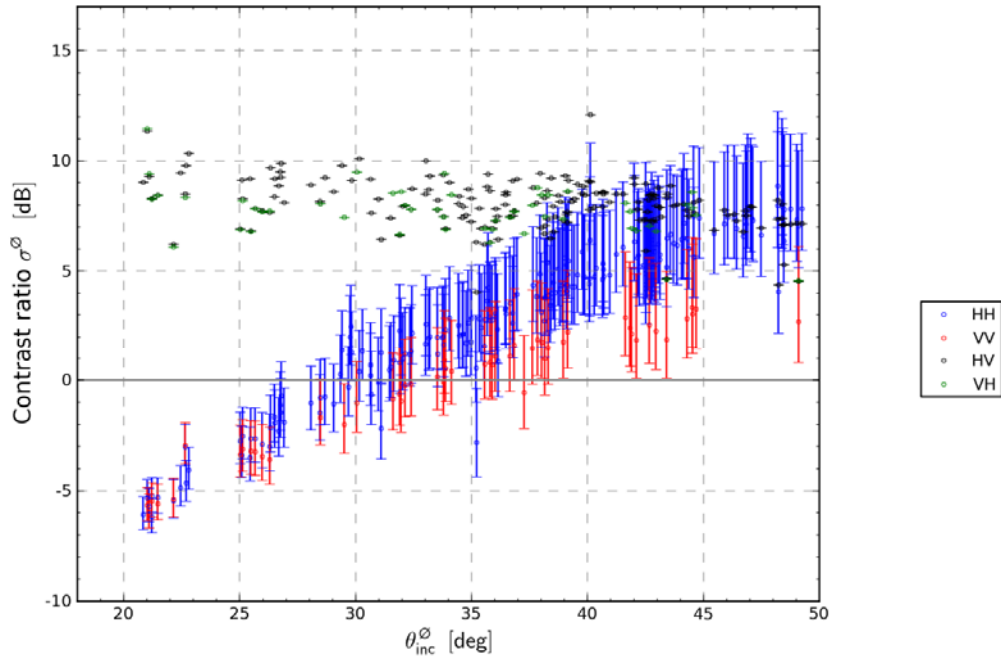


Figure 21: Contrast ratio between marine ice islands against an open ocean with a wind speed of 8 m/s at relative azimuth angles of  $0^\circ$  (lower error bar) and  $90^\circ$  (upper error bar).

### **3.3.2.2 Open water / FYI**

When present, OW and/or FYI types were sampled as a specific background to ice islands; these observations yielded high contrast ratios ( $>3$  dB) with all polarizations for meteoric ice islands (data not shown). Contrast ratios for marine ice ranged from 6 dB to -2 dB, with only 3 observations out of 13 in co-polarized bands at or below 0 dB (data not shown). Note that it is far more likely that these samples represented FYI in refrozen leads than OW, since the majority of these observations were made in the middle of winter.

### **3.3.2.3 Undeformed MYI**

Meteoric ice islands generally had higher backscatter than the sampled undeformed MYI floes and this is reflected in the positive contrast ratios in Figure 22. A notable exception is a group of about 12 samples from Target 1 whose contrast ratios were negative at temperatures near  $-20^{\circ}\text{C}$ . Marine ice islands had lower backscatter than nearby MYI floes and therefore their contrast ratios were invariably negative (Figure 23). In both cases, the HV and VH contrast ratios appeared to be better suited to the detection of ice islands over the co-polarized channels. It should be noted that data for temperatures above  $-15^{\circ}\text{C}$  are lacking for marine ice islands and above  $0^{\circ}\text{C}$  for meteoric ice islands.

### **3.3.2.4 Ridged MYI**

MYI with a high degree of ridging was found to have a broad range of backscatter with respect to meteoric ice islands which resulted in a wide dispersion of contrast ratios from -5.1 dB to 2.5 dB across all temperatures (Figure 24). Meteoric ice islands have high backscatter values in all polarizations as does severely deformed multiyear ice. However, ridged ice signatures may be quite variable depending on the SAR look direction and the incidence angle [35], which may be enough to change the meteoric ice island contrast ratio from positive to negative. Marine ice islands always had far lower backscatter than ridged ice regions, so contrast ratios were always large and negative (Figure 25).

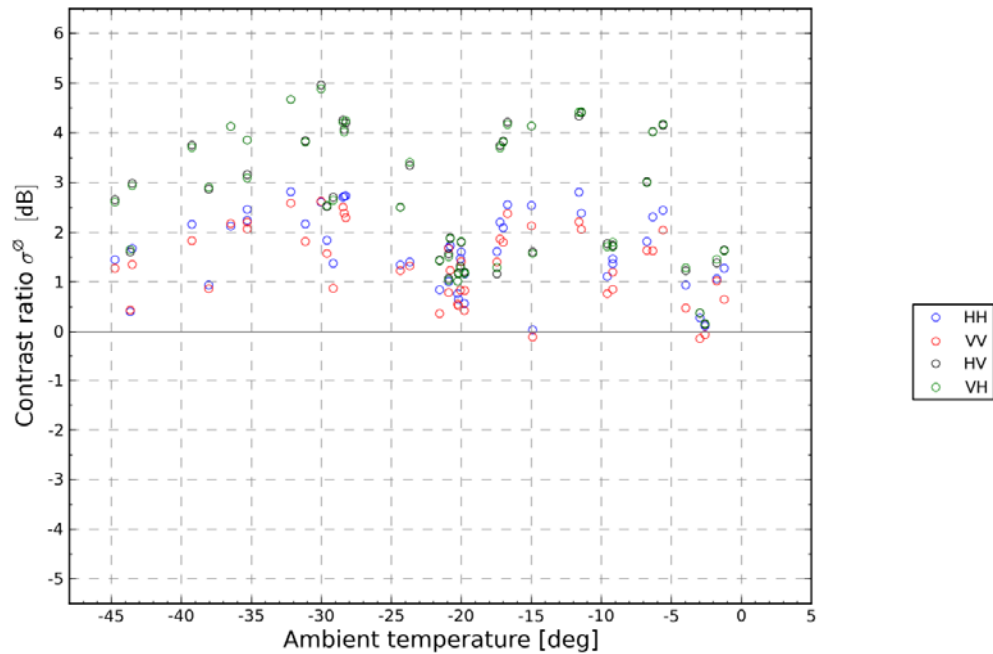


*Figure 22: Contrast ratio between meteoric ice island and undeformed MYI vs. ambient temperature.*

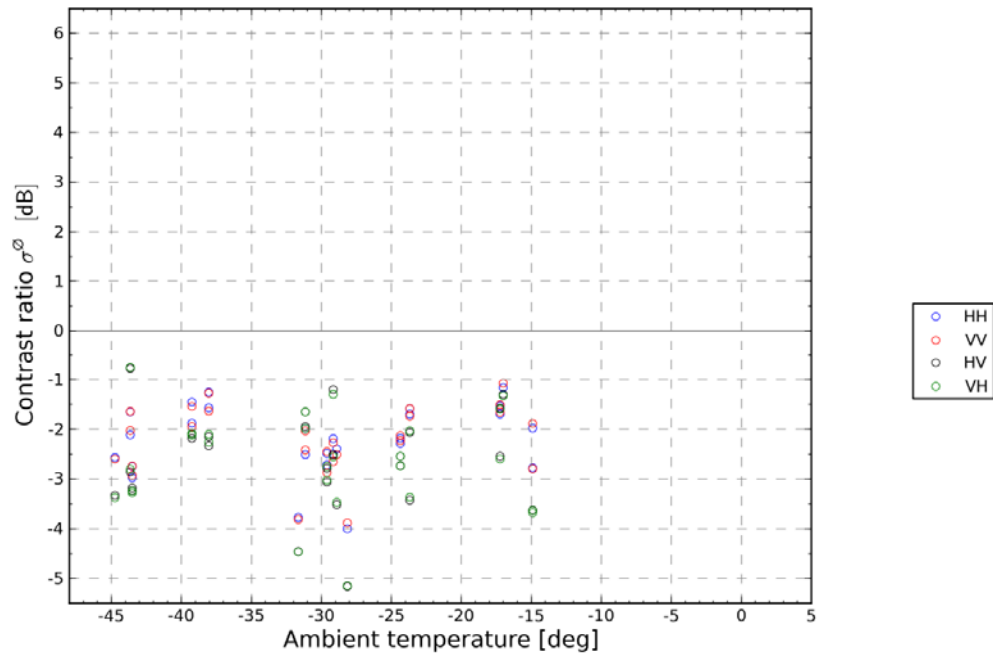


*Figure 23: Contrast ratio between marine ice island and MYI vs. ambient temperature.*

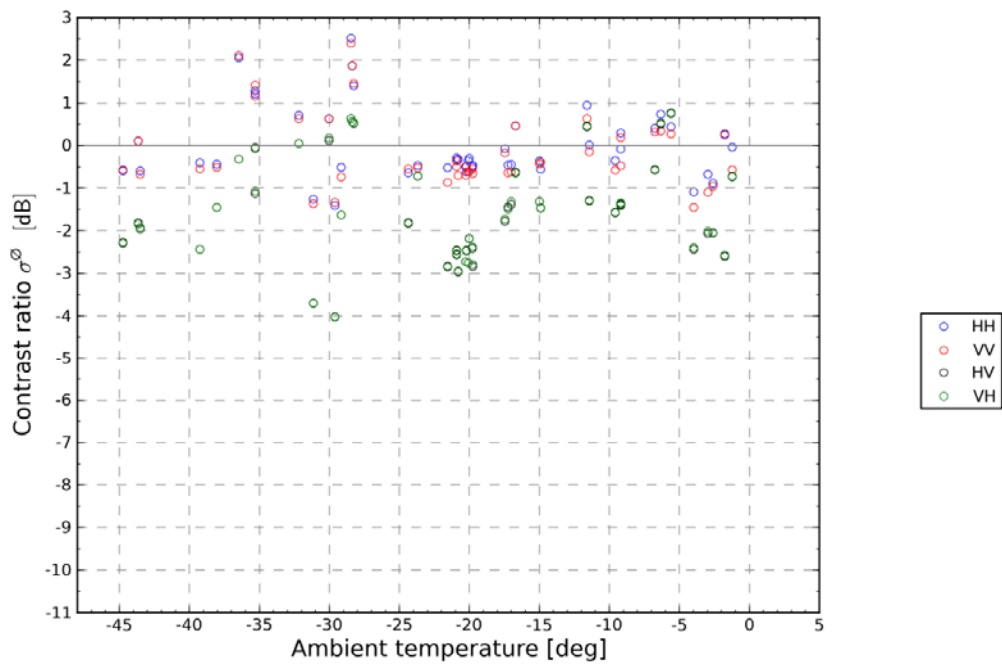


Figure 24: Contrast ratio between meteoric ice island and ridged MYI vs. ambient temperature.

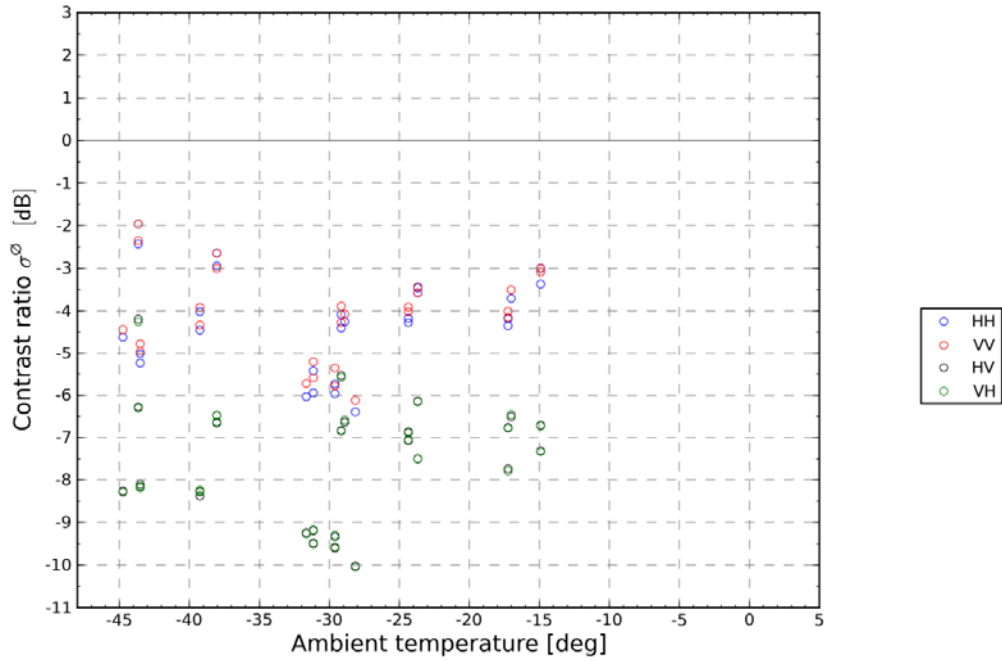


Figure 25: Contrast ratio between marine ice island and ridged MYI vs. ambient temperature.

### **3.3.3 Analysis of covariance**

The bivariate plots above show the association between contrast ratio and variables such as date, temperature, and incidence angle for the two types of ice islands. Another approach to analyzing the data is to examine all these variables at once in a multivariate ANCOVA model. This type of analysis can test the hypothesis that all four polarizations are equally good at detecting ice islands against a background while simultaneously accounting for potentially confounding effects such as incidence angle, temperature and ice island type. These models also account for interactions between these main effects, which are frequently significant. The two-way interactions between variables were modelled, but these effects are not discussed here for the sake of brevity. An added benefit to these models is that they appropriately consider repeat observations of the same ice islands on the population variance of ice islands as a whole.

A multiple comparison of the ANCOVA models indicated what differences there were between the four different polarizations for detection of ice islands (in this case, the square root transformed absolute contrast ratio) and whether these differences were statistically significant (Table 7). In other words, this method indicates the polarization that is furthest from the x-axis on the contrast ratio graphs (Figure 18 to Figure 25) and hence the most useful for discriminating an ice island from a given background. For example, the best choice for discriminating any ice island from a generic background is VH polarization, but this is not significantly different from HV or HH polarizations (Table 7). Likewise, no one polarization is significantly better than another for detecting marine ice islands against an undeformed multiyear sea ice floe (Table 7).

It is instructive to examine the importance of other effects besides polarization on the detectability of ice islands. Each ANCOVA model was simplified based on how much dependent variable variance was explained by each factor or covariate (and interaction terms). It is possible to test the remaining significant terms to evaluate the hypothesis that their effect size differs significantly from zero. For factors (*e.g.*, ice type in models including both marine and meteoric ice islands) the effect would be a difference in model intercept and for covariates (temperature and incidence angle) effects are represented as a change in slope. Table 8 shows that temperature is an important covariate in most cases whereas incidence angle is only important in certain situations. This table does not include any of the two-way factor/covariate interactions some of which can greatly influence model outcome. For example, for meteoric ice islands against a generic background, the interaction between ambient temperature and SAR polarization changed the order of preferred polarizations to VV from the more typical cross-polarized channels in other situations (see Table 7). In this particular case, the model implies that as temperature rises, the effectiveness of VV is reduced. This may be a geophysical phenomenon, but this is more likely a reflection of a lack of VV data at higher temperatures (Figure 18).

*Table 7: Multiple comparisons between polarizations in analysis of covariance models. Polarizations are listed from left to right according to decreasing effect on the absolute contrast ratio (best to worst polarization). Significantly different pairs are marked with superscript letters. Covariate and interaction effects were held constant for these comparisons.*

Background \ Ice island type	Both	Marine	Meteoric
<b>Generic</b>	VH <sup>a</sup> HV <sup>b</sup> VV HH <sup>ab</sup>	HV <sup>ab</sup> VH <sup>cd</sup> HH <sup>ac</sup> VV <sup>bd</sup>	VV <sup>a</sup> VH HH HV <sup>a†</sup>
<b>Open water / FYI</b>	VH <sup>ab</sup> HV <sup>cd</sup> VV <sup>ac</sup> HH <sup>bd</sup>	VH <sup>a</sup> HV <sup>b</sup> VV HH <sup>ab</sup>	HV <sup>ab</sup> VH <sup>cd</sup> HH <sup>ac</sup> VV <sup>bd</sup>
<b>Undeformed MYI</b>	VH HV VV HH	VH HV VV HH	HV <sup>ab</sup> VH <sup>cd</sup> HH <sup>ac</sup> VV <sup>bd</sup>
<b>Ridged MYI</b>	VH <sup>ab</sup> HV <sup>cd</sup> HH <sup>ac</sup> VV <sup>bd</sup>	VH <sup>ab</sup> HV <sup>cd</sup> HH <sup>ac</sup> VV <sup>bd</sup>	VH <sup>ab</sup> HV <sup>cd</sup> VV <sup>ac</sup> HH <sup>bd</sup>

<sup>†</sup>This scenario has a high variability for HH and HV backscatter above 0°C and yet is underrepresented by VV and VH at these temperatures. It is likely that this has led to spurious results (see text above). From a visual inspection of the data, it is likely that HH polarization is the most promising for meteoric ice island detection against a generic background.

*Table 8: Factors and covariates in ANCOVA models aside from polarization with main effect (not including factor/covariate interactions) sizes significantly greater than zero.*

Background \ Ice island type	Both	Marine	Meteoric
<b>Generic</b>	-	Temperature	Temperature, Incidence angle
<b>Open water / FYI</b>	Temperature	Temperature	Temperature
<b>Undeformed MYI</b>	Incidence angle	Temperature, Incidence angle	-
<b>Ridged MYI</b>	Ice type, Incidence angle	Temperature, Incidence angle	Temperature

## 3.4 Mode recommendations

### 3.4.1 RADARSAT-2

Based on the multiple comparisons presented in Table 7, cross-polarized SAR was significantly better than co-polarized SAR in the majority of situations. This was also the case for modeled contrast ratios in wind-roughened open water. Not surprisingly, no significant differences were noted between HV and VH performance in this study. The only situation where co-polarized SAR outperformed cross-polarized SAR was for meteoric ice islands against a generic background. However, this outlying result should not affect the overall conclusion that cross-polarized SAR (either HV or VH) is preferred for detecting ice islands by signature differences alone.

The results indicate that there is a sufficient signal to noise ratio in the vast majority of cases to detect ice islands across all evaluated modes. This study used a great variety of imaging modes, in particular SCW and FQ. The former mode was included since it was readily available and the second mode was acquired to address the question of best polarization. The resolution of the images was not statistically associated with changes in contrast ratio. However, since ice islands and their associated fragments exist across a range of scales and the choice of low resolution SCW will result in loss of detectability of all but the largest ( $> 1$  to  $2$  km) ice islands. The detectability of ice islands at suboptimal spatial resolution will be influenced by the experience of the analyst and the historical context of the target along with other factors discussed above (ice temperature, ice type, background state, incidence angle, *etc.*).

As mentioned in Section 3.1, the texture and shape of ice islands likely contribute substantially to ice island detectability. These variables will most likely vary according to polarization, ice temperature, spatial resolution and the relative azimuth between radar look direction and ridges on the ice surface. Since target shape, size and texture were not evaluated in this study it is important to consider that cross-polarization SAR improves contrast but optimal texture may potentially be found in co-polarization. In light of this possibility (and the potential utility for other applications), a dual-channel mode is recommended for ice island surveillance. Acquiring both a cross-polarized and a co-polarized channel ensures that the preferred mode is available along with any additional information that might be found in co-polarization.

### **3.4.2 RCM**

The proposed modes for sea ice monitoring will be the Low Noise mode (100 m resolution, nominal  $-25$  dB NESZ) and Medium Resolution 50 m mode (nominal  $-22$  dB NESZ). As discussed above, the higher the spatial resolution of the imagery, the smaller a given detectable target can be. This study cannot provide insight into limitations with respect to resolution, however; the impact of a higher noise floor can be estimated from the data at hand. The Low Noise mode NESZ would exceed the mean cross-polarization backscatter of up to 3% of the ice island targets. The NESZ in this mode would also exceed the first quartile of the cross-polarization backscatter signature for up to 41% of the targets. This would lead to a biased mean backscatter since much of the sample data would be tainted by a poor SNR. With the Medium and Low Resolution RCM modes, the mean cross-polarization backscatter would be lower than the NESZ in up to 41% of the targets, while up to 85% of target cross-polarization first quartiles would be lower than the NESZ. It is important also to understand that the signatures of the background ocean state/cover would also be affected by the higher NESZ as this would also degrade the ability to detect ice islands, especially marine ice islands, against low backscatter backgrounds. Fortunately, the co-polarized signatures would be less affected by the increased NESZ in the RCM modes (the first quartile was lower than  $-22$  dB for only 1% of targets). It is also noteworthy that the RCM will be capable of compact polarimetric measurement, which may enhance detectability.

## **3.5 Future analysis**

A particular weakness of this study is the lack of ice island polarimetric data for the spring and summer. This has hampered the determination of the relative performance of all polarizations during a dynamic period with respect to both ice signature and movement. It is also important to

image more ice island targets to gain more of an appreciation of variability between individual ice island signatures. These two goals are being met through a continuation of this study that includes a new acquisition plan and a newly beaconsed ice island target.

Knowledge of how ice island backscatter changes seasonally, with incidence angle and with respect to polarization and ice type is not enough for the interpretation of contrast ratios. A complete understanding of contrast ratios includes some notion of how background signature changes with the parameters listed above as well as the differences in background type and sampling bias among observations. The study of generic contrast ratios should continue, but with more interpretive emphasis placed on how/why the contrast ratio changes with time. Generic contrast ratios most closely represent the ‘real-life’ ice island detection problem, since ice islands are unlikely to be surrounded by a homogeneous specific background type. Alternatively, specific background contrast ratios provide users with best and/or worst case scenarios although some thought needs to be given to how background categories are selected and sampled from a continuum of ice types to be meaningful.

The goal of this study was to examine the contrast in ice signatures to enhance detection of ice islands. Future work should incorporate textural differences between ice islands and ice backgrounds. The ridge and trough morphology of ice islands make them easy to detect when contrast ratios are high and it is important to determine how texture can aid detection in situations where contrast ratios are low (across all polarizations, incidence angles and seasons). Textural differences should be analyzed with a variety of SAR products to determine how image resolution impinges on the ability to detect ice islands of all sizes. Furthermore, the utility of multi-frequency SAR for detecting ice islands should be examined with coincident imagery.

Finally, in the RCM context, the potential role of CP for ice island detection should be explored, perhaps through simulation of RCM CP mode products starting from existing R-2 FQ imagery of ice islands.

## **4      Iceberg detection**

---

### **4.1    Background**

An iceberg is a massive piece of ice that originates from a glacier. Icebergs can vary greatly in shape and protrude 5 metres or more above the ocean surface. Icebergs may be floating or grounded. About 90% of all icebergs encountered in Canadian waters are calved from the glaciers of Western Greenland. That adds up to between 10,000 and 40,000 icebergs annually [6]. Monitoring and tracking of these icebergs is critical to safe and efficient marine travel.

Iceberg detection with SAR is a mature technology [37], [41] that is being used operationally, generally focused on larger incidence angle, higher resolution beam modes. The objective of this work was to quantify the iceberg detection capability of R-2 for the SCN mode. The probability of detection (POD) was quantified based on detection with a constant false alarm rate (CFAR) methodology in terms of a variety of important parameters including resolution, polarization, NESZ, incidence angle, iceberg size, wind speed and wind direction. In addition, iceberg POD in three types of winter sea ice was also determined as a function of incidence angle.

### **4.2    Data and methods**

CIS collected both quad and dual polarization R-2 Fine mode imagery of icebergs off West Greenland (near Disko Bay) from August to October 2009<sup>1</sup>. The ground validation was conducted by C-CORE, with funding from an oil and gas client who was willing to share the iceberg validation data with CIS. Finally, the CIS provided SAR sea ice signatures that were collected from 2008 to 2010.

While the data collected for this project were predominately R-2 Fine mode, ultimately the purpose of the project was to evaluate R-2 SCNB mode imagery. The SCN evaluation was accomplished by re-sampling the Fine mode imagery to the same resolution, equivalent number of looks and noise floor as that of the SCN mode.

There are a number of parameters that are pertinent to iceberg detection. Unfortunately, iceberg ground truthing rarely presents opportunities to collect samples that span all the important parameters such as incidence angles, iceberg size, wind direction, and wind speed. Also of interest are iceberg signatures captured in different sea ice types and seasonal states at various incidence angles. To further complicate matters, if all these occurrences were to exist in a given geographical area at a given time, collecting all information regarding sea ice, wind and iceberg metrics would be challenging. To even further complicate matters, iceberg validation in sea ice is more difficult than in open water considering potential missed detections and false alarms from the field validation source (fixed wing, helicopter, or ship). This is due to the vast background of sea ice that can produce similar radar backscatter in marine or fixed wing radar sources to that of an iceberg. Similarly, visual inspection from an aerial reconnaissance source is also significantly

---

<sup>1</sup> These data were provided to C-CORE under the auspices of the European Space Agency project entitled STSE SAR Ice Constellation and were collected under the same Canadian Space Agency supported Government Research Initiatives Project.

limited compared to open ocean iceberg validation considering target to background colour contrast.

The methodology proposed here avoids these obstacles by using signatures of icebergs captured in an open ocean environment and comparing the segmented backscatter (*i.e.*, backscatter that has been separated from the surrounding background) to that of varying ocean and sea ice backscatter, captured independently in separate imagery. While the iceberg backscatter of a specific iceberg may vary somewhat in different environments, it is expected that this variability is masked by the high variation in geometry that is inherent in iceberg targets that would also lead to (higher) backscatter variation. This speculation has not been confirmed by comparing the same iceberg in different environments, and given that icebergs can rapidly melt over time, the speculation would be challenging to confirm with actual data. Therefore, for the purposes of this report, the assumption is made that this approach is valid, with the caveat that there may be some variability in actual results that may not have been taken into consideration here.

#### 4.2.1 Fine mode iceberg data

During the summer of 2009 in coastal West Greenland waters, C-CORE conducted an iceberg area density survey for an oil and gas client. From this study, 121 icebergs with specific waterline lengths were validated that coincided with R-2 quad and dual polarization Fine mode imagery. Figure 26 presents a sample validation photograph of a large pinnacle iceberg collected during this study. Figure 27 presents a histogram of the iceberg waterline length for the targets collected during the iceberg campaign. The figure shows that the targets ranged in waterline length from 10 to 256 m and had an average waterline length of 95 m. This sample is considered representative of iceberg populations located in Eastern Canada, particularly along the coasts Newfoundland and Labrador. This work uses the CIS standard nomenclature for iceberg waterline length, in that Small, Medium and Large icebergs range in size from 15 to 60 m, 60 to 120 m, and 120 to 200 m respectively [6].



Figure 26: Large pinnacle iceberg validated during the 2009 West Greenland campaign. Photo provided by Provincial Aerospace Limited (PAL) 2009.

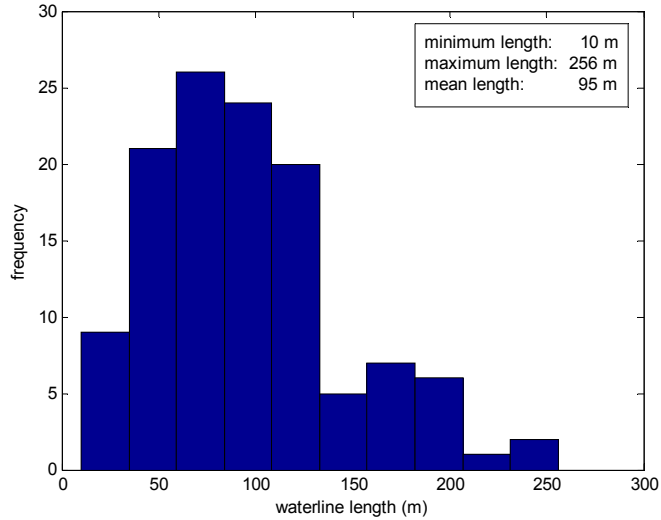


Figure 27: Iceberg waterline length histogram for 2009 West Greenland campaign.

#### 4.2.1.1    Iceberg signature – Fine mode

Iceberg signatures for both the HH and HV polarizations were investigated with respect to their dependence on incidence angle and iceberg size. Here, the maximum and mean calibrated  $\sigma^0$  signatures were extracted for the 121 sample icebergs. The target measurements are presented according to waterline length as collected during the field program in 2009. Iceberg shape information was also collected in this data set. It is believed that the iceberg shape plays a role in the target backscatter due to varying predominant geometry. Relatively speaking, domed icebergs present a low radar cross section, while pinnacled and dry-dock icebergs present a high radar cross section. An investigation of the effects of iceberg shape on POD is outside the scope of this chapter, but as the data has been collected and archived, it could be investigated at a later date.

Figure 28 through Figure 31 present the iceberg signatures as a function of size, polarization, and incidence angle. From these figures, the effects of incidence angle on iceberg target signatures in both the HH and HV channels were observed to be small. It should be noted that the mean iceberg signatures are derived from the linear scale and converted to a decibel scale after the average has been computed. However, as a measure of central tendency on the dB scale, the dB signature for the mean of the target mean or the mean of the target maximum, as appropriate, is also presented for each case. The mean of the HH maximum iceberg intensity was 7 dB and the mean of the HH mean iceberg intensity was -5.9 dB. The average of the HV maximum iceberg intensity was -1.5 dB and the average of the HV mean iceberg intensity was -13.7 dB. From this, considering the maximum intensity pixel (which is most relevant to CFAR target detection), icebergs were, on average, measured to have 8.5 dB higher backscatter for HH polarization than for HV polarization.

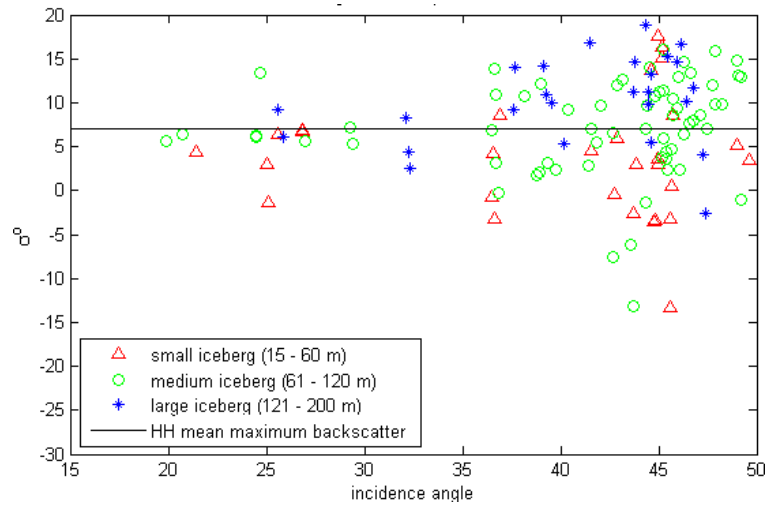


Figure 28: HH maximum pixel intensity as a function of iceberg size and incidence angle.

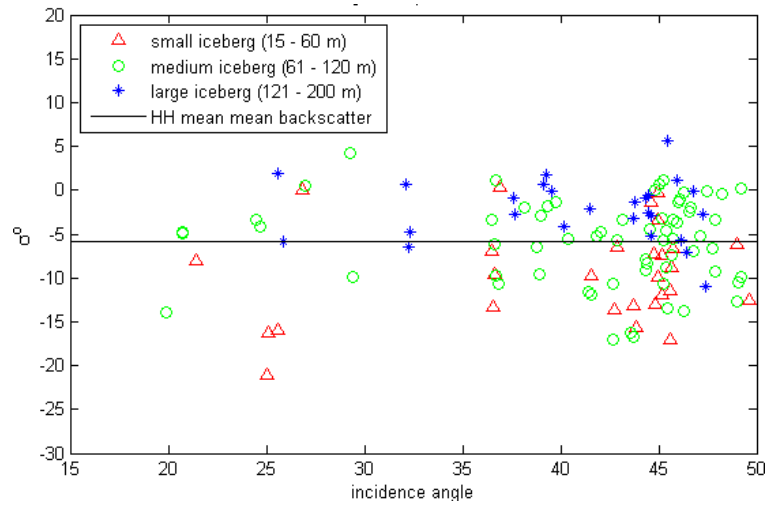


Figure 29: HH mean pixel intensity as a function of iceberg size and incidence angle.

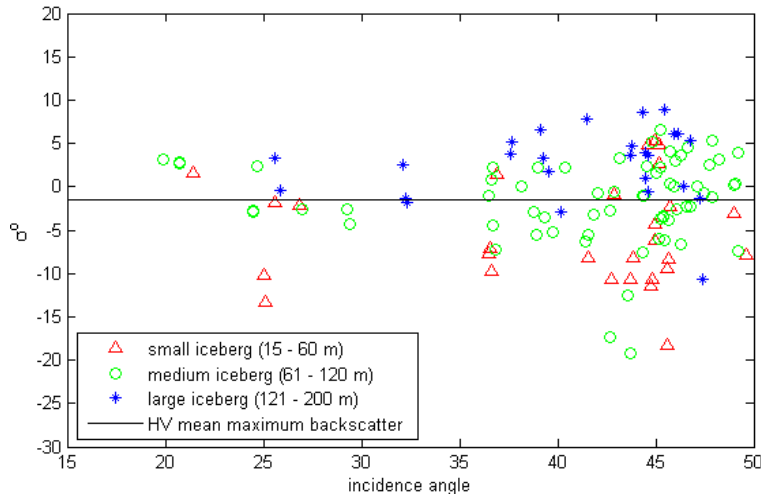


Figure 30: HV maximum pixel intensity as a function of iceberg size and incidence angle.

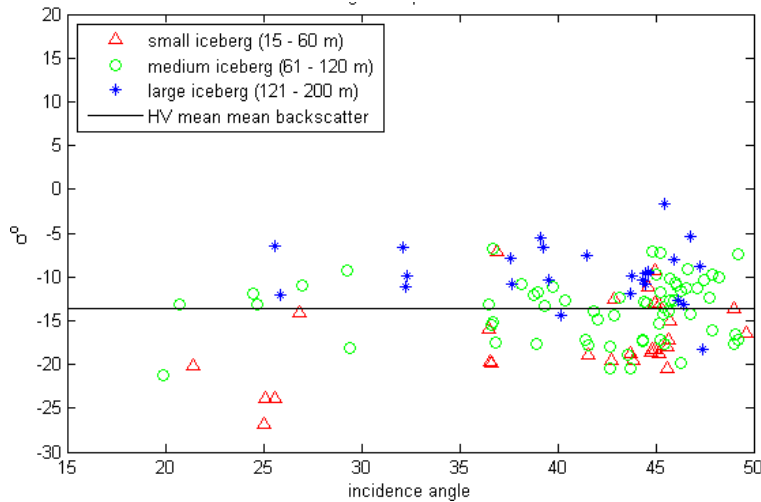


Figure 31: HV mean pixel intensity as a function of iceberg size and incidence angle.

Figure 32 through Figure 37 present samples of iceberg Fine mode SAR signatures for icebergs ranging in waterline length from 20 to 256 metres. The targets were selected from the available data set to represent the variation in SAR target signatures with respect to their actual measured waterline length. Of particular interest are two icebergs (Figure 34 and Figure 36) that are visible in the SAR data with corresponding wind speed estimates of around 19 m/s, as determined from the HV signature (Section 6); these wind speeds are particularly high, yet the iceberg targets are still visible in the data.

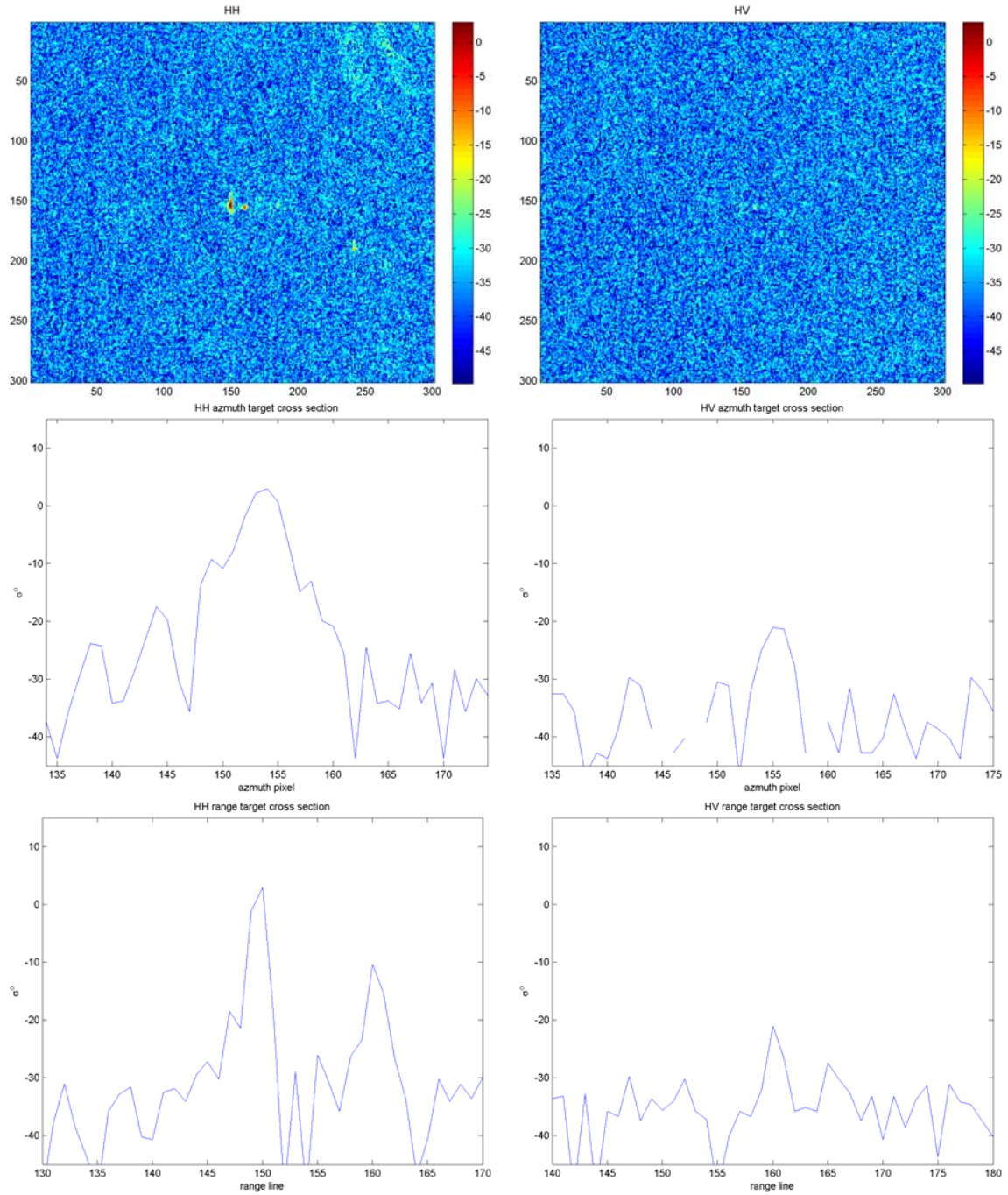
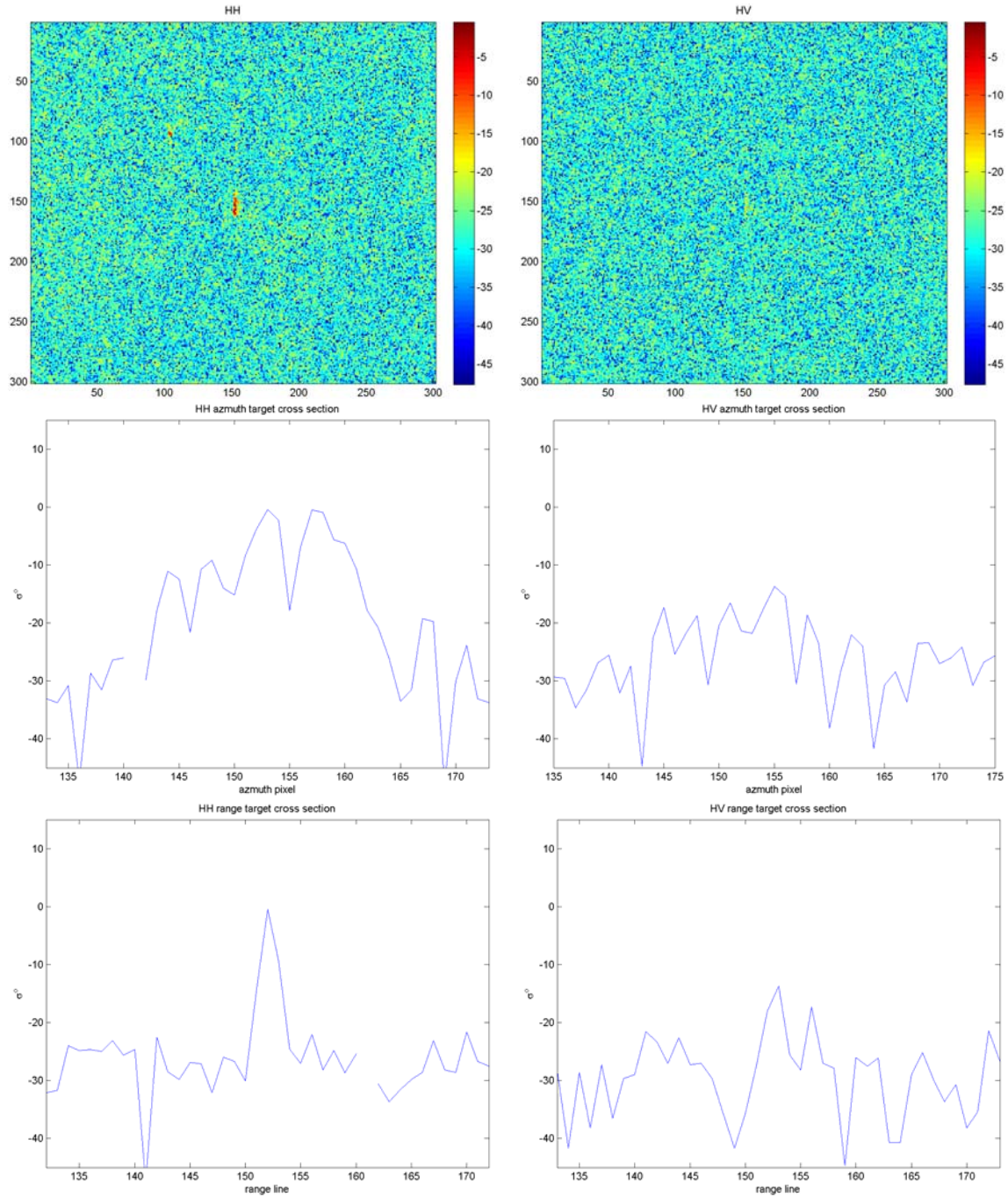
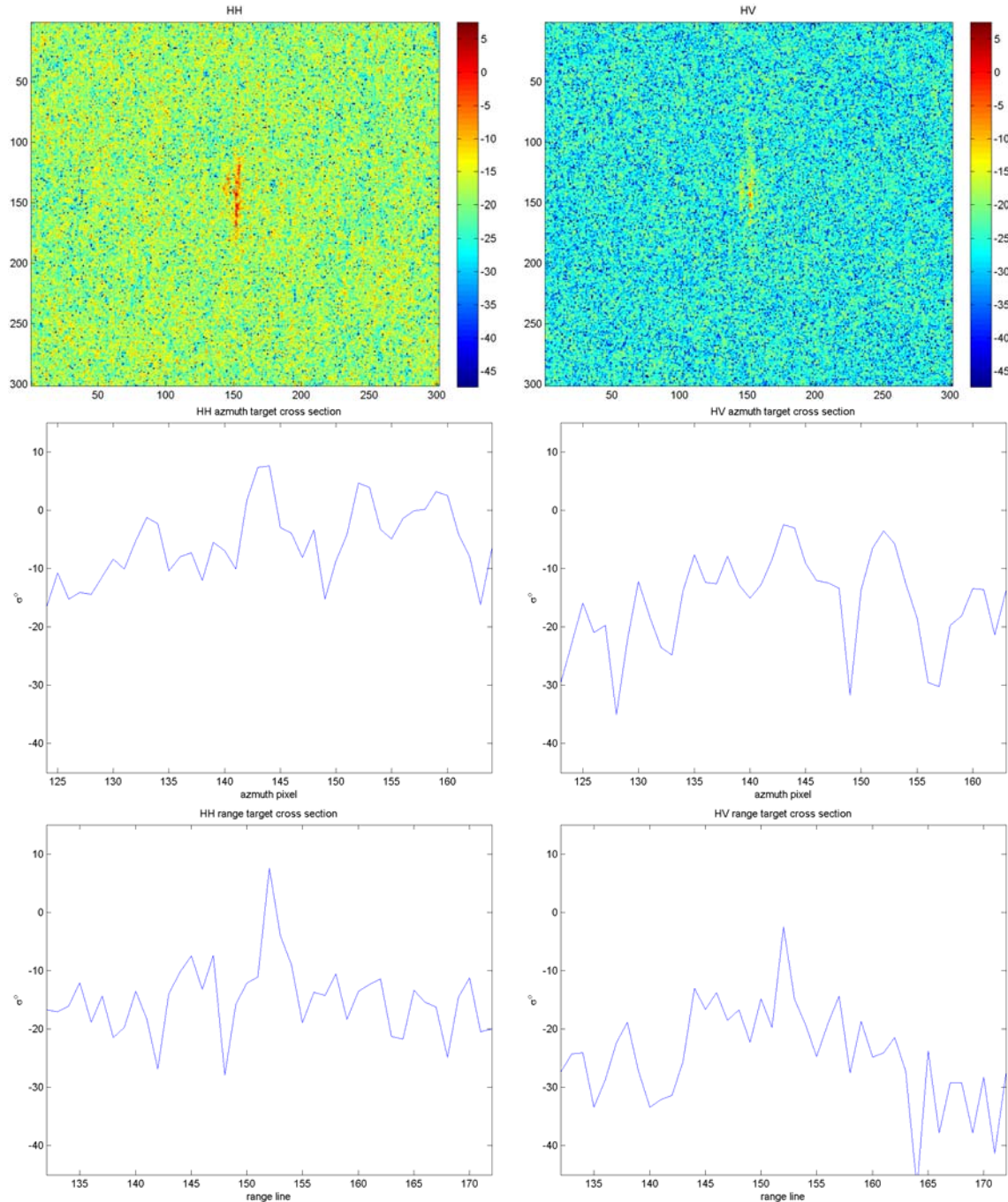


Figure 32: 20 m small dome iceberg Fine mode SAR signature in decibels (wind speed: 0.9 m/s).



*Figure 33: 44 m small wedge iceberg Fine mode SAR signature in decibels (wind speed: 13.2 m/s).*



*Figure 34: 70 m medium pinnacle iceberg Fine mode SAR signature in decibels (wind speed: 18.2 m/s).*

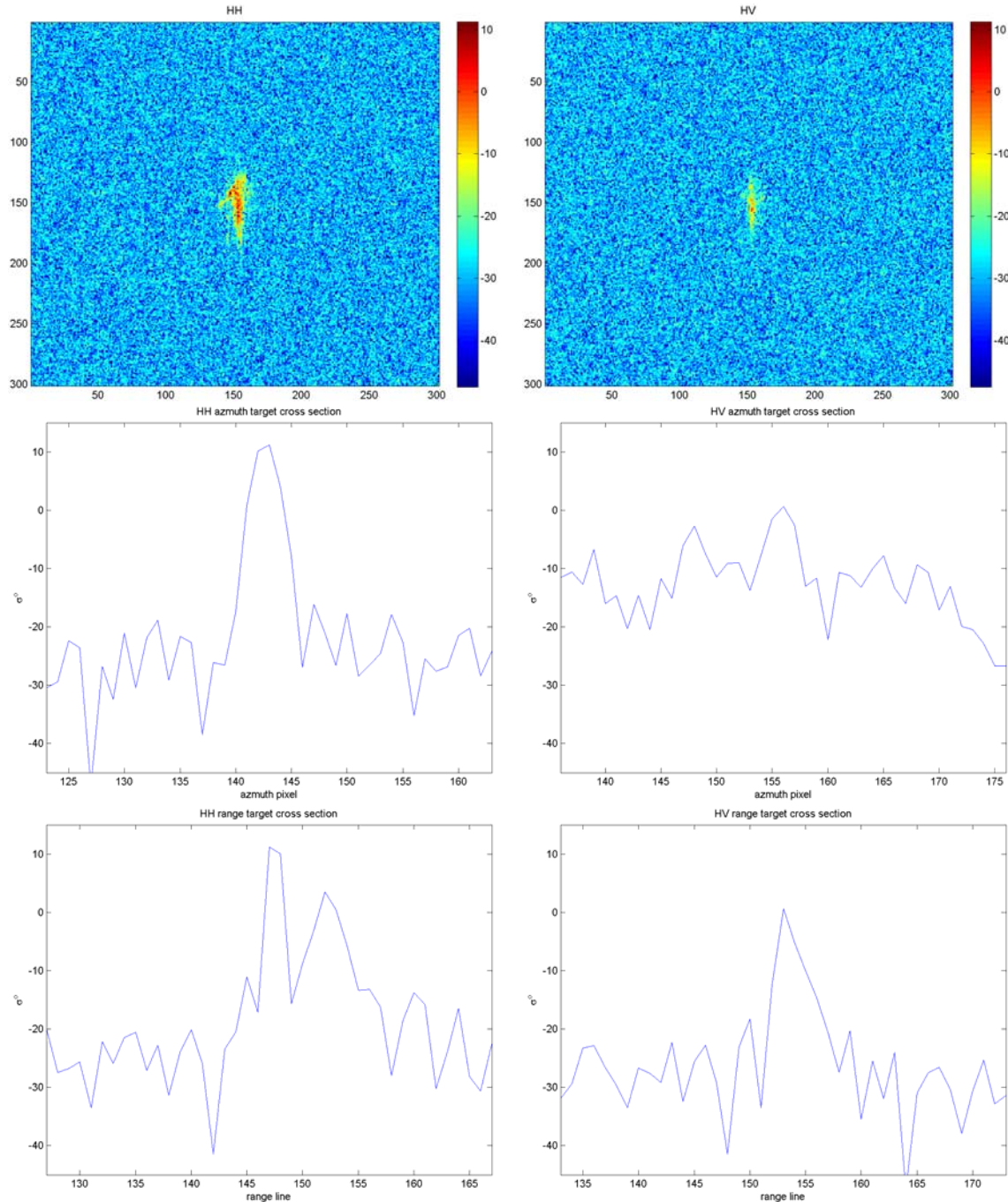


*Figure 35: 109 m medium pinnacle iceberg Fine mode SAR signature in decibels (wind speed: 12.0 m/s).*

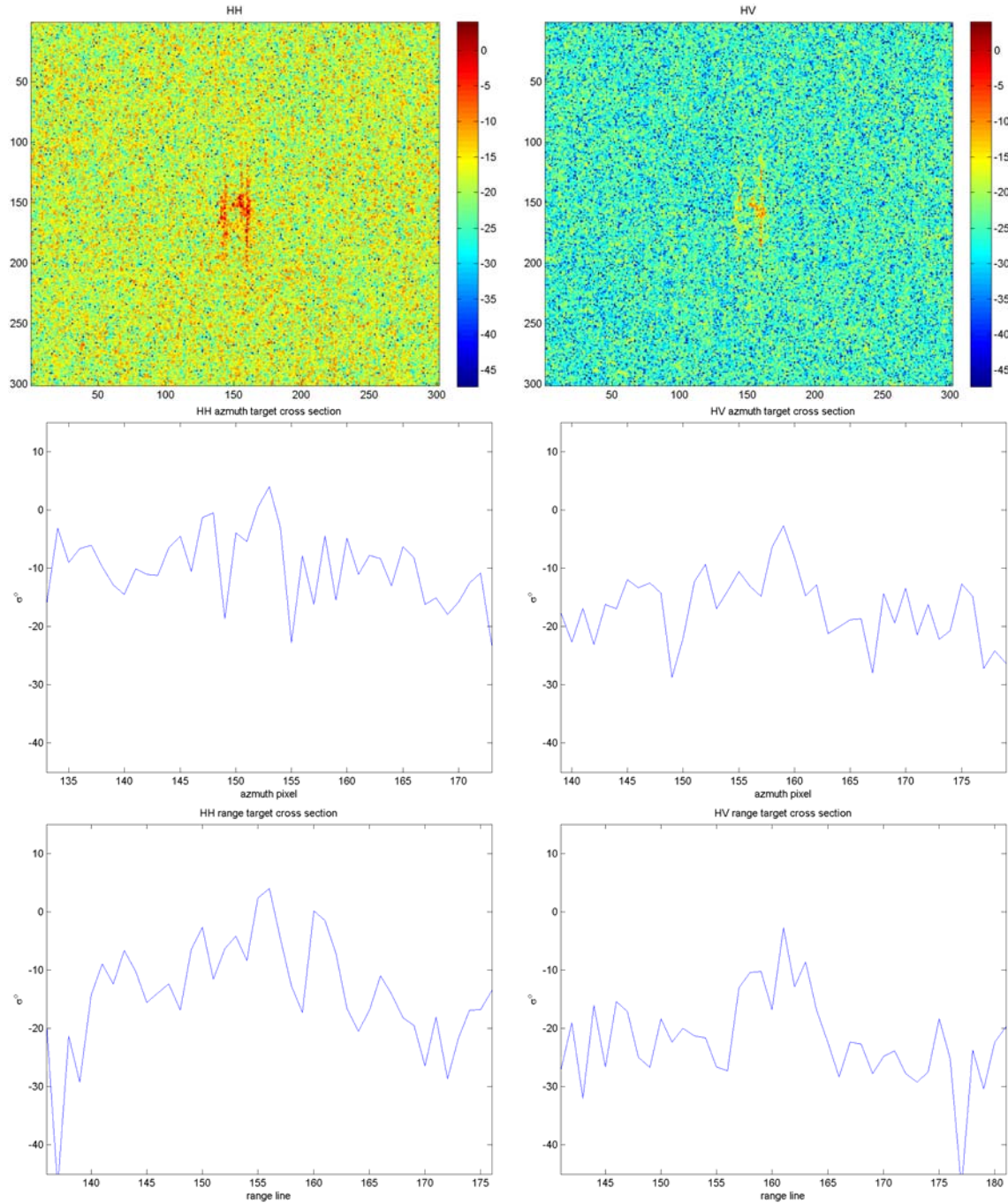


*Figure 36: 180 m large drydock iceberg Fine mode SAR signature in decibels (wind speed 19.0 m/s).*

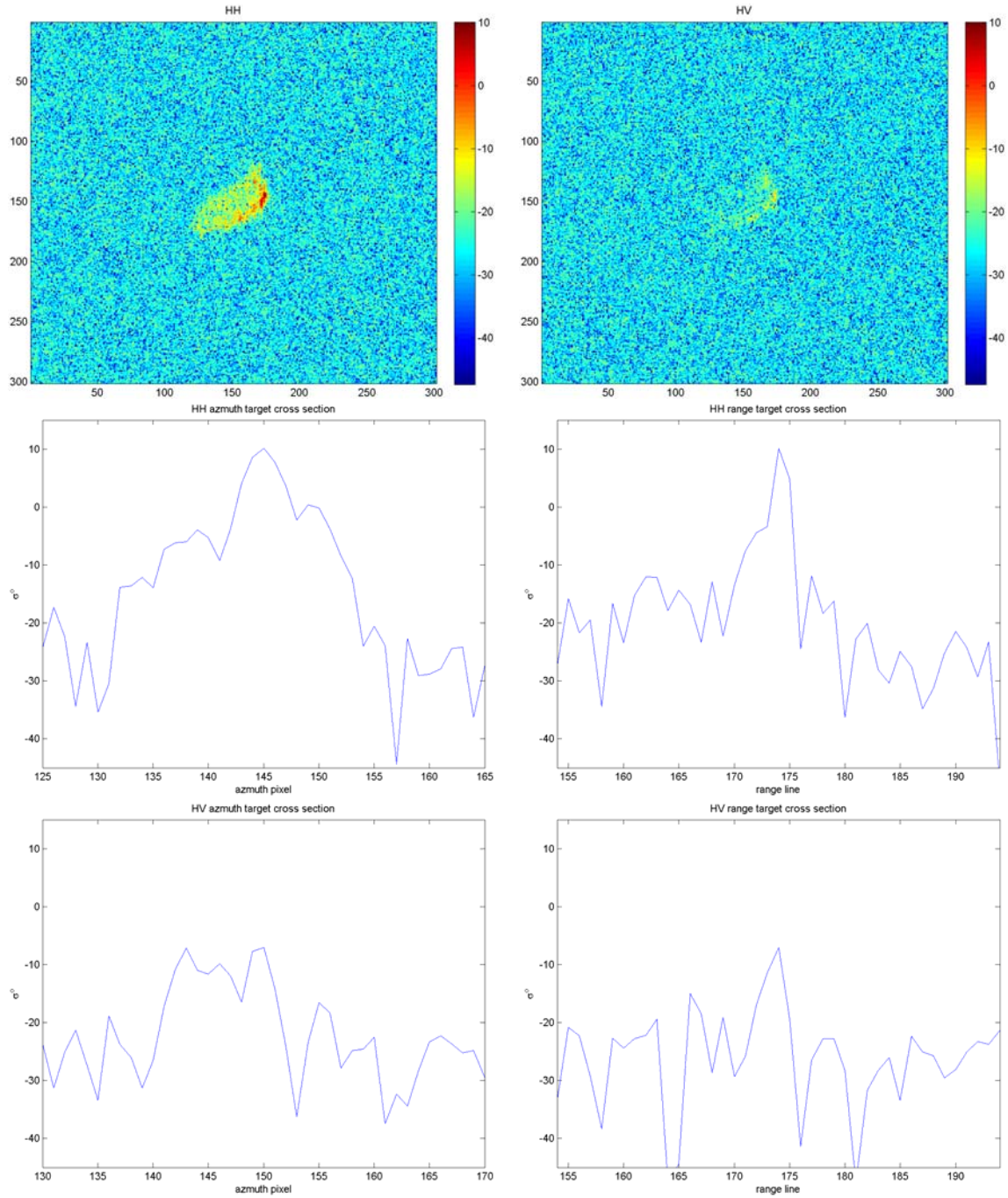


*Figure 37: 256 m large tabular iceberg Fine mode SAR signature in decibels (wind speed 16.7 m/s).*

#### **4.2.1.2      Iceberg signature – Simulated SCN mode**

C-CORE has developed a software tool for simulating lower resolution SAR data from higher resolution imagery. For the purposes of this project, the higher resolution data was R-2 Fine data and the simulated output was R-2 SCN. The simulation process involves noise addition, resampling and inserting speckle to achieve the expected noise level, resolution, pixel spacing and speckle of the SCN product.

The Fine mode data were input as 300 by 300 pixel image chips in slant range as sigma nought backscatter. The incidence angle for each target was known and was used to find the corresponding noise floor value in SCN. For steeper incidence angles, outside the SCN range, the noise for the closest incidence angle was used. Noise, which is introduced in the I and Q channels, was added by simulating noise distributions for the I and Q channels and combining them to determine the detected noise floor distribution.

The resolution degradation process used a sinc interpolation to convert the Fine mode data, nominally 5 m pixel spacing, to the SCN slant range pixel spacing and resolution. The azimuth pixel spacing and resolution were set to 25 m and 50 m, respectively and the range values were multiplied by the sine of the incidence angle.

Finally, the mixture model of distributed scatter was used to reintroduce speckle noise into the images. The mixture model is a combination of a gamma reflectivity map multiplied by Rayleigh-distributed speckle. The premise is that, in degrading the resolution, the speckle is essentially removed resulting in the scene reflectivity. The appropriate Rayleigh distribution was selected according to the constraint that speckle has a mean of one and a variance of one divided by the effective number of looks [42]. A Rayleigh distributed random variable was sampled from the distribution and multiplied by each pixel in the image, except for those pixels suspected to be resulting from coherent point target backscatter (i.e., the ‘brightest’ pixels were excluded from the multiplicative speckle). The resulting image was normalized to its original mean since the speckle should not change the mean value of the backscatter.

Figure 38 through Figure 43 present simulated SCN mode SAR signatures. The icebergs in these images are the same as those presented previously in Figure 32 through Figure 37.

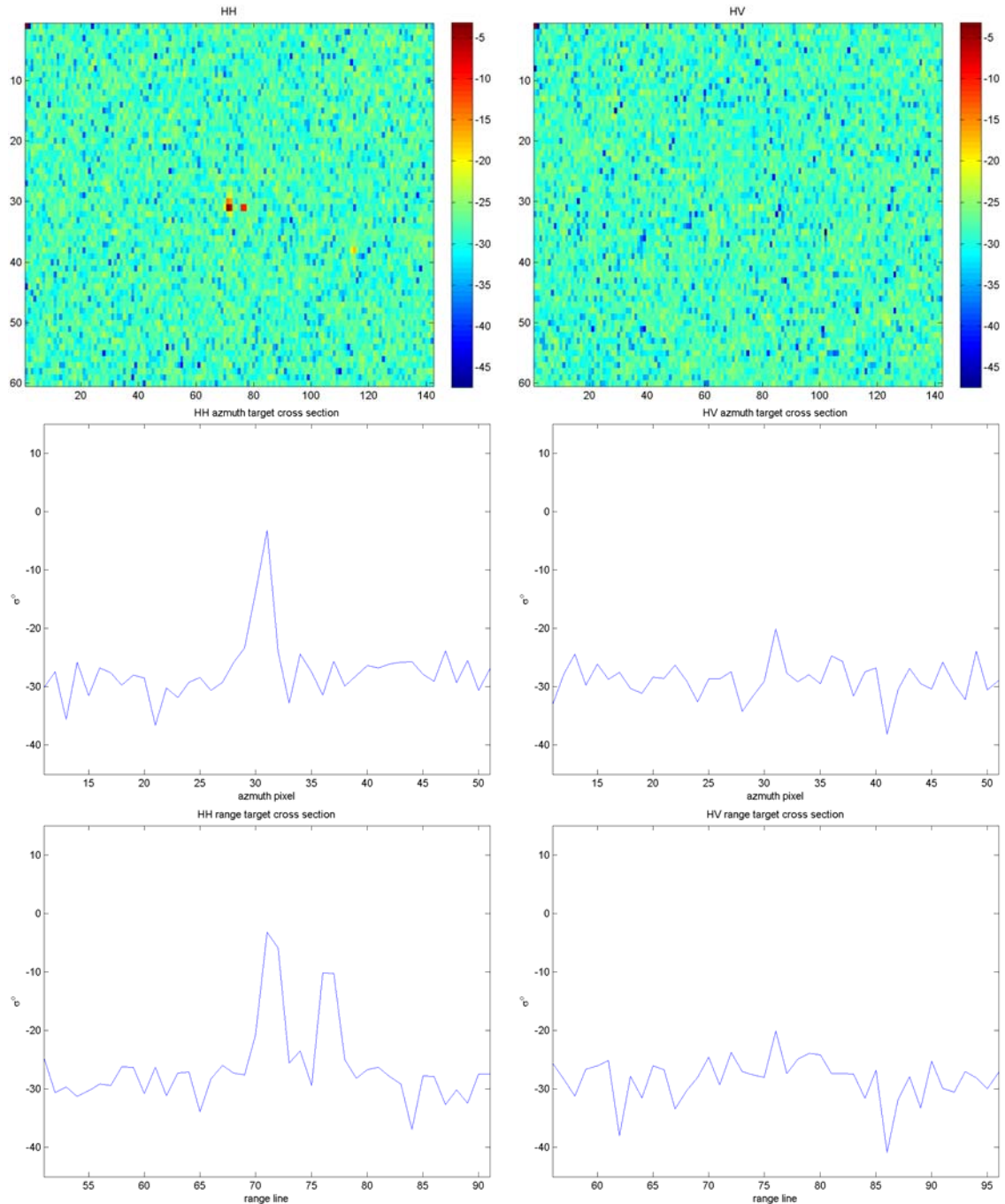


*Figure 38: 20 m small dome iceberg simulated SCN mode SAR signature in decibels (see Figure 32).*

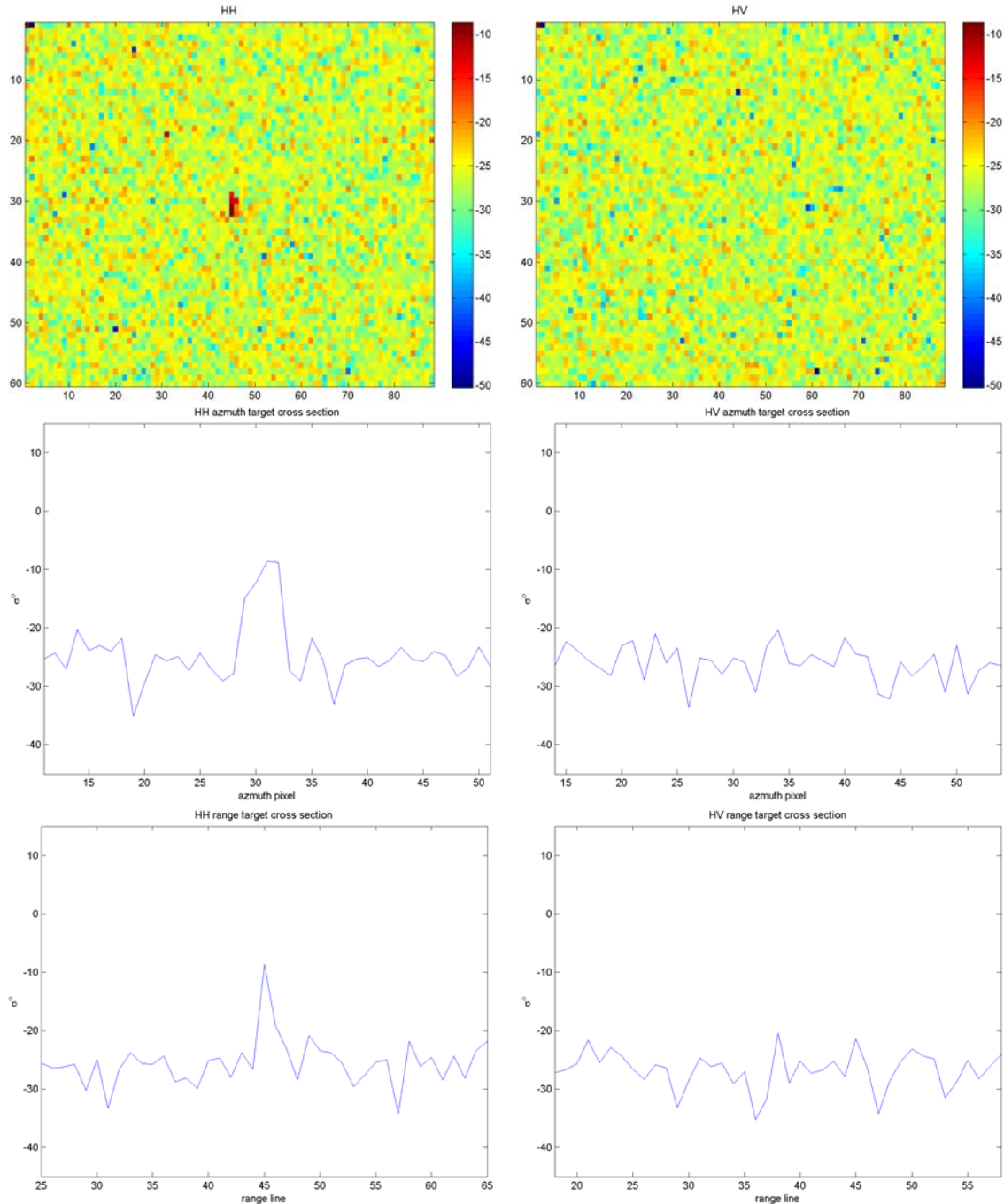


*Figure 39: 44 m small wedge iceberg simulated SCN mode SAR signature in decibels (see Figure 33).*

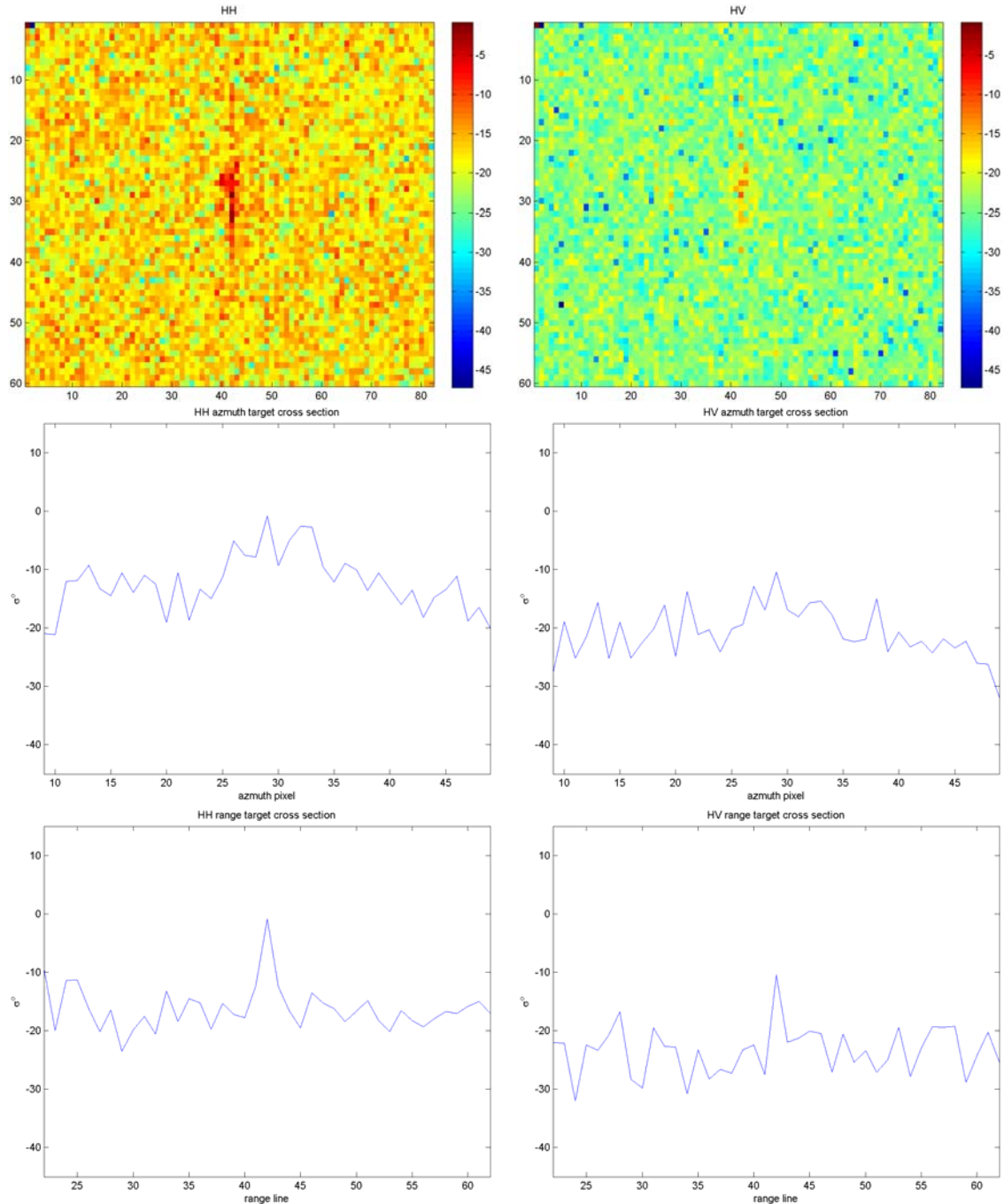


*Figure 40: 70 m medium pinnacle iceberg simulated SCN mode SAR signature in decibels (see Figure 34).*

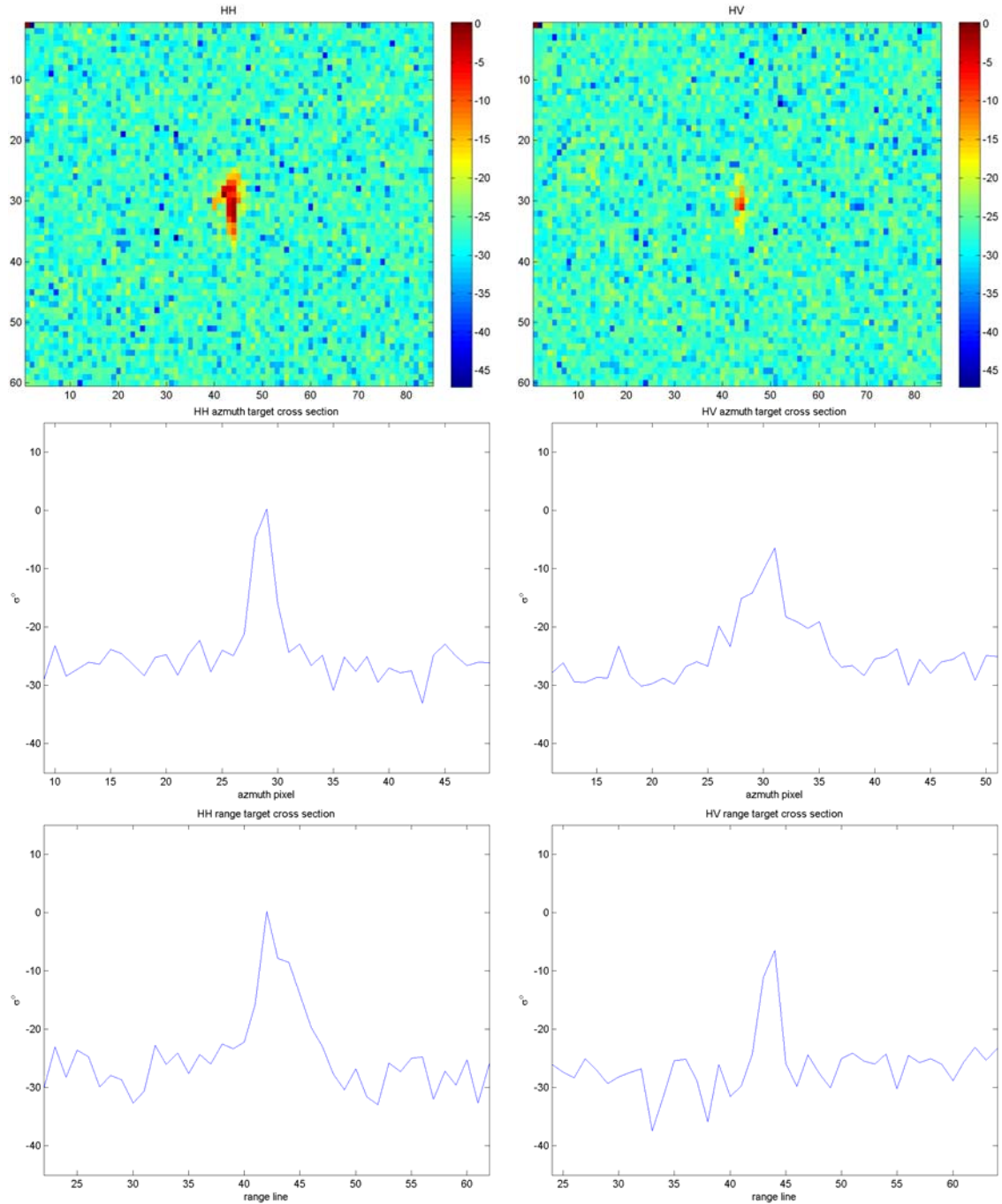


*Figure 41: 109 m medium pinnacle iceberg simulated SCN mode SAR signature in decibels (see Figure 35).*

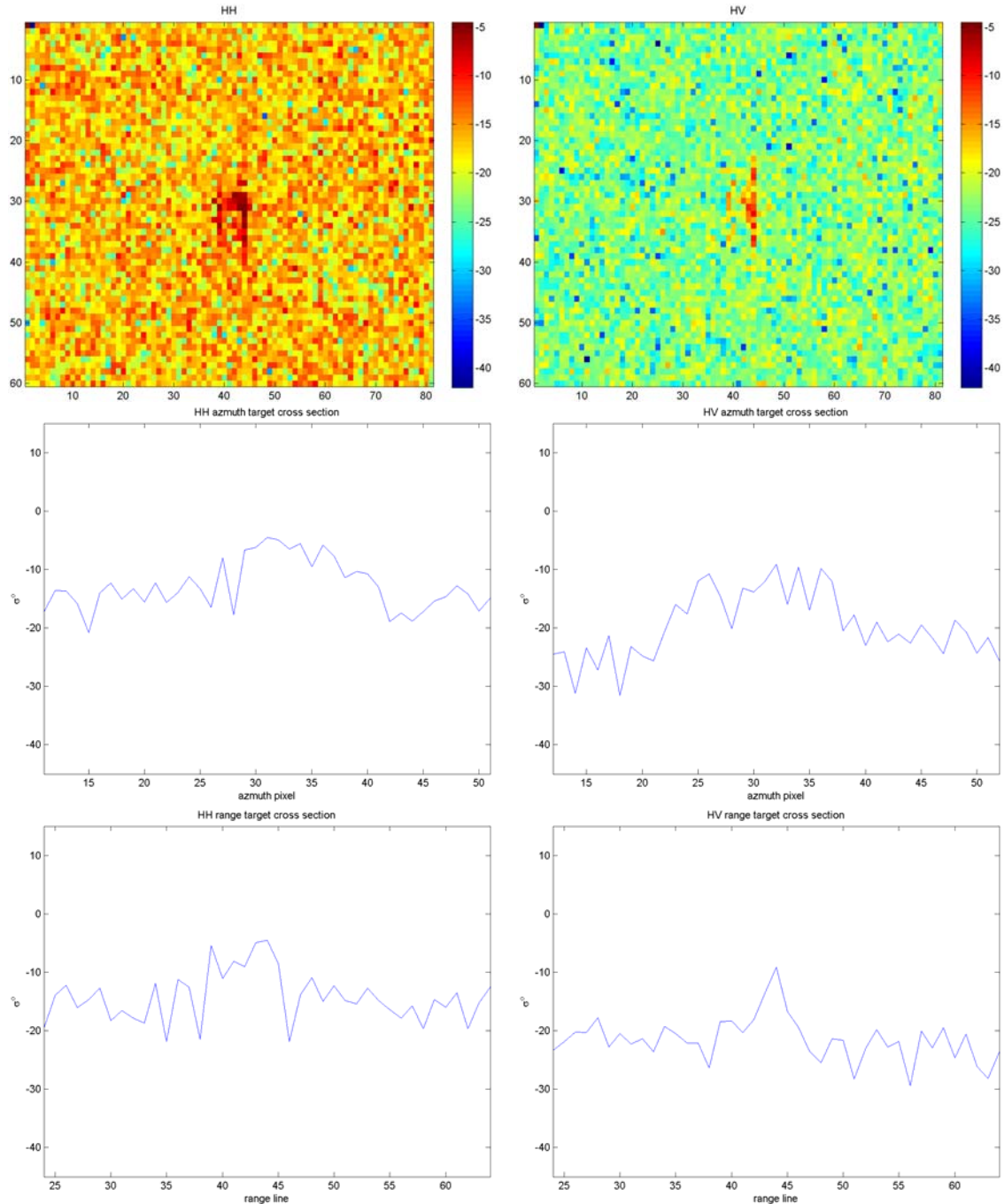


*Figure 42: 180 m large drydock iceberg simulated SCN mode SAR signature in decibels (see Figure 36).*

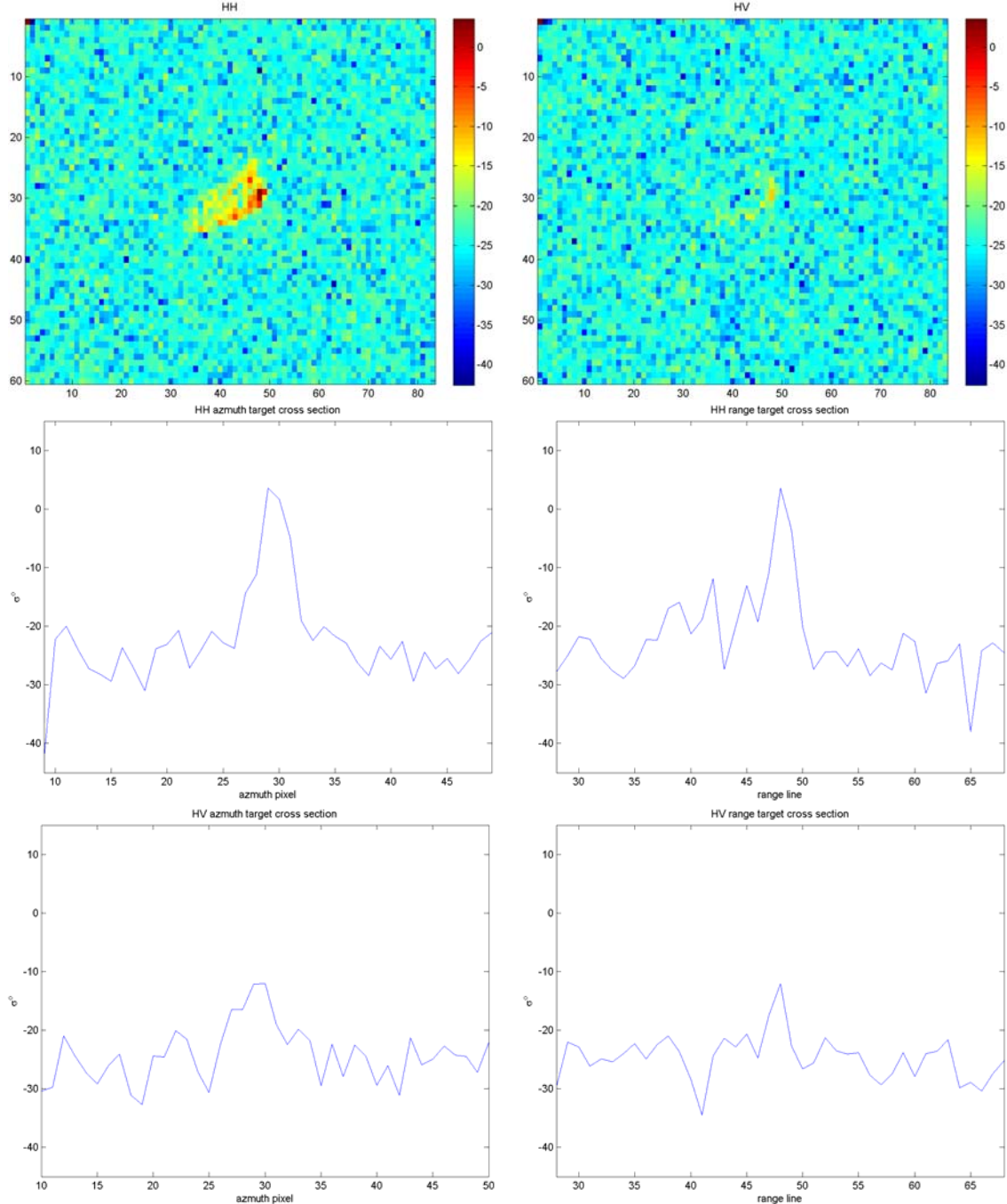


*Figure 43: 256 m large tabular iceberg simulated SCN mode SAR signature in decibels (see Figure 37).*

#### 4.2.2 Fine mode wind data

Determining iceberg probability of detection in varying wind conditions involves comparing iceberg SAR signatures to those of wind clutter. The wind signatures were provided by DRDC

Ottawa, whereby R-2 Fine mode scenes that coincided temporally and spatially with metrological ocean data collection from buoys were used for data correlation and extraction. In particular, DRDC Ottawa provided a post-processed spreadsheet with relevant information including wind speed, wind direction, SAR mean signature at buoy location, SAR variance signature at buoy location, SAR incidence angle and satellite look direction.

The effects of wind speed and direction on C-band SAR imagery have been extensively studied and are relatively well understood for the co-polarization (HH and VV) channels. For example, increasing wind causes increased ocean backscatter for a given SAR incidence angle. Wind direction must also be considered since ocean backscatter is highest when the wind direction is blowing towards the radar look direction. Furthermore, ocean backscatter is lowest for cross wind directions, *i.e.*, for wind blowing orthogonal to the radar look direction. The SAR ocean backscatter signature is also significantly affected by incidence angle, where steep incidence angles produce a higher backscatter signature than those at shallower ones when exposed to the same wind speed and direction. Wind models such as CMOD4 and CMOD-IFR2 use the SAR signature to estimate the wind speed based on the oceans geophysical backscatter which is affected by these parameters [51], [52], [38], [39].

#### **4.2.2.1 Advances in cross-polarization wind speed estimation**

While the ocean backscatter has been extensively studied in the co-polarization channels (HH and VV), very little work has been done to measure SAR signatures in the cross-polarization channels (HV and VH). Recent work conducted by DRDC Ottawa with SAR wind observations has resulted in new insight to cross-polarization SAR wind signatures (see Section 6 and [60]). For HV (or VH) C-band SAR, increasing wind causes increased ocean backscatter, which is the same effect that is observed with VV and HH polarization. However, it was found that the cross-polarization ocean backscatter is largely independent of wind direction and incidence angle. This is significant because SAR wind field extraction from the co-polarization channel generally results in an ambiguity in wind direction that must be resolved using other data sources. By using the cross-polarization channel to extract wind fields, it has been shown that SAR wind speeds can be extracted unambiguously, without knowing the wind direction. It also means that the cross-polarization target POD does not vary with incidence angle (beam position) and thus any R-2 beam position (of a given resolution) should provide consistent POD, under the assumption that the target radar cross section is also invariant with incidence angle. The derived relationship is almost trivial and is given in Equation (10) (see Section 6).

The only potential issue is whether the HV geophysical signature is above the sensor noise floor, as described by the NESZ. Here, an HV signature was considered predominately geophysical if the mean HV signature was 3 dB above the NESZ for the specified NESZ measure at a particular incidence angle. For R-2 Fine mode, the specified NESZ is better than  $-33$  dB, thus wind speeds greater than 8 m/s can be estimated irrespective of incidence angle. For other modes such as R-2 ScanSAR Narrow with NESZ levels nominally at  $-25$  dB or better, wind speeds greater than 22 m/s can be estimated irrespective of incidence angle. Furthermore, for sensors such as ASAR in Alternating Polarization mode with NESZ levels as high as  $-19$  dB, wind speeds greater than 32 m/s can be estimated irrespective of incidence angle.

An immediate utility is seen for this information, since a quick and accurate assessment of the wind speed can now be ascertained during an operational marine target detection process.

Generally, operations of this type employ automated target detection with a manual quality control component. An image interpreter can now easily consider the wind speed in addition to the target and the background signature in both channels. This potentially improves interpreter judgment considering target strength relative to the environmental conditions.

#### 4.2.2.2 Ocean signature – Fine mode

From the data provided by DRDC, there were 1332 samples containing polarization, mean  $\sigma^0$ , variance  $\sigma^2$ , wind speed (m/s), wind direction (0° to 360°), NESZ, and SAR track angle. Table 9 presents sample rows from the available data set. From the table, the mean and variance were used to model a K-distribution of the ocean backscatter where the shape parameter  $v$  is defined by the mean, variance and the number of looks [34]. Here, only SAR signatures that produced a positive  $v$  were considered. This is based on limiting the input Bessel function to real numbers only.

Table 9: Sample wind signature data.

Wind Speed [m/s]	Wind Direction [°]	Polarization	Back-Scatter Mean	Back-Scatter Variance	NESZ	Incidence Angle [°]
0.0	0	HH	0.00534	0.00018	0.00019	24.1859
0.0	0	VV	0.00780	0.00037	0.00019	24.1859
0.0	0	HV	0.00027	0.00000	0.00019	24.1859
0.0	0	VH	0.00026	0.00000	0.00019	24.1859
5.0	328	HH	0.27944	0.10144	0.00021	22.6085
5.0	328	VV	0.30130	0.11435	0.00021	22.6085
5.0	328	HV	0.00074	0.00000	0.00021	22.6085
5.0	328	VH	0.00077	0.00000	0.00021	22.6085
10.0	344	HH	0.01435	0.00025	0.00033	38.3721
10.0	344	VV	0.02562	0.00069	0.00033	38.3721
10.0	344	HV	0.00091	0.00000	0.00033	38.3721
10.0	344	VH	0.00086	0.00000	0.00033	38.3721
15.1	307	HH	0.03502	0.00120	0.00038	38.3692
15.1	307	VV	0.05848	0.00240	0.00038	38.3692
15.1	307	HV	0.00228	0.00001	0.00038	38.3692
15.1	307	VH	0.00226	0.00001	0.00038	38.3692
19.7	54	HH	0.35376	0.08669	0.00023	28.3646
19.7	54	VV	0.38172	0.09304	0.00023	28.3646
19.7	54	HV	0.00678	0.00005	0.00023	28.3646
19.7	54	VH	0.00676	0.00005	0.00023	28.3646

For a sample of SAR data consisting of  $n$  pixels, a vector  $\mathbf{I}$  may be formed from the individual pixels, *i.e.*,  $\mathbf{I} = [I_1 \ I_2 \ \dots \ I_n]$ . The mean and variance of the backscatter are denoted as  $\bar{I}$  and  $\sigma^2$ , respectively. The shape parameter is defined by:

$$\nu = \left( \frac{\sigma^2 + \bar{I}^2}{(1+L^{-1})\bar{I}^2} - 1 \right)^{-1} = (\delta - 1)^{-1}. \quad (2)$$

From this, it can be seen that:

$$\nu = \begin{cases} > 0 & \text{for } \delta > 1 \\ < 0 & \text{for } \delta < 1 \\ \text{undefined} & \text{for } \delta = 1 \end{cases} \quad (3)$$

From (3), it can be shown that  $\nu$  is positive if:

$$\sigma^2 > \frac{\bar{I}^2}{L}, \quad (4)$$

where  $L$  is the equivalent number of looks. Only SAR signatures that met the criterion defined by (4) were used to derive the probability of detection.

The K-distribution model for each of the environmental conditions was then used to derive a  $\sigma^0$  threshold associated with a specific CFAR. The CFAR evaluated here was  $1 \times 10^{-7}$ , which for R-2 FQ imagery (consisting of images of approximately 3500 x 6000 pixels) translates into two false alarm pixels per image. This CFAR is representative of what is currently used in marine target detection operations by C-CORE.

The CFAR methodology is based on the fact that iceberg targets with a signature above the associated CFAR threshold will be identified in the SAR imagery. What is important here is that, if a higher CFAR is used, the detection rate will go up at the expense of having more false targets. Conversely, if a lower CFAR is used, the detection rate will go down with the advantage of having fewer false alarm targets to consider. CFAR can be used for comparing different polarizations and even different imagery modes because it is based on setting a threshold at a constant rate relative to the area under the K-distribution curves. Thus, as long as the K-distribution model adequately fits the SAR data under variable parameters such as polarization, wind speed, and wind direction, it can be used as a useful benchmark.

#### 4.2.2.3 Ocean signature – Simulated SCN mode

In Table 9, the ocean  $\sigma^0$  mean and variance are presented for R-2 FQ HH and HV data. It is assumed that the mean ocean signature is the same for both SCN and Fine mode considering that the incidence angle, wind speed and wind direction is constant. From this, if the product model is considered [34], then:

$$\frac{\sigma^2}{\bar{I}^2} = \frac{1}{L} + \frac{1}{v} + \frac{1}{Lv^2}, \quad (5)$$

where  $v^2$  is the normalized geophysical variance. If:

$$L_1 \ll v_1^2, \quad (6)$$

then:

$$\frac{\sigma^2}{\bar{I}_1^2} \approx \frac{1}{L_1}. \quad (7)$$

Here the sub index represents data from a particular image mode. As stated, if  $\bar{I}_1 = \bar{I}_2$ , then the variance of data from one mode can be used to estimate that of another through the following equation:

$$\sigma_1^2 = \frac{L_2}{L_1} \sigma_2^2. \quad (8)$$

This function, which is just the ratio of the effective number of looks, is what was used to scale the Fine mode ocean backscatter variance to that of SCN mode data. Here, the effective number of looks was taken as three for SCN mode and one for Fine mode [29]. The assumption from Equation (6) may not be correct for all cases of ocean backscatter, however this assumption was empirically supported based on random samples taken from the Fine mode Greenland iceberg data set, which produced values of the geophysical variance to be at least an order of magnitude less than the speckle variance for both the HH and HV polarization Fine mode data. From this, using Equation (8) is seen to be an acceptable method for scaling the variance from one image mode to another for the cases presented here.

#### 4.2.3 SCN mode sea ice data

Also of interest is the probability of iceberg detection in sea ice. Here, sea ice signatures were provided by the CIS that were collected from 2008 to 2010.<sup>2</sup> These data were collected with dual polarization (HH and HV) in ScanSAR Wide (SCW) mode, but the signature measurements were scaled appropriately to simulate Fine and SCN mode mean and variance values.

---

<sup>2</sup> These data were provided to C-CORE under the auspices of the European Space Agency project entitled STSE SAR Ice Constellation and were collected under the same Canadian Space Agency supported Government Research Initiatives Project

#### 4.2.3.1 Sea Ice signature – SCW mode

There were 113 HH and HV samples containing polarization, backscatter mean and variance, and NESZ for the winter ablation state. Table 10 presents sample rows from the available data set, where NESZ was stated to range from  $-24.5$  to  $-30$  dB, and the number of looks was six [29].

*Table 10: Sample sea ice signature data as provided by CIS.*

Type	Polarization	Incidence Angle [°]	Mean	Variance
New Ice	HH	20.0	0.03692783	0.00065024
New Ice	HV	20.0	0.00200155	0.00000062
New Ice	HH	34.3	0.01937703	0.00021573
New Ice	HV	34.3	0.00219081	0.00000098
New Ice	HH	48.8	0.00918486	0.00001561
New Ice	HV	48.8	0.00176861	0.00000046
FYI	HH	20.8	0.09709595	0.00182207
FYI	HV	20.8	0.00250250	0.00000117
FYI	HH	34.1	0.02066487	0.00008147
FYI	HV	34.1	0.00257439	0.00000108
FYI	HH	49.0	0.01139638	0.00004025
FYI	HV	49.0	0.00223438	0.00000102
MYI	HH	20.5	0.07484570	0.00230481
MYI	HV	20.5	0.00650072	0.00002383
MYI	HH	34.0	0.12121594	0.00384689
MYI	HV	34.0	0.02400428	0.00024402
MYI	HH	48.8	0.03844673	0.00034717
MYI	HV	48.8	0.00659896	0.00001235

#### 4.2.3.2 Sea Ice signature – Simulated SCN and Fine mode

From Table 10, the mean and variance are presented for SCW mode HH and HV data. It is assumed that the mean sea ice signature is the same for SCW, SCN and Fine mode considering that the incidence angle and ice type are constant. This is analogous to the situation presented in Equations (2) to (4).

As a first estimate of the sea ice SCN and Fine mode variance, the variance is simply taken as the ratio of the equivalent number of looks. That is, the SCW sea ice variance was scaled by a factor of two to simulate SCN sea ice variance and by a factor of six to simulate Fine mode sea ice variance.

## 4.3 Results and analysis

The goal of this work was to evaluate iceberg POD for the R-2 SCN mode. Since this was accomplished using R-2 Fine mode imagery, tables of POD were generated for both Fine and SCN modes to facilitate a tradeoff analysis of the two modes. This provides a benchmark for two extremes of SAR imagery – high resolution (*i.e.*, Fine mode) and low resolution (*i.e.*, SCN mode). POD tables were generated as a function of wind direction, wind speed, iceberg size, polarization and incidence angle. While some FQ data were collected for this study, the majority of data were collected with HH+HV. Thus, POD is reported for HH and HV and not for VV.

### 4.3.1 Fine mode iceberg detection

Fine mode iceberg POD analyses for both ocean and sea ice backgrounds were carried out. For the ocean background, this was accomplished by binning the available ocean data based on wind speed at 5 m/s increments, wind direction at 30° increments, and incidence angle at 5° increments. For sea ice backscatter, the data were binned based on incidence angle at 5° increments. The ice types evaluated were New Ice, FYI and MYI, all in the winter ablation state.

There was no significant trend in the data with respect to iceberg signature and incidence angle. Thus, all iceberg targets were used in evaluating the ocean and sea ice background in each of the binned data samples. The results in each bin are presented for Small (15 to 60 m – red), Medium (61 to 120 m – blue), and Large (121 to 200 m – green) icebergs, as shown in Table 11 through Table 14. All of the results were generated using a CFAR of  $1 \times 10^{-7}$ .

*Table 11: R-2 Fine mode iceberg POD for wind directions 0° to 30° from the SAR look direction (Red small; Blue medium; Green large).*

Polarization	HH				HV			
	0-5	5-10	10-15	15-20	0-5	5-10	10-15	15-20
40-45							0.77	
							0.92	
							1.00	
35-40	0.94	0.88	0.82		0.85	0.92	0.85	0.70
	0.96	0.95	0.95		0.93	0.97	0.95	0.91
	1.00	0.99	0.98		0.99	1.00	1.00	1.00
30-35	0.76	0.74	0.64		0.85	0.89	0.77	0.53
	0.90	0.92	0.86		0.95	0.96	0.92	0.78
	0.96	0.96	0.95		1.00	0.99	1.00	0.98
25-30	0.51	0.43	0.29		0.92	0.93	0.79	0.53
	0.77	0.74	0.62		0.98	0.98	0.93	0.77
	0.87	0.87	0.76		1.00	1.00	1.00	0.98
20-25	0.28	0.15	0.13	0.13	0.87	0.90	0.72	0.65
	0.47	0.36	0.31	0.28	0.95	0.97	0.90	0.85
	0.63	0.60	0.52	0.52	1.00	1.00	0.99	0.98

Table 12: R-2 Fine mode iceberg POD for wind directions  $30^\circ$  to  $60^\circ$  from the SAR look direction  
(Red small; Blue medium; Green large).

Polarization	HH				HV			
Wind Speed [m/s]	0-5	5-10	10-15	15-20	0-5	5-10	10-15	15-20
Inc. Angle [°]								
40-45	0.97		0.97				0.87	
	0.98		0.95				0.95	
	1.00		1.00				1.00	
35-40	0.91	0.91	0.79		0.83	0.94	0.80	0.70
	0.96	0.96	0.92		0.95	0.99	0.93	0.89
	0.99	0.99	0.96		0.99	1.00	1.00	1.00
30-35	0.81	0.75	0.55	0.67	0.80	0.95	0.77	0.80
	0.93	0.93	0.81	0.88	0.94	0.99	0.92	0.92
	0.97	0.97	0.91	0.96	1.00	1.00	1.00	1.00
25-30	0.64	0.48	0.32		0.90	0.94	0.88	
	0.87	0.76	0.60		0.97	0.99	0.95	
	0.94	0.88	0.78		1.00	1.00	1.00	
20-25	0.39	0.23	0.13	0.13	0.97	0.97	0.72	0.50
	0.63	0.52	0.24	0.32	1.00	1.00	0.88	0.74
	0.75	0.73	0.43	0.54	1.00	1.00	0.99	0.96

Table 13: R-2 Fine mode iceberg POD for wind directions  $60^\circ$  to  $90^\circ$  from the SAR look direction  
(Red small; Blue medium; Green large).

Polarization	HH				HV			
Wind Speed [m/s]	0-5	5-10	10-15	15-20	0-5	5-10	10-15	15-20
Inc. Angle [°]								
40-45	0.96				0.87	0.60		
	0.97				0.95	0.86		
	1.00				0.99	1.00		
35-40	0.90	0.94	0.90		0.90	0.92	0.83	
	0.96	0.96	0.94		0.97	0.98	0.95	
	0.99	1.00	0.99		1.00	1.00	1.00	
30-35	0.84	0.75	0.72	0.70	0.96	0.87	0.89	0.70
	0.94	0.91	0.92	0.91	0.99	0.96	0.97	0.91
	0.98	0.97	0.96	0.96	1.00	1.00	1.00	1.00
25-30	0.80	0.53	0.40	0.33	0.87	0.96	0.86	0.67
	0.91	0.79	0.70	0.69	0.94	0.99	0.95	0.89
	0.96	0.90	0.81	0.77	0.99	1.00	1.00	1.00
20-25	0.19	0.18	0.14		0.97	0.96	0.79	
	0.45	0.46	0.35		1.00	1.00	0.92	
	0.66	0.69	0.58		1.00	1.00	0.99	

Table 14: R-2 Fine mode iceberg POD in sea ice (Red small; Blue medium; Green large).

Polarization	HH			HV		
	New	FYI	MYI	New	FYI	MYI
40-45		0.80	0.45		0.17	0.11
		0.91	0.73		0.35	0.21
		0.96	0.85		0.56	0.38
35-40	0.88	0.72	0.43	0.76	0.44	0.11
	0.95	0.90	0.71	0.90	0.67	0.24
	0.99	0.95	0.84	0.99	0.86	0.44
30-35	0.81	0.70	0.20	0.60	0.45	0.08
	0.91	0.91	0.50	0.86	0.70	0.15
	0.96	0.96	0.73	1.00	0.92	0.38
25-30		0.69	0.20	0.20	0.62	0.00
		0.88	0.49	0.58	0.83	0.02
		0.96	0.73	0.88	0.99	0.08
20-25		0.50	0.13		0.51	0.00
		0.70	0.37		0.72	0.02
		0.84	0.60		0.91	0.04

#### 4.3.2 SCN mode iceberg detection

SCN mode iceberg POD analyses for both ocean and sea ice backgrounds were carried out. The data were binned in identical manner to the Fine mode data. The results are shown in Table 18.

Table 15: Simulated R-2 SCN mode iceberg POD for wind directions  $0^\circ$  to  $30^\circ$  from the SAR look direction (Red small; Blue medium; Green large).

Polarization	HH				HV			
	0-5	5-10	10-15	15-20	0-5	5-10	10-15	15-20
40-45							0.70	
							0.88	
							0.98	
35-40	0.86	0.74	0.67		0.56	0.67	0.76	0.60
	0.95	0.91	0.88		0.77	0.80	0.93	0.82
	0.99	0.97	0.96		0.96	0.93	1.00	1.00
30-35	0.60	0.56	0.36		0.54	0.78	0.67	0.33
	0.80	0.82	0.68		0.76	0.89	0.87	0.65
	0.91	0.93	0.88		0.97	0.98	0.99	0.94
25-30	0.33	0.29	0.15		0.70	0.83	0.67	0.28
	0.57	0.52	0.40		0.84	0.93	0.89	0.59
	0.80	0.78	0.68		0.98	0.99	0.99	0.94
20-25	0.12	0.04	0.02	0.02	0.67	0.84	0.57	0.48
	0.26	0.15	0.09	0.08	0.85	0.94	0.81	0.75
	0.47	0.37	0.29	0.25	0.97	0.98	0.98	0.98

Table 16: Simulated R-2 SCN mode iceberg POD for wind directions  $30^\circ$  to  $60^\circ$  from the SAR look direction (Red small; Blue medium; Green large).

Polarization	HH				HV			
	0-5	5-10	10-15	15-20	0-5	5-10	10-15	15-20
40-45	1.00		0.77				0.87	
	0.97		0.95				0.97	
	1.00		0.96				1.00	
35-40	0.84	0.81	0.56		0.59	0.69	0.73	0.54
	0.94	0.93	0.76		0.78	0.82	0.90	0.79
	0.98	0.98	0.85		0.98	0.96	0.99	0.99
30-35	0.72	0.60	0.34	0.37	0.66	0.97	0.70	0.67
	0.87	0.84	0.61	0.68	0.84	1.00	0.88	0.91
	0.96	0.94	0.85	0.88	0.98	1.00	0.99	1.00
25-30	0.46	0.30	0.18		0.81	0.95	0.79	
	0.74	0.53	0.38		0.90	0.99	0.95	
	0.88	0.79	0.65		0.99	1.00	1.00	
20-25	0.22	0.11	0.01	0.02	0.95	0.85	0.59	0.27
	0.43	0.32	0.06	0.12	0.97	0.91	0.83	0.57
	0.64	0.60	0.21	0.31	1.00	0.98	0.99	0.90

Table 17: Simulated R-2 SCN mode iceberg POD for wind directions 60° to 90° from the SAR look direction (Red small; Blue medium; Green large).

Polarization	HH				HV			
	0-5	5-10	10-15	15-20	0-5	5-10	10-15	15-20
40-45		0.89				0.80	0.43	
		0.95				0.89	0.72	
		0.99				0.98	0.96	
35-40	0.85	0.83	0.74		0.74	0.80	0.61	
	0.94	0.94	0.92		0.86	0.89	0.79	
	0.98	0.98	0.96		0.95	0.98	0.93	
30-35	0.71	0.59	0.52	0.53	0.68	0.65	0.89	0.60
	0.88	0.82	0.82	0.82	0.83	0.81	0.97	0.82
	0.95	0.94	0.94	0.92	0.98	0.97	1.00	1.00
25-30	0.67	0.33	0.23	0.20	0.61	0.76	0.83	0.53
	0.83	0.59	0.47	0.45	0.80	0.87	0.95	0.77
	0.92	0.83	0.76	0.73	0.97	0.97	1.00	0.96
20-25	0.10	0.08	0.04			0.77	0.69	
	0.24	0.25	0.15			0.87	0.87	
	0.47	0.52	0.35			0.98	0.99	

Table 18: Simulated R-2 SCN iceberg POD in sea ice (Red small; Blue medium; Green large).

Polarization	HH			HV		
	New	FYI	MYI	New	FYI	MYI
40-45		0.71	0.30		0.08	0.05
		0.85	0.55		0.19	0.12
		0.95	0.78		0.35	0.24
35-40	0.79	0.57	0.28	0.39	0.30	0.05
	0.92	0.82	0.50	0.58	0.53	0.10
	0.97	0.92	0.75	0.78	0.75	0.22
30-35	0.59	0.55	0.17	0.43	0.28	0.05
	0.84	0.80	0.37	0.69	0.52	0.07
	0.94	0.91	0.65	0.96	0.79	0.21
25-30		0.50	0.13	0.10	0.43	0.00
		0.78	0.32	0.17	0.71	0.00
		0.92	0.62	0.42	0.96	0.04
20-25		0.31	0.05		0.32	0.00
		0.55	0.17		0.57	0.00
		0.75	0.42		0.84	0.04

### **4.3.3    POD trends**

The R-2 iceberg data collected for this project is a significant accomplishment. A large quantity of SAR iceberg detections were collected and ground verified over a period of only several months; previous attempts to collect iceberg data on the Grand Banks and Labrador Sea for R-1 and ASAR have taken significantly longer periods of time to collect similar quantities of icebergs. Therefore, these data represent a very valuable contribution to the knowledge of SAR iceberg detection capabilities. When combined with the additional DRDC and CIS data, the quantities allow for the derivation of statistically significant detection rates for icebergs of varying size, as a function of wind speed, sea state, detection threshold, incidence angle and ice type.

The results here represent the trends as a function of wind speed, iceberg size, incidence angle, polarization, and resolution in open water. For the discussion here, specific cases have been selected that best characterize these trends.

The iceberg POD for wind speeds from 10 to 15 m/s taken from Table 12, as shown in Figure 44, demonstrates that when using HH polarization, iceberg POD increases as a function of increasing incidence angle and target size. Using HV polarization, it is observed that iceberg POD also increases as a function of increasing incidence angle and target size, although the effect of incidence angle on iceberg POD is far less than for HH polarization. Thus for Medium and Large icebergs, the POD for Fine mode data is higher in HV polarization than in HH. Small icebergs at shallow incidence angles were found to have a higher POD in HH than in HV, whereas at steep incidence angles they were found to have a higher POD in HV than in HH. Thus, for Small icebergs either HH or HV should be considered depending on the incidence angle.

The iceberg POD for incidence angles from 25° to 30° (wind direction from 60° to 90°) taken from Table 13, as shown in Figure 45, demonstrates that when using HH polarization iceberg POD decreases as a function of increasing wind speed. It is apparent that smaller icebergs are more susceptible to increasing wind speeds than larger ones in the HH channel; the same can be said for the HV channel with higher wind speeds. Here, the polarization selection of HV over HH was found to produce an improved iceberg POD for all wind speeds, considering the incidence angle range of 25° to 30°.

From the iceberg POD from Table 12 and Table 16 for wind speeds in the 5 to 10 m/s range, it is apparent that for the decrease in resolution and the increase in NESZ when going from Fine mode to SCN, there is an associated decrease in iceberg POD for both the HH and HV channels. Figure 46 demonstrates a specific example where Medium and Small icebergs had on average a (nominally) 10 to 15 percent decrease in POD for both HH and HV. Thus, as expected, decreasing resolution and increasing NESZ levels yields a decrease in the corresponding iceberg POD rates.

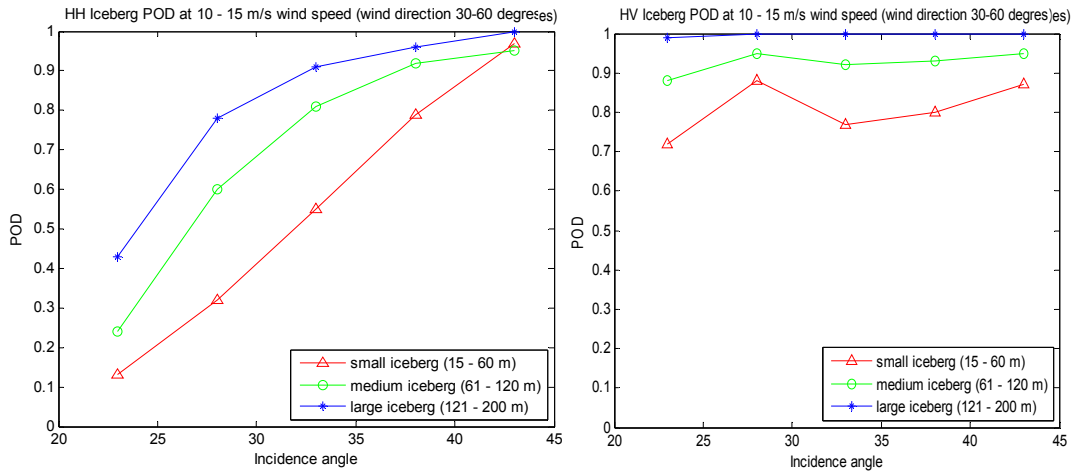


Figure 44: Fine mode Iceberg POD as a function of incidence angle and polarization.

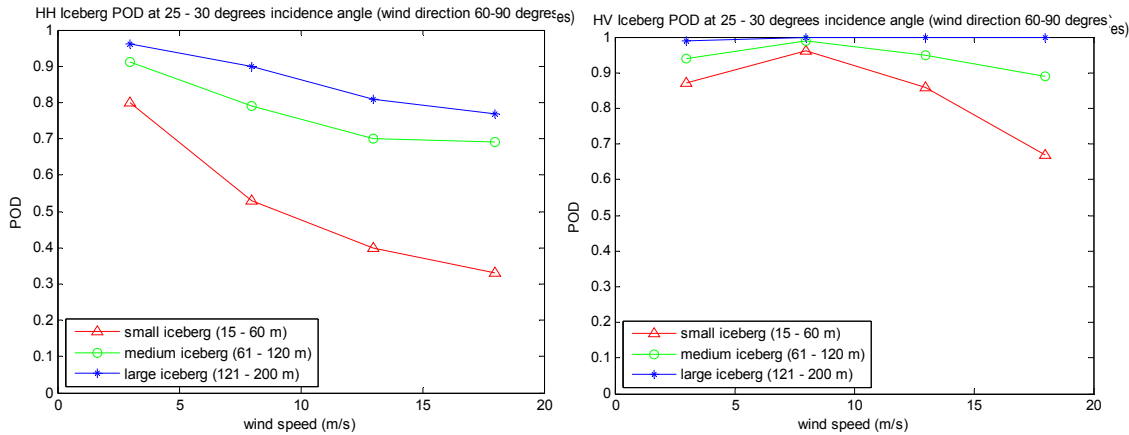


Figure 45: Fine mode Iceberg POD as a function of wind speed and polarization.

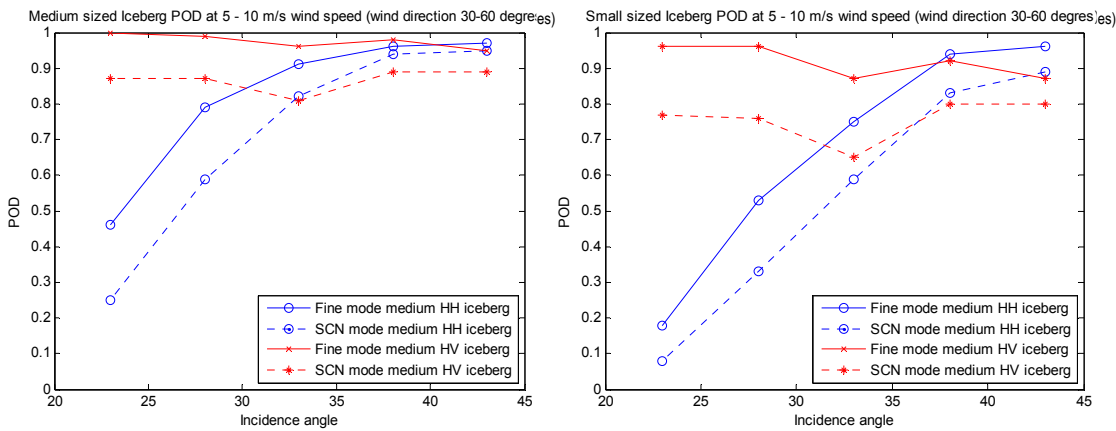


Figure 46: Iceberg POD as a function of image mode, target size, incidence angle and polarization.

Also of interest from Figure 46 is an apparent trend which implies that, for both SCN and Fine mode data, iceberg POD is lower at steep incidence angles for icebergs in the HH channel. Specifically for this example, Small iceberg detection in Fine mode favours HH over HV for incidence angles greater than 38°. Small iceberg POD in SCN mode was found to favour HH over HV for incidence angles greater than 36°. A similar trend was observed for the detection of Medium sized icebergs, with the HH channel being preferred over the HV for incidence angles greater than 40° for Fine mode and greater than 33° for SCN mode. For iceberg POD optimization as a function of image mode, polarization and incidence angle, the influences of increasing the NESZ and decreasing the resolution “shift” the incidence angle limit where HV should be utilized as opposed to HH. This has been attributed to the weaker geophysical ocean and target signature response in the HV channel relative to the HH channel. Essentially (under moderate to low wind speed conditions) the ocean background and target signature become buried (or partially obscured) in the NESZ in the HV channel. This effect may also happen in the HH channel but to a much lesser extent than that of the HV channel.

Turning attention to the iceberg POD in sea ice, the results demonstrate trends considering sea ice type, iceberg size, incidence angle, polarization, and resolution. It is important to note that only a winter ablation state for sea ice was evaluated. To demonstrate these trends, specific cases have been selected that best characterize the trends.

The iceberg POD in sea ice from Table 18, as shown in Figure 47, demonstrates that iceberg detection in sea ice favours HH polarization over HV. As well, iceberg POD increases as a function of increasing iceberg size. For the HH polarization, iceberg POD increases as a function of increasing incidence angle. This has been attributed to the HH sea ice signature decreasing as a function of increasing incidence angle. For the HV polarization, iceberg POD nominally decreases as a function of increasing incidence angle. It is important to note that there were only two samples of winter ablation for FYI in the 40° to 45° incidence angle range, as presented in Figure 47. One of those samples had a particularly high HV sample variance, which in turn decreased the POD for small, medium and large icebergs in that range bin. The omission of this outlier sample would result in a near constant POD for the HV channel across the incidence angle range, with the only parameter of importance being iceberg size. Figure 48 demonstrates similar trends for iceberg detection in MYI, with the exception that iceberg POD is considerably less in winter ablation MYI than in FYI.

One interesting observation from this work on iceberg POD in sea ice is that iceberg POD in HH at steep incidence angles can actually be higher than in open water. This is based on the ocean backscatter generally having a higher intensity than sea ice at steep incidence angles. Thus, it is conceivable that an iceberg target could be detectable in the sea ice but not in the open water at 20°. Of course, at shallower incidence angles where the sea ice is brighter than the ocean backscatter, iceberg POD is higher in open water. The bounding incidence angle region between where open water or sea ice provides for higher iceberg POD is variable. This is due to the fact that the ocean backscatter is dependent on wind speed and direction, the sea ice backscatter is dependent on ablation state, sea ice type, and the percentage of rafting and rough surface structure. These parameters are all susceptible to incidence angle effects for varying geophysical backscatter, which further complicates the variable boundary. Nonetheless, it has been demonstrated here that iceberg POD in sea ice at steep incidence angles can be higher than that of open water in the HH channel.

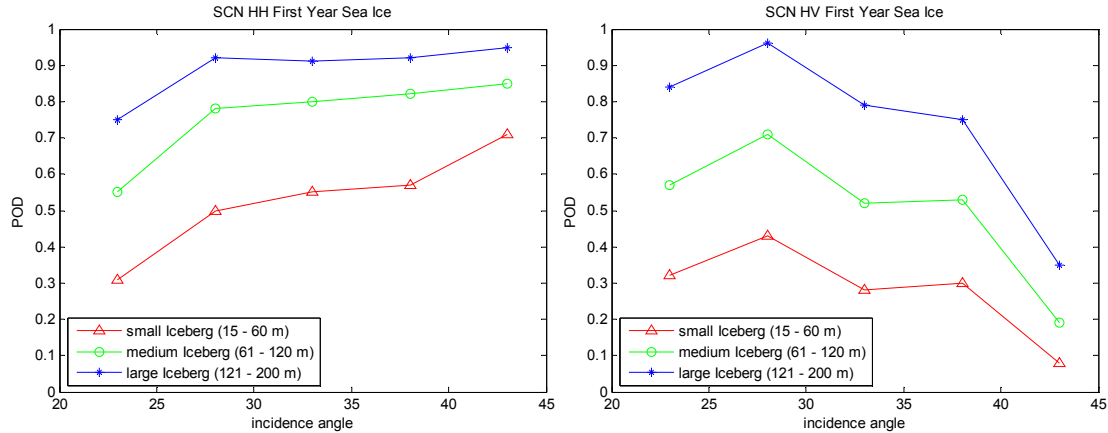


Figure 47: Iceberg POD in FYI for SCN as a function of target size, incidence angle and polarization.

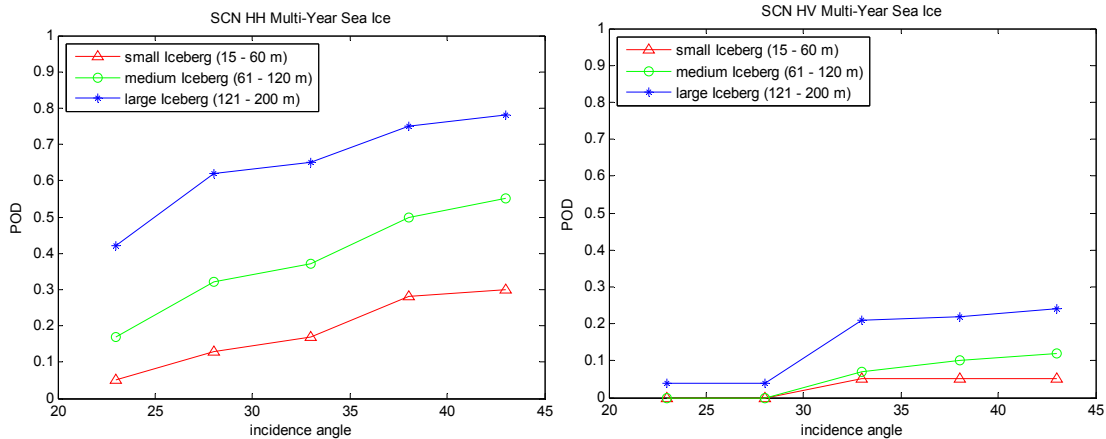


Figure 48: Iceberg POD in MYI for SCN as a function of target size, incidence angle and polarization.

## 4.4 Mode recommendations

### 4.4.1 RADARSAT-2

The detection results shown here demonstrate that icebergs can be detected reliably in various wind and sea ice conditions. Detection rates are detrimentally affected by decreased SAR resolution, increased wind speed and increased sea ice brightness. In addition, HV polarization was shown to produce better results at small incidence angles while HH polarization provides better results at large incidence angles. This is consistent with previous work on iceberg detection with R-1, ASAR and the Convair-580 [7]. In fact, the superior noise floor (NESZ) offered by R-2 compared to R-1 and ASAR provides for enhanced iceberg detection. This was particularly relevant for detection in the cross-polarization channel (HV) at steep incidence angles which had previously been shown to be challenging in the HH or VV channel.

Focussing on ScanSAR modes, a higher resolution is in general desirable. However, the best bet is SCNB acquired in dual polarization, HH+HV. SCNA could be satisfactory for icebergs in a sea ice background.

#### **4.4.2 RCM**

The situation is similar for RCM, with higher resolution desirable. In this context, the Medium Resolution 50 m mode is recommended, again acquired in dual polarization, HH+HV.

### **4.5 Future analysis**

Several gaps are apparent from this work, not the least of which is a lack of validated iceberg data in R-2 ScanSAR modes. It is recommended that this gap be filled as soon as possible, perhaps by piggy-backing on planned iceberg surveillance trials that are carried out for the oil and gas industry from time to time. In particular, an OSVN data set should be acquired.

The CP mode on RCM will represent a new capability that should be evaluated well in advance of RCM's launch. Preliminary analysis has already been carried out [8], but more work is warranted.

## **5 Ship Detection**

---

### **5.1 Background**

Ship detection using RADARSAT is well understood, *e.g.*, [55], and has been operationalized within EC's Integrated Satellite Tracking of Polluters (ISTOP) program, and will soon be operationalized within DND by the Polar Epsilon (PE) project. R-2 data in SCN mode are routinely utilized, with co-polarization being used at larger incidence angles and cross-polarization being used at lower incidence angles to maximize the contrast between the ship signature and the background ocean clutter. Better ship detection performance is achieved for higher resolution modes of operation, but usually the lower resolution SCN mode is used since it provides a higher rate of area coverage.

One component of the PE project is to implement the MSSR modes of R-2 for maritime surveillance. Two MSSR modes have been defined. OSVN amounts to a beefed-up SCN mode with a swath width of 530 km and dual polarization operation. DVWF is intended to serve ship detection requirements only and uses larger incidence angles with a swath width of 450 km.

In order to assess ship detection performance for various SARs, DRDC Ottawa has developed the Ship Detectability Performance Tool (SDPT) [59], which has been validated for R-1, R-2, ASAR, and Sentinel-1 ship detection performance. The SDPT includes models for ocean clutter and its variability (K-distribution), the noise floor and its variability (Chi-squared distribution), and ship RCS and its variability. Performance is expressed in terms of the CFAR setting and the probability of detection.

In future, SAR-based ship detections will be associated with concurrent Automatic Identification System (AIS) data, received via coastal station, aircraft, or satellite, to establish improved ship detection and classification under various sea state conditions.

### **5.2 Data and method**

Since the models implemented in the SDPT have already been validated, no additional data were acquired for this study for validation purposes. However, the SDPT was extended and improved as part of this project by implementing improved models for ocean clutter (see Section 6) and including new R-2 beam modes as follows:

- The R-2 FQ-mode-derived co-polarization ratio of Equation (9) for both R-1 and R-2;
- The R-2 FQ-mode-derived cross-polarization ocean clutter model of Equation (10);
- MSSR modes for nominal OSVN and DVWF parameters; and
- New R-2 beam modes including specific Fine Quad and Ultra Fine modes.

## 5.3 Results and analysis

Details of SDPT models and outputs are described elsewhere [59]. Here we include a few screenshots of the tool, which is implemented in Matlab™ and includes a GUI. From the main GUI window (Figure 49), four options are available:

1. Sensor-Specific Ship Detectability Calculator - Estimate the minimum detectable ship length, the minimum detectable RCS, the clutter to noise ratio, the ocean clutter level, and the minimum peak to clutter ratio for a pre-defined set of sensor parameters.
2. Sensor-Specific Full Swath Analysis - Plot the minimum detectable ship length (across the full swath of the beam) versus incidence angle for all the beams of one or more selected sensors, at the selected polarization, and at the desired performance and environmental parameter settings.
3. Generic Ship Detectability Calculator - The same as the Sensor Specific Ship Detectability Calculator, but without any sensor dependence. As such, all the model parameters are editable with no constraints or dependencies.
4. Ship Detectability Sensitivity Analysis - Sensor specific and designed to provide the sensitivity of the minimum detectable ship length with respect to varying wind speed, wind aspect angle, K-distribution order parameter, probability of false alarm, and model Margin.

Here we will consider a run of SDPT for Sensor-Specific Full Swath Analysis (Figure 50) and will select the various supported R-2 beam modes (Figure 51).

SDPT outputs for co-polarization and cross-polarization are shown in Figure 52 through Figure 57. The plots are generated automatically by the tool, and appear quite “busy” due to the large number of modes represented and the various curves being labelled automatically at their centres (so some of the labels overlap). Figure 52 and Figure 53 focus on the R-1 heritage modes (*i.e.*, SCN, SCW, S, W, EL, and EH) for HH and HV polarizations, respectively. Figure 54 and Figure 55 focus on SCN and the new MSSR modes for HH and HV polarizations, respectively. Figure 56 and Figure 57 focus on MSSR, UF, and FQ modes for HH and HV polarizations, respectively. We note the following:

- For HH, the minimum detectable ship length decreases with increasing incidence angle due to the decrease in ocean clutter;
- The minimum detectable ship length decreases for modes with increasing spatial resolution (of course, the available swath coverage also decreases);
- For HV, the minimum detectable ship length is less dependent on incidence angle, and in many cases, is noise limited such that the shape of the noise floor is readily apparent; and
- MSSR performance is comparable to or better than SCN performance for both OSVN and DVWF.



Figure 49: Main GUI window for the SDPT.

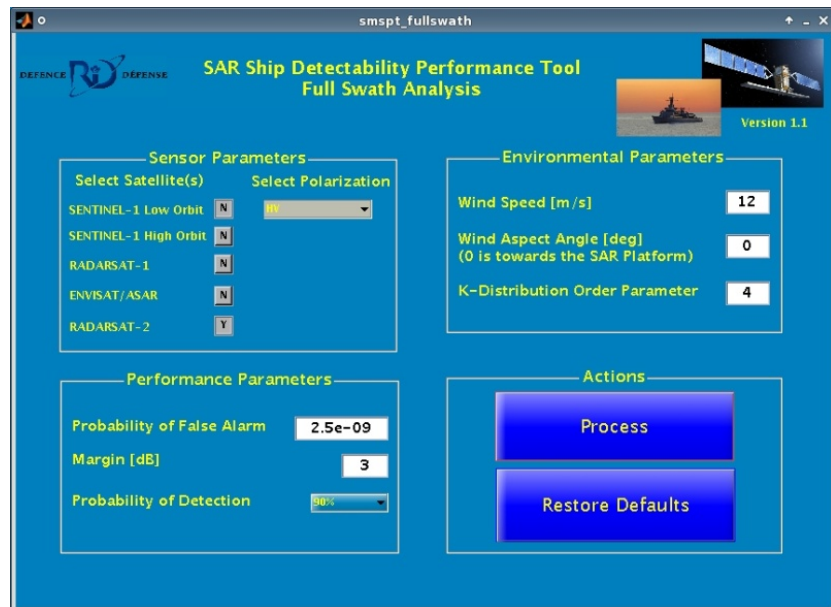


Figure 50: GUI illustrating the Full Swath Analysis component of the SDPT.

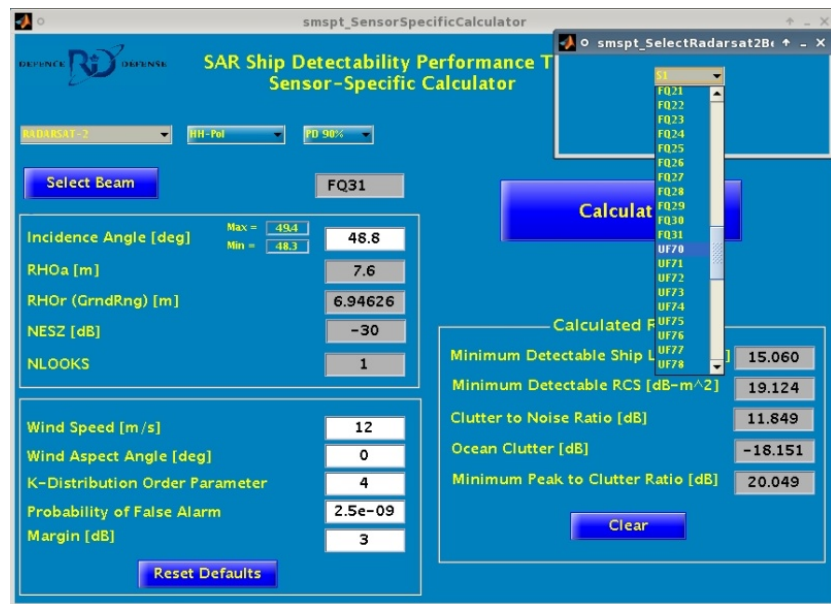
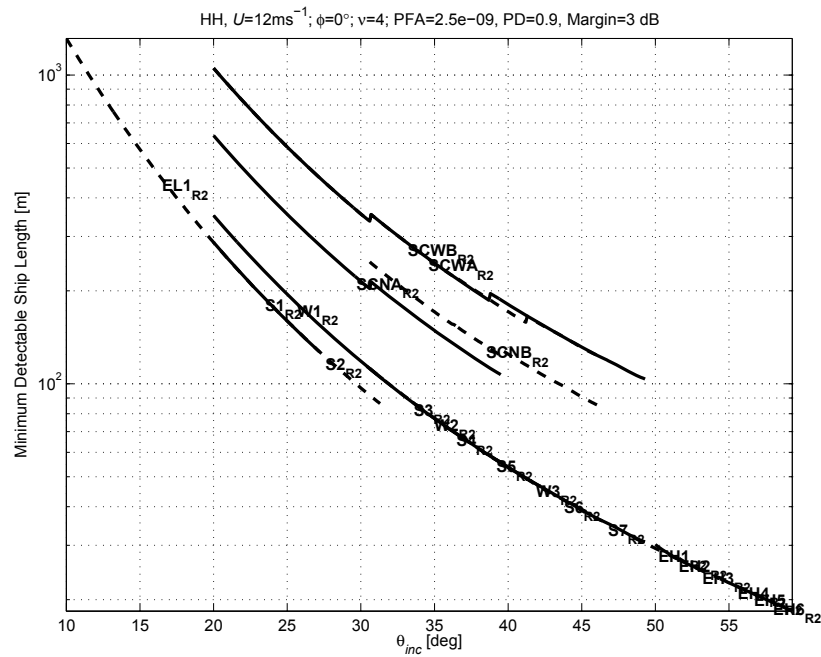


Figure 51: GUI illustrating the Sensor-Specific Calculator of the SDPT.



*Figure 52: Full-Swath Analysis of Minimum Detectable Ship Length in meters vs. incidence angle for R-2 heritage beam modes, HH-polarization.*

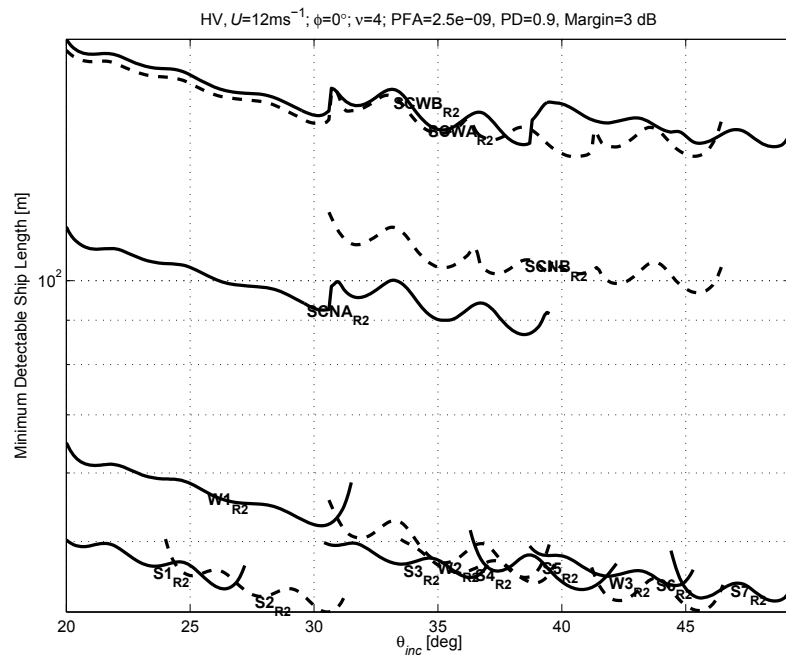


Figure 53: Full-Swath Analysis of Minimum Detectable Ship Length in meters vs. incidence angle for R-2 heritage beam modes, HV-polarization.

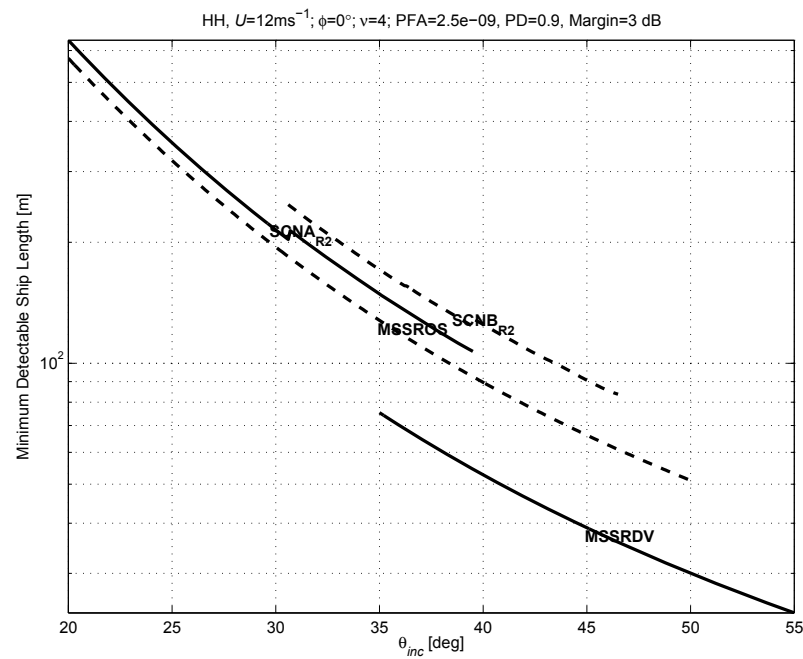


Figure 54: Full-Swath Analysis of Minimum Detectable Ship Length in meters vs. incidence angle for R-2 SCN and MSSR modes, HH-polarization.

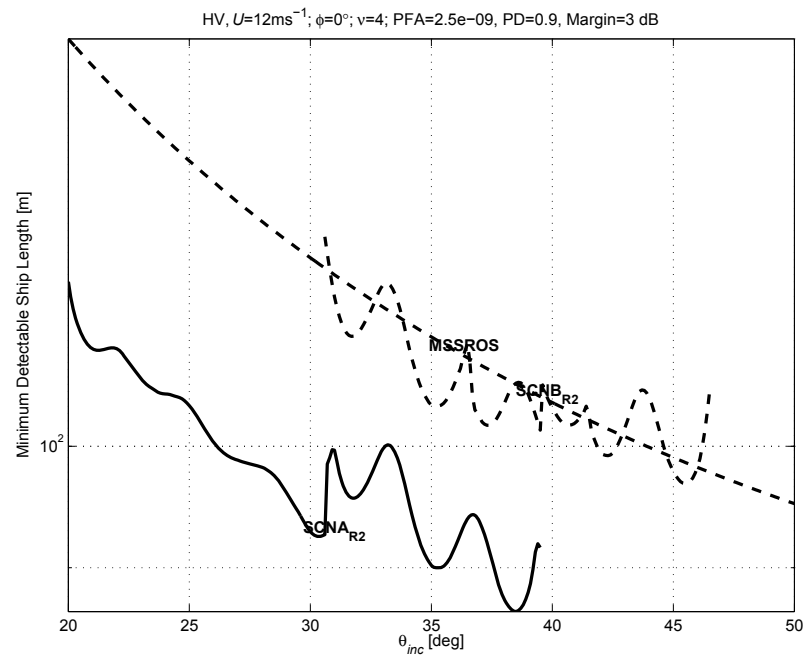


Figure 55: Full-Swath Analysis of Minimum Detectable Ship Length in meters vs. incidence angle for R-2 SCN and MSSR modes, HV-polarization.

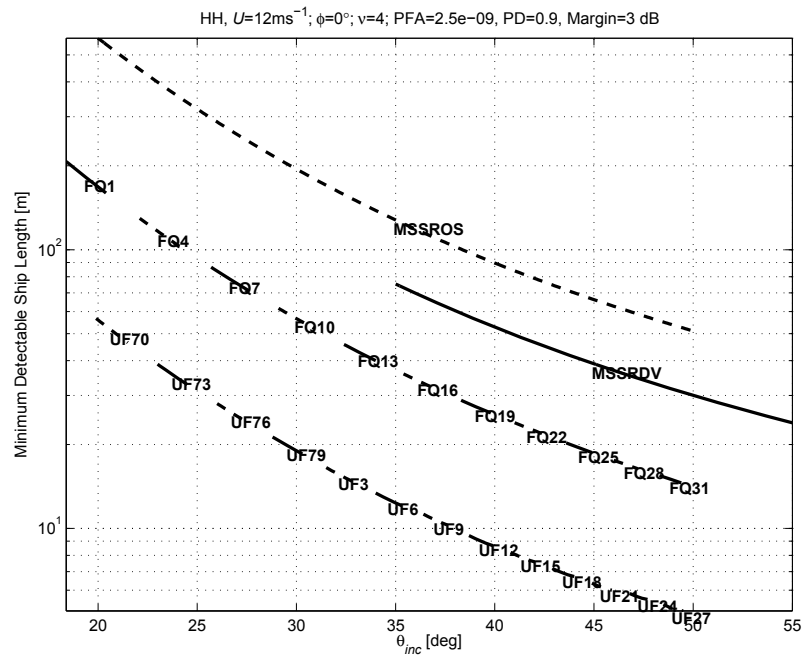


Figure 56: Full-Swath Analysis of Minimum Detectable Ship Length in meters vs. incidence angle for R-2 MSSR, FQ, and UF modes, HH-polarization.

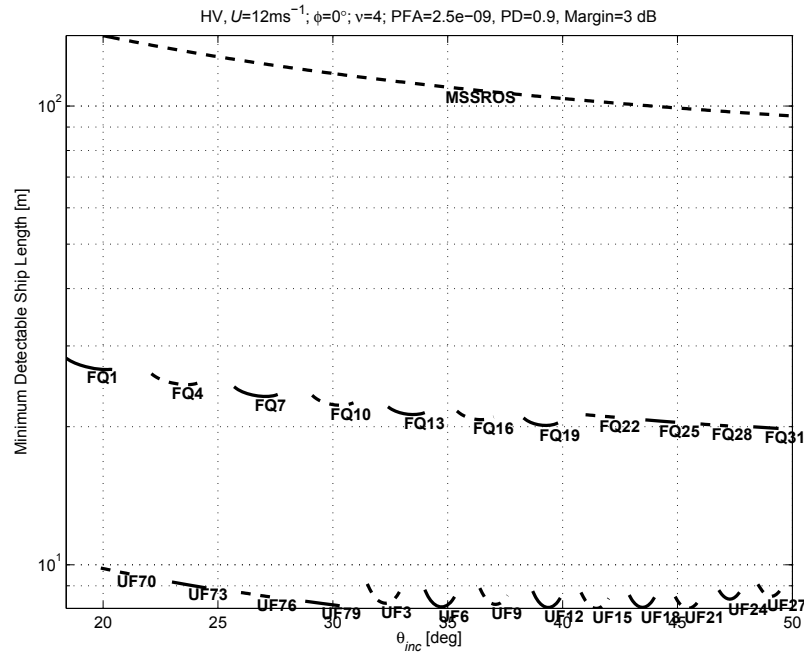


Figure 57: Full-Swath Analysis of Minimum Detectable Ship Length in meters vs. incidence angle for R-2 MSSR, FQ, and UF modes, HV-polarization.

## 5.4 Mode recommendations

### 5.4.1 RADARSAT-2

It is expected that DVWF will become the work-horse ship detection mode for DND in the absence of mode conflicts with other users, and hopefully OGDs will be willing to evaluate and adopt OSVN into their operations. In general, cross-polarization will provide good ship detection for all incidence angles, but co-polarization will provide better ship detection for larger incidence angles that have reduced clutter. Higher resolution modes would be suitable for ship detection within small scale choke points.

### 5.4.2 RCM

Similar to R-2 MSSR DVWF and OSVN modes, RCM will have a Ship Detection mode and a 50 m Medium Resolution mode. One difference is that the Ship Detection mode will be available in dual polarization, which is the recommended configuration. Similar to R-2, some of the higher resolution modes would be suitable for ship detection within choke points.

## **5.5 Future analysis**

The SDPT includes a MSSR model that is based on nominal parameters. The model should be upgraded to account for actual MSSR implementation. Furthermore, the SDPT should be extended to include at least the RCM Ship Detection and 50 m Medium Resolution modes, at least in their nominal form. This would facilitate straightforward intercomparison of ship detection performance between RCM and R-2. Finally, RCM will feature CP which, in common with other marine applications considered in this document, should be evaluated for ship detection [8]. Preliminary analysis has been carried out, but further evaluation is still warranted.

## **6 Wind speed estimation**

---

### **6.1 Background**

An emerging maritime application of SAR is ocean wind speed estimation. The principle is straightforward in that the ocean clutter depends on the wind speed, so a model that relates these two parameters can be used to retrieve the wind speed from a radiometrically-calibrated SAR ocean image, knowing the incidence angle and the wind direction. Over the years, many C-band models (CMODs) have been developed for C-band, VV polarization scatterometer wind retrieval (*e.g.*, CMOD5 [20]) in the context of ESA scatterometer missions. These models have also been applied to SAR imagery (*e.g.*, [30], [56]) to provide high resolution wind fields, especially in the coastal zone. EC through the National SAR Winds project is operationalizing SAR-derived winds, making SAR-derived wind products available on the weather forecaster's desktop.

CMODs have been developed for the specific case of C-band, VV polarization. Conversion to HH polarization, as required for R-1 wind speed retrieval, has relied on an *ad hoc* co-polarization ratio. There are several possible models for the co-polarization ratio [56]. One objective of this work is to empirically derive an improved co-polarization ratio from simultaneous observations of ocean backscatter using the R-2 FQ mode. A second objective is to derive a cross-polarization clutter model to improve ship detectability modeling, in particular within the SDPT. There have been rather few observations of cross-polarization ocean backscatter reported in the literature (*e.g.*, [19], [58]). With FQ mode data, the cross-polarization backscatter would also be available, permitting empirical derivation of a cross-polarization ocean clutter model [60].

### **6.2 Data and processing methodology**

Data acquisition of R-2 FQ mode data in SLC form began in October 2008 over operational weather buoys off the East and West coasts of Canada (see Figure 58 and Figure 59). FQ is favoured for this work since it features an extremely low noise floor, and inter-channel cross talk can be corrected for quad-polarization data [28]. For each acquisition, the buoy was located within the image footprint and the SAR acquisition time was less than 30 minutes removed from the buoy measurement. The buoy wind speed was corrected to equivalent neutral stability wind speed at 10 m height above ocean surface (*i.e.*,  $U_N^{10}$ ) using the observed air-sea temperature difference and the known anemometer height.

Mean  $\sigma^0$  was calculated by spatially averaging over a 3 km by 3 km sub-scene centered on the buoy location. Figure 60 shows a FQ18 case study that shows the FQ scene coverage, the analysis region over the buoy, and the wind speed and direction as measured by the buoy. Also indicated in the figure are the wind speed from the QuikSCAT scatterometer and the wind speeds derived from the HH and VV channels. To date, more than 700 FQ images with concurrently-observed wind speed and direction were available for analysis.



East Coast Buoy Locations

UNCLASSIFIED



RADARSAT-2 Data and Products (c) MacDonald, Dettwiler and Associates Ltd., 2008 - All Rights Reserved

UNCLASSIFIED

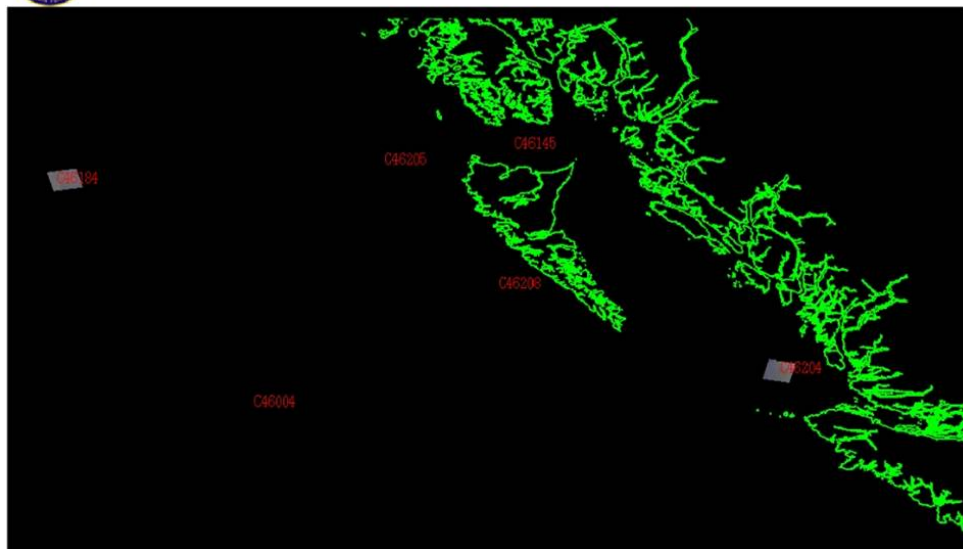
Canada

Figure 58: East coast buoy locations considered.



West Coast Buoy Locations

UNCLASSIFIED



RADARSAT-2 Data and Products (c) MacDonald, Dettwiler and Associates Ltd., 2008 - All Rights Reserved

UNCLASSIFIED

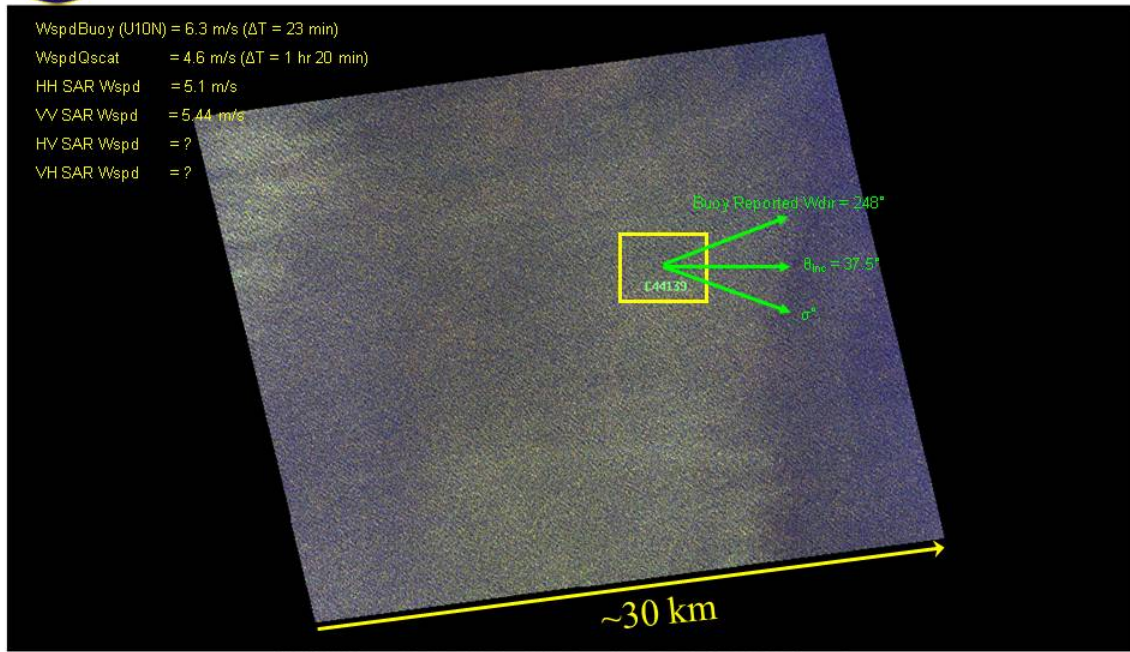
Canada

Figure 59: West coast buoy locations considered.



R-2, 05-Apr-2009 21:43, FQ18

UNCLASSIFIED



UNCLASSIFIED

Figure 60: Case study showing buoy location, sub-scene over which a mean  $\sigma^o$  is calculated, the associated incidence angle and buoy reported wind direction.

## 6.3 Results and analysis

### 6.3.1 Co-polarization ratio

Figure 61 is a plot of the observed co-polarization ratio as a function of incidence angle with various other polarization models overlaid (see [56] for a full explanation). Figure 62 is a plot of the co-polarization ratio versus incidence angle with the following function fitted to the data:

$$\frac{\sigma^o_{VV}}{\sigma^o_{HH}} = 0.327 \exp(2.304\theta_{inc}) - 0.273. \quad (9)$$

This C-band co-polarization ratio is independent of wind speed and direction. Figure 63 shows a plot of the HH-SAR-derived wind speed using the Kirchhoff co-polarization ratio [56], while Figure 69 shows a plot of the HH-SAR-derived wind speed using the empirical co-polarization ratio of Equation (9). The Kirchhoff results have an RMS error of 2.65 m/s, which improves to 2.34 m/s by using the empirical co-polarization ratio.

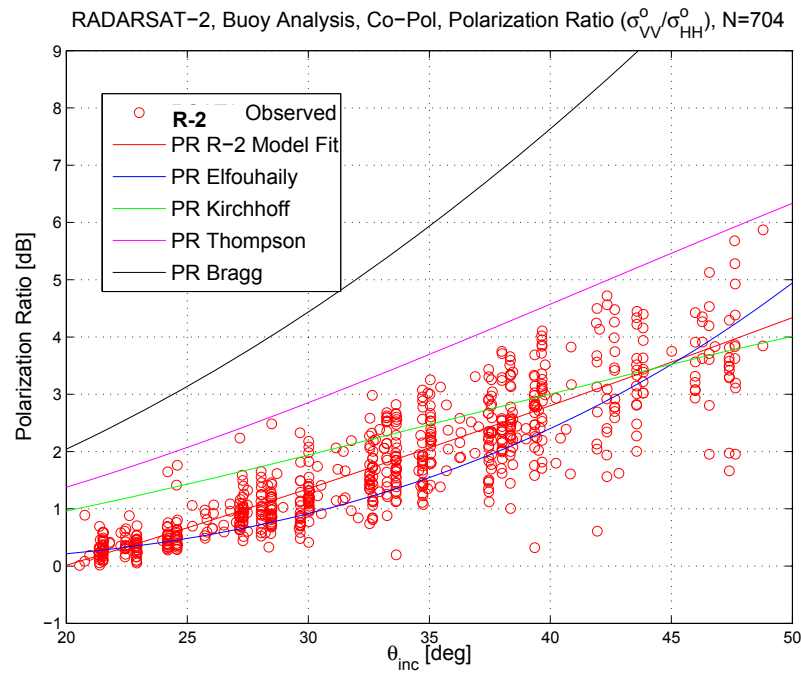


Figure 61: Plot of observed co-polarization ratio vs. incidence angle with various polarization ratio models overlaid.

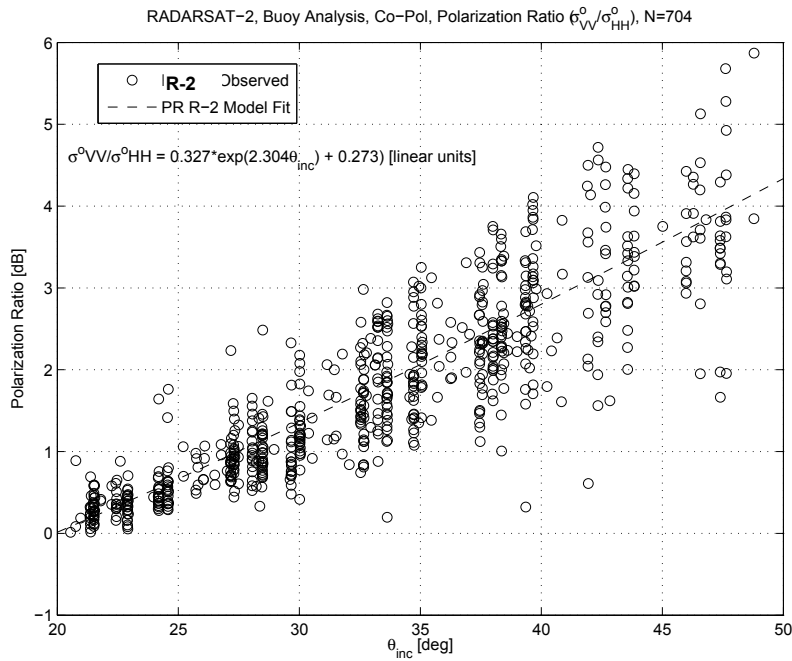


Figure 62: Observed co-polarization ratio vs. incidence angle along with the model fit.

RADARSAT-2, Buoy Analysis, Kirchoff Polratio, UHH vs U10N, N=704

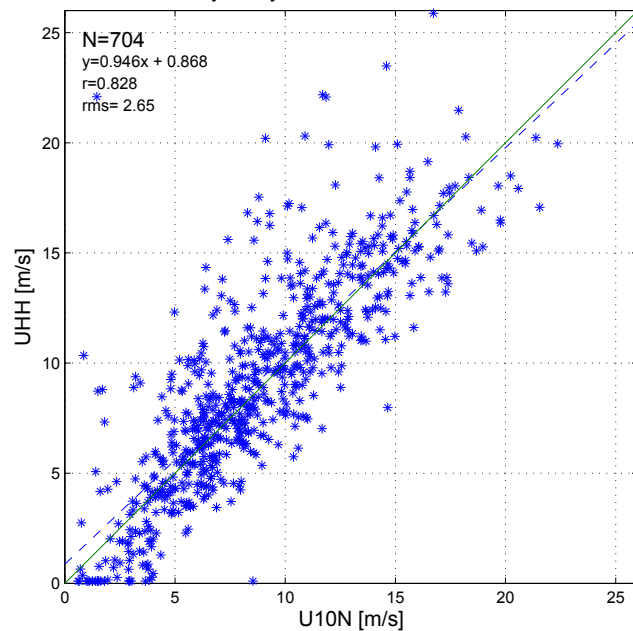


Figure 63: Scatter plot of HH-derived wind speed vs. buoy wind speed using Kirchhoff co-polarization ratio.

### **6.3.2 Cross polarization ocean backscatter**

Figure 64 and Figure 65 provide plots of the co-polarization and cross-polarization C-band backscatter as a function of incidence angle. Also plotted is the instrument NESZ, which is provided along with the R-2 product with an error of  $\pm 1$  dB [Anthony Luscombe, personal communication].

The co-polarization data shows the expected downward trend in backscatter with increasing incidence angle. Note that the VV backscatter is larger than the HH backscatter; in both cases, the variability arises due to the wind speed and wind direction. Also note that the co-polarization observations generally have an excellent signal-to-noise ratio, especially for smaller incidence angles.

On the other hand, the cross-polarization backscatter data do not show any particular trend with incidence angle. The cross-polarization observations have a relatively poor signal-to-noise ratio at all incidence angles.

Figure 66 and Figure 67 provide plots of the co-polarization and cross-polarization C-band backscatter as a function of the *in-situ*-observed wind speed. Again, the instrument noise floor is plotted for each observation. The co-polarization data show the expected upward trend with increasing wind speed; again, the variability arises due to the incidence angle and wind direction.

The cross-polarization data also shows an upward trend with increasing wind speed, but with rather little variability. In fact, the data are essentially independent of incidence angle and wind direction. This suggests the possibility of wind speed retrieval from C-band cross-polarization observations, without the need for any geometry information (*i.e.*, incidence angle or wind direction), for sufficiently high wind speeds.

Note that the radar backscatter observable is composed of the backscattered radar signal plus the receiver noise. We did attempt to subtract the noise component, which could be important for low signal-to-noise ratio cross-polarization observations in particular, but this did not help the correlation. We concluded that the noise floor is not adequately known to accurately carry out noise subtraction.

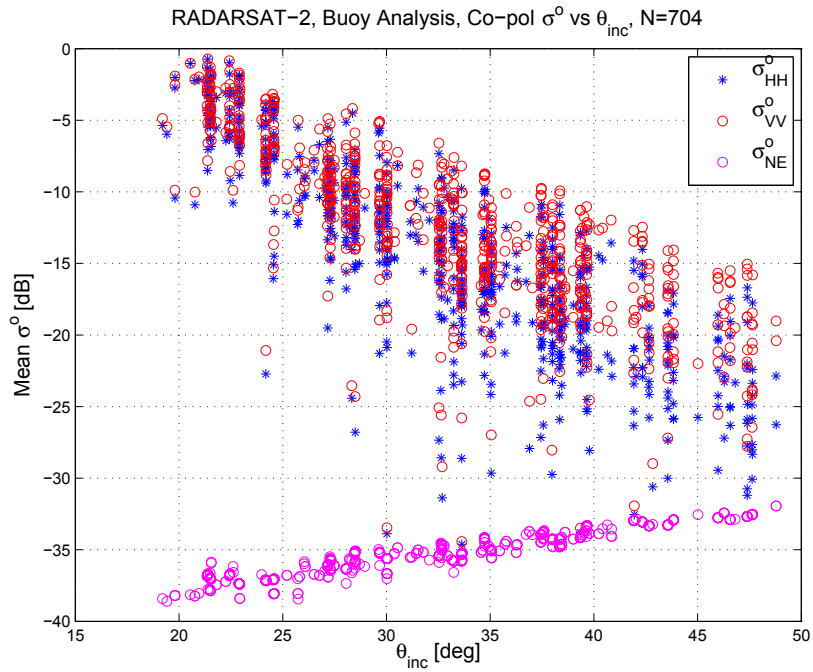


Figure 64: Co-polarization  $\sigma^0$  vs. incidence angle along with the associated NESZ.

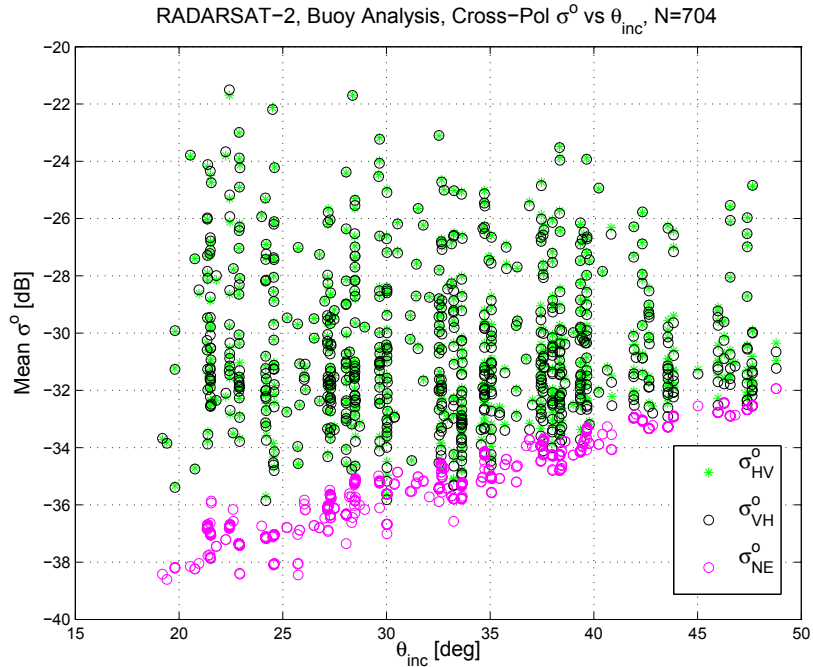


Figure 65: Cross-polarization  $\sigma^0$  vs. incidence angle along with the associated NESZ.

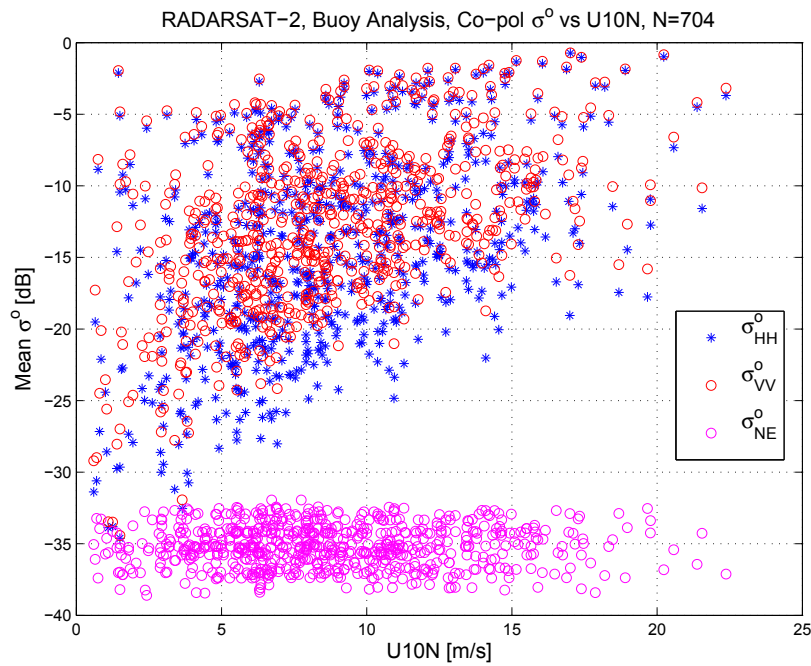


Figure 66: Co-polarization  $\sigma^0$  vs. wind speed along with the associated NESZ.

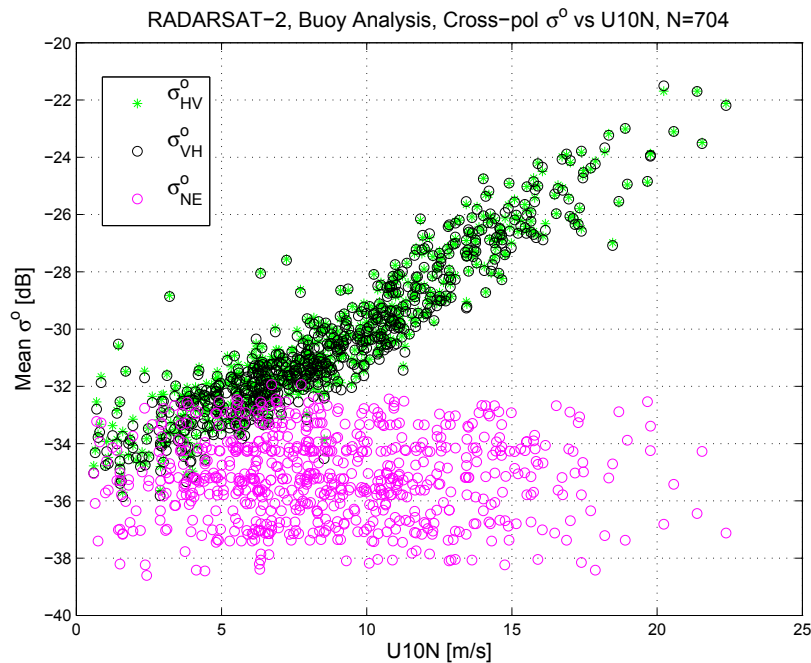


Figure 67: Cross-polarization  $\sigma^0$  vs. wind speed along with the associated NESZ.

Based on these data, we carried out a very simple fit to the observed cross-polarization data to derive a model for the relationship between C-band cross-polarization backscatter and wind speed (Figure 68):

$$\sigma^o_{\text{cross-pol}} = 0.587 U_N^{10} - 35.55 \quad [\text{dB}]. \quad (10)$$

This cross-polarization model is independent of incidence angle and wind direction, and may be inverted trivially to permit estimation of wind speed from observed C-band cross-polarization ocean backscatter.

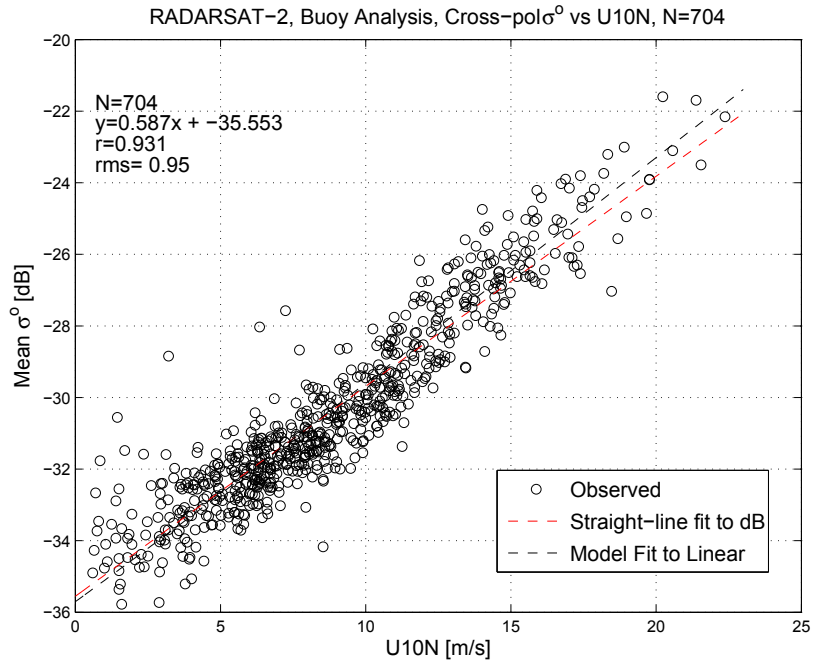


Figure 68: Observed cross-polarization backscatter vs. observed wind speed with model fits.

We carried out wind retrieval for the data set, as shown in Figure 69 through Figure 72. For the co-polarization cases, the *in-situ*-observed wind direction was used along with the CMOD\_IFR2 geophysical model function. For the HH case the co-polarization ratio of Equation (9) was used. For the cross-polarization cases, the cross-polarization model function of Equation (10) was used.

The observed root-mean-square (RMS) errors are: C-band HH, 2.34 m/s; C-band VV, 2.23 m/s; C-band HV, 1.61 m/s; and C-band VH, 1.64 m/s. The co-polarization RMS errors are comparable to previous comparisons of SAR-derived wind speeds with operational weather buoy data, *e.g.*, [30], [56]. Note also that the cross-polarization-retrieved wind speed is better correlated than the co-polarization-retrieved wind speed with the *in-situ*-observed wind speed.

Of course, these wind retrieval results are biased since we trained the models of Equations (9) and (10) using the same data set that was inverted to obtain wind speed. However, nearly identical RMS values were realized when using a jackknife (*i.e.*, leave one out) sampling method.

Finally, we show an image of SAR-derived wind speed using QuikSCAT wind directions of Hurricane Bertha acquired by R-2 configured in SCWA, VV-polarization (Figure 73) and in SCWA, VH-polarization (Figure 74). In this case, the model of Equation (10) was extrapolated to higher wind speeds. The cross-polarization result provides more uniform wind speeds around the eye of the storm. However, the noise floor of the instrument is visible as the large-scale azimuth-oriented bands for the lower wind speed regions.

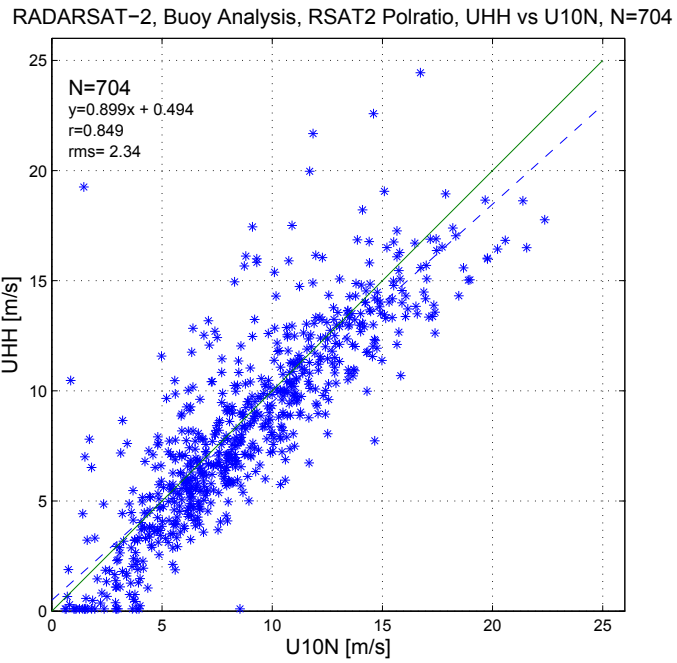


Figure 69: Scatter plot of HH-derived wind speed vs. buoy wind speed using Equation (9).

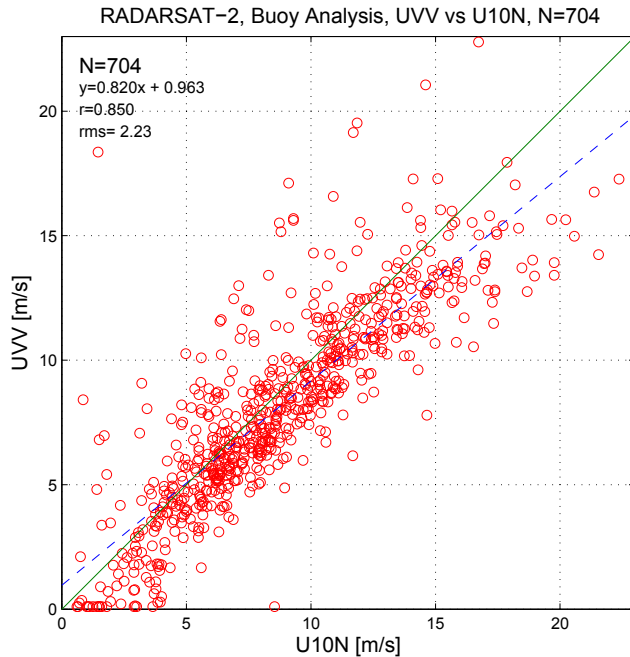


Figure 70: Scatter plot of VV-derived wind speed vs. buoy wind speed.

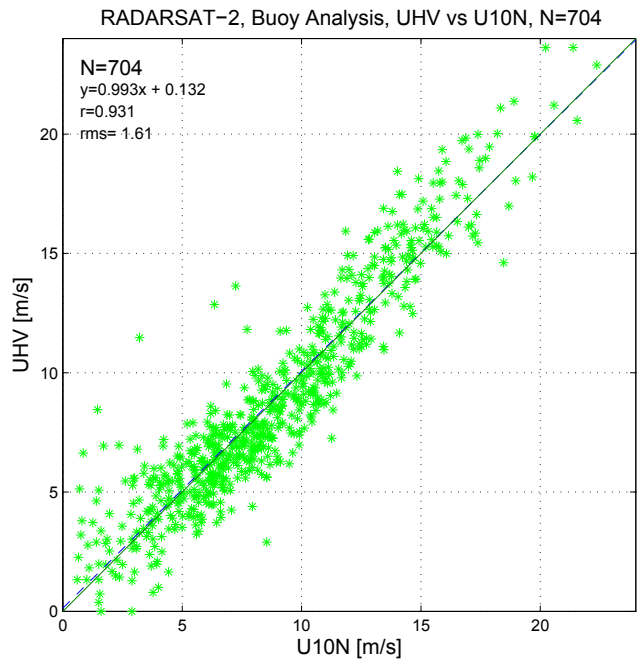


Figure 71: Scatter plot of HV-derived wind speed vs. buoy wind speed using Equation (10).

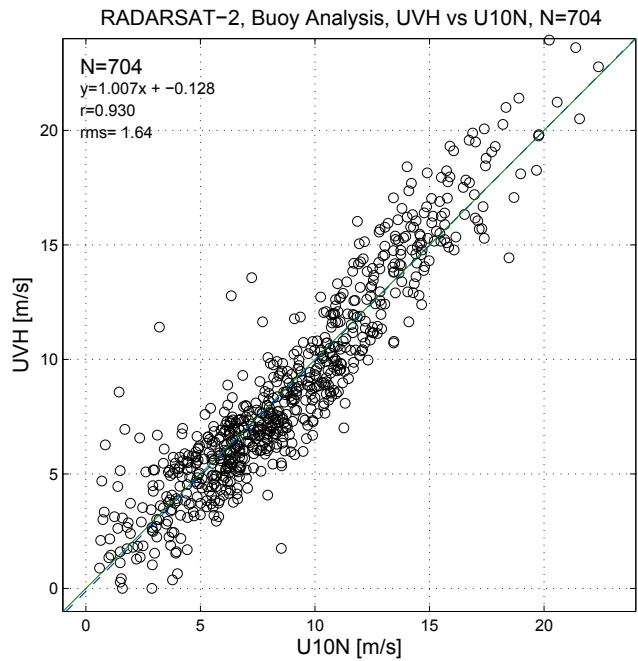
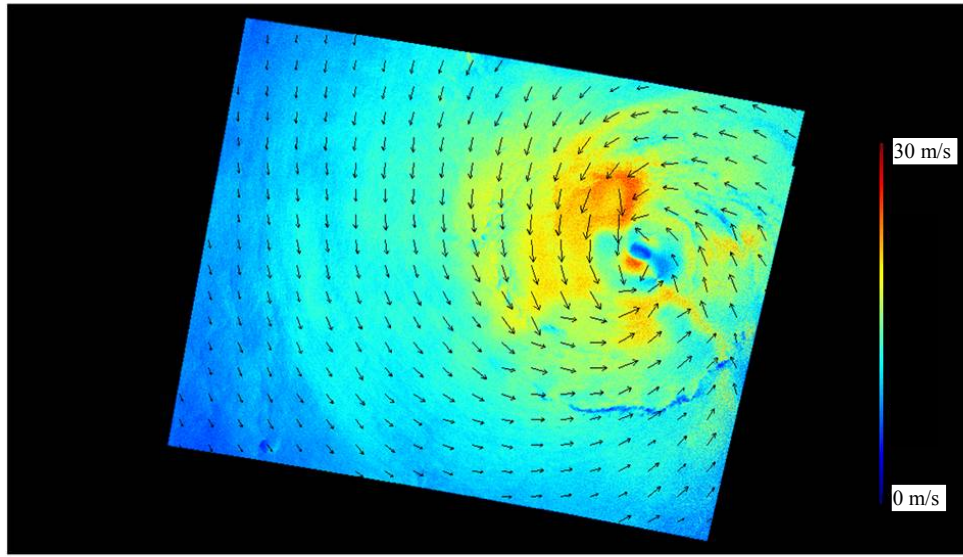


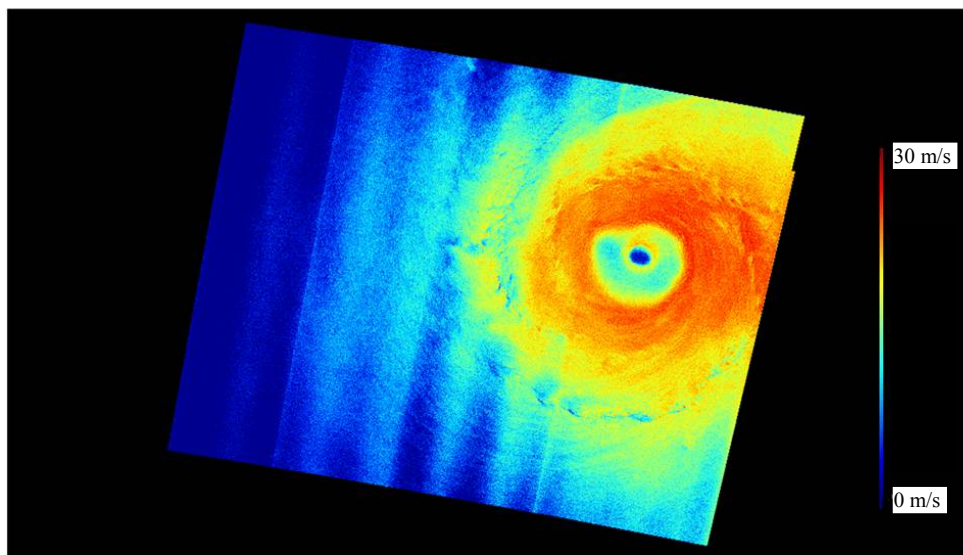
Figure 72: Scatter plot of VH-derived wind speed vs. buoy wind speed using Equation (10).



UNCLASSIFIED

Canada

*Figure 73: R-2 SCWA VV-polarization derived wind speed for Hurricane Bertha.*



UNCLASSIFIED

Canada

*Figure 74: R-2 SCWA VH-polarization derived wind speed for Hurricane Bertha.*

### **6.3.3 Summary**

Based upon R-2 FQ images acquired over operational marine meteorology buoys, a database of SAR observations have been compiled as a function of polarization and wind speed. This database has been used to derive a new C-band co-polarization ratio that is independent of wind speed and wind direction, as well as a new and very simple C-band cross-polarization model for deriving wind speed from SAR that is independent of wind direction and incidence angle. The latter model can be extended to beam modes other than FQ by requiring that the wind speed be sufficiently high such that the cross-polarization signal level is above the actual noise floor of the mode in question.

Observed RMS errors for SAR-retrieved wind speeds using these new model functions are similar for VV and HH at around 2.3 m/s, but improve to better than 2 m/s for cross-polarization.

It is interesting to note that, unlike co-polarization, the cross-polarization backscatter data considered do not show evidence of saturation with increasing wind speed. This suggests that cross-polarization could be suitable for observation of extreme weather events such as hurricanes, polar lows, and cold air outbreaks.

## **6.4 Mode recommendations**

### **6.4.1 RADARSAT-2**

It is apparent that FQ mode data are excellent for ocean wind retrieval. Unfortunately, they suffer from a rather narrow swath. To get the broader area coverage, SCN or SCW modes should be used, preferably acquired with dual polarization, specifically VV+VH. In this way, the cross-polarization channel could be used to estimate the wind speed in a trivial manner, provided the wind speed is sufficiently high. Furthermore, with the two channels available, the cross-polarization-derived wind speed could be used in connection with the observed co-polarization backscatter to derive the wind direction (with four ambiguities).

For lower wind speeds, it is necessary to rely on the co-polarization channel, meaning that an external source of wind direction is required. This could be from a scatterometer or from a numerical weather prediction model.

Of course, HH polarization is also viable and use of the new co-polarization ratio presented here is recommended.

The MSSR OSVN mode should also be suitable for wind speed estimation.

Wind field estimation from SAR imagery is a good example of a dual use application. Any ocean imagery with sufficiently high clutter to noise ratio can in principle be used to estimate the wind speed.

### **6.4.2 RCM**

Similar to R-2, virtually any RCM mode may be used to estimate marine winds, with the Low Resolution mode providing the largest swath coverage and the Low Noise mode providing the best cross-polarization performance. Again, dual polarization acquisitions (VV + VH) are recommended, but any dual polarization mode should work well.

## **6.5 Future analysis**

The database of FQ imagery over operational buoys is still being acquired. The statistics are not expected to change, of course, but the observations continue in order to try and obtain cases with higher wind speed. The highest wind speed represented in the current database is only around 23 m/s. In this vein, R-2 images of hurricanes acquired through the CSA's Hurricane Watch activity could provide insight to the performance of cross polarization wind speed retrieval for extreme weather events.

With the advent of RCM, CP mode imagery will be available. This mode should be studied for wind speed estimation.

## **7 Oil spill detection**

---

### **7.1 Background**

Large scale oil spill disasters such as the Exxon Valdez oil spill in Prince William Sound in 1989 and the Deepwater Horizon oil rig explosion in the Gulf of Mexico in 2010 are accentuated in the media for their massive discharges and resulting ecological damage. However, ships regularly produce oily bilge wastes which are often illegally discharged to avoid costly disposal fees at port. Although these regular releases are small in amount, it has been estimated that the amount of illegal discharges collectively exceed the amounts released from major accidents [13], [17], [48]. These illegal discharges have a severe impact on Canadian marine ecosystems, particularly seabirds. The released oil forms a thin layer on the surface of the water, where it is either absorbed by seabirds' feathers leading to hypothermia for the birds, or through ingestion leading to fatal effects on internal organs [53]. Areas of intense shipping activity that overlap high concentrations of seabirds result in increased seabird mortality. An example of this is the northwest Atlantic region around Newfoundland, which has disproportionately high seabird mortality rates from illegal oil pollution when compared to the rest of the world [64]. A conservative estimate on seabird mortality in Atlantic Canada places the figure at 300,000 deaths annually [54].

Along with its mandate to monitor coastal ice conditions, CIS is also responsible for the daily monitoring of Canadian coastal waters for the presence of oil-based pollution and potential oil sources (*e.g.*, ships and platforms). The ISTOP program uses R-2 HH data to vector pollution surveillance assets to areas where oil discharges/spills are suspected in support of enforcement and/or cleanup efforts. Both automated and visual detection techniques are used to identify potential pollution and source targets. Illegal oil discharges are not unique to Canadian maritime zones. In Europe, the European Marine Safety Agency operates a similar SAR-based service called CleanSeaNet which uses both RADARSAT and ASAR data to detect oil slicks.

The presence of oil dampens Bragg scale ocean waves, effectively lowering the backscatter of oil relative to the brighter adjacent oil-free ocean background [1], [2]. Remote sensing using SAR satellites for oil spill detection has been well documented as the preferred method over optical sensors due to its wide coverage and this ability to detect oil spills against an ocean background, regardless of time of day or amount of cloud cover, *e.g.*, [50].

Oil slick detection in SAR imagery primarily requires a sufficient level of contrast between the backscatter of slicks and the typically dynamic background ocean. This level of contrast depends on a variety of systematic and environmental factors:

- SAR viewing geometry (incidence and relative azimuth angles);
- SAR polarization;
- SAR NESZ;
- SAR effective spatial resolution;
- Wind speed and direction as it affects surface roughness; and
- Properties of the oil slick (*e.g.* viscosity).

Look-alikes in SAR imagery can include, but are not limited to, low wind areas, biogenic slicks, algae blooms, rain cells, fish oil, run-off waters, grease ice, controlled chemical spills and drilling fluids from oil rigs [50]. Even if sufficient contrast exists to identify a slick-like feature within a SAR image, the detection process still requires a means to ensure that the target is indeed oil and not one of the many look-alike features prevalent in the maritime domain.

Operational oil spill monitoring services typically rely on wide swath SAR modes (*e.g.*, ScanSAR) to detect potential oil targets over large coastal areas. Currently RADARSAT-1 HH mode provides ISTOP with acceptable performance for both oil slick and ship detection. The concurrent detection of ships in the vicinity of discharged oil is a program objective. R-2 offers the ability to collect these data in single channel (HH or HV or VV or VH) or dual channel (HH+HV or VV+VH) polarizations. Of specific interest here is the oil detection performance of R-2 VV mode compared to that of HH, given that HH is the current ISTOP mode of choice.

Using natural oil seeps as a proxy for spilled oil, the following evaluates the detectability of oil slicks as a function of polarization (HH vs. VV). Wind conditions (*i.e.*, sea state) and observation geometry are also considered.

## 7.2 Data and methods

It is difficult to obtain imagery with multiple polarizations over illegal oil discharges as they randomly occur. Therefore, this study focused on the Coal Oil Point Seep Field located near Santa Barbara, California (Figure 75), where oil is naturally released into the ocean. Hornafius et al. [21] have documented that the Coal Oil Point seep field is  $18 \text{ km}^2$  and releases hydrocarbon gases at an emission rate of  $1.7 \pm 0.3 \times 10^5 \text{ m}^3/\text{day}$  and oil at  $1.6 \pm 0.2 \times 10^4 \text{ L/day}$  (100 barrels/day). Estimated methane releases have been documented at an emission rate of  $80 \pm 12 \text{ tons/day}$ , with very little change in the location of the oil seeps themselves over time. The oil and gas releases in this region are visible on the sea surface and have been well documented [44], [49], allowing for the remote sensing of a constant source of oil at a fixed location. The outlines of the oil seeps were identified using the sonar return amplitude map of the seep bubble plumes surveyed in 2005 [26]. The sonar returns were used as an independent means of locating the oil seeps within the imagery. The seeps are spatially continuous at scales larger than nine metres [62].

For this study, the seeps were grouped into three areas: Trilogy Seeps (including Shane Seep and Horseshoe Seep), Seep Tent Seeps, and La Goleta Seeps (including the Patch Seep Area). The sonar return amplitude maps indicate the underwater sources of the seeps and not the surface extents. Between February 2009 and March 2010, a total of 101 R-2 FQ polarization (HH, HV, VV, VH) SLC images were acquired of the seep field at different incidence angles (Table 19). The images were processed with a mixed output LUT and a terrain height of zero. IA Pro was used to convert the acquired images to absolute backscatter. The data were then imported into a GIS for sampling and analysis.

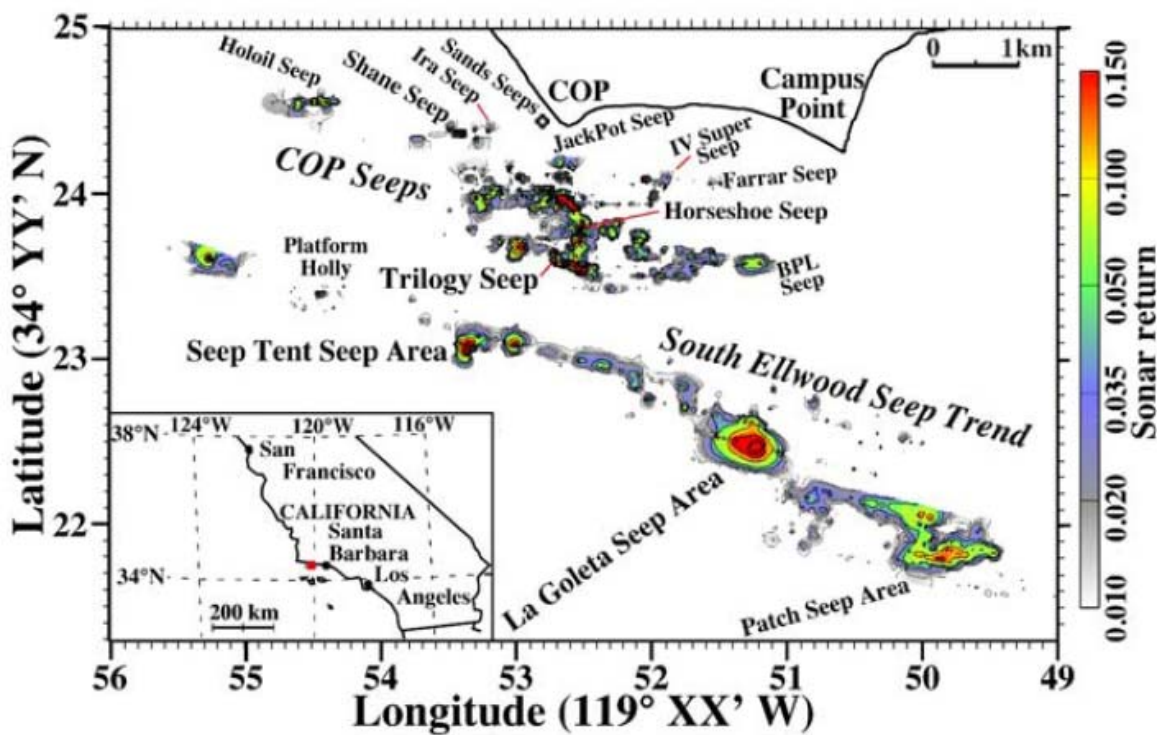
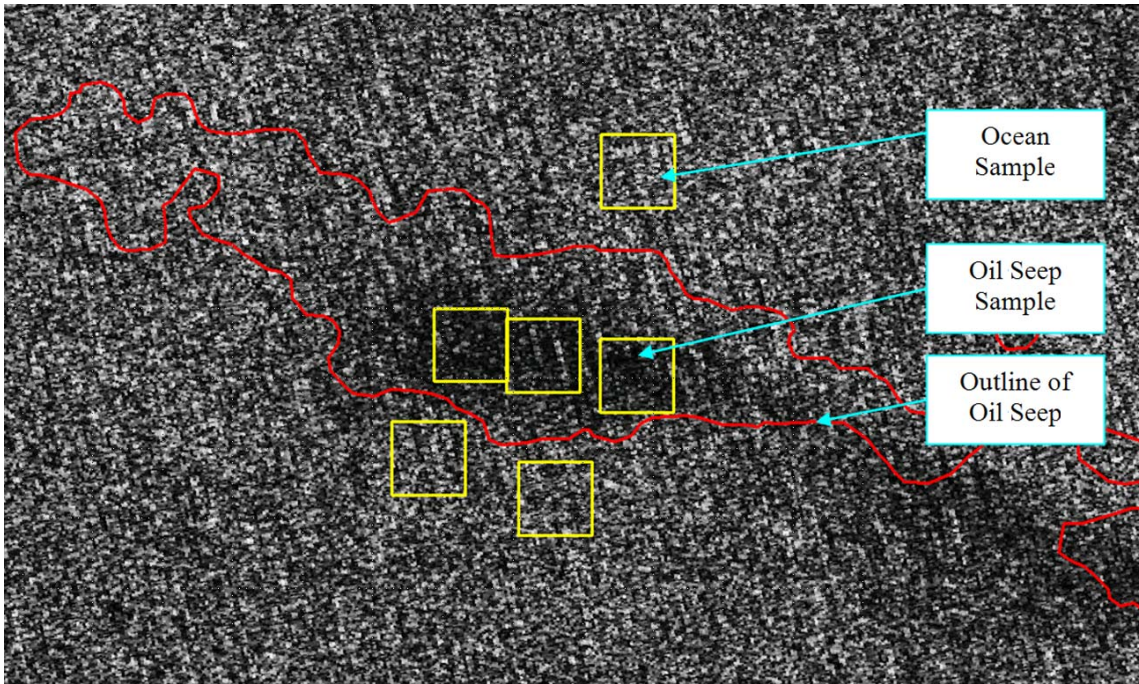


Figure 75: Sonar return amplitude map of the Coal Oil Point Seep Field used in this study to determine the location of the oil seeps [26].

Table 19: Number of images collected for each oil seep.

Oil Seep	Total Images	Image Distribution by Incidence Angle		
		20° to 30°	30° to 40°	40° to 50°
La Goleta	101	37	64	0
Seep Tent	95	37	58	0
Trilogy	97	37	60	0
Total	293	111	182	0



*Figure 76: An example of the sampling method used on the oil seep and the surrounding ocean clutter background.*

Based upon the sonar amplitude returns, the seep areas to be sampled were delineated with polygons. Although the sonar amplitude returns were used to map the locations of the oil seeps, a perfectly direct relationship between the oil seep outline and the shape of the dark features found in the SAR imagery did not exist (e.g., see Figure 76). Instead, the dark features in the SAR imagery either: extended beyond the known boundaries of the oil seeps, matched the boundaries, or existed within the boundaries. Any dark features within the boundaries of the polygons were assumed to be oil. Dark features outside of the polygon boundaries were assumed to have an unknown source and were not sampled. Oil seep samples included at least 650 pixels. In order to determine the detectability of each feature, each sample taken of the oil seeps was matched with a corresponding sample of the adjacent ocean at the nearest location free of any dark features. For each HH and VV oil and ocean sample, mean absolute backscatter in power, mean incidence angle, and level of local NESZ were calculated. These statistics were then grouped by seep area.

The wind speed for each scene, accurate to  $\pm 2$  m/s, was estimated using the cross-polarization ocean backscatter (see Section 6). Estimated wind speeds compared well to wind speed observations from the nearest local buoy, which was approximately 12 kilometres away from the seep locations.

The detectability of the oil seeps were evaluated via the contrast ratio:

$$\text{Contrast Ratio} = \sigma^o_{\text{Ocean}} - \sigma^o_{\text{Oil}} \quad (11)$$

where the backscatters are expressed in dB. Higher contrast ratios indicate better oil slick detectability with respect to the surrounding ocean background. The contrast ratio was calculated for both HH and VV polarizations.

To determine the difference in detectability of oil seeps against an ocean background between HH and VV polarizations, a difference in contrast ratios was also calculated:

$$\text{Difference in Contrast Ratios} = (\text{Contrast Ratio})_{\text{VV}} - (\text{Contrast Ratio})_{\text{HH}} \quad (12)$$

A greater positive difference in contrast ratios indicates that VV performed better than HH, and a greater negative difference in contrast ratios indicates the opposite. A difference in contrast ratios near zero would indicate that there was little difference between polarizations in terms of detectability of oil slicks. The difference in contrast ratios was then grouped according to local wind speeds and plotted against the incidence angle.

Finally, as previously mentioned, the detectability of oil within SCW imagery is of primary interest in this analysis. However, FQ imagery has a significantly lower noise floor than SCW imagery, which allows for potentially higher contrast ratios between oil and ocean samples. To address this, samples with backscatters below the SCW NESZ were increased to the SCW NESZ. This ensures that the results reflect the anticipated contrast ratios in SCW imagery.

## 7.3 Results and analysis

### 7.3.1 Oil vs. ocean backscatter

Oil backscatter values were similar between polarizations and showed a clear relationship between incidence angle and wind speed (HH in Figure 77 and Table 20, VV in Figure 78 and Table 21). As the wind speeds increased, the oil backscatter increased in both HH and VV. As the incidence angle increased, the oil backscatter decreased and showed less sensitivity to wind speed. This suggests that the oil is also roughened by local winds resulting, in backscatter above the instrument noise floor.

At lower wind speeds (0 to 4 m/s), the oil backscatter was less than -15 dB and near the SCW NESZ in the mid to far range portion of the swath. At higher wind speeds (over 8 m/s), the oil behaves more like the background ocean, with backscatter increasing sharply with decreasing incidence angle.

The difference in oil backscatter values between VV and HH became greater as the incidence angle increased (Figure 79).

As expected, ocean backscatter values for both HH and VV showed a clear relationship between wind speed, incidence angle and backscatter value. Ocean backscatter values in VV were consistently higher than in HH. Ocean clutter in HH and VV behaved similarly at all wind speeds across all incidence angles. As the wind speed increased, ocean clutter increased. As incidence angle increased, ocean clutter decreased (see Figure 80 and Figure 81).

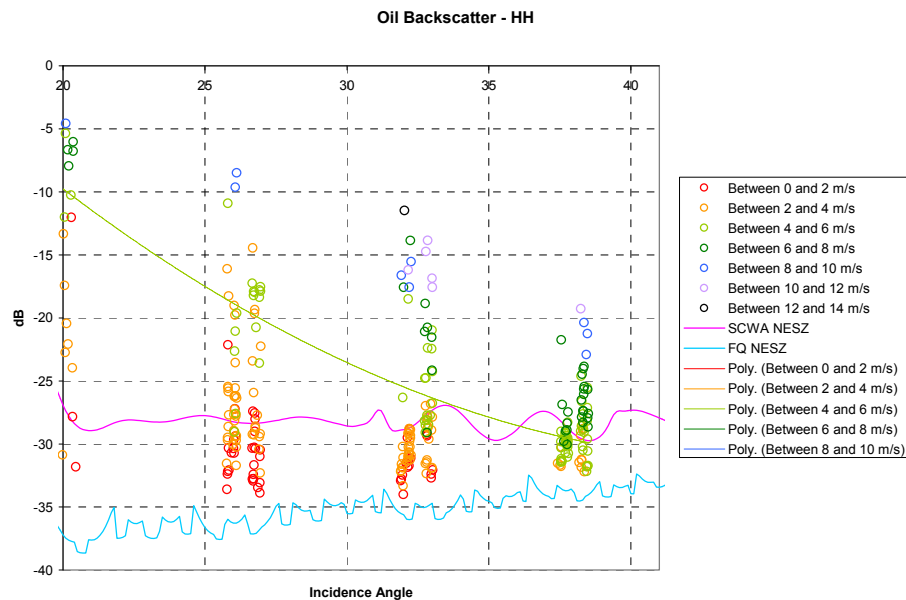


Figure 77: HH oil backscatter as a function of wind speed and incidence angle.

Table 20: HH oil backscatter arranged by wind speed and incidence angle.

HH	Incidence Angle [°]			
	20 to 25	25 to 30	30 to 35	35 to 40
Wind Speed [m/s]				
<b>0 to 2</b>	-15.90	-25.93	-28.12	-
<b>2 to 4</b>	-16.95	-23.88	-27.81	-28.81
<b>4 to 6</b>	-8.31	-18.16	-24.37	-28.21
<b>6 to 8</b>	-6.82	-10.47	-19.28	-26.24
<b>8 to 10</b>	-4.44	-9.13	-17.76	-22.32
<b>10 to 12</b>	-	-	-16.08	-20.13
<b>12 to 14</b>	-	-	-11.50	-

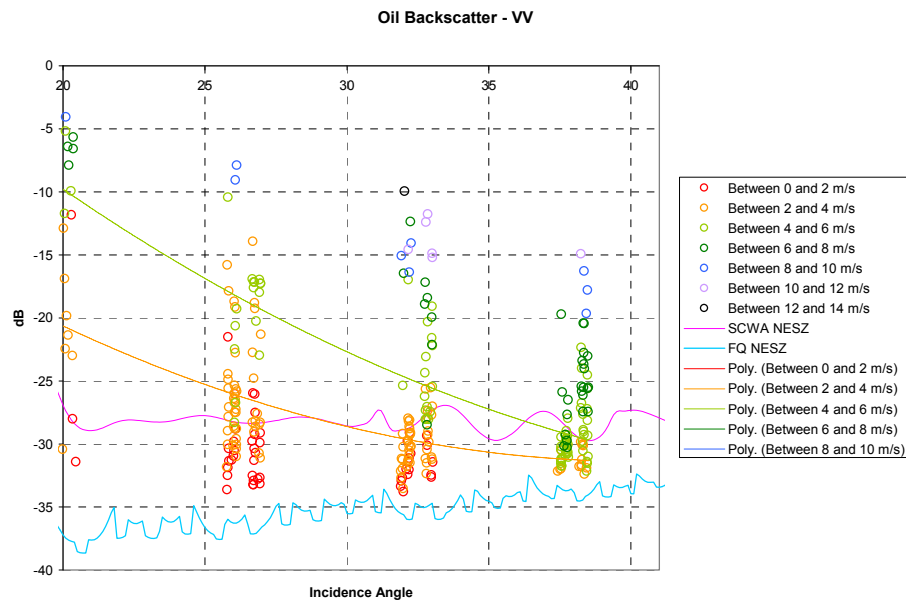
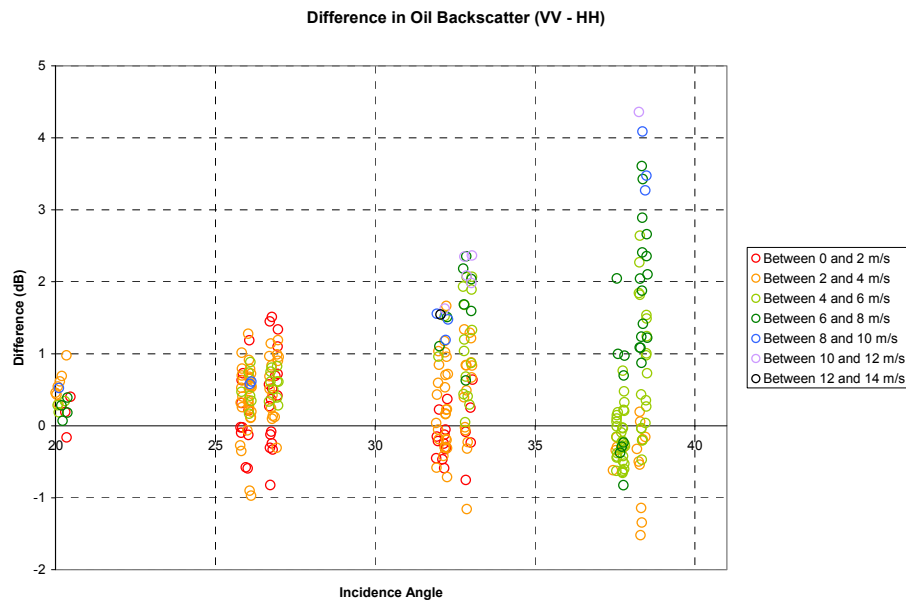


Figure 78: VV oil backscatter as a function of wind speed and incidence angle.

Table 21: VV oil backscatter arranged by wind speed and incidence angle.

VV	Incidence Angle [°]			
	20 to 25	25 to 30	30 to 35	35 to 40
Wind Speed [m/s]				
<b>0 to 2</b>	-15.76	-25.66	-28.13	-
<b>2 to 4</b>	-16.53	-23.48	-27.46	-28.93
<b>4 to 6</b>	-8.10	-17.64	-23.05	-27.56
<b>6 to 8</b>	-6.55	-10.01	-17.82	-24.38
<b>8 to 10</b>	-3.96	-8.47	-16.16	-18.86
<b>10 to 12</b>	-	-	-14.03	-16.11
<b>12 to 14</b>	-	-	-9.96	-



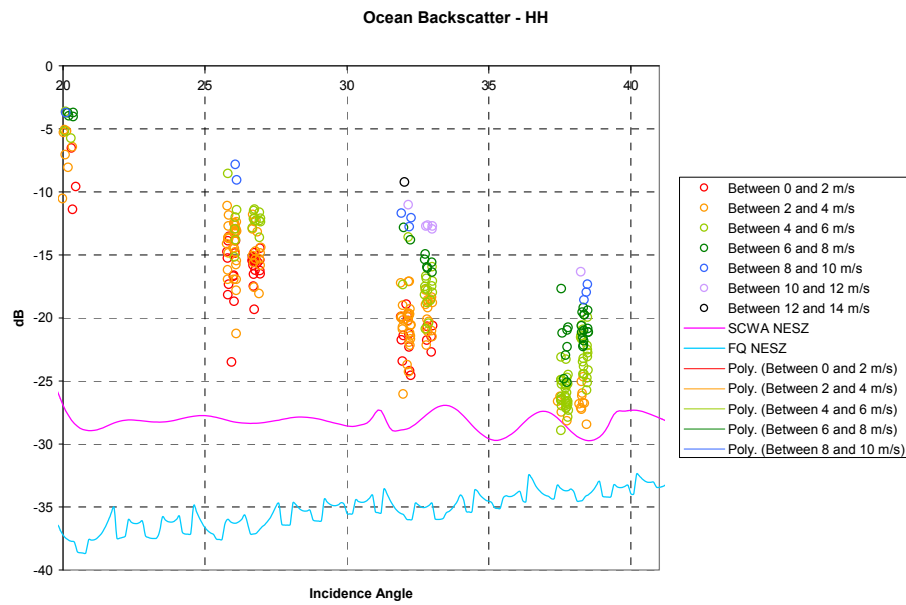
*Figure 79: Difference in oil backscatter values (VV – HH).*

Figure 82 shows the difference in ocean backscatter values (VV – HH). As most of the difference was greater than zero, ocean backscatter values were not the same in HH as they were in VV. The difference between HH and VV for ocean backscatter values steadily increased with increasing incidence angle, showing that VV ocean backscatter values increased more than HH ocean backscatter values. Differences in ocean backscatter between polarizations were found to be statistically significant ( $p < 0.00001$ ).

Oil slick backscatter values between HH and VV were not statistically significant ( $p > 0.05$ ) whereas ocean clutter differences between HH and VV were statistically significant ( $p < 0.00001$ ); therefore, VV ocean backscatter values were higher than HH while oil slick backscatter values remained the same, regardless of polarization.

The optimal wind speeds for oil slick detection is thought to be between 3 and 12 m/s [16], [18], [25], [27]. At higher wind speeds, the waves become too rough and the oil breaks down naturally from the surface roughness and gets mixed downwards into the water column, causing lower contrast between the oil and the ocean. On the other hand, at low wind speeds, the waves are too calm and there is not enough Bragg scattering to cause differences in backscatter between the oil and the ocean.

Multiple regression analysis of backscatter (Table 22 and Table 23) showed the extent that the variation in results could be explained by wind speed or incidence angle. Analysis of variance in oil slick backscatter values showed that wind and incidence angle accounted for 72% to 74% of the variation, respectively. The wind speed coefficient was consistently larger than the incidence angle coefficient, showing that wind speed has a larger impact on backscatter than incidence angle. Therefore, ordering imagery for oil slick detection based on wind speed will yield a larger impact on contrast ratios than ordering based on incidence angle.



*Figure 80: HH ocean backscatter for all oil seeps grouped by estimated wind speed.*

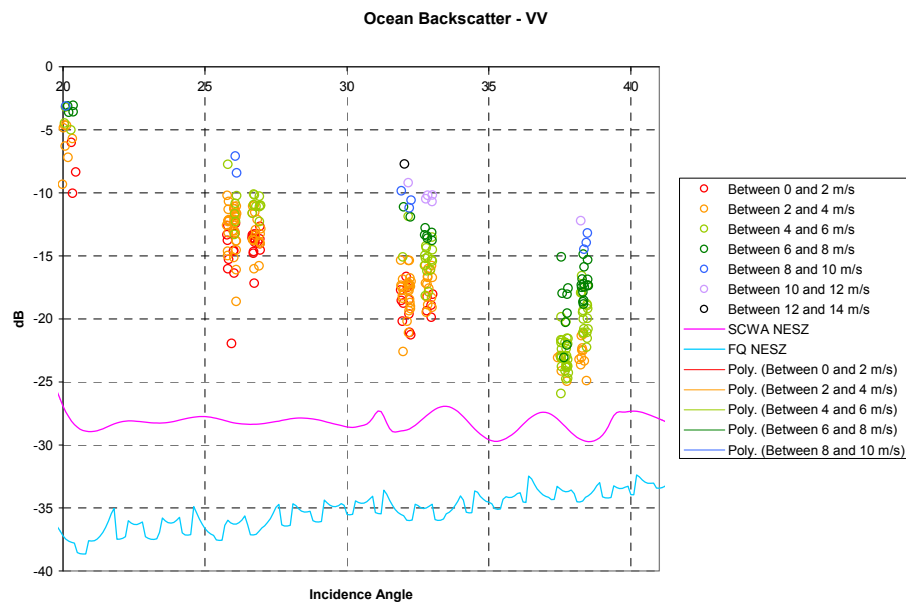


*Figure 81: VV ocean backscatter for all oil seeps grouped by estimated wind speed.*

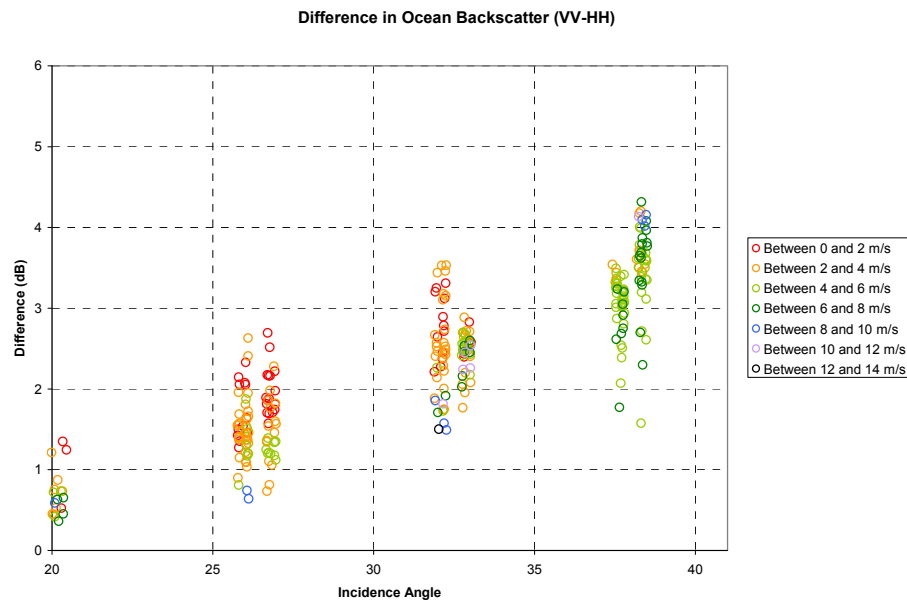


Figure 82: The difference in ocean backscatter values (VV – HH).

Table 22: Multiple regression of backscatter (dependent variable) against wind speed and incidence angle (independent variables).

Parameter	Adjusted $R^2$	Wind Speed Coefficient ( $U$ )	Incidence Angle Coefficient ( $\theta$ )	Intercept Coefficient	Fit
Oil Backscatter (HH)	0.72804	2.19642	-0.76202	-11.76242	$y = -11.76 + 2.20U - 0.76\theta$
Oil Backscatter (VV)	0.74513	2.41815	-0.77916	-11.59293	$y = -11.59 + 2.42U - 0.78\theta$
Ocean Backscatter (HH)	0.89135	1.15684	-1.05183	10.18575	$y = 10.19 + 1.16U - 1.05\theta$
Ocean Backscatter (VV)	0.86111	1.08063	-0.89125	7.76637	$y = 7.77 + 1.08U - 0.89\theta$

*Table 23: Multiple regression of contrast ratio (dependent variable) against wind speed and incidence angle (independent variables).*

Parameter	Adjusted $R^2$	Wind Speed Coefficient ( $U$ )	Incidence Angle Coefficient ( $\theta$ )	Intercept Coefficient	Fit
Oil Backscatter (HH)	0.54148	-1.03523	-0.29117	21.97684	$y = 21.98 - 1.04U - 0.29\theta$
Oil Backscatter (VV)	0.56035	-1.33333	-0.11339	19.38686	$y = 19.39 - 1.33U - 0.11\theta$
Ocean Backscatter (HH)	0.59397	-0.29810	0.17778	-2.58997	$y = -2.59 - 0.3U + 0.18\theta$
Ocean Backscatter (VV)	0.54148	-1.03523	-0.29117	21.97684	$y = 21.98 - 1.04U - 0.29\theta$

Wind speed and incidence angle were well correlated with ocean clutter in both HH and VV, accounting for 89% and 86% of the variation, respectively. The wind speed coefficient and incidence angle coefficient were both nearly at one, indicating a nearly linear relationship between wind, incidence angle, and ocean backscatter values.

Wind speed and incidence angle were also well correlated with oil backscatter values in HH and VV (72% and 74% of the variation, respectively), although they explained less of the variation than ocean backscatter. For oil, the wind speed coefficient was greater than two in both polarizations, and the incidence angle coefficient was close to 0.8. Therefore, wind speed had at least twice the impact on oil backscatter values in both polarizations than the incidence angle.

Contrast ratios between the oil and ocean background decreased as the incidence angle increased for both polarizations as the signal drops off. However, the contrast ratio decreased more rapidly in HH than VV. Therefore, at higher incidence angles, VV provided better contrast between the oil and the ocean background. Wind speed and incidence angle accounts for between 54% and 56% of the variation in contrast ratios and 59% of the variation in the difference in contrast ratios between VV and HH. Again, wind speed had a greater effect on the contrast than the incidence angle.

A comparison of the backscatter of the three oil seeps (while taking wind speed into consideration) showed they were different ( $p < 0.00001$ ), which shows that composition of the oil slick itself will affect backscatter values. It is known that the seeps vary in gas composition by 10% to 20% [9]. Composition of the oil seeps affecting viscosity are also important to note as they can interact differently with the wind, thereby affecting backscatter values. Thicker oil slicks will have lower backscatter values, take more time to break down, and require increased wind speeds before a change can be detected in the backscatter value. Although the means (and

compositions) of the three seeps were different, the difference was small and would not affect ISTOP requirements as all of them would be detectable in satellite SAR imagery.

### 7.3.2 Contrast ratios between ocean and oil

As described, HH and VV contrast ratios were calculated using the oil and ocean backscatter values after adjusting for the SCW noise floor. Contrast ratios in HH ranged from 0.05 dB at high wind speeds and 18.65 dB at low wind speeds. As wind speeds increased, the contrast ratio—and therefore, the detectability of oil—decreased. Contrast ratios also decreased as incidence angle increased, although the oil seeps were detectable in most scenarios using the HH polarization only.

Contrast ratios could be divided into three levels of detectability: easy, moderate, and difficult. Easy detectability consists of images where the contrast ratio between oil and ocean is greater than nine decibels. Moderate detectability falls within the range of five to nine decibels, and difficult consists of contrast ratios below five decibels. Figure 83 through Figure 85 show example images of the three levels of detectability.

Contrast ratios in HH and VV ranged from difficult detectability to easy detectability (HH in Figure 86 and Table 24, VV in Figure 87 and Table 25). The degree of detectability was dependent on wind speed and incidence angle.

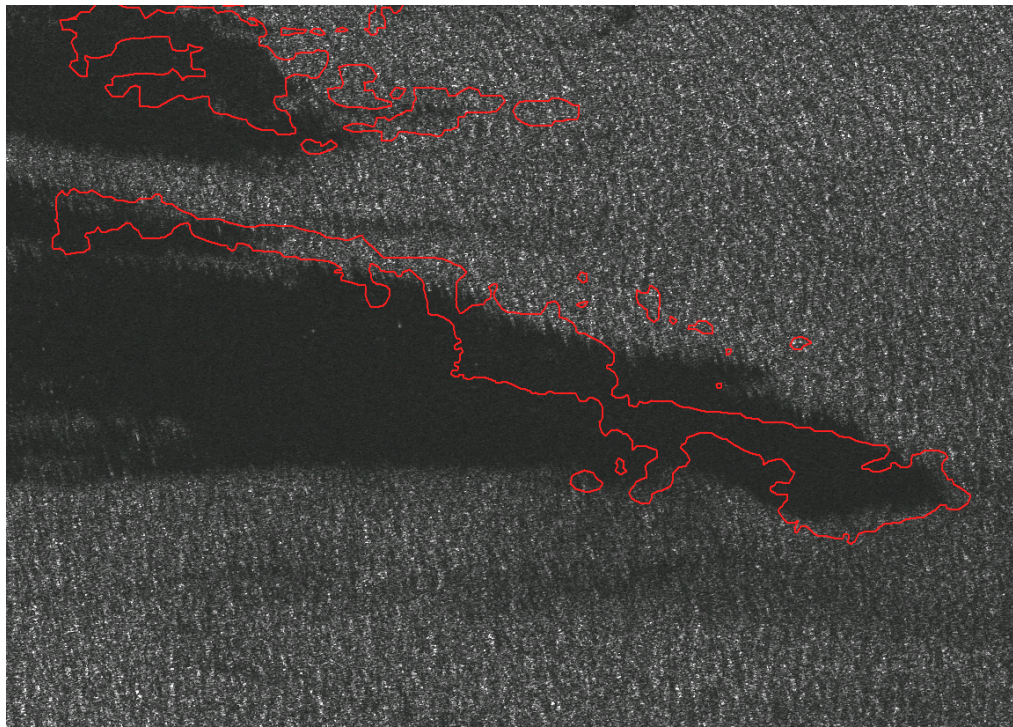


Figure 83: Easy detectability: La Goleta Seeps, 2009-11-20 (contrast ratio of 11.8 dB in HH).  
The outline of the seep is shown in red.

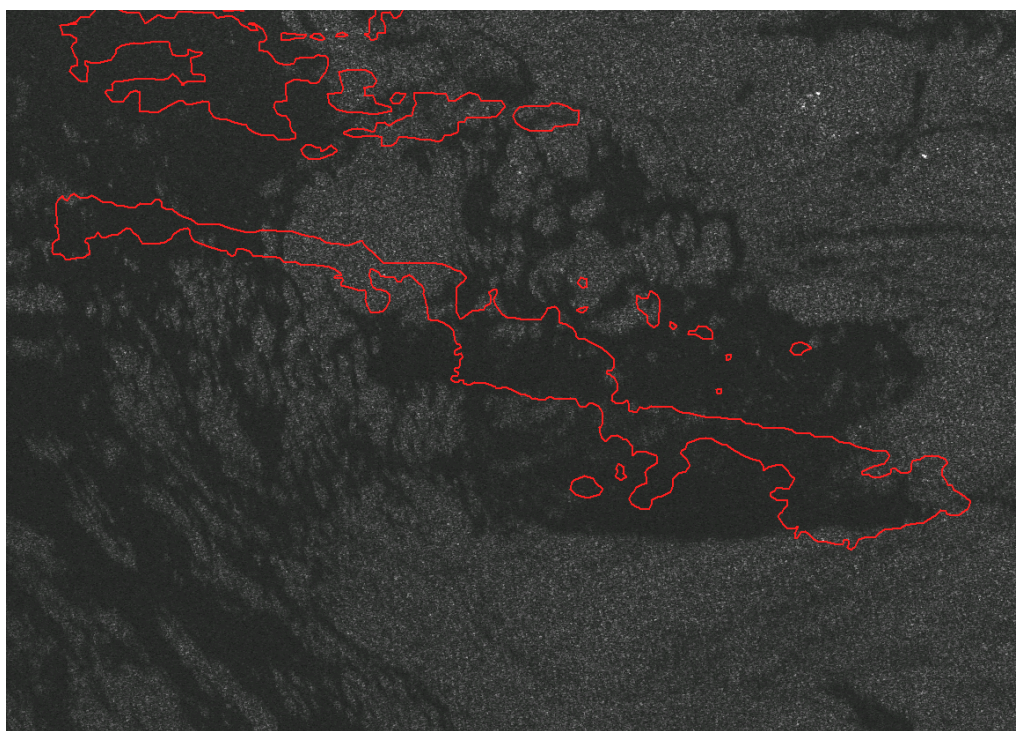


Figure 84: Moderate detectability: *La Goleta Seeps*, 2009-09-02 (contrast ratio of 6.3 dB HH).

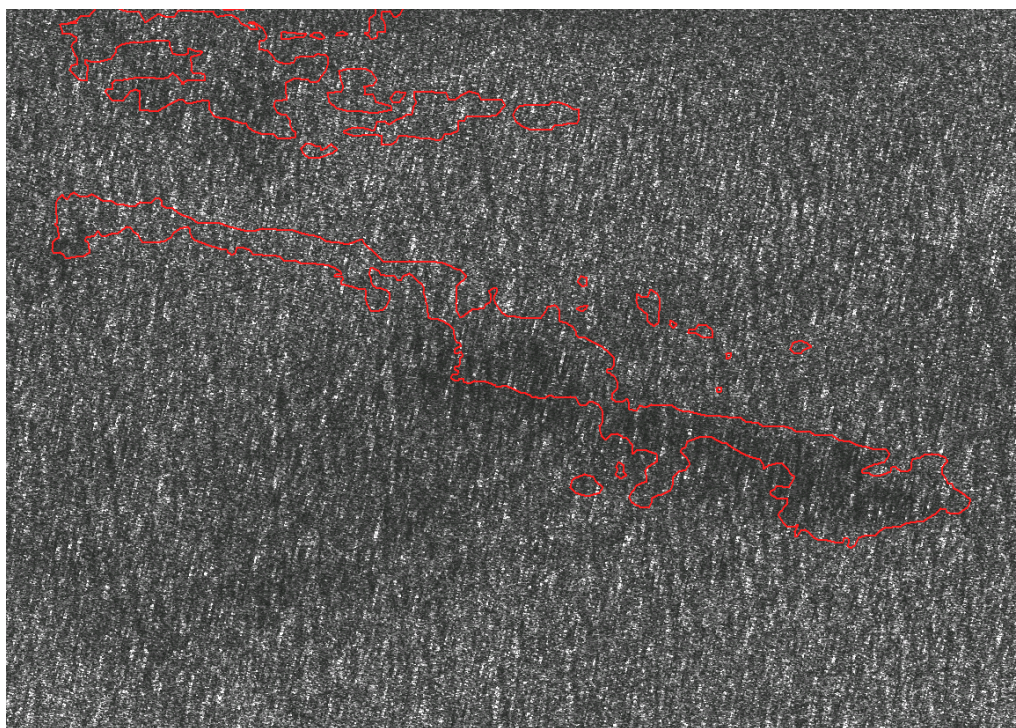
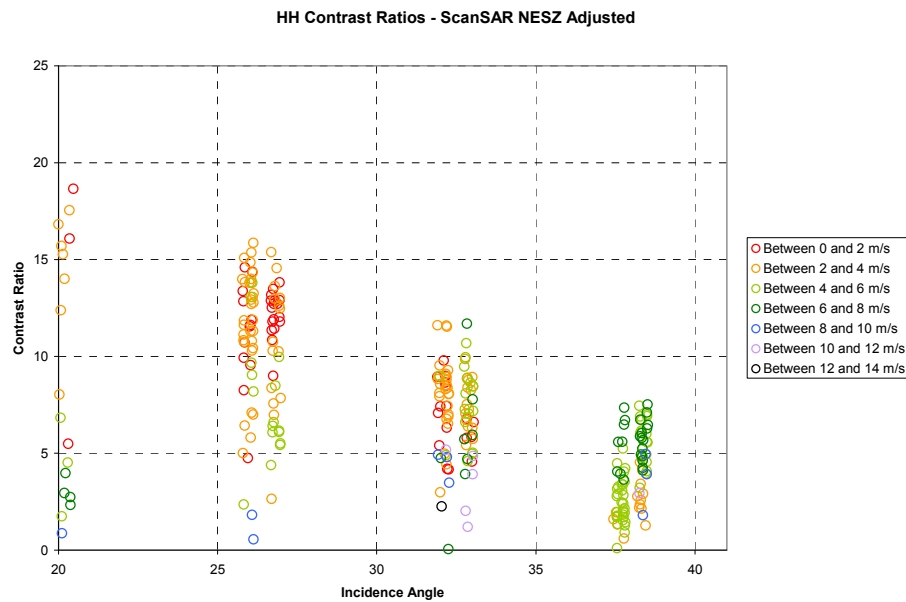


Figure 85: Difficult detectability: *La Goleta Seeps*, 2009-10-27 (contrast ratio of 2.4 dB in HH).



*Figure 86: Contrast ratios between the oil slick and ocean clutter in HH adjusted relative to the SCW noise floor.*

*Table 24: Mean contrast ratios between oil and ocean in the HH channel, arranged by wind speed and incidence angle.*

HH	Incidence Angle [°]			
	20 to 25	25 to 30	30 to 35	35 to 40
Wind Speed [m/s]				
<b>0 to 2</b>	7.84	11.92	10.69	-
<b>2 to 4</b>	10.40	10.10	9.86	4.60
<b>4 to 6</b>	3.57	6.01	7.10	5.25
<b>6 to 8</b>	3.03	2.08	4.86	5.49
<b>8 to 10</b>	0.71	1.05	5.05	4.29
<b>10 to 12</b>	-	-	3.69	3.52
<b>12 to 14</b>	-	-	2.26	-

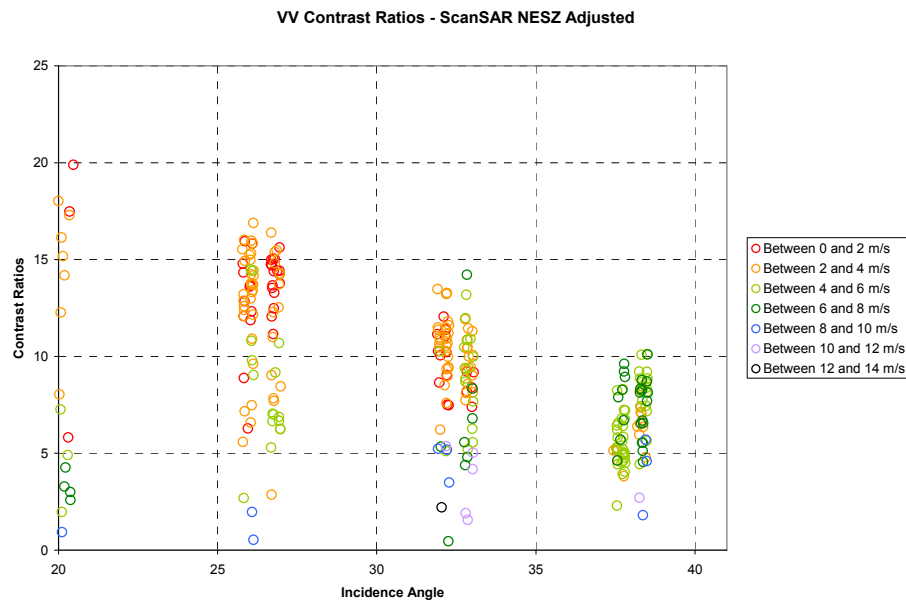


*Figure 87: Contrast ratios between the oil slick and ocean clutter in VV adjusted relative to the SCW noise floor.*

*Table 25: Mean contrast ratios between oil and ocean in the VV channel, arranged by wind speed and incidence angle.*

VV	Incidence Angle [°]			
	20 to 25	25 to 30	30 to 35	35 to 40
Wind Speed [m/s]				
<b>0 to 2</b>	8.51	13.08	13.23	-
<b>2 to 4</b>	10.64	11.07	11.62	8.45
<b>4 to 6</b>	3.90	6.70	8.05	7.69
<b>6 to 8</b>	3.31	2.40	5.50	6.95
<b>8 to 10</b>	0.83	1.06	5.40	4.90
<b>10 to 12</b>	-	-	3.88	3.68
<b>12 to 14</b>	-	-	2.21	-

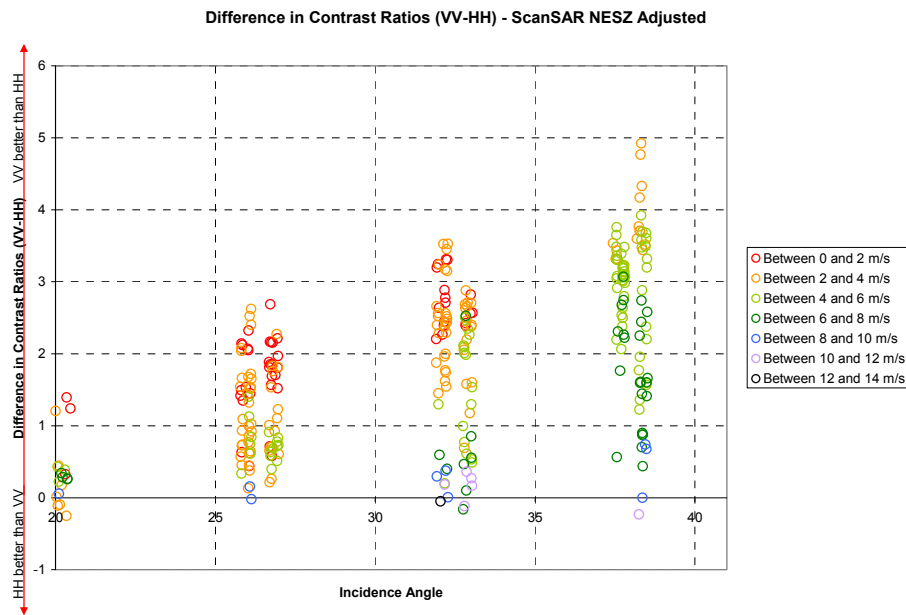


*Figure 88: Difference in contrast ratios between VV and HH adjusted relative to the SCW noise floor.*

### 7.3.3 Difference in contrast ratios between HH and VV

With superior contrast between oil and ocean, results show that VV consistently performed better than HH in essentially all sea states and positions in the image swath. As shown in Figure 88, the improvement in performance was greatest at higher incidence angles and low wind speeds. In cases with high wind speeds ( $> 10 \text{ m/s}$ ), there is effectively no difference between HH and VV performance.

Table 26 shows the estimated gain or loss in contrast ratios by using VV over HH, where  $y$  is predicted increase in contrast of VV over HH (expressed in dB). Table 27 summarizes the mean difference in contrast ratios between VV and HH, grouped by wind speed and incidence angle. The difference in contrast ratios shows that VV performed better than HH for oil slick detectability, especially at higher incidence angles and lower wind speeds.

Table 26: Predicted increase in contrast ratio ( $y$ ) for oil slick detection when using VV over HH.

Wind Speed [m/s]	Predicted increase in contrast between VV and HH	$R^2$
<b>0 to 2</b>	$y = 0.0031\theta^2 - 0.0183\theta + 0.0002$	0.8097
<b>2 to 4</b>	$y = 0.0042 \theta^2 - 0.0488\theta - 0.4365$	0.7201
<b>4 to 6</b>	$y = 0.0086 \theta^2 - 0.3659\theta + 4.3005$	0.6778
<b>6 to 8</b>	$y = 0.0081 \theta^2 - 0.3906\theta + 4.864$	0.3706
<b>8 to 10</b>	$y = 0.0015 \theta^2 - 0.0657\theta + 0.759$	0.3754
<b>10 to 12</b>	Negligible difference (< 0.25 dB) between HH and VV	n/a
<b>Over 12</b>	Wind roughened waves too high; slick detection unlikely	n/a

Table 27: Mean difference of contrast ratios between VV and HH, arranged by wind speed and incidence angle

VV-HH	Incidence Angle [°]			
Wind Speed [m/s]	20 to 25	25 to 30	30 to 35	35 to 40
<b>0 to 2</b>	0.67	1.16	2.54	-
<b>2 to 4</b>	0.24	0.96	1.76	3.85
<b>4 to 6</b>	0.33	0.68	0.94	2.45
<b>6 to 8</b>	0.27	0.32	0.64	1.46
<b>8 to 10</b>	0.12	0.01	0.35	0.60
<b>10 to 12</b>	-	-	0.20	0.16
<b>12 to 14</b>	-	-	-0.05	-

## 7.4 Mode recommendations

### 7.4.1 RADARSAT-2

Based on the results presented in this study, VV consistently performed better than HH overall for almost all wind speeds and across all incidence angles. The only cases where VV did not perform better than HH was in instances of high wind speeds (e.g., above 10 m/s) where detectability is difficult in all polarizations, or in a few cases with very low incidence angles. However, any instances where VV did not perform better yielded very little difference between HH and VV—less than 0.25 dB—which would make the difference nearly negligible. VV particularly performed better than HH at higher incidence angles where contrast ratios of oil slicks in VV

were up to 5 dB higher than in HH, even after adjusting for the SCW noise floor. This allows for more usable swath across the entire range of the image.

For oil slick detection, VV is the recommended mode, although HH is an acceptable alternative when VV is not available; albeit with a reduction in usable swath. Table 27 and Figure 88 show the anticipated gain in contrast when ordering VV over HH for oil slick detection, based on wind speed and incidence angle.

#### **7.4.2 RCM**

Again, VV is recommended for oil spill detection. Dual co-polarization (*i.e.*, VV + HH) could also be of interest. CP should also be considered, but further evaluation of this mode is still required.

### **7.5 Future Analysis**

One of the main limitations of this study was the difference in composition of the oil/gas from the natural oil seeps from Coal Oil Point compared to the oily bilge waters released from ships. Differences in backscatter results between the oil seeps indicate that backscatter values are partially dependent on oil slick composition. However, as ISTOP's objectives are to identify anomalies in SAR satellite imagery that indicate the presence of possible oil slicks, any oil slick composition was useful for this study. Future work could investigate differences in backscatter values and textural differences for different oil slick compositions.

Much work has been done in discriminating between oil slicks and look-alikes in SAR satellite imagery with possible automated discrimination algorithms proposed, but it is difficult to separate the two consistently as they produce similar backscatter results [12], [22]. Therefore, until a robust algorithm can be used operationally for the ISTOP program, both potential oil slicks and look-alike features are of interest in SAR imagery with reliance on a human analyst to discern between slicks and look-alikes through other contextual information (*e.g.*, meteorology and area history). Future analysis of oil seeps for slick detection in SAR satellite imagery should incorporate look-alikes for further discrimination.

In the RCM context CP still requires performance evaluation. A subset of the FQ imagery collected for this study could form the basis for simulating the RCM CP mode.

## **8 Ocean feature detection**

---

### **8.1 Background**

Ocean features including thermal fronts, eddies and water mass boundaries are of operational importance for the CF. An R-2 based ocean feature analysis system is being implemented as part of the MetOc Halifax GRIP Project referred to as the Spaceborne Ocean Intelligence Network (SOIN) [65]. SOIN has been routinely acquiring R-2 SCNA imagery of the Gulf Stream, and using edge detection procedures and a classification scheme to identify features related to the north wall of the Gulf Stream. The polarization of choice is VV + VH, but the VV channel is used primarily since it is expected that this channel will provide the best clutter-to-noise ratio, and the best opportunity to detect the features of interest. The idea is to use R-2-derived features to fill in gaps when sea surface temperature (SST) is not available for ocean feature analysis due to cloud cover, which is frequent off Canada's east coast.

### **8.2 Data and method**

Ideally, we wanted to acquire FQ mode imagery over features of interest. However, the reality was that FQ mode imagery has too narrow a swath compared to the scale of the features of interest, making it difficult to image ocean features and then to identify them in the imagery. Unfortunately, we had to abandon this approach.

Instead we have carried out a very simple evaluation of a few case studies that were identified within the SOIN project. We present one example here, in which clear-sky SST imagery of the Gulf Stream are available (Figure 89), and ocean features are readily visible in the concurrent SCN imagery (Figure 90). The level of analysis that can be carried is limited and was restricted to contrast measures and ocean backscatter transects across the features of interest.

The IA Pro distributed target analysis tool was used to plot ocean backscatter along transects across several of the features that are readily apparent in the R-2 imagery (Figure 91). Each transect is composed of two plot panels. The lower panel contains the transect across the entire image, from near range to far range, which includes the regions outlined in Figure 90. The upper plot zooms-in on the area of interest, essentially covering the region delineated by the black rectangle in the lower panel. There are three lines in each panel representing the VV backscatter (red), the VH backscatter (green), and the NESZ (blue).

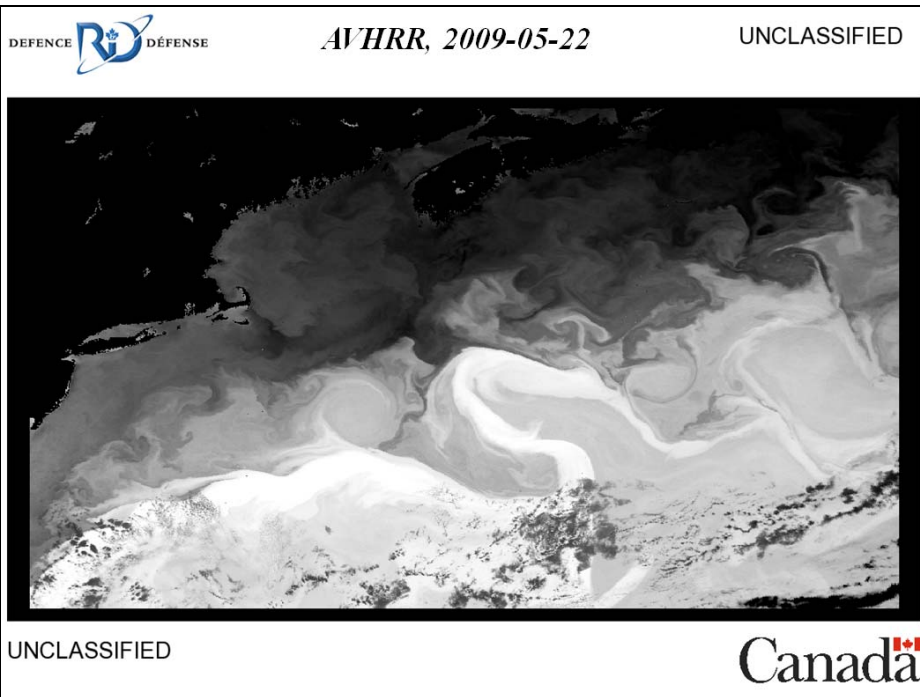


Figure 89: AVHRR image from 2009-05-22 of ocean features associated with the Gulf Stream.

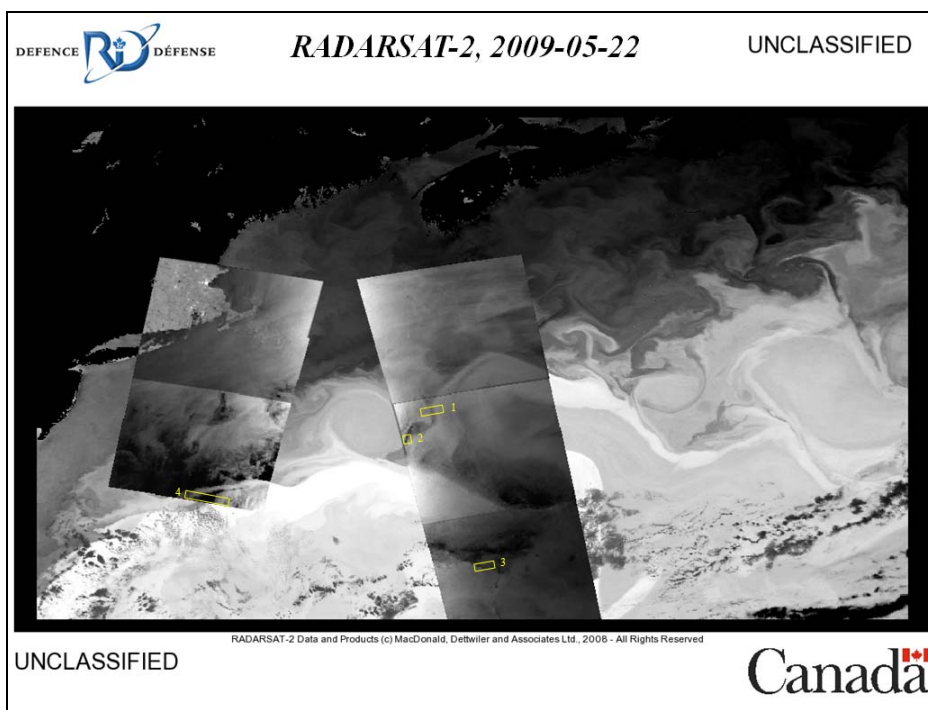


Figure 90: Nearly concurrent R-2 SCNA images overlaid on the AVHRR image of Figure 89. The yellow boxes outline the image chips over which distributed target analysis was performed

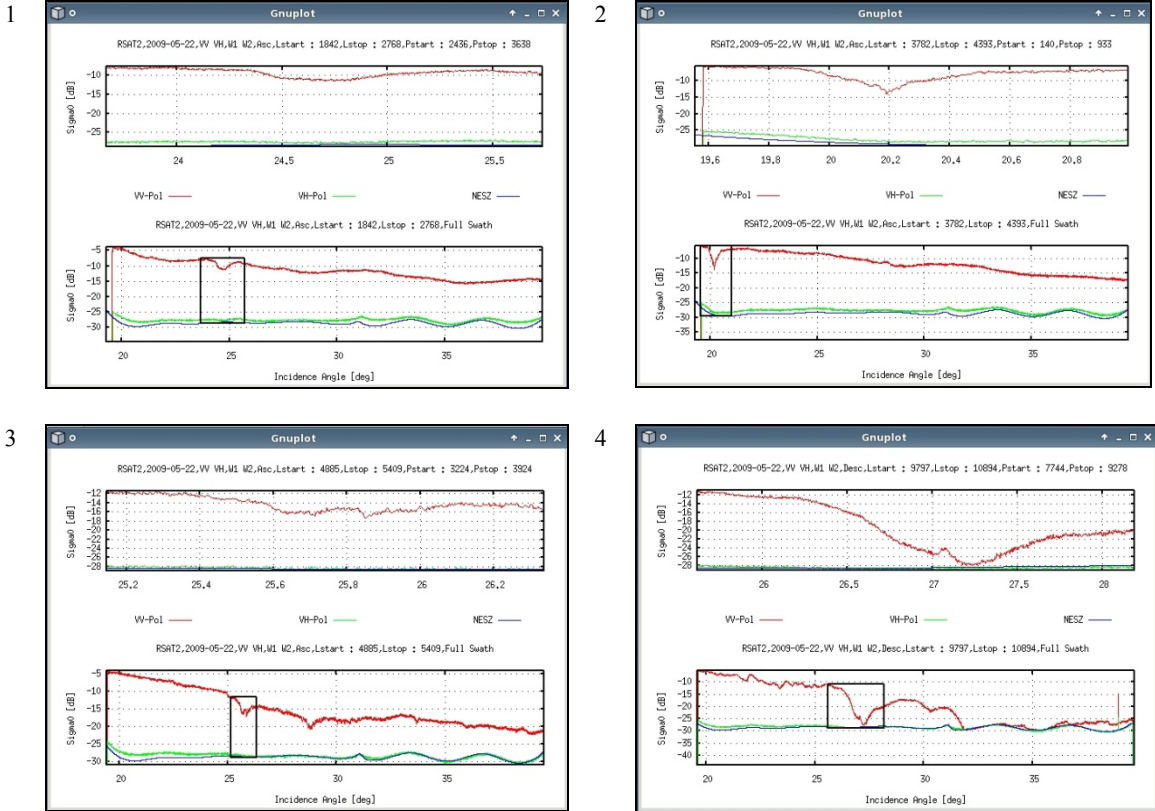


Figure 91: Ocean backscatter transects across ocean features enumerated in Figure 90.

## 8.3 Results and analysis

The Gulf Stream is one of the most significant ocean features, and is often readily visible in SAR imagery of the Atlantic region. For this feature with VV polarization, changes in backscatter of 5 dB to 15 dB were observed. On the other hand, for these moderate wind speed scenarios, there was rather little signature in the VH channel, which was at or only marginally above the instrument noise floor.

Unfortunately, we were unable to concurrently obtain radar imagery at other polarizations. As such, we can't compare performance at HH and VV in a systematic manner.

## 8.4 Mode recommendations

### 8.4.1 RADARSAT-2

Similar to oil spill detection, the best polarization for ocean feature detection is likely to be VV, with HH also able to provide useful results, though over a smaller portion of the swath. As such, SCNA is recommended, though SCW should also provide good results, perhaps with better overall context. The MSSR OSVN mode should also be suitable for ocean feature detection.

### **8.4.2 RCM**

The Low Resolution, Medium Resolution, and Low Noise modes will all be suitable for ocean feature detection, with VV polarization, smaller incidence angles, and wider swath preferred.

## **8.5 Future analysis**

The impact of polarization in ocean feature detection remains an open question and should be explored further. Perhaps a spatially recurrent feature could be identified that would facilitate this analysis. Recently announced wider swath quad-polarization modes for R-2 could help.

Furthermore, the CP mode that will be available on RCM should also be evaluated for ocean feature detection. It is likely that this will have to wait until RCM CP mode data become available. In the meantime, VV seems to a good choice for this application.

## **9 Image quality issues**

---

### **9.1 Background**

R-2 is a very flexible sensor with a rather flexible processor. At various stages in the system it is possible for the end user to make acquisition and processing choices that can impact the way in which the data are acquired by the sensor and cast into image form by the processor. While the immediate impact of such a choice can be a significant reduction in data volume or an increase in the available swath width, the impact of these choices on image quality can be rather subtle, and not at all apparent through inspection of the image alone.

In this context, two issues were addressed empirically: 8-bit and 16-bit output application LUTs, and 2-bit and 4-bit block adaptive quantization (BAQ). The LUT issue concerns the way in which floating point numbers in the processor are converted to digital numbers (DNs) in the image product. It is tempting to use 8-bit products since they are one-half the size of 16-bit products. The BAQ issue concerns the way in which the raw data received on the satellite are quantized prior to downlink. The data are digitized to 8-bit numbers, but are adaptively converted to a smaller number of bits plus a gain term in order to reduce the data volume. It is tempting to use 2-bit BAQ in order to maximize the image swath, or to include an additional polarization.

On the one hand, the impact of the LUT choice is straightforward to evaluate since the same scene can be ordered with different LUTs applied. On the other hand, the impact of the BAQ choice is more difficult to evaluate since once the data have been acquired with a chosen BAQ setting, it is not possible to reacquire the same scene simultaneously with a different BAQ. In principle, it would be possible to experiment with various BAQ choices by obtaining the full 8-bit raw data samples. However, the R-2 system precludes the ability to do this in a straightforward manner.

### **9.2 16-bits vs. 8-bits and application LUTs**

The dynamic range (DR) that can be represented by an  $N$ -bit DN is:

$$DR = 20 \log_{10} (2^N), \quad (13)$$

amounting to 48 dB for 8-bit numbers and 96 dB for 16-bit numbers. The DR of a wide-swath SAR image can be very large, indeed much larger than 96 dB. It is immediately apparent that choice of 8-bits or 16-bits will limit the available dynamic range leading to possible underflow (rounding down of floating point values smaller than 0.5 to DN = 0) or overflow (rounding down of floating point values larger than  $2^N - 1$  to DN =  $2^N - 1$ ) conditions.

The application LUT provides a number of choices (*e.g.*, ice, mixed, constant-beta, point target, etc., see Figure 92) that the user can make to control the scaling from floating point numbers in the processor to DNs in the image product. The LUT is generally chosen to create an image that is more-or-less radiometrically flat with increasing incidence angle.

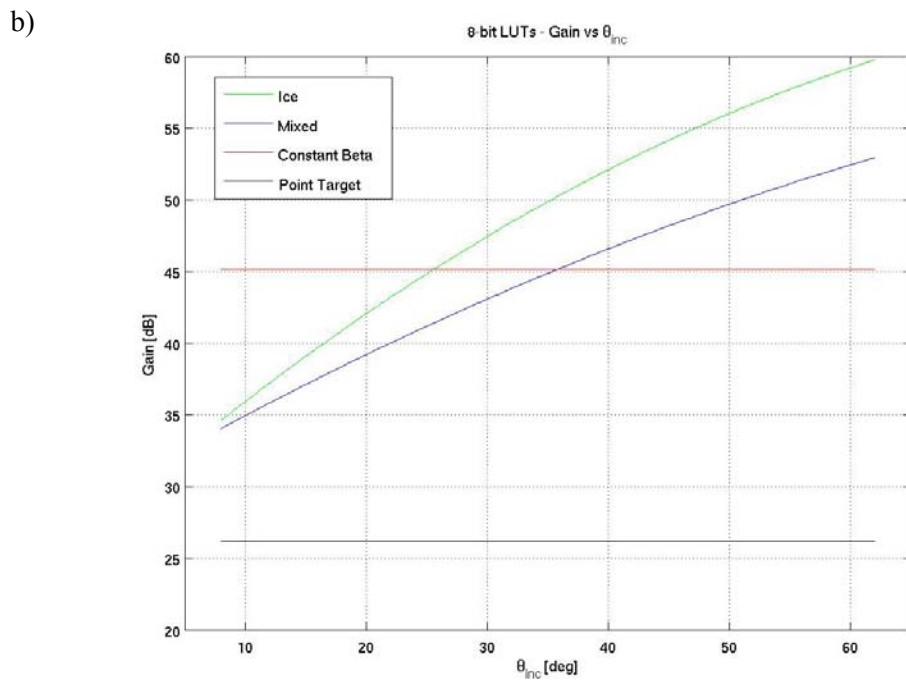
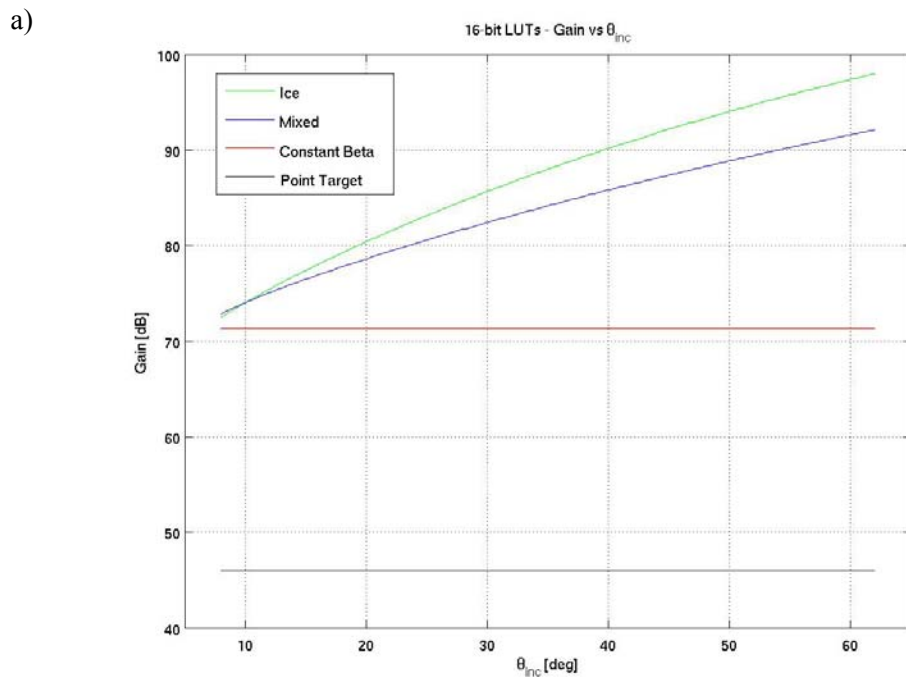


Figure 92: Gain in dB vs  $\theta_{inc}$  for various output LUTS for: a) 16-bit LUTs; and b) 8-bit LUTs.

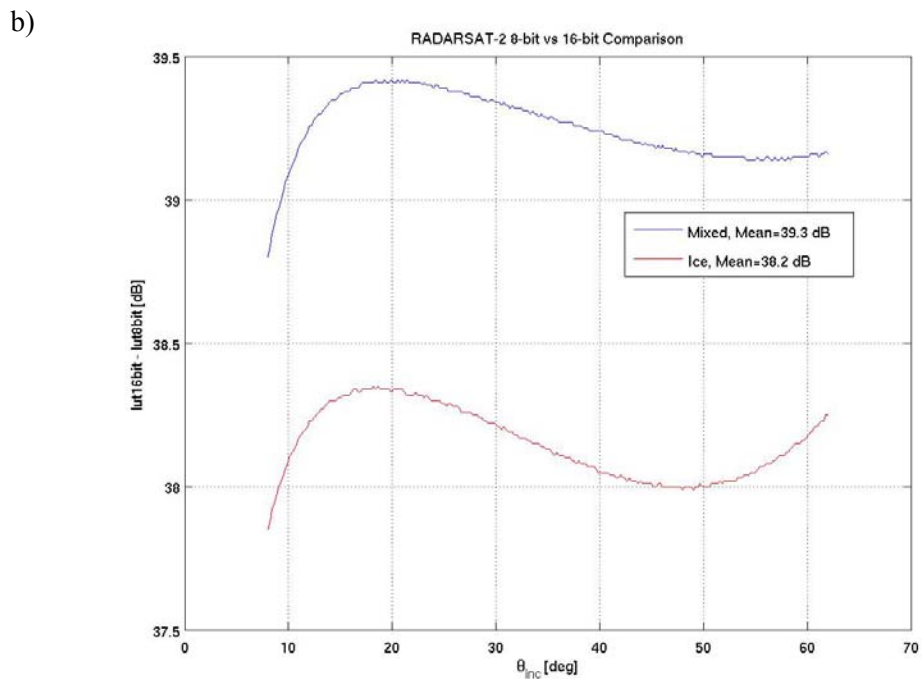
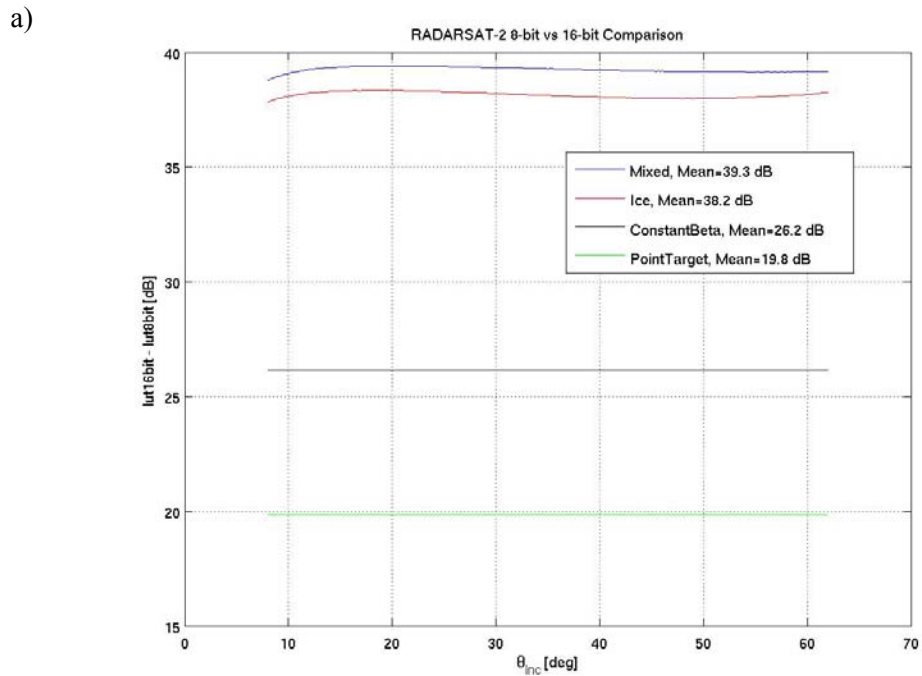


Figure 93: Ratio of 16-bit LUT to 8-bit LUT: a) for the 4 output LUTs considered; and b) zoom-in on the Mixed and Ice LUT ratios.

The ratio of the 16-bit and 8-bit application LUTs is shown in Figure 93. We were surprised to note that the ratio is not constant across the various output LUTs, and that the ratio of the Ice and Mixed LUTs exhibit incidence angle dependence amounting to 0.5 dB or so. While the reason for this result is not understood, it does indicate that choosing 8-bits rather than 16-bits may also require choice of a new output LUT.

The DN's in the image may be converted to  $\sigma^{\circ}$  via:

$$\sigma^{\circ} = 20 \log_{10}(\text{DN}) - \text{LUT}(\theta). \quad (14)$$

While the LUT controls the use of the dynamic range of the image, it does not control the quantization of the normalized radar backscatter. Specifically, the quantization is given by:

$$\left. \frac{\partial \sigma^{\circ}}{\partial \text{DN}} \right|_{\text{lin}} = \frac{20}{\ln(10)} \frac{1}{\text{DN}}, \quad (15)$$

where "lin" indicates linear quantization of  $\sigma^{\circ}$ . It is apparent that, aside from the singularity at  $\text{DN} = 0$ , the quantization of  $\sigma^{\circ}$  is very coarse for small DN's (8.7 dB for  $\text{DN} = 1$ ) and very fine for large DN's ( $1.3(10)^{-4}$  dB for  $\text{DN} = 65,535$ ). This fact has lead to the suggestion of using logarithmic quantization for the SAR image. In this case, a minimum ( $\sigma^{\circ}_{\min}$ ) and maximum ( $\sigma^{\circ}_{\max}$ ) normalized radar cross section would be chosen, with each DN representing equal logarithmic steps in between. The difference between  $\sigma^{\circ}_{\max}$  and  $\sigma^{\circ}_{\min}$  is the DR. The quantization would then be:

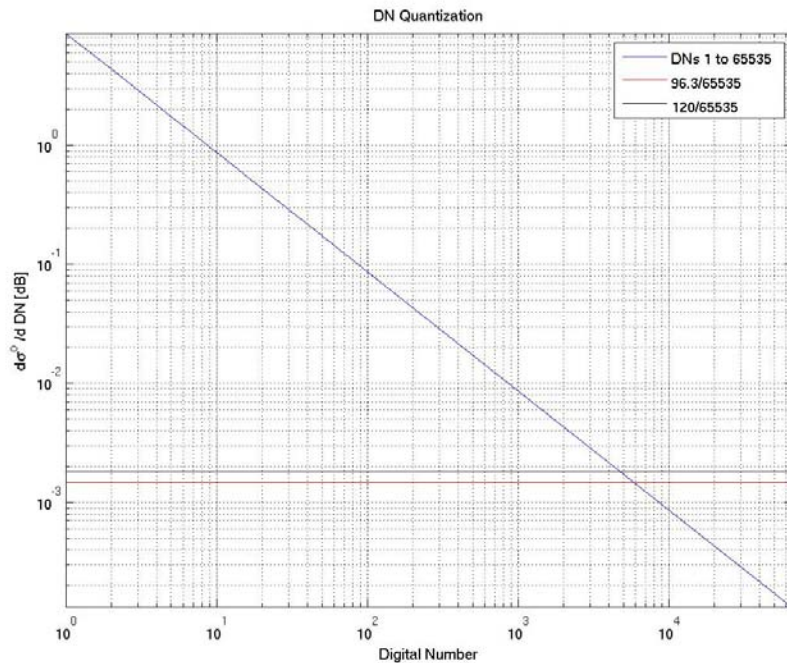
$$\left. \frac{\partial \sigma^{\circ}}{\partial \text{DN}} \right|_{\text{log}} = \frac{\text{DR}}{2^N - 1}, \quad (16)$$

where "log" indicates logarithmic quantization of  $\sigma^{\circ}$ . In this way, larger dynamic ranges could be chosen and the normalized radar backscatter quantization controlled independent of DN. The actual  $\sigma^{\circ}$  quantization in accordance with Equations (15) and (16) is illustrated in Figure 94 for 8-bit and 16-bit cases. The logarithmic quantization is notional only and is intended to illustrate, in contrast to linear quantization, the uniform quantization across both high and low backscatter values.

The actual LUT choice does select the range of  $\sigma^{\circ}$  that is represented in the output image. This is illustrated in Figure 95 through Figure 98, each of which represents a different incidence angle. This illustrates the importance of LUT choice to represent the actual dynamic range of an image.

To examine the impact of the LUT choice on actual data, we ordered a number of scenes with different numbers of bits and LUTs applied.

a)



b)

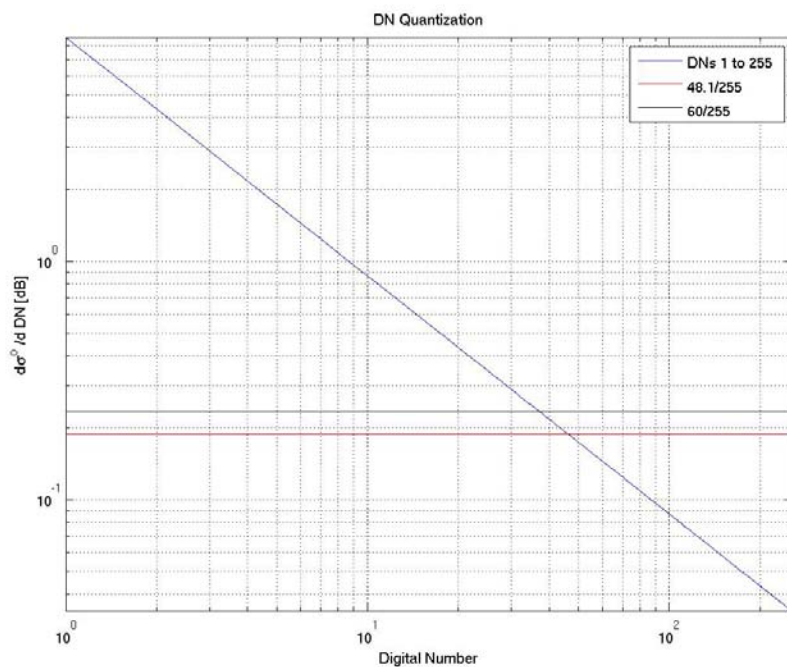


Figure 94:  $\sigma^0$  quantization as per Equations (15) and (16): a) 16-bits; and b) 8-bits. The logarithmic quantization cases are notional.

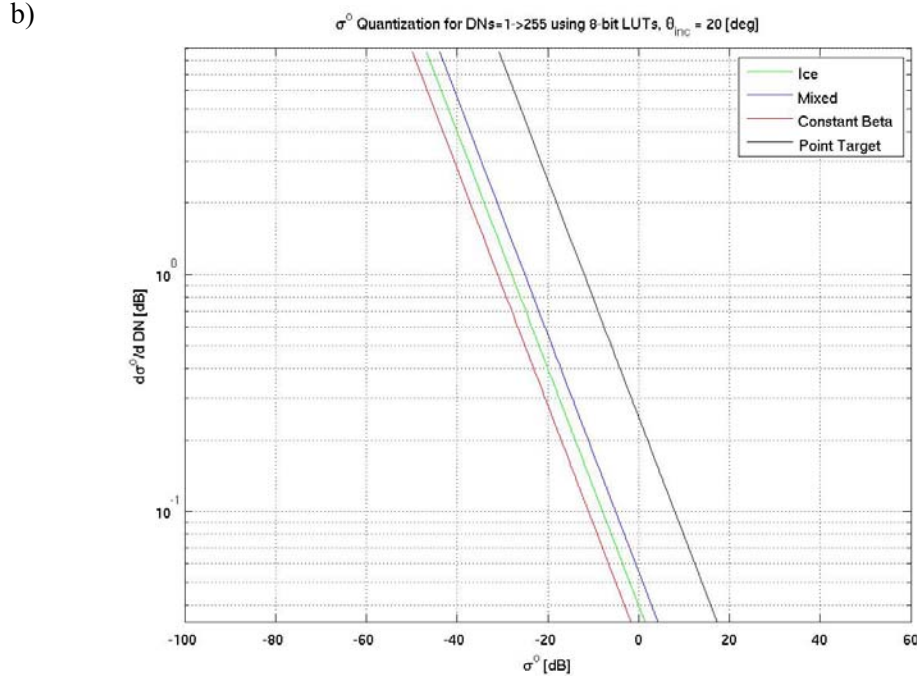
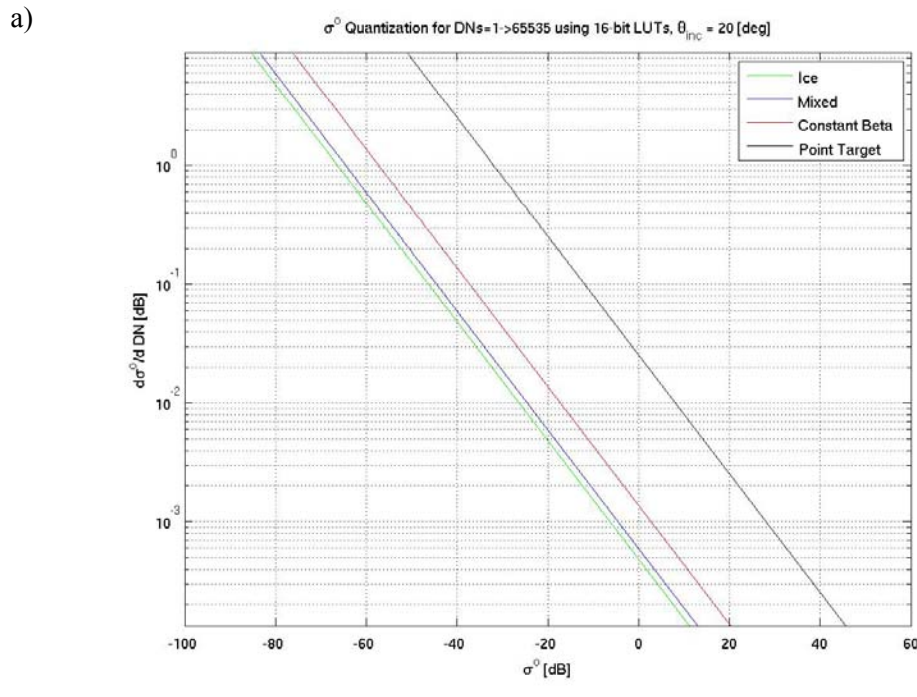


Figure 95: Linear  $\sigma^0$  quantization for  $\theta_{inc} = 20^\circ$  for various output LUTs for: a) 16-bit LUTs; and b) 8-bit LUTs.

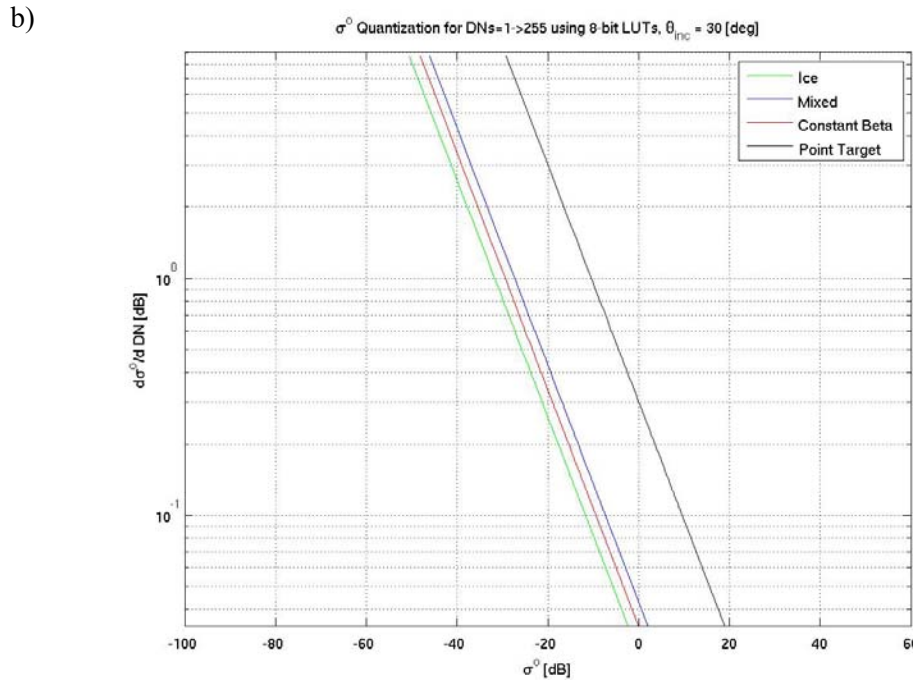
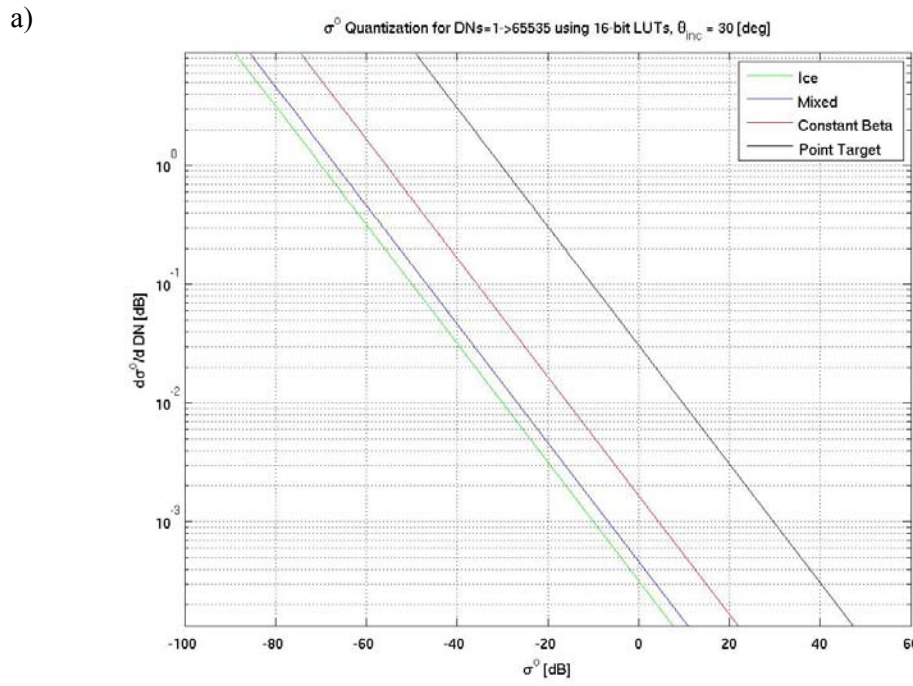


Figure 96: Linear  $\sigma^0$  quantization for  $\theta_{inc} = 30^\circ$  for various output LUTs for: a) 16-bit LUTs; and b) 8-bit LUTs.

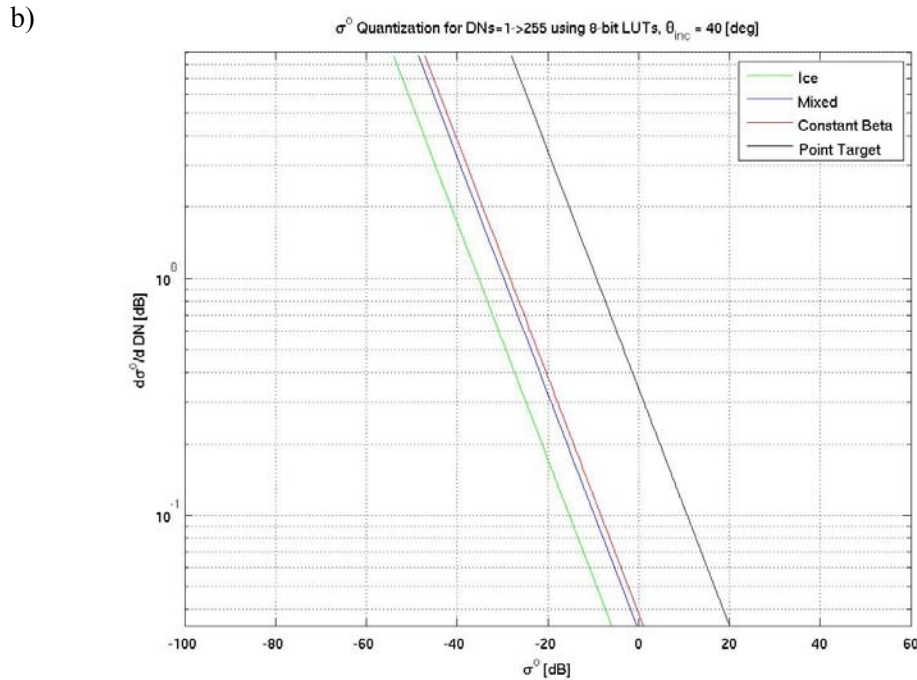
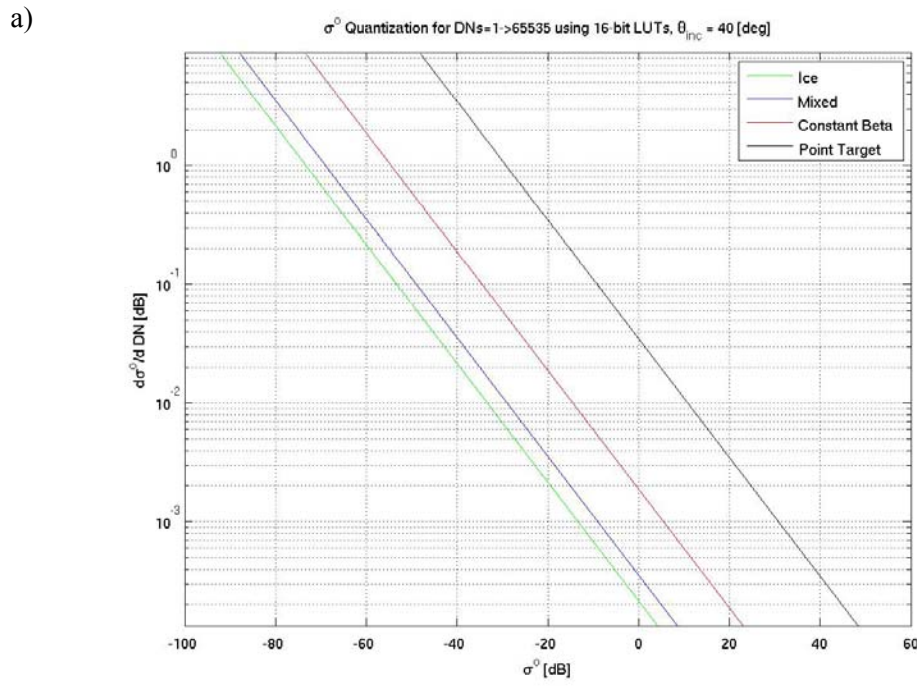


Figure 97: Linear  $\sigma^0$  quantization for  $\theta_{inc} = 40^\circ$  for various output LUTs for: a) 16-bit LUTs; and b) 8-bit LUTs.

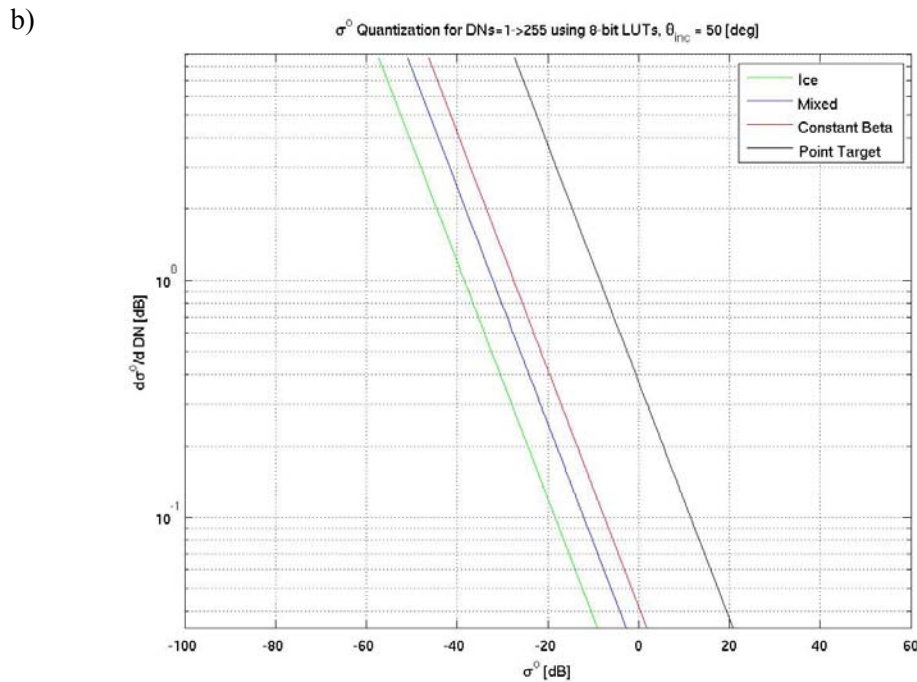
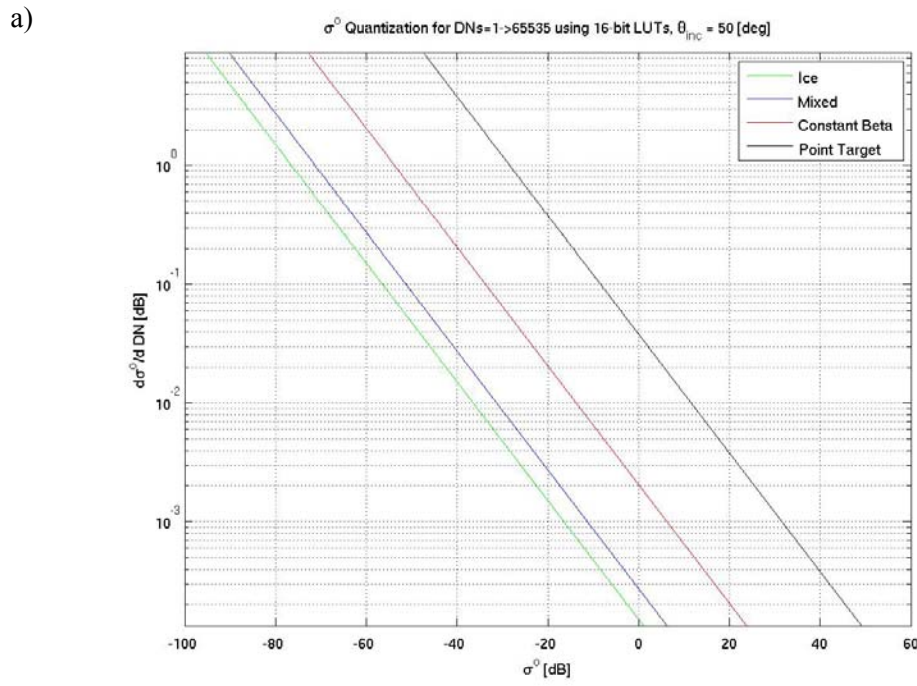


Figure 98: Linear  $\sigma^0$  quantization for  $\theta_{inc} = 50^\circ$  for various output LUTs for: a) 16-bit LUTs; and b) 8-bit LUTs.

To illustrate the impact of output LUT choice on derived image information, we consider two statistics that may be estimated from SAR images: the local mean value of  $\sigma^o$  (Figure 99) and the critical intensity for ship detection (the threshold above which a pixel is considered to be a candidate ship) (Figure 100). In each case, the quantization is plotted as a function of the mean backscatter, with three different output LUTs represented. The results for each scene considered are joined by a line, and the case of logarithmic backscatter scaling over a 160 dB DR is also included.

On the one hand, for the mean value of  $\sigma^o$ , it may be assumed that the Mixed LUT is providing the best mean estimate since it introduces the highest gain and therefore the best  $\sigma^o$  quantization. On the other hand, for the fairly low values of  $\sigma^o$  considered, underflow is likely occurring when the Point Target LUT is used, which introduces the lowest gain among the LUTs considered, resulting in a reduction in the estimated mean value of  $\sigma^o$  by more than 0.5 dB in for the HV channel. Less impact is noted for the HH channel, especially for the cases with highest backscatter. Note that logarithmic scaling would provide more favourable (*i.e.*, finer)  $\sigma^o$  quantization than any of the output LUTs considered for the low backscatter cases.

A similar story is apparent for estimation of the critical intensity for ship detection. Underflow associated with use of the Point Target output LUT leads to an overestimation of the critical intensity.

As a demonstration of the impact of logarithmic  $\sigma^o$  scaling on bright targets, an image containing ship targets was re-quantized to logarithmic scaling with 160 dB DR. Obviously the available quantization for lower  $\sigma^o$  values does not support this re-quantization, but the quantization for larger  $\sigma^o$  values associated with the ship targets will be coarser than in the case of linear  $\sigma^o$  scaling.

The re-quantization was carried out as follows. The 160 dB DR was chosen to range from -100 dB to 60 dB. A new DN was formed via:

$$DN' = \text{round} \left[ (\sigma^o + 100) \frac{65535}{100} \right]. \quad (17)$$

Then, the new DN was mapped into a new value of  $\sigma^o$ :

$$\sigma^o' = \frac{160}{65535} (DN' - 100) \quad [\text{dB}] \quad (18)$$

Table 28 provides some representative target measures following re-quantization. Based upon the minimal observed change in the ship values (only at the fourth decimal place), we conclude that logarithmic  $\sigma^o$  quantization would not negatively impact the analysis of large RCS targets, even though the quantization would be coarser than is achieved with linear  $\sigma^o$  quantization.

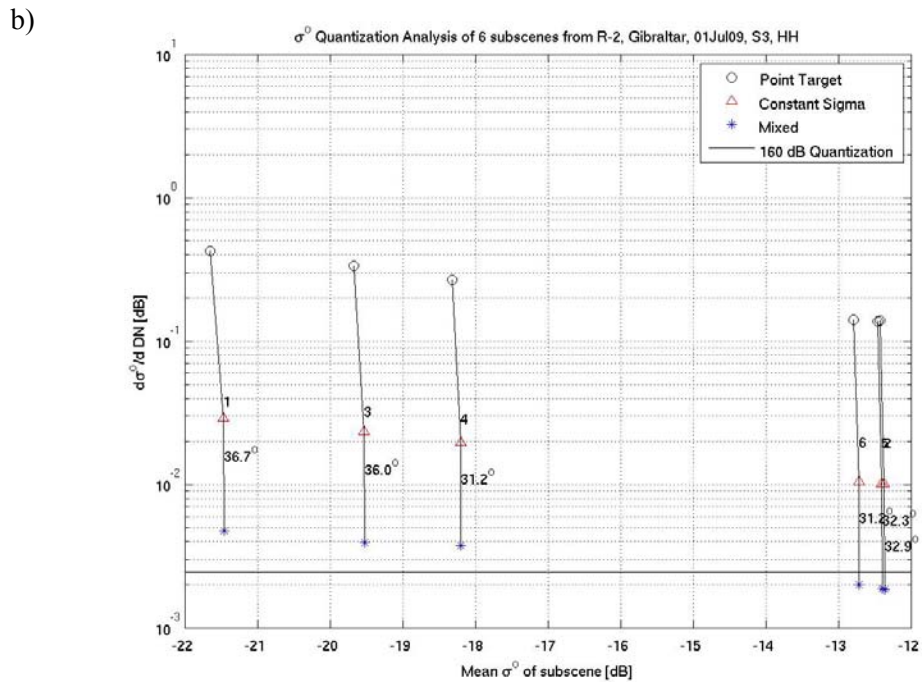
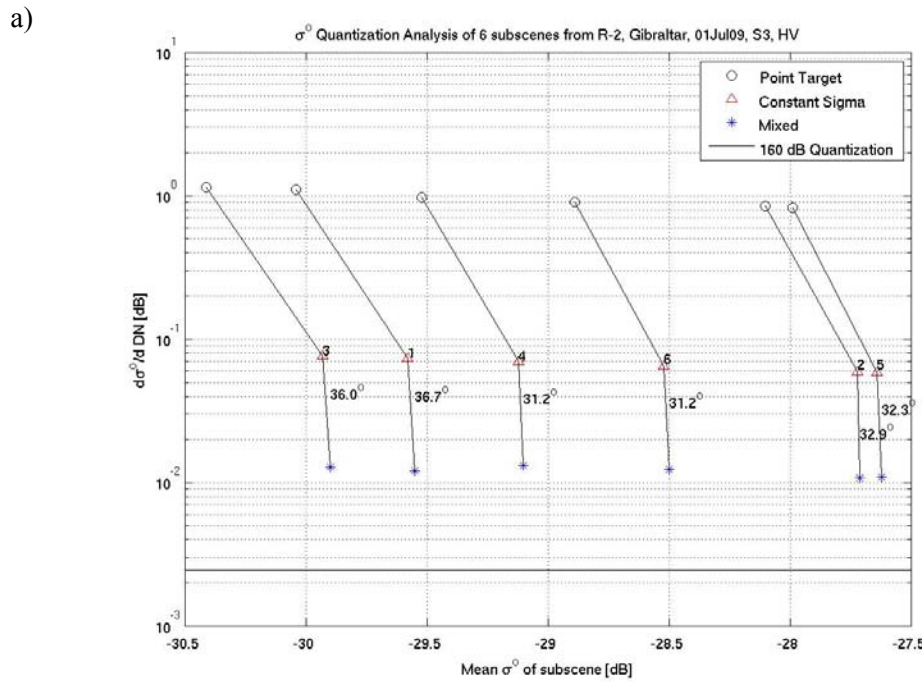


Figure 99:  $\sigma^0$  quantization for 6 ocean regions as a function of the estimated mean value of  $\sigma^0$  when using 3 different output LUTs for an R-2 S3 image of the Strait of Gibraltar acquired 2009-07-01: a) HV polarization; and b) HH polarization.

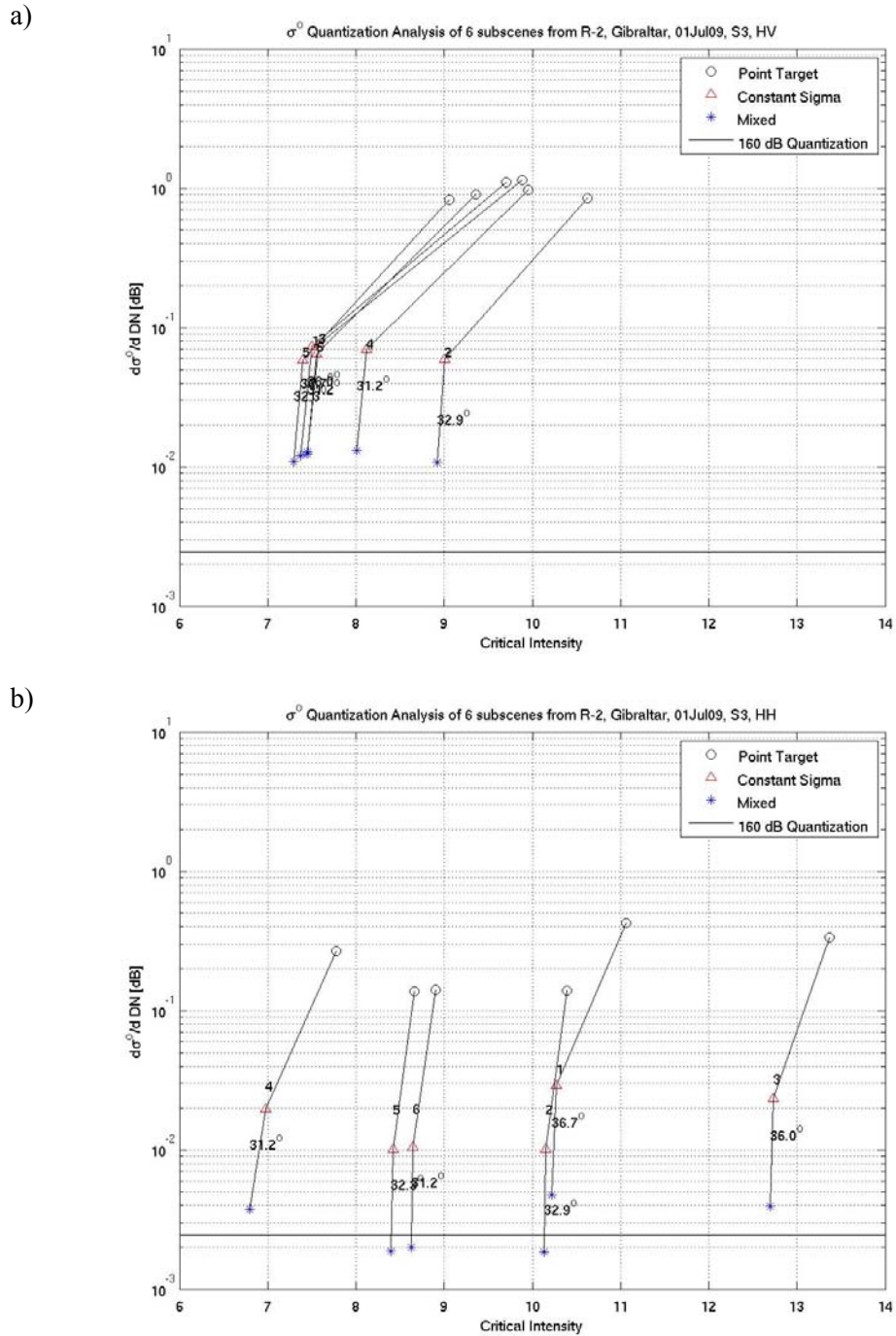


Figure 100:  $\sigma^0$  quantization for 6 ocean regions as a function of the critical intensity for ship detection when using 3 different output LUTs for an R-2 S3 image of the Strait of Gibraltar acquired 2009-07-01: a) HV polarization; and b) HH polarization.

Table 28: Point target analysis measurements of a ship comparing original data processed with various application LUTs with the same data sets logarithmically quantized to 160 dB DR.

	Mixed		Constant Sigma		Point Target	
	Lin.	Log.	Lin.	Log.	Lin.	Log.
<b>Peak Value [dB]</b>	10.2628	10.2629	15.3399	15.3411	15.3383	15.3387
<b>Total RCS [dB]</b>	44.1027	44.1030	44.6506	44.6506	44.6465	44.6467
<b>Mean Clutter [dB]</b>	-18.4504	-18.4505	-19.4949	-19.4948	-19.6265	-19.6264

### 9.3 BAQ selection

In a previous study using ERS-1 data [57], it was shown that processing an image with smaller numbers of raw data bits results in a loss of image texture, that is, the image statistics become more Gaussian in nature. It is expected that a similar trend would exist for the BAQ setting.

As noted above, with the current R-2 system, it is not possible to re-process an existing scene with a BAQ setting that is different from the BAQ setting that was used to acquire the data. Therefore, the only way to address this was to acquire images of the same region with different BAQ settings on subsequent passes. This approach is rife with flaws, but does provide a way ahead and some baseline observations. Several images of ice scenes were acquired, first in an ascending pass direction with a BAQ setting of 2-bits, then in a descending pass direction with a BAQ setting of 4-bits. This approach provides images of the same region with different BAQ settings, albeit with opposite side viewing geometries and at different times of day, such that image statistics may be estimated as a function of the BAQ setting. It must be kept in mind that the analysis results shown are from different points in the daily cycle and the ice could have advected between acquisitions.

Regions in the image pairs were selected such that their incidence angles were the same. This is illustrated in Figure 101. The lines were drawn using IA Pro at specific incidence angles. The intersection point is the location at which the distributed target analysis was carried out. Analysis opportunities are restricted by the incidence angle constraint. Note that not all ice types of interest may be visible in the scenes that were acquired, or located within the region of common incidence angle.

The two pairs of images that were acquired are shown in Figure 102 (near Baffin Island, HH+HV polarizations) and Figure 106 (northwest Arctic, HH polarization), with zoomed-in views of the analysis regions in the two images shown in Figure 103 through Figure 105 and in Figure 107 through Figure 109, respectively. The estimated image statistics are presented in Table 29 and Table 30 for the Baffin Island scene and in Table 31 for the northwest Arctic scene.

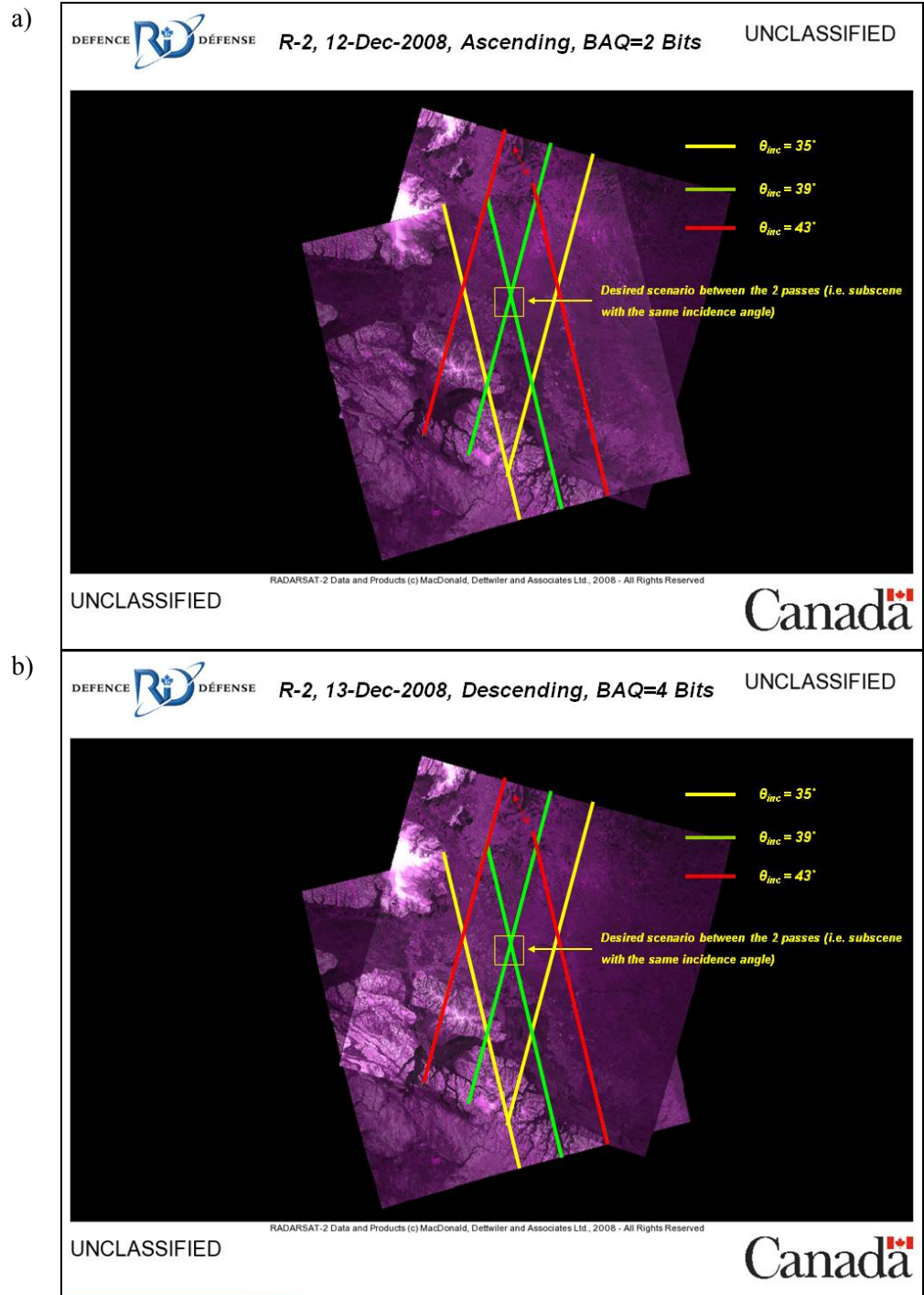
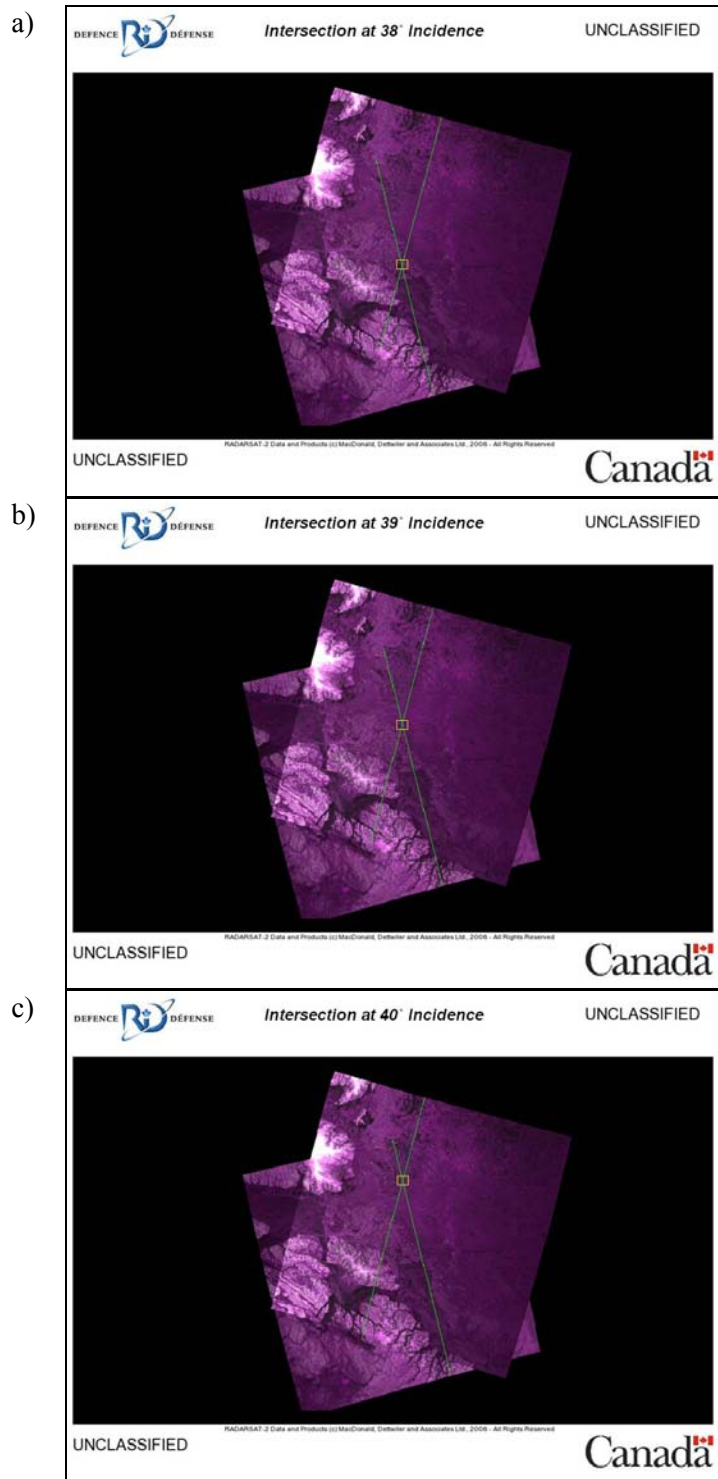
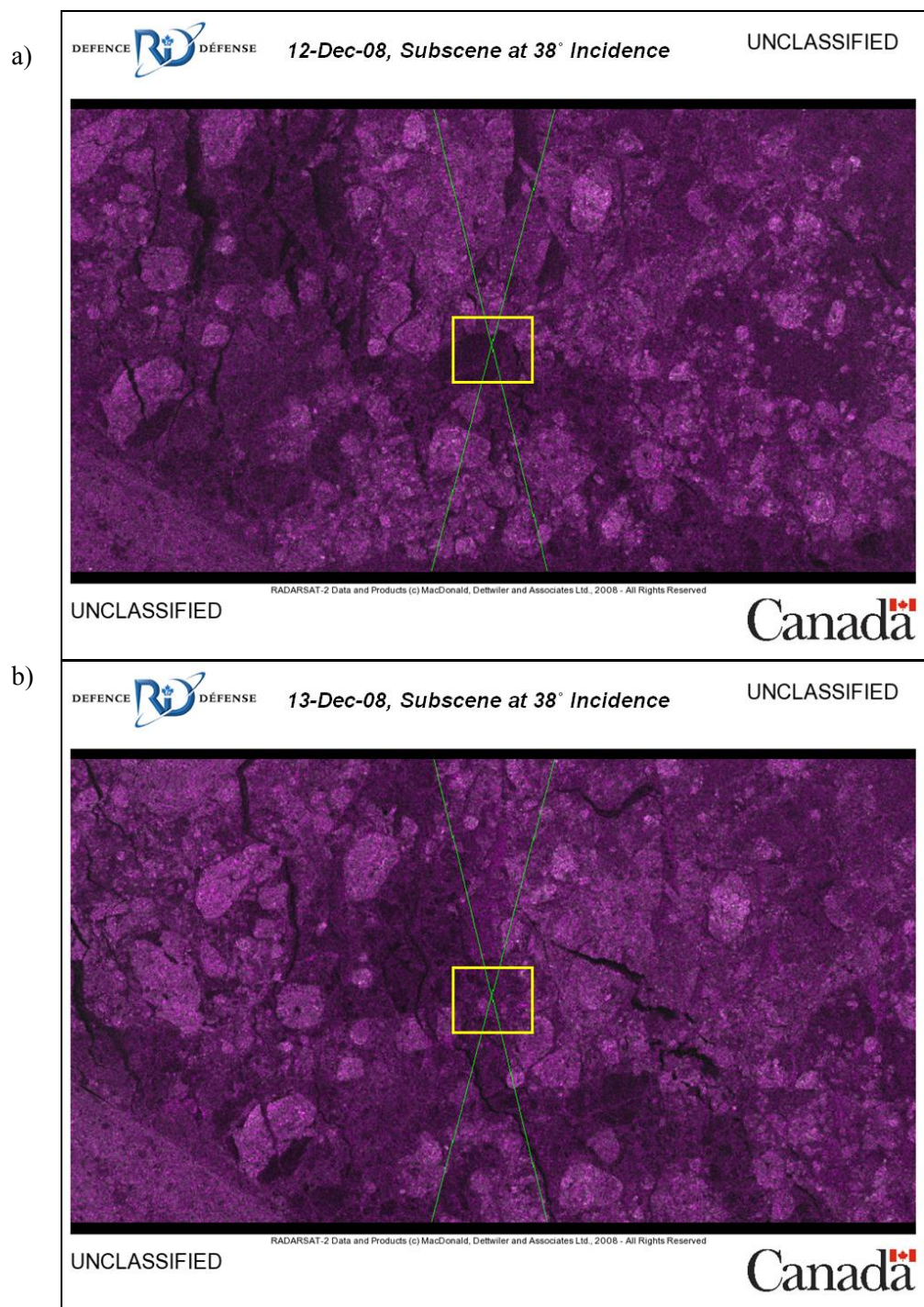


Figure 101: Scenario for BAQ analysis between two passes near Baffin Island indicating where a sub-scene (yellow box) can be analysed at the same incidence angle: a) ascending pass with 2-bits BAQ overlaid on the descending pass; and b) descending pass with 4-bits BAQ overlaid on the ascending pass.



*Figure 102: Analysis sub-scenes for the 12/13 December 2008 case near Baffin Island corresponding to incidence angles of: a) 38°; b) 39°; and c) 40°.*



*Figure 103: Approximate analysis sub-scene at 38° incidence for Baffin Island scene for: a) 2-bit BAQ; and b) 4-bit BAQ.*

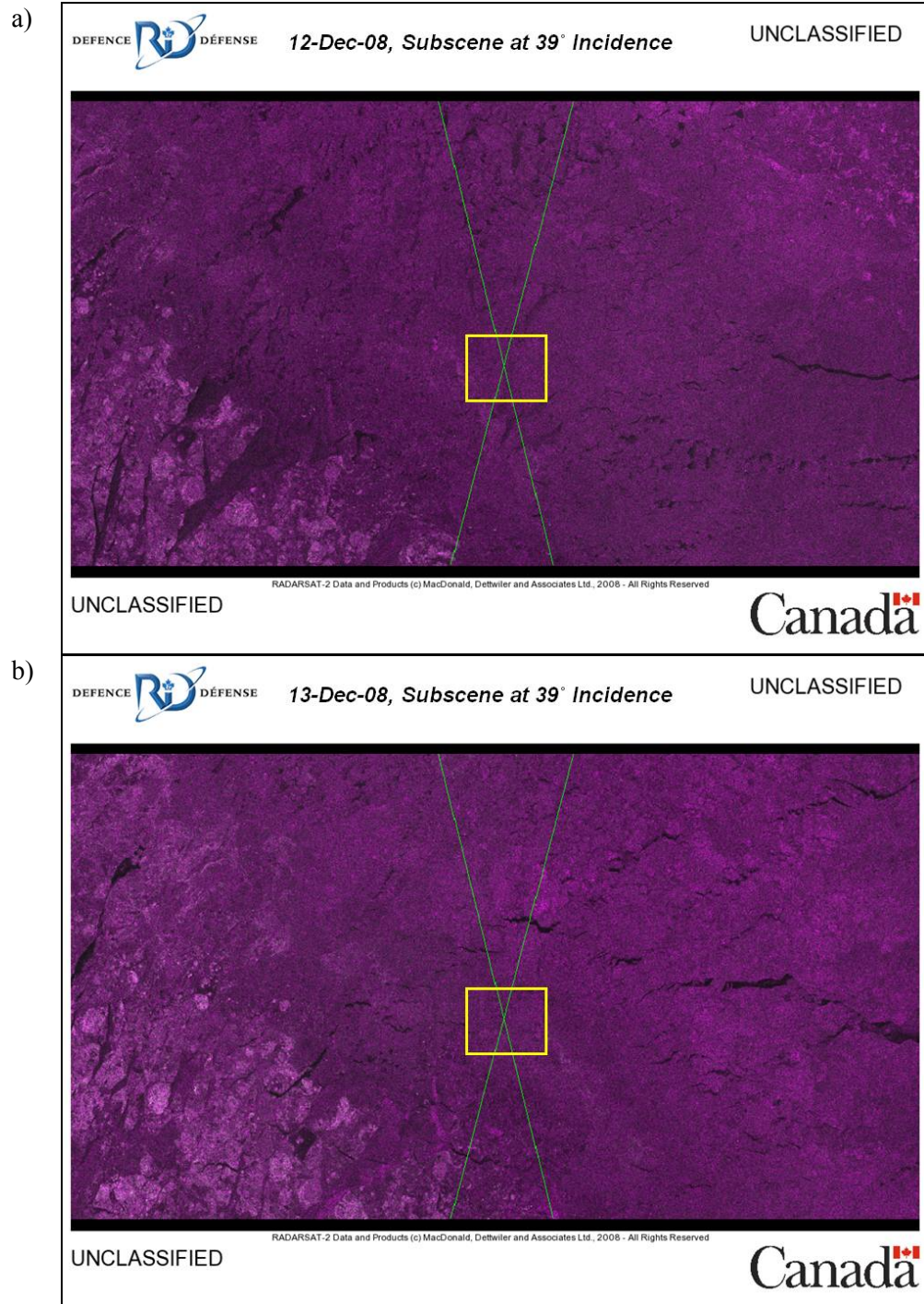
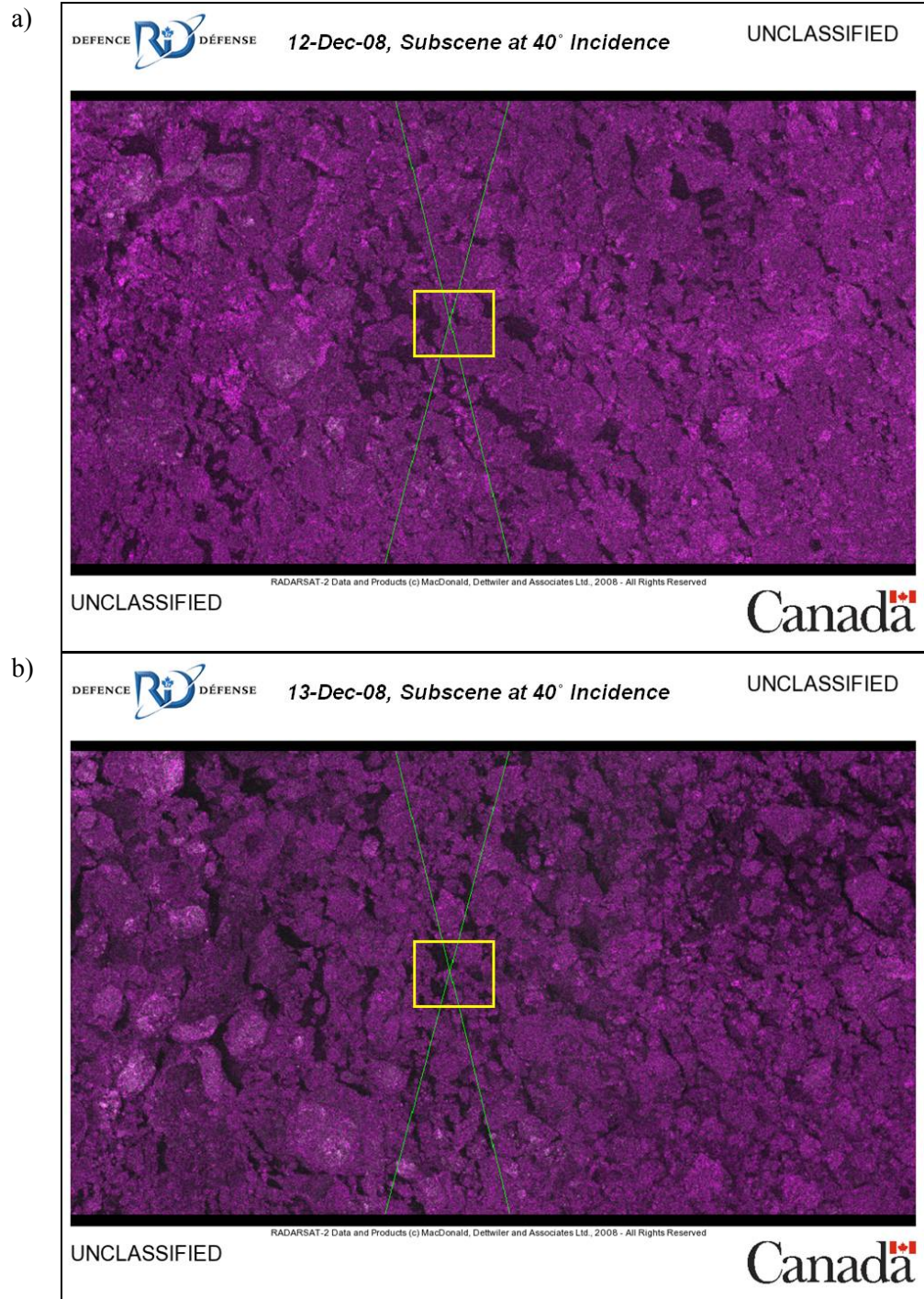
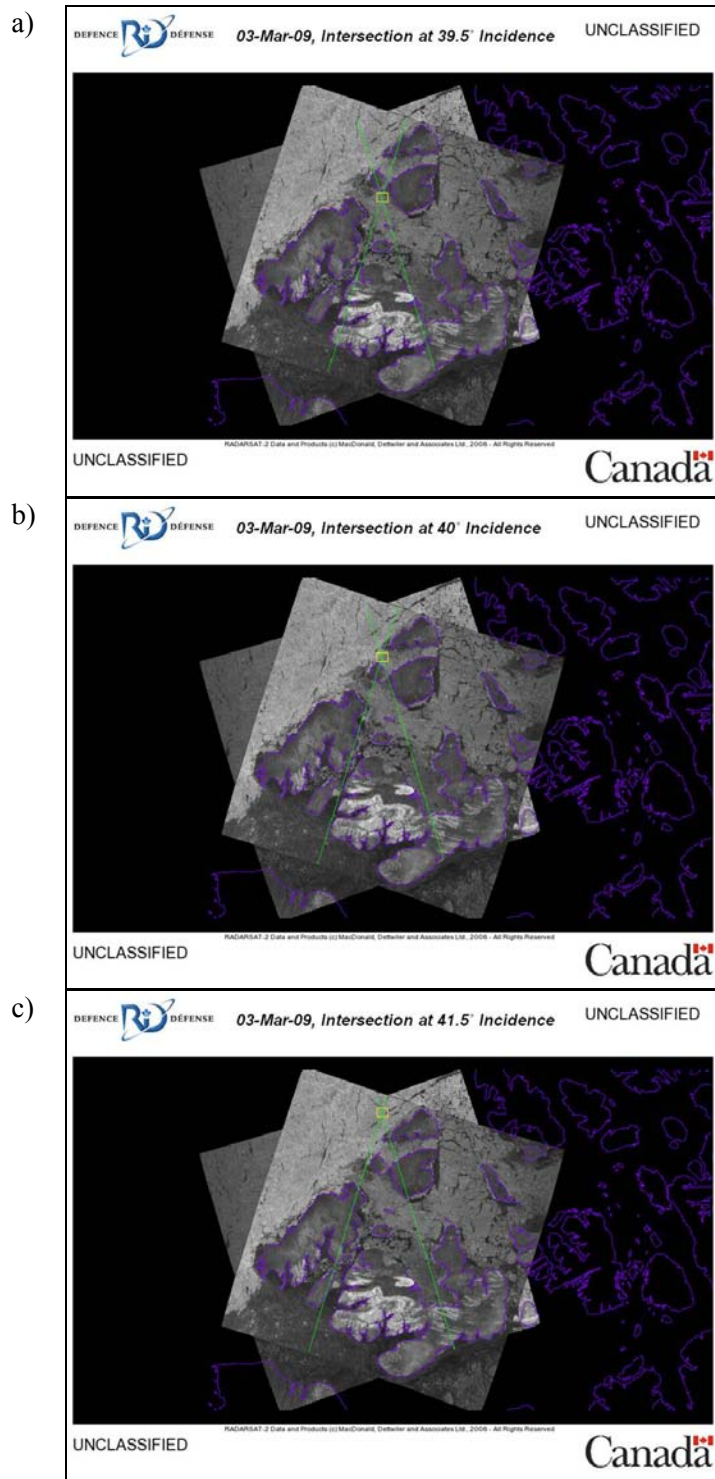


Figure 104: Approximate analysis sub-scene at 39° incidence for Baffin Island scene for: a) 2-bit BAQ; and b) 4-bit BAQ.



*Figure 105: Approximate analysis sub-scene at 40° incidence for Baffin Island scene for: a) 2-bits BAQ; and b) 4-bits BAQ.*



*Figure 106: Analysis sub-scenes for the 3/4 March 2009 case in the northwest Canadian Arctic corresponding to incidence angles of: a) 39.5°; b) 40°; and c) 41.5°.*

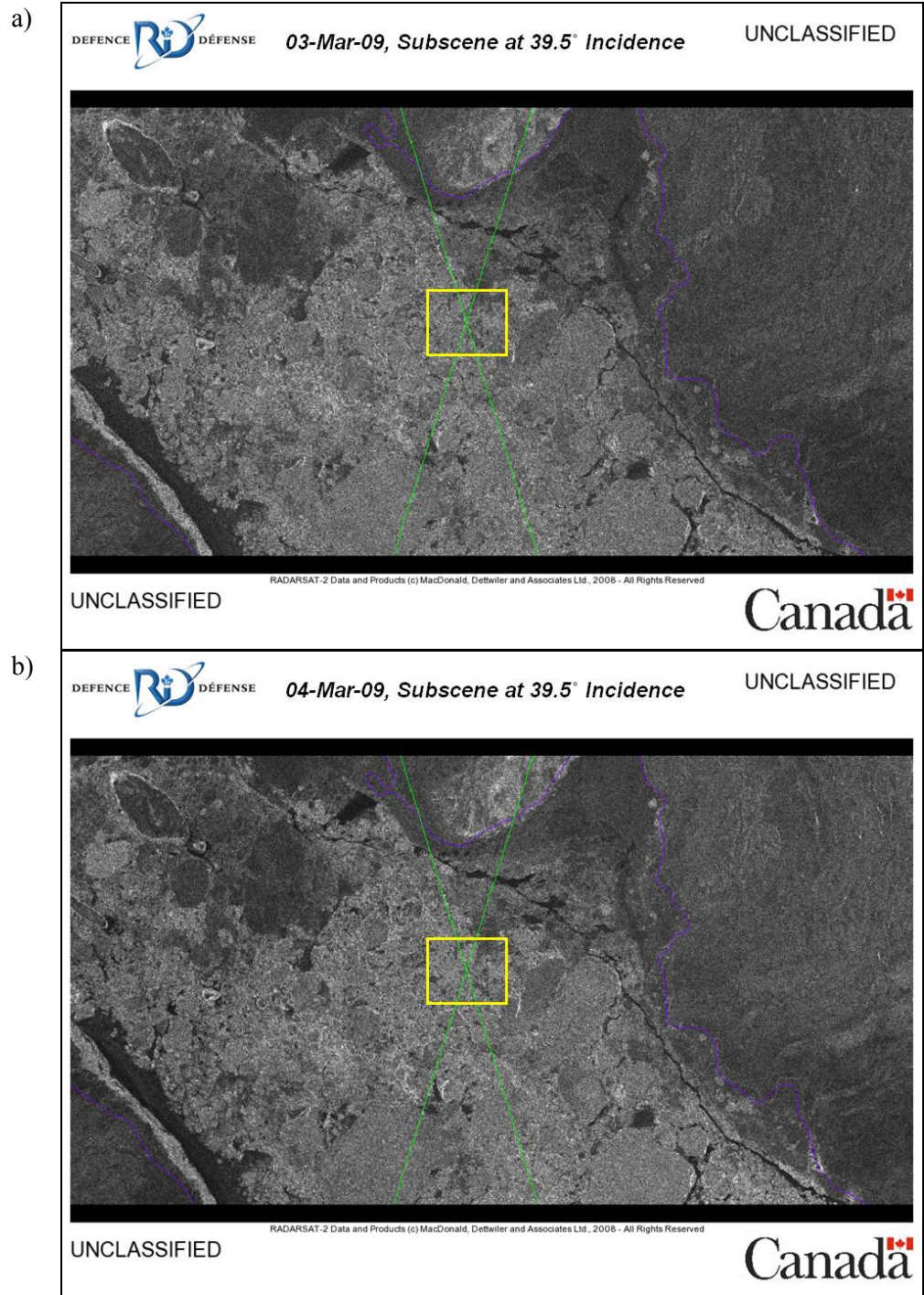


*Figure 107: Approximate analysis sub-scene at 39.5° incidence for the northwest Arctic scene for: a) 2-bits BAQ; and b) 4-bits BAQ.*

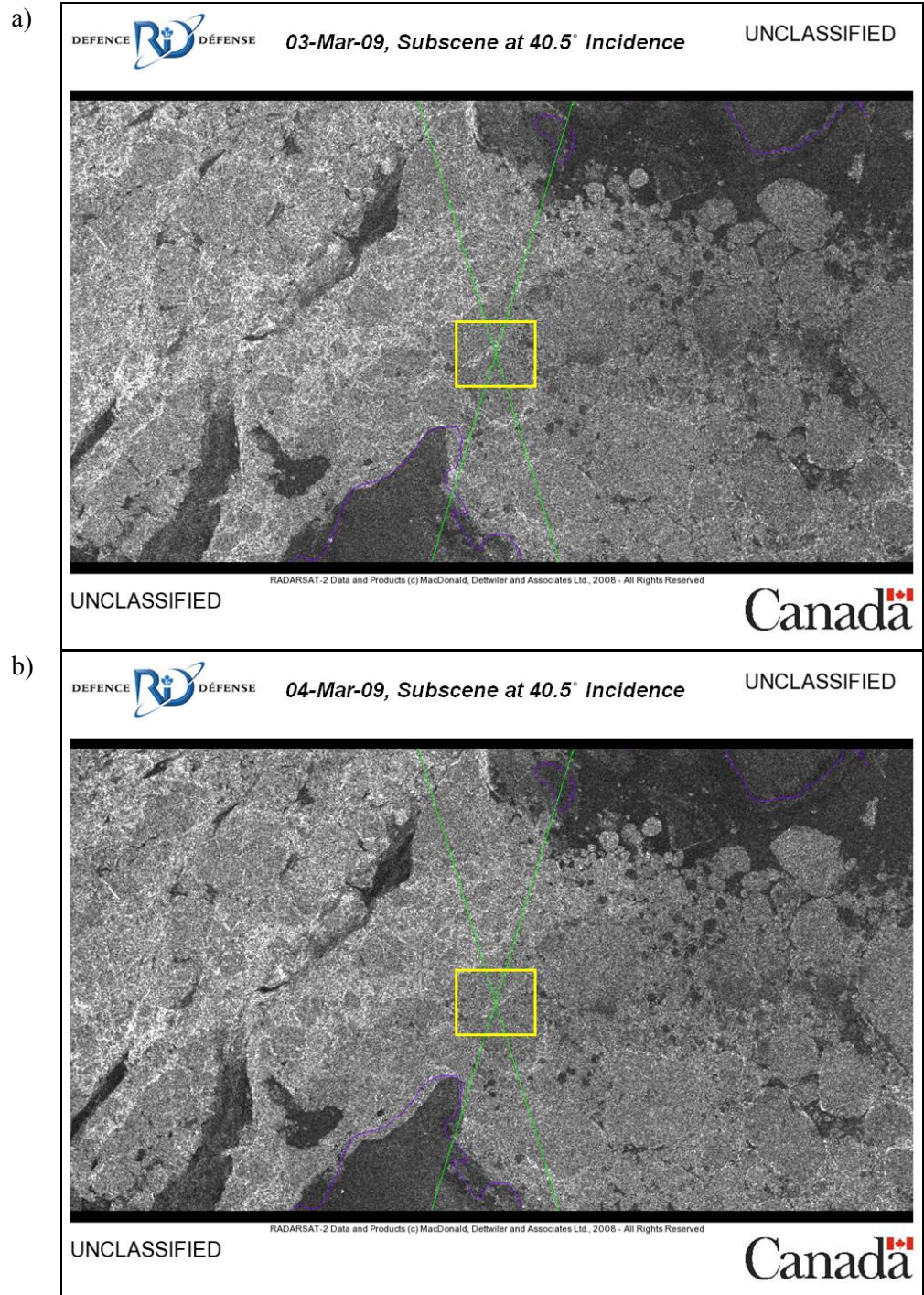


*Figure 108: Approximate analysis sub-scene at 40.5° incidence for the northwest Arctic scene for: a) 2-bits BAQ; and b) 4-bits BAQ.*

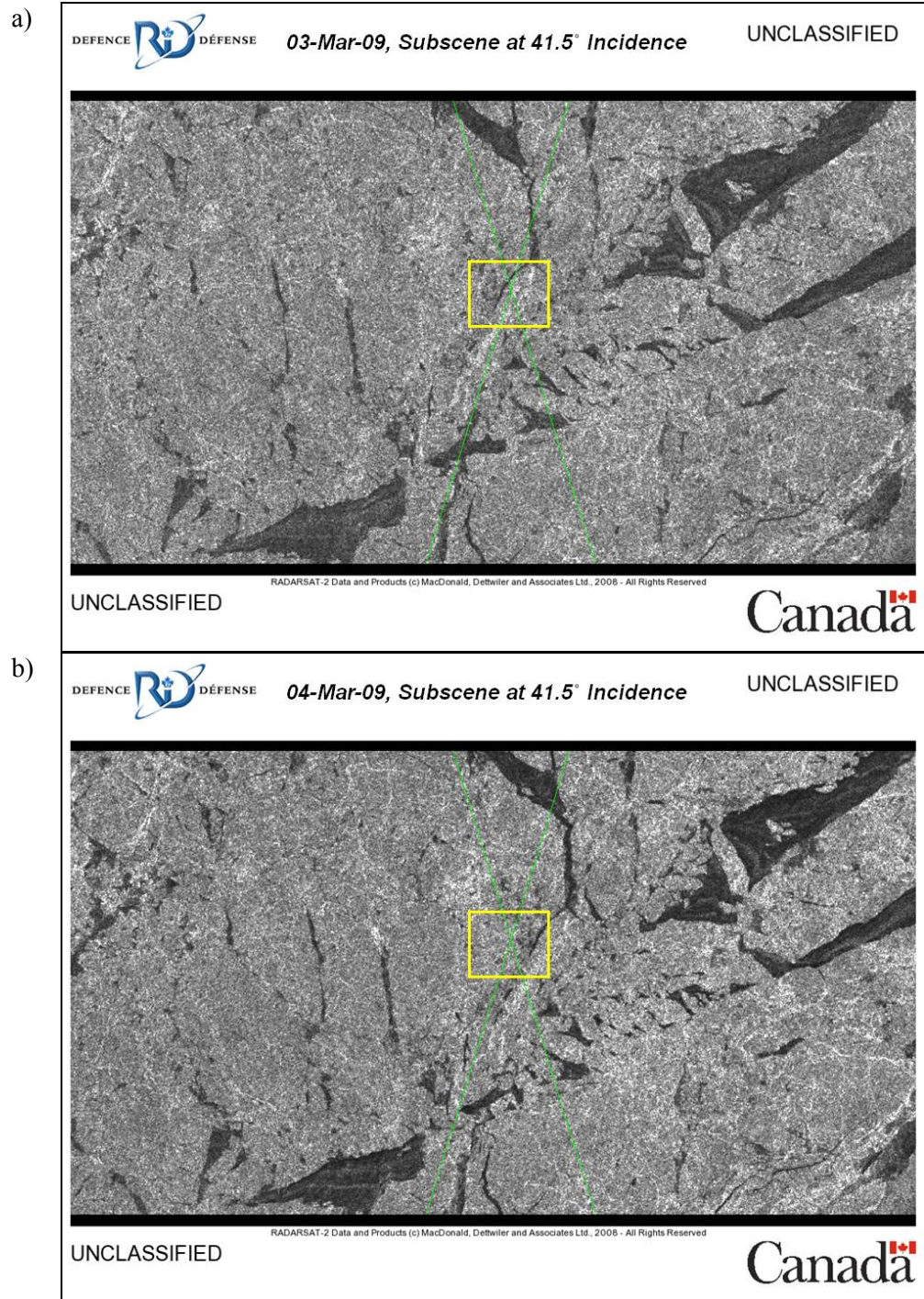


*Figure 109: Approximate analysis sub-scene at 41.5° incidence for the northwest Arctic scene for: a) 2-bits BAQ; and b) 4-bits BAQ.*

*Table 29: Distributed target analysis for the Baffin Island sub-scenes, HH polarization.*

Date	BAQ	$\theta$ [°]	Mean $\sigma^o$ [dB]	Std $\sigma^o$ [dB]	Skewness	Kurtosis
2008-12-12	2	38	-14.530	2.483	2.042	10.050
2008-12-13	4	38	-14.253	2.467	2.114	10.789
2008-12-12	2	39	-14.302	1.621	1.103	5.190
2008-12-13	4	39	-14.394	1.611	1.324	8.171
2008-12-12	2	40	-13.950	2.170	1.491	7.298
2008-12-13	4	40	-14.743	2.104	1.638	9.657

Table 30: Distributed target analysis for the Baffin Island sub-scenes, HV polarization.

Date	BAQ	$\theta$ [°]	Mean $\sigma^o$ [dB]	Std $\sigma^o$ [dB]	Skewness	Kurtosis
2008-12-12	2	38	-23.431	2.736	2.985	16.763
2008-12-13	4	38	-23.519	3.019	3.439	26.021
2008-12-12	2	39	-24.423	1.646	1.963	17.285
2008-12-13	4	39	-24.052	1.686	3.183	45.369
2008-12-12	2	40	-23.549	1.791	1.475	7.931
2008-12-13	4	40	-24.176	2.349	7.879	144.437

*Table 31: Distributed target analysis for the northwest Arctic sub-scenes, HH polarization.*

Date	BAQ	$\theta$ [°]	Mean $\sigma^0$ [dB]	Std $\sigma^0$ [dB]	Skewness	Kurtosis
2009-03-03	2	39.5	-12.766	1.863	1.252	5.933
2009-03-04	4	39.5	-12.762	1.974	1.304	6.049
2009-03-03	2	40.5	-11.952	1.788	1.490	6.737
2009-03-04	4	40.5	-12.260	1.766	1.343	6.314
2009-03-03	2	41.5	-11.288	1.875	1.098	4.545
2009-03-04	4	41.5	-11.349	1.958	1.050	4.431
2009-03-03*	2	40.5	-17.227	1.562	1.075	5.016
2009-03-04*	4	40.5	-16.555	1.715	1.766	12.646
2009-03-03*	2	40.5	-18.982	1.889	3.111	21.121
2009-03-04*	4	40.5	-20.056	2.124	3.848	29.183
2009-03-03*	2	41.5	-11.296	1.622	1.283	5.577
2009-03-04*	4	41.5	-12.054	1.891	0.718	3.857

\* Indicates that a second sub-scene was extracted from a nearby dark region of the image.

It is difficult to draw any firm conclusions from these analysis results. However, it is apparent that in moving from a BAQ setting of 2-bits to 4-bits we observe a decrease in the standard deviation, skewness, and kurtosis, suggesting that use of 2-bits tends to make the image more Gaussian in nature. The effect is largest for the darkest (i.e., lowest backscatter) sub-scenes, although the stated trend is not observed for all cases. Of course, the difference could also be due to the opposite side views or the time difference between the acquisitions rather than the change in BAQ setting.

## 9.4 Recommendations

In terms of selection of Application LUT and bit depth of the imagery, many different LUTs could be suitable. Both of these choices could impact statistics estimated from imagery. It is recommended that the DN's in the product be examined for the occurrence of large numbers of zeros and large numbers of saturated values. These could be indicators that an inappropriate LUT was used and that the data should be re-processed with a different LUT choice. Of course, 16-bits image quality will always be better than 8-bits image quality since the available dynamic range is double for the former choice.

In terms of the BAQ setting, it is possible that a lower number of bits will result in the image being more Gaussian in nature than anticipated. Of course, 4-bits BAQ imagery quality will always be better than 2-bits BAQ image quality since the raw data dynamic range is more finely sampled. However, we can't rule out 2-bit image quality being adequate for many maritime applications. It should be noted that 2-bit BAQ will become more common for new R-2 beam modes such as MSSR and for many RCM modes.

## 9.5 Future analysis

For output scaling, it is recommended that floating point products be made routinely available, at least for R&D purposes. Then the impacts of bit depth and application LUT could be better quantified. If staying with integer-based products, it is recommended that logarithmic  $\sigma^\circ$  scaling also be made routinely available. Certainly the availability of floating point products could obviate the need for logarithmic scaling, but on the other hand, for operational utilization there would be advantages to using logarithmic scaling including smaller product sizes and better quantization for scenes with very small backscatter.

It is well known that smaller values of BAQ will introduce noise into the resulting image. However, our analysis also suggests that smaller values of BAQ result in a loss of image texture. Our results are not definitive, however. As such, it is recommended that R-2 operators be encouraged to acquire and downlink 8-bit data from the satellite and use that to simulate and process various BAQ settings so that the impact of BAQ on quantitative image analysis can be more thoroughly evaluated. This could be particularly important for RCM for which lower BAQ settings will be used more routinely.

## **10 IA Pro upgrades**

---

Image Analyst Pro (IA Pro) is DRDC Ottawa's test bed system for validation and demonstration of new algorithms for geospatial intelligence [45], [46], [47]. The focus of IA Pro development was on tools that introduce automation, feature extraction and image combination/fusion to the exploitation of SAR and electro-optical imagery. IA Pro provides support for single- and multi-channel SAR and electro-optical imagery, and permits the image analyst to incorporate geospatial information (*i.e.*, thematic vector layers and digital maps) for contextual awareness and increased accuracy.

IA Pro was built using C++, Python, OpenEV and the Geospatial Data Abstraction Library (GDAL). Python is an open-source object-oriented interpreted programming language, OpenEV is an open-source library of raster and vector classes and functions, and GDAL is a translator library for raster geospatial data formats.

IA Pro provides a multitude of tools for the manipulation and exploitation of multi-sensor and multi-temporal imagery for geospatial intelligence, in particular to streamline the manipulation of SAR imagery from R-2. Several tools were explicitly developed in the context of this project, however, a detailed description of the tools and their operation is beyond the scope of this document (see [45], [46]). However, the key tools developed are outlined here along with example outputs in the subsequent sub-sections. Note that R2MS2 also supported maintenance of the software including bug fixes and improvements to several tools.

### **10.1 Scale-Lock tool and Re-projection tool**

Each SAR image displayed by IA Pro is self-normalized by clipping the image histogram. Since the image statistics vary spatially and there could be bright features such as land in some of the images, the overall displayed brightness will vary from image to image. This can be rather distracting, particularly if several sequential images have been loaded. The SAR Scale-Lock tool applies the same scaling to all SAR images to produce a uniform appearance from one image to the next. The impact of the Scale-lock tool is illustrated in Figure 110.

Until recently, IA Pro was unable to display imagery in an arbitrary map projection. This became problematic for R2MS2 since many of the scenes were acquired at high latitudes for which Lambert Conic Conformal (LCC) is an appropriate projection. With the introduction of the Re-projection tool in IA Pro, all data sets are first converted to a common projection prior to display, regardless of their native projections.

In the Re-projection tool, the user can also now select their projection of choice, thereby reducing the degree of distortion in area, shape, distance, or direction, as desired. The re-projection process is very fast since only the GCPs are re-projected. The original image file remains unchanged. The impact of the Re-projection tool from latitude/longitude to LCC is also illustrated in Figure 110.

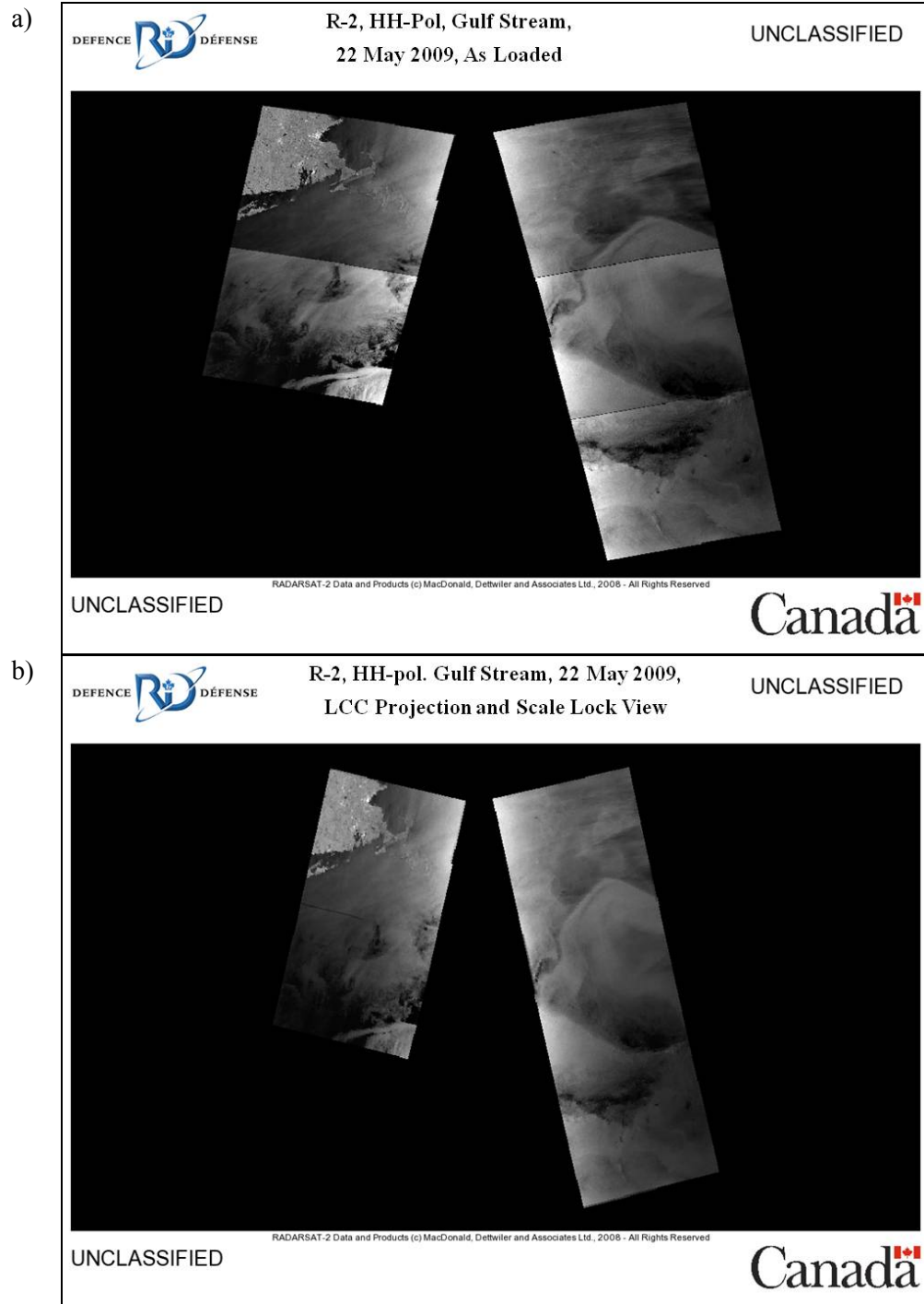


*Figure 110: Image sequence loaded in IA Pro: a) as loaded; and b) after application of the Scale-Lock tool and the Re-projection tool to LCC.*

## 10.2 Distributed Target Analysis tool

The IA Pro Distributed Target Analysis tool is used to assess image statistics over a region of an image including mean, standard deviation, skewness and kurtosis calculated on both amplitude and intensity versions of the image [45]. The results are also displayed for the radar backscatter expressed in decibels. The tool was initially restricted to analyzing the rectangular region in the main IA Pro display window, along with a data transect in the range direction averaged across the analysis region. Within R2MS2, the Distributed Target Analysis tool was upgraded to include two additional methods to assess image statistics:

- Along an arbitrary transect (Figure 111):
  - ◆ User drawn based upon two selected points and a configurable across-transect width;
- Within a polygonal region (Figure 112):
  - ◆ User drawn; or
  - ◆ Loaded from a ShapeFile.

The distributed target analysis tool displays separate windows for the transect and the summary statistics. The summary statistics are available for each polarization via separate tabs.

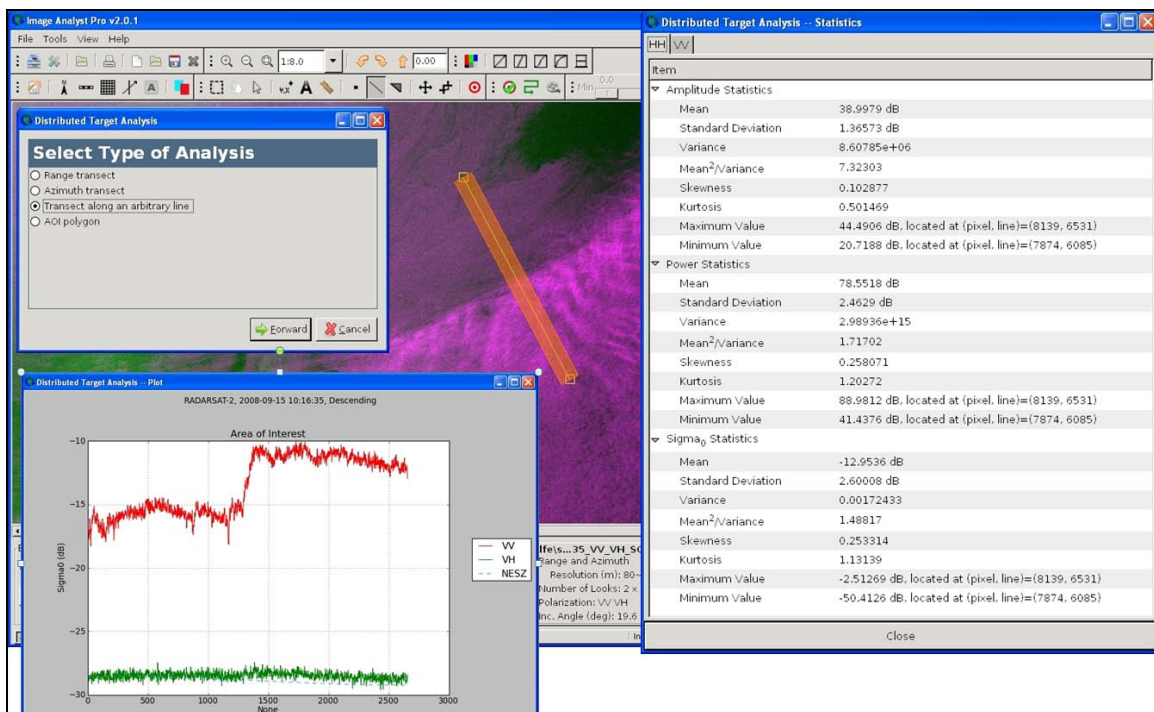


Figure 111: Arbitrary Transect option available in the IA Pro Distributed Target Analysis Tool.

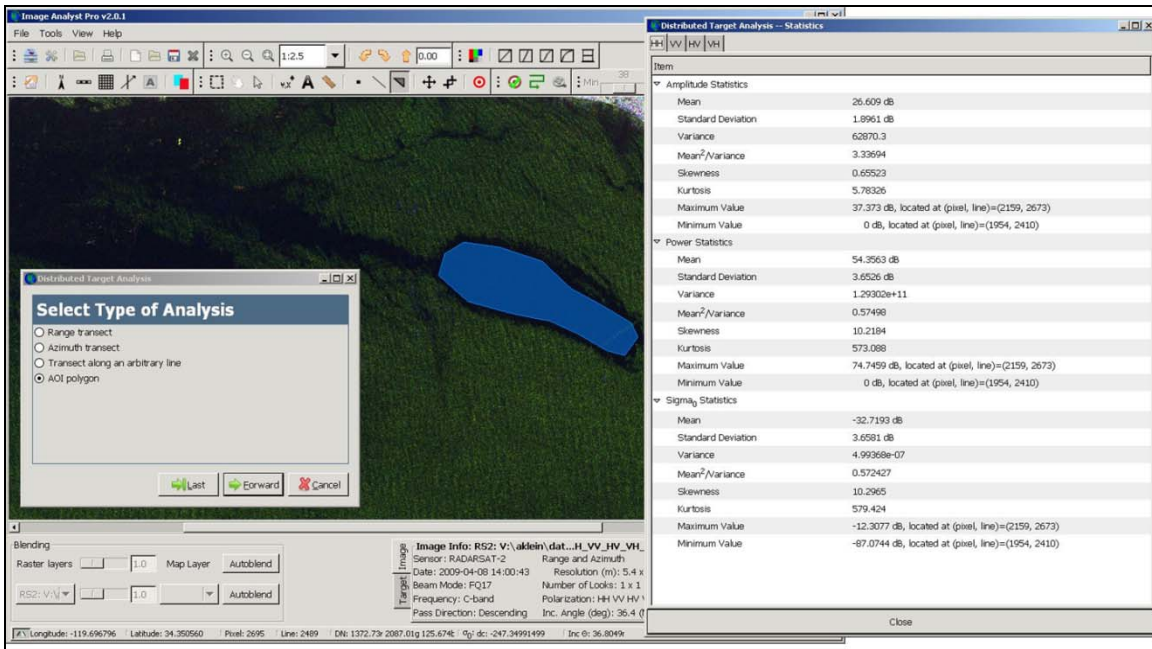


Figure 112: Polygonal Region option available in the IA Pro Distributed Target Analysis Tool.

### 10.3 Noise Subtraction tool

The IA Pro Noise Subtraction tool is intended to mitigate the visual appearance of the image noise floor for low signal-to-noise ratio images. This is particularly important for the cross-polarization channel for which the ocean backscatter is rather low. In low SNR cases the noise floor of the image is visible as azimuth bands, which essentially follow the shape of the elevation antenna pattern. The Noise Subtraction tool reconstructs the instrument noise floor from the product metadata, and then subtracts it in linear power space. The result is a smoother product with less visible impact from the elevation antenna pattern. The noise-subtracted image may be more suitable for visual interpretation.

Noise subtraction could be even more important for the new R-2 MSSR modes and for certain RCM modes since these modes use a single azimuth look. The impact of this is that the noise floor not only varies in range due to the elevation antenna pattern, but also various in azimuth, becoming cusped over the spatial scale of the azimuth burst.

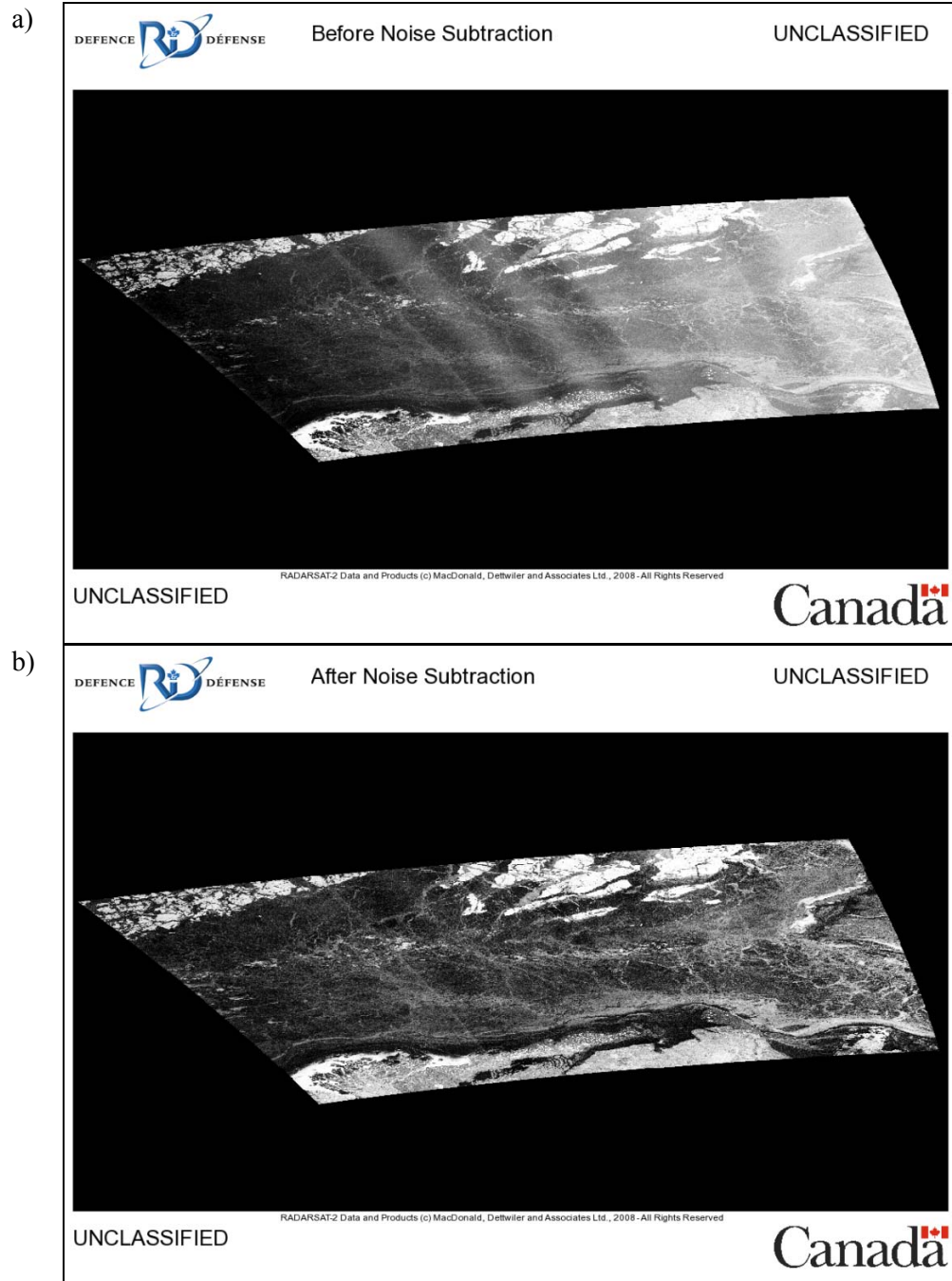


Figure 113: R-2 SCWA HV-polarization image near Mackenzie Delta, 2008-03-06: a) as processed; and b) following noise subtraction.

## 11 RADARSAT mode selection

---

The routine use of SAR in the maritime domain is expanding rapidly across various applications in Canada, Europe and the rest of the world. As shown in this study, maritime users have access to a wide range of R-2 modes to choose from. A major objective of this work was to present users with a clear recommendation concerning which wide swath mode best suited their surveillance requirements. Table 32 summarizes the recommendations from this study regarding a Primary Mode and a Secondary Mode for R-2 and RCM. The Primary Mode is the recommended mode when users have priority or no acquisition conflict exists. Increasingly, users are conflicting with each other in terms of mode selection and their Primary Mode may not be available. In this case, users are provided here with a Secondary Mode for consideration. Occasionally, due to downlink bandwidth limitations, users must confine themselves to single channel modes. As such, both dual channel and single channel recommendations for a Secondary Mode are provided. Although just recently implemented, the recommended MSSR modes are also included, based on their technical specifications and early results to date. In most cases, the related performance trade-offs involved with switching from the Primary Mode to the Secondary Mode are described in each applications section earlier in this document.

*Table 32: Primary, Secondary, and MSSR mode recommendations.*

Application	RADARSAT-2				RCM	
	Primary Mode	Secondary Mode		MSSR Mode	Primary Mode	Secondary Mode
		Dual Pol.	Single Pol.			
Sea ice monitoring	SCW HH+HV	SCW VV+VH	SCW HH	OSVN HH+HV	LN or LR HH+HV	MR 50 m HH+HV
Ice island monitoring	SCW HH+HV or VV+VH	SCNA HH+HV or VV+VH	SCNA HH	OSVN HH+HV or VV+VH	LN or MR 50 m HH+HV	MR 50 m HH+HV
Iceberg detection	SCNB HH+HV	SCNB VV+VH	SCNB HH	OSVN HH+HV	LN or MR 50 m HH+HV	MR 50 m HH+HV
Ship detection	DVWF HH	SCN HH+HV	SCNB HH	OSVN HH+HV	SD HH+HV	MR 50 m HH+HV
Wind speed estimation	SCW VV+VH	SCNA VV+VH	SCNA VV	OSVN VV+VH	LR VV+VH	MR 50 m VV+VH
Oil spill detection	SCNA VV	SCW VV+VH	SCW VV	OSVN VV	LN VV	MR 50 m VV
Ocean feature detection	SCNA VV	SCNA VV+VH	SCW VV	OSVN VV	LN or LR VV	MR 50 m VV

## **12 Conclusions**

---

Before the launch of R-2, the performance of dual co-pol C-band SAR in the maritime domain was largely understood. After the launch of R-2, the continued use of these heritage modes (*e.g.*, HH) for operational maritime surveillance was expected, at least in the immediate term following launch. Despite the advantages offered by R-2, mature maritime surveillance operations required a full understanding of the performance of these new modes and related trade-offs before integrating them into their existing workflows. This study, for the first time, has quantified the performance of R-2 ScanSAR modes across mature and new maritime applications.

The findings of the pre-launch assessment that kicked off this study were largely upheld. Higher resolution, multi-polarization datasets (*e.g.*, ASAR AP, CV-580) demonstrated the potential of dual polarization for maritime surveillance before the launch of R-2. This study and users experience to date has shown that dual-channel modes bring significant and worthy improvements to C-band-based maritime surveillance. Indeed, results of this investigation were the basis of the operational integration of dual channel R-2 within the Canadian Ice Service.

This study has helped to advance the understanding and use of cross-polarization for marine wind retrieval. It is fair to claim that these results represent a quantum leap ahead, especially for high wind speed scenarios. As a result, the soon to be operational marine wind program at Environment Canada will utilize a dual channel approach to provide marine users with routine estimations of surface wind speed.

This study also strongly suggests that dual channel modes should be considered the default mode for maritime surveillance. Future systems and related ground segments should be designed around this requirement. Downlink bandwidth should be large enough to routinely downlink two channels at high BAQ rates, thus preserving image quality by minimizing quantization effects. As well, system NESZ over wide surveillance swaths should be as low as possible to take full advantage of the benefits of the cross-polarization channel where SNR is typically poorer than the co-polarization channel over distributed targets like sea ice. In this regard, results show that users could find their applications (*e.g.*, sea ice monitoring) noise limited within some wide swath modes in future constellations including Sentinel-1 and RCM; in both cases the NESZ is expected to be poorer than that of R-2.

When considered together, the results of this project have highlighted the considerable synergy amongst maritime applications in terms of R-2 mode selection. This bodes well for a domain that is becoming increasingly crowded with operational users. The reality is that maritime SAR users are often in conflict with each other and sharing acquisitions with some compromise on mode selection is common. The results presented here provide users with an understanding of the associated tradeoffs when their primary mode is not available. Oil slick and ship detection are but one example where dual channel R-2 data can ease conflicts through the provision of two channels of information that meet the requirements of both applications. R-2's new OSVN mode, through its design, will provide maritime users with an alternative compromise mode designed to improve swath and resolution and maintain performance. Further investigation of this new maritime mode, as well as CP on RCM, is warranted.

## References

---

- [1] Alpers, W., and Huhnerfuss, H. (1988). Radar signatures of oil films floating on the sea surface and the marangoni effect. *Journal of Geophysical Research*, 98(C4), 3642-3648.
- [2] Alpers, W., and Huhnerfuss, H. (1989). The damping of ocean waves by surface films: A new look at an old problem. *Journal of Geophysical Research*, 94(C5), 6251-6265.
- [3] Beckett, K., Thompson, A., Luscombe, A., and Stirling, G. (2010). Optimization of RADARSAT-2 SAR imagery for vessel detection applications. In *Remote Sensing of the Ocean, Sea Ice, and Large Water Regions 2010*, edited by Bostater Jr., C.R., Mertikas, S.P., Neyt, X., and Velez-Reyes. M., Proc. of SPIE Vol. 7825, 78250A, 20-23 September 2010, Toulouse, France, SPIE.
- [4] Belkin, I., and Kessel, S. (2012). Russian drifting stations on Arctic ice islands. In *Arctic Ice Shelves and Ice Islands*, edited by Copland, L., and Mueller, D.R., Springer-Verlag, New York, In Press.
- [5] Canadian Ice Service (2005). Manual of Ice (MANICE). [Available: <http://www.ec.gc.ca/glaces-ice/default.asp?lang=En&n=4FF82CBD-1>.]
- [6] Canadian Ice Service (2010). Iceberg coding tables. [Available: <http://www.ec.gc.ca/glaces-ice/default.asp?lang=En&n=2E32310A-1>.]
- [7] C-CORE (2009). Analysis of single, dual and polarimetric Synthetic Aperture Radar data for iceberg/ship detection and discrimination – ASAR and Convair-580 SAR datasets from 2003 to 2007. C-CORE Report R-08-090-673, v2.0, December 2009.
- [8] Charbonneau, F.J., Brisco, B., Raney, R.K., McNairn, H., Liu, C., Vachon, P.W., Shang, J., DeAbreu, R., Champagne, C., Merzouki, A., and Geldsetzer, T. (2010). Compact polarimetry overview and applications assessment. *Canadian Journal of Remote Sensing*, 36(Suppl. 2), S298-S315.
- [9] Clark, J.F., Schwager, K., and Washburn, L. (2005). Variability of gas composition and flux intensity in natural marine hydrocarbon seeps. University of California Energy Institute, Berkeley, Nov. 2005. [Available: <http://www.escholarship.org/uc/item/59f9450h>.]
- [10] Copland, L., Mueller, D.R., and Weir, L. (2007). Rapid loss of the Ayles Ice Shelf, Ellesmere Island, Canada. *Geophysical Research Letters*, 34, L21501.
- [11] Crawley, M. J. (2007). *The R Book*. John Wiley and Sons, Ltd., Chichester, UK, 942 pp.
- [12] Espedal, H. (1999). Detection of oil spill and natural film in the marine environment by spaceborne SAR. Proc. IEEE Geoscience and Remote Sensing Symposium, 28 June - 2 July 1999, Hamburg, Germany, IEEE, Volume 3, 1478-1480.

- [13] Farwell, C., Reddy, C., Peacock, E., Nelson, R., Washburn, L., and Valentine, D. (2009). Weathering and the fallout plume of heavy oil from strong petroleum seeps near coal oil point, CA. *Environmental Science and Technology*, 43(10), 3542 -3548.
- [14] Flett, D., Crevier, Y., and Girard, R. (2009). The RADARSAT Constellation Mission: Meeting the Government of Canada's needs and requirements. Proc. IEEE Geoscience and Remote Sensing Symposium, 12-17 July 2009, Cape Town, South Africa, IEEE, Volume II, 910-912.
- [15] Fuglem, M., and Jordaan, I. (2012). Risk analysis and hazards of ice islands. In *Arctic Ice Shelves and Ice Islands*, edited by Copland, L., and Mueller, D.R., Springer-Verlag, New York, In Press.
- [16] Gadimova, S. (2000). Towards the development of an operational strategy for oil spill detection and monitoring in the Caspian Sea based upon a technical evaluation of satellite SAR observations in Southeast Asia. Proc. ISPRS XIXth Congress, 16023 July 2000, Amsterdam, the Netherlands, ISPRS, 295-300. [Available: [http://www.isprs.org/proceedings/XXXIII/congress/part1/295\\_XXXIII-part1.pdf](http://www.isprs.org/proceedings/XXXIII/congress/part1/295_XXXIII-part1.pdf).]
- [17] Girard-Ardhuin, F., Mercier, G., and Garello, R. (2003). Oil slick detection by SAR imagery: potential and limitation. Proc. Marine Technology and Ocean Science Conference, 22-26 September 2003, San Diego, USA, Marine Technology Society and IEEE, 22-26.
- [18] Hamre, T., and Espedal, H. (1996). Operational use of wind data for slick detection. Proc. 3<sup>rd</sup> ERS Symposium, 14-21 March 1997, Florence, Italy, ESA, 1417-1422.
- [19] Hauser, D., Caudal, G., Dechambre, M., and Podvin, T. (2003). Polarimetric measurements over the sea-surface with the airborne STORM radar in the context of the geophysical validation of the ENVISAT ASAR. Proc. PolinSAR 2003, 14-16 Jan. 2003, Frascati, Italy, ESA. [Available: <http://earth.esa.int/workshops/polinsar2003/participants/hauser5/POLINSAR-VALPARESO.pdf>]
- [20] Hersbach, H., Stoffelen, A., and de Haan, S. (2007). An improved C-band scatterometer ocean geophysical mode function: CMOD5. *Journal of Geophysical Research*, 112(C3), doi:10.1029/2006JC003743.
- [21] Hornafius, J.S., Quigley, D., and Luyendyk, B.P. (1999). The world's most spectacular marine hydrocarbon seeps (Coal Oil Point, Santa Barbara Channel, California): Quantification of emissions. *Journal of Geophysical Research*, 104(C9), 703-720.
- [22] Hovland, H.A., Johannessen, J.A., and Digranes, G. (1994). Slick detection in SAR images. Proc. IEEE Geoscience and Remote Sensing Symposium, 8-12 August 1994, Pasadena, USA, IEEE, volume 4, 2038 – 2040.

- [23] Jeffries, M.O. (1992). Arctic ice shelves and ice islands: Origin, growth and disintegration, physical characteristics, structural-stratigraphic variability, and dynamics. *Reviews of Geophysics*, 30, 245-267.
- [24] Jeffries, M.O. (2002). Ellesmere Island ice shelves and ice islands. In *Satellite Image Atlas of Glaciers of the World: North America*, edited by Williams, R.S., and Ferrigno, J.G., pp. J147-J164, United States Geological Survey, Washington.
- [25] Johannessen, J.A., Digranes, G., Espedal, H., Johannessen, O.M., Samuel, P., Browne, D., Vachon, P.W. (1994). *SAR Ocean Feature Catalogue*. ESA SP-1174, Noordwijk, the Netherlands.
- [26] Leifer, I., Kamerling, M.J., Luyendyk, B.P., and Wilson, D.S. (2010). Geologic control of natural marine seep hydrocarbon emissions, Coal Oil Point seep field, California. *Geo-Marine Letters*, 30, 331-338. [Available: <http://www.springerlink.com/content/w14n351tn2267g77/fulltext.pdf>.]
- [27] Litovchenko, K., Ivanov, A., and Ermakov, S. (1999). Detection of oil slicks parameters from ALMAZ-1 and ERS-1 SAR imagery. Proc. IEEE Geoscience and Remote Sensing Symposium, 28 June - 2 July 1999, Hamburg, Germany, IEEE, volume 3, 1484-1486.
- [28] Luscombe, A. (2008). RADARSAT-2 polarimetric mode calibration and data quality assessment. Proc. CEOS SAR Calibration and Validation Workshop, 27-28 Nov. 2008, Oberpfaffenhofen, Germany, DLR.
- [29] MDA (2011). Radarsat-2 Product Description. Document Number RN-SP-52-1238, Issue 1/8, April 2011. [Available: [http://gs.mdacorporation.com/includes/documents/RN-SP-52-1238%20RS-2%20Product%20Description%201-8\\_15APR2011.pdf](http://gs.mdacorporation.com/includes/documents/RN-SP-52-1238%20RS-2%20Product%20Description%201-8_15APR2011.pdf)]
- [30] Monaldo, F.M., Thompson, D.R., Beal, R.C., Pichel, W.G., and Clementé-Colón, P. (2001). Comparison of SAR-derived wind speed with model predictions and ocean buoy measurements. *IEEE Transactions on Geoscience and Remote Sensing*, 39(12), 2587-2600.
- [31] Mueller, D.R., Copland, L., Hamilton, A., and Stern, D. (2008). Examining Arctic ice shelves prior to 2008 breakup. *Eos, Transactions of the American Geophysical Union*, 89, 502-503.
- [32] Mueller, D.R., Vincent, W.F., and Jeffries, M.O. (2003). Break-up of the largest Arctic ice shelf and associated loss of an epishelf lake. *Geophysical Research Letters*, 30(20), 2003.
- [33] Mueller, D.R., Vincent, W.F., and Jeffries, M. (2006). Environmental gradients, fragmented habitats and microbiota of a northern ice shelf cryoecosystem, Ellesmere Island, Canada. *Arctic, Antarctic, and Alpine Research*, 38, 593-607.
- [34] Oliver, C., and Quegan, S. (2004). *Understanding synthetic aperture radar images*. SciTech Publishing, North Carolina.

- [35] Onstott, R.G., and Shuchman, R.A. (2004). SAR measurements of sea ice. In *Synthetic Aperture Radar Marine User's Manual*, National Oceanic and Atmospheric Administration, Washington D.C., 81-115.
- [36] Pinheiro, J.C., and Bates, D.M. (2000). *Mixed-effects models in S and S-Plus*. Springer, New York, 528 pp.
- [37] Power, D., Youden, J., Lane, K., Randell, C., and Flett, D. (2001). Iceberg detection capabilities of RADARSAT synthetic aperture radar. *Canadian Journal of Remote Sensing*, 27(5), 476-486.
- [38] Quilfen, Y., and Cavanie, A. (1991). A high precision wind algorithm for ERS-1 scatterometer and its validation. Proc. IEEE International Geoscience and Remote Sensing Symposium, 3-6 June 1991, Helsinki, Finland, IEEE, 873-876.
- [39] Quilfen, Y., Chapron, B., Elfouhaily, T.M., Katsaros, K., and Tournadre, J. (1998). Observation of tropical cyclones by high-resolution scatterometry. *Journal of Geophysical Research*, 103(C4), 7767-7786.
- [40] Ramsay, B., Flett, D., Andersen, H.S., Gill, R., Nghiem, S., and Bertoia, C. (2004). Preparation for the operational use of RADARSAT-2 for ice monitoring. *Canadian Journal of Remote Sensing*, 30(3), 415-423.
- [41] Randell, C., Rokonuzzaman, M., Youden, J., and Khan, R. (1999). Evaluation of RADARSAT for detection, classification and discrimination of icebergs. Proc. Application Development and Research Opportunity (ADRO) Final Symposium, 15-18 Oct. 1998, Montreal, Canadian Space Agency.
- [42] Raney, R.K., and Wessels, G.J. (1988). Spatial considerations in SAR speckle simulation. *IEEE Transactions on Geoscience and Remote Sensing*, 26(5), 666-672.
- [43] Raney, R.K. (2007). Hybrid-polarity SAR architecture. *IEEE Transactions on Geoscience and Remote Sensing*, 45(11), 3397-3404.
- [44] Saenz, J.M. (2002). Geological controls of hydrocarbon seeps in Santa Maria Basin, offshore California. M.S. thesis, California State University at Northridge, Northridge, California, 292 p.
- [45] Secker, J., and Vachon, P.W. (2010). New tools and products for SAR-based geospatial intelligence (GEOINT): Implementation in Image Analyst Pro Version 1.9. DRDC Ottawa TR 2010-222, Defence R&D Canada – Ottawa.
- [46] Secker, J., and Vachon, P.W. (2007). Exploitation of multi-temporal SAR and EO satellite imagery for geospatial intelligence. Proc. Fusion 2007: The 10<sup>th</sup> International Conference on Information Fusion, 9-12 July 2007, Quebec City, IEEE.

- [47] Secker, J., Walter, G. and Espeset, A. (2005). Image Analyst Pro: A new multi-sensor imagery exploitation system for geospatial intelligence. DRDC Ottawa TR 2005-219, Defence R&D Canada – Ottawa.
- [48] Shaw, B., Winslett, B., and Cross, F.B. (1987). The global environment: A proposal to eliminate marine oil pollution. *Natural Resource Journal*, 157.
- [49] Sigalove, J. (1985). Geochemical identification of resource potential. *Oil and Gas Journal*, 20(9), 77-79.
- [50] Solberg, A.H.S., and Brekke, C. (2005). Oil spill detection by satellite remote sensing. *Remote Sensing of Environment*, 95(1), 1-13.
- [51] Stoffelen, A., and Anderson, D.L.T. (1993). Wind retrieval and ERS-1 scatterometer radar backscatter measurements. *Advances in Space Research*, 13(5), 53-60.
- [52] Stoffelen, A., and Anderson, D.L.T. (1997). Scatterometer data interpretation: Estimation and validation of the transfer function CMOD4. *Journal of Geophysical Research*, 102(C3), 5767-5780.
- [53] Stout, H.B. (1993). Overview of oiled bird rehabilitation. Proc. Third International Conference on the Effects of Oil on Wildlife, 27-29 January 1993, New Orleans, USA, Tri-State Bird Rescue and Research, 38-39.
- [54] Thurston, H. (2005). Sea Birds in the Wake. *Canadian Geographic*, September/October 2005.
- [55] Vachon, P.W., Campbell, J., Bjerkelund, C., Dobson, F., and Rey, M. (1997). Ship detection by the RADARSAT SAR: Validation of detection model predictions. *Canadian Journal of Remote Sensing*, 23(1), 48-59.
- [56] Vachon, P.W., and Dobson, F.W. (2000). Wind retrieval from RADARSAT SAR images: Selection of a suitable C-band HH polarization wind retrieval model. *Canadian Journal of Remote Sensing*, 26(4), 306–313.
- [57] Vachon, P.W., A.L. Gray, C.E. Livingstone, and A.P. Luscombe (1997). Adaptive compensation of RADARSAT SAR analogue-to-digital converter saturation power loss. Geomatics in the ERA of RADARSAT (GER'97), CD-ROM Proceedings, 27-30 May 1997, Ottawa, CCRS.
- [58] Vachon, P.W., Wolfe, J., and Hawkins, R.K. (2004). Comparison of C-band wind retrieval model functions with airborne polarimetric SAR data. *Canadian Journal of Remote Sensing*, 30(3), 462-469.
- [59] Vachon, P.W., and Wolfe, J. (2008). GMES Sentinel-1 Analysis of Marine Applications Potential (AMAP). DRDC Ottawa ECR 2008-218, Defence R&D Canada – Ottawa.
- [60] Vachon, P.W. and Wolfe, J. (2011). C-band Cross-polarization wind speed retrieval. *IEEE Geoscience and Remote Sensing Letters*, 8(3), 456-459.

- [61] Van Wychen, W., and Copland, L. (2012). Ice island drift mechanisms in the Canadian High Arctic. In *Arctic Ice Shelves and Ice Islands*, edited by Copland, L., and Mueller, D.R., Springer-Verlag, New York, In Press.
- [62] Washburn, L., Clark, J.F., and Kyriakidis, P. (2005). The spatial scales, distribution and intensity of natural marine hydrocarbon seeps near Coal Oil Point, California. *Marine and Petroleum Geology*, 22(4), 569-578.
- [63] Whitehouse, B.G. (2009). RADARSAT-2 for maritime surveillance: Preferred ScanSAR polarizations and observed knowledge gaps. DRDC Ottawa CR 2009-027, Defence R&D Canada – Ottawa.
- [64] Wiese, F. (2002). Seabirds and Atlantic Canada's ship-source oil pollution. World Wildlife Fund, Toronto, Canada. [Available: [http://assets.wwfca.panda.org/downloads/wwf\\_northwestatlantic\\_seabirdsandshipsourceoilproduction.pdf](http://assets.wwfca.panda.org/downloads/wwf_northwestatlantic_seabirdsandshipsourceoilproduction.pdf).]
- [65] Williams, D., DeTracey, B., Vachon, P.W., Wolfe, J., Secker, J., Perrie, W., Larouche, P., Jones, C., and Buckley, J. (2010). Spaceborne Ocean Intelligence Network: SOIN - fiscal year 09/10 year-end summary and proposal for Phase II. DRDC Ottawa ECR 2010-094, Defence R&D Canada - Ottawa.

## **List of symbols/abbreviations/acronyms/initialisms**

---

AIS	Automatic Identification System
ALOS	Advanced Land-Observation Satellite (Japan)
ANCOVA	Analysis of Covariance
AOI	Area of Interest
ASAR	Advanced SAR (on ENVISAT)
ASF	Alaska SAR Facility
AVHRR	Advanced Very High Resolution Radiometer
B	Blue
BAQ	Block Adaptive Quantization
CF	Canadian Forces
CFAR	Constant False Alarm Rate
CIS	Canadian Ice Service
CMOD	C-band Model
CP	Compact Polarimetry
CSA	Canadian Space Agency
dB	Decibel
DN	Digital Number
DND	Department of National Defence
DR	Dynamic Range
DRDC	Defence Research & Development Canada
DVWF	Detection of Vessels, Wide swath, Far incidence (MSSR)
EC	Environment Canada
ECR	External Client Report
EH	Extended High (mode)
EL	Extended Low (mode)
ENL	Equivalent Number of Looks
ENVISAT	Environmental Satellite (ESA)
ERS	Earth Resources Satellite (ESA)
ESA	European Space Agency
FQ	Fine Quad polarization

FYI	First-Year Ice
G	Green
GCP	Ground Control Point
GDAL	Geospatial Data Abstraction Library
GMES	Global Monitoring for Environment and Security
GPS	Global Positioning System
GRIP	Government Related Initiative Program
GUI	Graphical User Interface
HH	Horizontal transmit, Horizontal receive
HV	Horizontal transmit, Vertical receive
I	In-phase
IA Pro	Image Analyst Professional
ISTOP	Integrated Satellite Tracking Of Polluters
IW	Interferometric Wide (mode on Sentinel-1)
JAXA	Japanese Aerospace Exploration Agency
LCC	Lambert Conic Conformal
LN	Low Noise (RCM)
LR	Low Resolution (RCM)
LUT	Look-Up Table
MDA	MacDonald Dettwiler and Associates, Ltd.
MetOc	Meteorological and Oceanographic
MR	Medium Resolution (RCM)
MSSR	Maritime Satellite Surveillance Radar
MYI	Multi-Year Ice
NESZ	Noise-Equivalent Sigma Zero
NESZ sc	NESZ for ScanSAR
NESZ st	NESZ for single beam (i.e., strip map)
NIC	National Ice Center (USA)
OGD	Other Government Department
OSVN	Ocean Surveillance, Very wide swath, Near incidence (MSSR)
OW	Open Water
PAL	Provincial Aerospace Ltd.

PALSAR	Phased Array type L-band SAR (on ALOS)
PE	Polar Epsilon
POD	Probability of Detection
Q	Quadrature
R	Red
R&D	Research & Development
R-1	RADARSAT-1
R-2	RADARSAT-2
R2MS2	RADARSAT-2 Mode Selection for Maritime Surveillance
RCM	RADARSAT Constellation Mission
RCS	Radar Cross Section
RMS	Root-Mean-Squared
RxA	Range by Azimuth
S	Standard (mode)
SAR	Synthetic Aperture Radar
SCF	ScanSAR Fine (Re: MSSR)
SCN	ScanSAR Narrow
SCNA	ScanSAR Narrow A (mode)
SCNB	ScanSAR Narrow B (mode)
SCS	ScanSAR Sampled (Re: MSSR)
SCW	ScanSAR Wide
SCWA	ScanSAR Wide A (mode)
SCWB	ScanSAR Wide B (mode)
SD	Ship Detection (RCM)
SDPT	Ship Detection Performance Tool
SLC	Single Look Complex
SNR	Signal to Noise Ratio
SOIN	Spaceborne Ocean Intelligence Network
SST	Sea Surface Temperature
STSE	Support to Science Element
UF	Ultra Fine
var.	Variable

VH	Vertical transmit, Horizontal receive
VV	Vertical transmit, Vertical receive
W	Wide (mode)
WMO	World Meteorological Organization

**DOCUMENT CONTROL DATA**

(Security markings for the title, abstract and indexing annotation must be entered when the document is Classified or Designated)

<p>1. ORIGINATOR (The name and address of the organization preparing the document. Organizations for whom the document was prepared, e.g. Centre sponsoring a contractor's report, or tasking agency, are entered in section 8.)</p> <p>Defence Research and Development Canada – Ottawa 3701 Carling Avenue Ottawa, Ontario K1A 0Z4</p>		<p>2a. SECURITY MARKING (Overall security marking of the document including special supplemental markings if applicable.)</p> <p><b>UNCLASSIFIED</b></p>
		<p>2b. CONTROLLED GOODS  (NON-CONTROLLED GOODS) DMC A REVIEW: GCEC DECEMBER 2013</p>
<p>3. TITLE (The complete document title as indicated on the title page. Its classification should be indicated by the appropriate abbreviation (S, C or U) in parentheses after the title.)</p> <p><b>RADARSAT-2 mode selection for maritime surveillance</b></p>		
<p>4. AUTHORS (last name, followed by initials – ranks, titles, etc. not to be used)</p> <p><b>De Abreu, R.; Arkett, M.; Cheng, A.; Zagon, T.; Mueller, D.; Vachon, P.; Wolfe, J.</b></p>		
<p>5. DATE OF PUBLICATION (Month and year of publication of document.)</p> <p>November 2011</p>	<p>6a. NO. OF PAGES (Total containing information, including Annexes, Appendices, etc.)</p> <p><b>188</b></p>	<p>6b. NO. OF REFS (Total cited in document.)</p> <p><b>65</b></p>
<p>7. DESCRIPTIVE NOTES (The category of the document, e.g. technical report, technical note or memorandum. If appropriate, enter the type of report, e.g. interim, progress, summary, annual or final. Give the inclusive dates when a specific reporting period is covered.)</p> <p><b>External Client Report</b></p>		
<p>8. SPONSORING ACTIVITY (The name of the department project office or laboratory sponsoring the research and development – include address.)</p> <p>Defence Research and Development Canada – Ottawa 3701 Carling Avenue Ottawa, Ontario K1A 0Z4</p>		
<p>9a. PROJECT OR GRANT NO. (If appropriate, the applicable research and development project or grant number under which the document was written. Please specify whether project or grant.)</p>	<p>9b. CONTRACT NO. (If appropriate, the applicable number under which the document was written.)</p>	
<p>10a. ORIGINATOR'S DOCUMENT NUMBER (The official document number by which the document is identified by the originating activity. This number must be unique to this document.)</p> <p><b>DRDC Ottawa ECR 2011-168</b></p>	<p>10b. OTHER DOCUMENT NO(s). (Any other numbers which may be assigned this document either by the originator or by the sponsor.)</p>	
<p>11. DOCUMENT AVAILABILITY (Any limitations on further dissemination of the document, other than those imposed by security classification.)</p> <p><b>Unlimited</b></p>		
<p>12. DOCUMENT ANNOUNCEMENT (Any limitation to the bibliographic announcement of this document. This will normally correspond to the Document Availability (11). However, where further distribution (beyond the audience specified in (11) is possible, a wider announcement audience may be selected.)</p> <p><b>Unlimited</b></p>		

13. ABSTRACT (A brief and factual summary of the document. It may also appear elsewhere in the body of the document itself. It is highly desirable that the abstract of classified documents be unclassified. Each paragraph of the abstract shall begin with an indication of the security classification of the information in the paragraph (unless the document itself is unclassified) represented as (S), (C), (R), or (U). It is not necessary to include here abstracts in both official languages unless the text is bilingual.)

The main objective of the RADARSAT-2 Mode Selection for Maritime Surveillance (R2MS2) project was to identify and recommend ScanSAR-based maritime surveillance modes for RADARSAT-2 (R-2), while also preparing for exploitation of the RADARSAT Constellation Mission (RCM). The primary focus of R2MS2 *was on* the performance of wide swath, ScanSAR modes of operation including ScanSAR Wide (SCW) and ScanSAR Narrow (SCN). The following maritime surveillance applications were considered: sea ice surveillance; ice island monitoring; iceberg detection; ship detection; wind speed estimation; oil spill detection; and ocean feature detection. Furthermore, several image quality issues were considered: application look-up table (LUT) performance in converting floating point numbers in the processor into integers in the image product; the block adaptive quantization (BAQ) setting for reduction of raw data volume; and noise subtraction for mitigation of the visual impact of the noise floor for low signal to noise ratio acquisitions. Finally, several tools were developed for DRDC Ottawa's Image Analyst Pro (IA Pro) software test bed to support R2MS2 data processing needs. For the maritime surveillance applications considered, the approach included a combination of theoretical analysis and field trials to gather new data sets of known targets, with validation whenever possible. The trials often focused on the collection of R-2 Fine Quad (FQ) mode imagery such that all linear polarization choices (i.e., HH, HV, VV, and VH) were simultaneously available. Then, observations could be extended to the ScanSAR cases *through appropriate* modification of the noise floor, spatial resolution, and radiometric resolution. Along with recommended surveillance modes by application, multiple use (i.e., one acquisition serving multiple maritime applications) opportunities were identified that would streamline order planning and maximize R-2 utilization.

Le principal objectif du projet de sélection de modes RADARSAT-2 adaptés à la surveillance maritime (R2MS2) était d'identifier et de recommander des modes de surveillance maritime ScanSAR pour RADARSAT-2 (R-2), tout en préparant l'exploitation de la mission de la constellation RADARSAT (MCR). Le projet R2MS2 a mis l'accent principalement sur la performance des modes de fonctionnement ScanSAR à large bande, y compris le mode ScanSAR large (SCW) et le mode ScanSAR étroit (SCN). Voici les applications de surveillance maritime qui ont été examinées : surveillance des glaces de mer; surveillance des îles de glace; détection des icebergs; détection des navires; estimation de la vitesse du vent; détection de déversements d'hydrocarbures et détection des caractéristiques des océans. On a aussi tenu compte de plusieurs questions liées à la qualité des images : performance de la table de consultation (LUT) des applications dans la conversion des nombres à point flottant du processeur en nombres entiers dans les produits d'image; le réglage de la quantification adaptative des blocs (BAQ) en vue d'une réduction du volume de données brutes et de la soustraction du bruit en vue de l'atténuation de l'incidence visuelle du plancher de bruit pour les acquisitions du rapport signal/bruit. Enfin, plusieurs outils ont été mis au point pour le banc d'essai du logiciel Image Analyst Pro (IA Pro) de RDDC Ottawa à l'appui des besoins en traitement de données du projet R2MS2. Pour les applications de surveillance maritime examinées, l'approche a compris une combinaison d'analyses théoriques et d'essais sur le terrain en vue de la collecte de nouveaux jeux de données de cibles connues, moyennant validation dans la mesure du possible. Les essais ont souvent porté sur la collecte d'images en mode fin à quadruple polarisation (FQ) R-2, de sorte que tous les choix de polarisation rectiligne (c'est-à-dire HH, HV, VV et VH) étaient disponibles simultanément. Il était alors possible d'élargir les observations aux cas ScanSAR par la modification appropriée du plancher de bruit, la résolution spatiale et la résolution radiométrique. Outre les modes de surveillance recommandés par application, on a repéré des possibilités d'utilisation multiple (c'est-à-dire une acquisition pouvant servir dans le cas de plusieurs applications maritimes) qui permettraient de rationaliser la planification de l'ordonnancement et d'optimiser l'utilisation de R-2.

14. KEYWORDS, DESCRIPTORS or IDENTIFIERS (Technically meaningful terms or short phrases that characterize a document and could be helpful in cataloguing the document. They should be selected so that no security classification is required. Identifiers, such as equipment model designation, trade name, military project code name, geographic location may also be included. If possible keywords should be selected from a published thesaurus, e.g. Thesaurus of Engineering and Scientific Terms (TEST) and that thesaurus identified. If it is not possible to select indexing terms which are Unclassified, the classification of each should be indicated as with the title.)

RADARSAT-2; synthetic aperture radar; maritime surveillance; sea ice monitoring; ice island monitoring; iceberg detection; ship detection; wind speed estimation; oil spill detection; ocean feature detection; image quality



## **Defence R&D Canada**

Canada's leader in Defence  
and National Security  
Science and Technology

## **R & D pour la défense Canada**

Chef de file au Canada en matière  
de science et de technologie pour  
la défense et la sécurité nationale



[www.drdc-rddc.gc.ca](http://www.drdc-rddc.gc.ca)